

Mechanisms and Machine Science

Giuseppe Carbone
Med Amine Laribi *Editors*

Robot Design

From Theory to Service Applications



IFToMM



Springer

Mechanisms and Machine Science

Volume 123

Series Editor

Marco Ceccarelli , Department of Industrial Engineering, University of Rome Tor Vergata, Roma, Italy

Advisory Editors

Sunil K. Agrawal, Department of Mechanical Engineering, Columbia University, New York, USA

Burkhard Corves, RWTH Aachen University, Aachen, Germany

Victor Glazunov, Mechanical Engineering Research Institute, Moscow, Russia

Alfonso Hernández, University of the Basque Country, Bilbao, Spain

Tian Huang, Tianjin University, Tianjin, China

Juan Carlos Jauregui Correa , Universidad Autonoma de Queretaro, Queretaro, Mexico

Yukio Takeda, Tokyo Institute of Technology, Tokyo, Japan

This book series establishes a well-defined forum for monographs, edited Books, and proceedings on mechanical engineering with particular emphasis on MMS (Mechanism and Machine Science). The final goal is the publication of research that shows the development of mechanical engineering and particularly MMS in all technical aspects, even in very recent assessments. Published works share an approach by which technical details and formulation are discussed, and discuss modern formalisms with the aim to circulate research and technical achievements for use in professional, research, academic, and teaching activities.

This technical approach is an essential characteristic of the series. By discussing technical details and formulations in terms of modern formalisms, the possibility is created not only to show technical developments but also to explain achievements for technical teaching and research activity today and for the future.

The book series is intended to collect technical views on developments of the broad field of MMS in a unique frame that can be seen in its totality as an Encyclopaedia of MMS but with the additional purpose of archiving and teaching MMS achievements. Therefore, the book series will be of use not only for researchers and teachers in Mechanical Engineering but also for professionals and students for their formation and future work.

The series is promoted under the auspices of International Federation for the Promotion of Mechanism and Machine Science (IFToMM).

Prospective authors and editors can contact Mr. Pierpaolo Riva (publishing editor, Springer) at: pierpaolo.riva@springer.com

Indexed by SCOPUS and Google Scholar.

Giuseppe Carbone · Med Amine Laribi
Editors

Robot Design

From Theory to Service Applications



Springer

Editors

Giuseppe Carbone 
DIMEG
University of Calabria
Arcavacata di Rende, Italy

Med Amine Laribi 
SP2MI - Site du Futuroscope
University of Poitiers
Poitiers, France

ISSN 2211-0984

ISSN 2211-0992 (electronic)

Mechanisms and Machine Science

ISBN 978-3-031-11127-3

ISBN 978-3-031-11128-0 (eBook)

<https://doi.org/10.1007/978-3-031-11128-0>

© The Editor(s) (if applicable) and The Author(s), under exclusive license to Springer Nature Switzerland AG 2023

This work is subject to copyright. All rights are solely and exclusively licensed by the Publisher, whether the whole or part of the material is concerned, specifically the rights of translation, reprinting, reuse of illustrations, recitation, broadcasting, reproduction on microfilms or in any other physical way, and transmission or information storage and retrieval, electronic adaptation, computer software, or by similar or dissimilar methodology now known or hereafter developed.

The use of general descriptive names, registered names, trademarks, service marks, etc. in this publication does not imply, even in the absence of a specific statement, that such names are exempt from the relevant protective laws and regulations and therefore free for general use.

The publisher, the authors, and the editors are safe to assume that the advice and information in this book are believed to be true and accurate at the date of publication. Neither the publisher nor the authors or the editors give a warranty, expressed or implied, with respect to the material contained herein or for any errors or omissions that may have been made. The publisher remains neutral with regard to jurisdictional claims in published maps and institutional affiliations.

This Springer imprint is published by the registered company Springer Nature Switzerland AG
The registered company address is: Gewerbestrasse 11, 6330 Cham, Switzerland

Preface

Nowadays, robotics is developing at a much faster pace than ever in the past, both inside and outside industrial environments. This book is an attempt to address this wide topic with a multidisciplinary approach. While other publications focus on describing the theoretical basis of robot motion, this book pays special attention to explain the fundamentals through real applications. Thus, it represents a perfect combination for studying this topic along with other theoretical books.

Each chapter has been authored by experts in specific areas spanning from the mechanics of machinery to control theory, informatics and mechatronics. Chapters have been divided into two parts. The first one is aiming to give a theoretical background. The second part is focused on applications.

The book is arranged in ten chapters where Chap. 1 deals with historical backgrounds on robot design. Chapter 2 introduces mathematical formulations for robot modelling: serial versus parallel structures. Chapter 3 deals with simulating vibrations of two-wheeled self-balanced robots with road excitations in MATLAB environment. Chapter 4 introduces the path planning for special robotic operations. Chapter 5 deals with the robot design by proposing optimization methods and a task-based design approach. Chapter 6 covers the topic of robots for inspection and maintenance of power transmission lines. Chapter 7 presents a human activity recognition for enhanced robot-assisted surgery. Chapter 8 describes some metamorphic manipulators. Chapter 9 compiles the analysis of redundancy and the elasticity of actuators in the hopping control of the bipedal robot CARL as based on a SLIP model. Chapter 10 completes the book with a dynamic modelling for stability evaluation of an asbestos removal mobile manipulator.

This book project can be foreseen as a reference for young professionals/researchers to overview the most significant aspects in robotics. Given the wideness of the topic, this book can be considered as a first edition, and, as Editors, we shall be pleased to consider additional contents/suggestions for a future edition.

We wish to acknowledge all the authors and expert blind reviewers for their significant contributions to this project. Also acknowledged is the professional assistance by the staff at Springer Nature that have supported this project with their help and advice in the preparation of the book.

Finally, we would like to thank our families. Without their patience and understanding, it would not have been possible for us to work on this book.

Arcavacata di Rende, Italy
Poitiers, France
June 2022

Giuseppe Carbone
Med Amine Laribi

Contents

Part I Fundamentals

1	Historical Backgrounds on Robot Mechanism Design	3
	Marco Ceccarelli	
2	Mathematical Formulations for Robot Modelling: Serial Versus Parallel Structures	23
	Lotfi Romdhane, Mohammad Jaradat, and Zouhaier Affi	
3	Simulating Vibrations of Two-Wheeled Self-balanced Robots with Road Excitations by MATLAB	51
	William Guo and Wei Li	
4	Path Planning for Special Robotic Operations	69
	Paolo Boscaroli, Alessandro Gasparetto, and Lorenzo Scalera	
5	Robot Design: Optimization Methods and Task-Based Design	97
	Med Amine Laribi, Giuseppe Carbone, and S. Zeghloul	

Part II Applications

6	Review: Robots for Inspection and Maintenance of Power Transmission Lines	119
	Rogério Sales Gonçalves, Frederico Costa Souza, Rafael Zimmermann Homma, Daniel Edgardo Tio Sudbrack, Paulo Victor Trautmann, and Bruno Cordeiro Clasen	
7	Towards Human Activity Recognition Enhanced Robot Assisted Surgery	143
	Hang Su and Elena De Momi	
8	Metamorphic Manipulators	169
	Charalampos Valsamos, Nikolaos Stravopodis, Vassilis Moulianitis, and Nikos A. Apsragathos	

9 Analysis of Redundancy and Elasticity of Actuators in Hopping Control of Bipedal Robot CARL Based on SLIP Model	207
Atabak Nejadfar, Nicolas Franz Schmitt, Steffen Schütz, Krzysztof Mianowski, Patrick Vonwirth, and Karsten Berns	
10 Dynamic Modeling of an Asbestos Removal Mobile Manipulator for Stability Evaluation	239
Siddharth Maraje, Chedli-Belhassen Bouzgarrou, Jean-Christophe Fauroux, and Lounis Adouane	

About the Editors

Giuseppe Carbone received the M.Sc. (cum laude) and the Ph.D. degree in Robotics from the University of Cassino, Italy, where he has been Key Member of LARM Laboratory, for about 20 years. From 2015 to 2017, he has been Senior Lecturer at Sheffield Hallam University, UK. Since 2018, he is Associate Professor with the Department of Mechanical, Energy and Management Engineering (DIMEG), University of Calabria, Italy. From 2020, he is Chair of the IFToMM TC Robotics and Mechatronics. He also serves as Member of the Board of Directors for the Society of Bionics and Biomechanics, Treasurer of the IFToMM Italy Society. Prof. Carbone serves as Editor-in-Chief, Section Editor-in-Chief, and Associate Editor in several reputed international journals including *Robotica* (Cambridge University Press), *Journal of Bionic Engineering*, IEEE/ASME *Transactions on Mechatronics*, *Advanced Robotic Systems* (Sage), *MDPI Robotics*, and *MDPI Machines*. His research interests include aspects on mechanics of manipulation and grasp, cable-driven robots, rehabilitation robotics with more than 350 published papers, five edited books, ten edited journal special issues, 20 patents, and 12 Ph.D. students. He has been leading more than 20 research projects including the 7th European Framework and Horizon 2020. He received several awards including two JSPS invitation awards in Japan, three IFToMM Young Delegate awards, more than 30 best papers, and ten international best patent awards.

Med Amine Laribi is Associate Professor in the Fundamental and Applied Sciences Faculty of the University of Poitiers (UP), where he teaches robotics and mechanic. He has Mechanical Engineer Degree (specialization on Mechanical Design) from École Nationale d'Ingénieurs de Monsatir (E.N.I.M.) in 2001 and M.S. in Mechanical Design, 2002. He received his Ph.D. in Mechanics from University of Poitiers in 2005 and National Habilitation in Mechanics from University of Poitiers in 2018. He serves as Associate Editor in several reputed international journals including *ASME Journal of Medical Devices*, *Assembly Automation* (Emerald Publishing), *Mechanical Sciences* (Copernicus Publications), and *MDPI Robotics*. He is Member of international scientific committee of RAAD and MESROB. His research interests, at the Department of G.M.S.C. of Prime Institute, include aspects on robots

design, mechanism synthesis, cable-driven robots, parallel robots, haptic interfaces, and collaborative robots with more than 41 published peer-reviewed journal papers, seven edited books, eight edited journal special issues, and six Ph.D. students. He is leading several national and international research projects in the fields of medical robotics and biomimetics.

Fundamentals

Chapter 1

Historical Backgrounds on Robot Mechanism Design



Marco Ceccarelli

Abstract In this chapter an outline of History of Robotics is presented on how robot designs have been evolved with a special reference to mechanism designs. The chapter gives main information on main milestones in Robotics History with an illustrative approach focused on mechanism designs as a short account of the large number of solutions that contributed to the development and success of robot designs.

1.1 Introduction

Robotics has recently developed with modern concepts and is constantly evolving with expansion in application fields and with new design solutions. The History of modern Robotics is characterized above all by a technological development that has allowed current robot solutions also inspired to concepts of the past. The History of Robotics is outlined in many publications in a vast literature (not indicated due to limits of editorial space but referring mainly to the authors' works) in sections or chapters of encyclopaedic and monographic frames like for example in [1–4], or in specific papers like for example in [5–9], and even within conference proceedings like for example [10] with general views and even specific studies on specific applications and specific personalities and manufacturers.

In this chapter, attention is focused on the History of the mechanical structures of robots in terms of mechanisms that carry out interactions with their surroundings and with human operators in operating the typical tasks of both industrial and service robots. In particular, this short chapter aims to be a brief reference of the main concepts and moments of development of robots since ancient times by referring to emblematic examples with the help of diagrams and figures representing these peculiarities in the History of Robotics.

M. Ceccarelli (✉)

LARM2: Laboratory of Robot Mechatronics, Department of Industrial Engineering, University of Rome Tor Vergata, Via del Politecnico 1, 00133 Roma, Italy

e-mail: marco.ceccarelli@uniroma2.it

1.2 Robot Structure and Mechanism Role

A robot is defined as a system with the aim of replacing and helping humans in especially dangerous or tedious tasks and as such it was developed especially in industrial applications in the early stages of the History of Robotics. Even today, robots are considered useful systems to replace or support human operators in a large variety of tasks, among which service ones have seen considerable development in the last 20 years.

From a technological point of view, a robot is defined in standardized terminology by national and international bodies and institutions such as IFR (International Federation of Robotics), IFToMM (International Federation for the Promotion of mechanism and machine science), and IEEE (Institution of Electric and Electronic Engineers) as a modern mechatronic system that is characterized by a structure with different capabilities in versatility in tasks and flexibility in reprogramming.

Figure 1.1a shows a scheme of general structure of robotic systems as mechatronic design with a technological layout that has been possible in modern time due to the great advances in many other disciplines than traditional mechanical area. Today a robot is understood as a mechatronics system in which the mechanical part is one of the components and very often it is even considered of minor importance as per the great advances that the other components have experienced in the last decades. However, the mechanical design pays an important role as related to the fact that is the component of a robot that interacts with the environment and operates the task in substitution or helping a human operator in according to robot definition in general term from technical viewpoint and even from general understanding.

Figure 1.1b shows a scheme of the structure of a robot with a central role of the mechanical component that is designed mainly with mechanisms in performing the tasks that are assigned to the robot in terms of manipulation and interaction with objects and environment as schematized in actions of movement and force. Therefore,

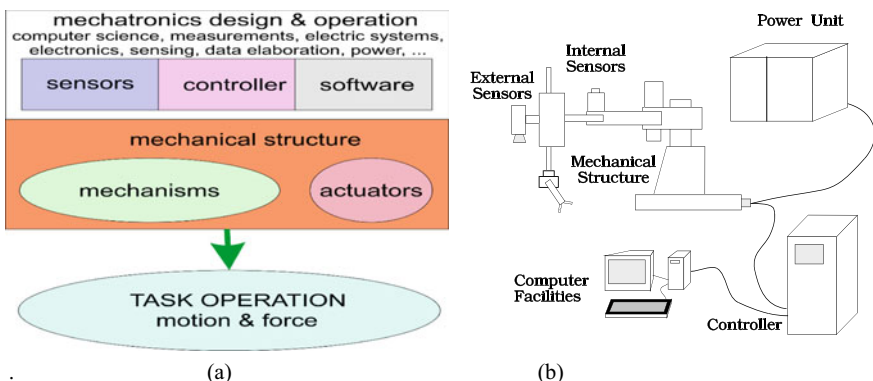


Fig. 1.1 A scheme of the structure of a modern robot: **a** with discipline indication; **b** a general unit composition [4]

the role of the mechanical structure as mechanism design can be recognized not only in the mechanical versatility to perform tasks in force and motion of different and variable configurations but it can also be recognized in a synergistic role in realizing the mechatronic function and the flexibility of application when the mechanical structure interacts and is integrated with other components typical of a robot, such as especially sensors and control. The role of the structure of the mechanisms in a robot can therefore be summarized in the functional characteristic aspects that are also recognized as the basis for a characterization of a robot, that is, for example, the workspace and payload capacity that qualify a robotic system in general terms.

The mechanical structure of robotic systems presents extremely variable configurations depending not only on the structures of the robots but also on the applications to which they are intended, and their historical evolution is indicative and interesting to trace and characterize this historical development and also to indicate solutions from the past that they can be further developed for innovative applications and/or be adapted for tasks updated in their characteristics.

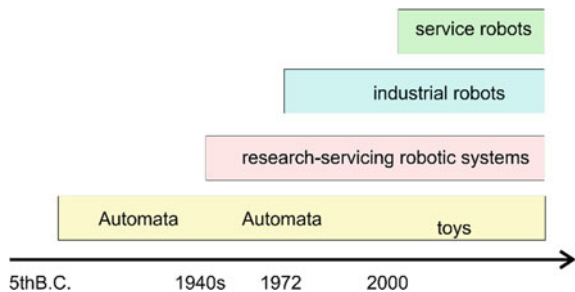
1.3 A Short Account of a History of Robot

Robots have been developed in the modern era especially with the advent of efficient technologies in the components that today characterize the mechatronic structure and flexible functionality, despite the concept has been defined in modern terms at the beginning of the twentieth century but in conceptual terms already in Antiquity. In an overview of historical development, while recognizing that the History of modern Robotics was developed from the first robotic manipulative arm robots of the 1940s, it is possible to outline a historical-technical development since ancient times, considering mainly typical concepts of the structure and functionality of robots as autonomous and/or intelligent systems that have helped or replaced human operators in operations of various kinds. Therefore, a historical examination of the development of robots and more precisely of their construction and functional concepts requires a description of a long time period and a great breadth of solutions and applications of which in this chapter we want to give only main ideas and indicative illustrative examples not only of the vastness of the discipline but also of the perspectives and results that are obtained and obtainable with the development and use of robots.

Despite the modern definition of robot, robotic systems can be considered within a large variety of systems that realize the typical functions and characteristics of a robot that is functional versatility and flexibility of reprogramming and readjustment to operating regimes of the assigned tasks.

Therefore, we can consider robots those industrial systems that properly carry out manipulations and operations of various kinds in industrial environments as well as those initially produced in modern Robotics. But robots are recognized also in mechanical and mechatronic systems that provide support or replacement of functions for human operators in a wide variety of applications such as for playful, religious purposes, assistance to other activities of various kinds as summarized in

Fig. 1.2 A timeline scheme of robot evolution



the today term ‘service’ for all those robotic systems that are characterized by functionality very different from that one in industrial fields but they still show the typical characteristics of autonomy and versatility of robotic structures.

Figure 1.2 summarizes an historical perspective of the evolution of robotic systems from general viewpoint with timeline indicating the main robot frames as function of their successful application more than their design. One can say that modern Robotics started by copying and mimicking the human arm, but soon attention was addressed to other solutions that got inspiration from the living world in nature and/or were conceived with artificial architectures to obtain the nature-like solutions and beyond.

The timeline diagram of Fig. 1.2 wants to emphasize the historical development according to the structural and functional concepts of a robot, also considering the applications and purposes of those systems that have been conceived and built with the modern idea of robots. The first applications that have these characteristics can be recognized as developed in ancient times in systems with a certain autonomy and with limited analogic re-programmability for purposes that are the basic concepts of modern robots since they operated without the intervention of a human operator differently from what happens for many other systems and machines developed in past technology and development of society. These systems, called automata for this main characteristic, had a development since ancient times and they can still be recognized today in many systems which, although not responding to the modern concept of robots, nevertheless have these characteristics. The automata concepts can be found in very early literature with characters of today science-fiction:

- In the Iliad, (Il. 18.369–377), Hephaestus building a number of wheeled tripods capable of moving by themselves back and forward serving food to the gods (Il. 18.369–377).
- In the Odyssey, (Od. 7.78–94), two guardian-mastiffs made of gold and silver, by Hephaestus, were the doorkeepers of the magnificent palace of King Alcinous in Phaeacia. invulnerable against assaults
- In the Iliad, (Il. 18.410–422), Hephaestus was using two “female” robots as personal assistants, who supported him at his work in the forge and ‘had voice and sense’

In the history of automata development, particular mention can be made of toy solutions since these systems can be representative of those solutions that, although

based on mechanics. They are widespread in fields of application of enormous dissemination with a wide success within general public as expected for the solutions of modern robots. A second area emphasized in the timeline of Fig. 1.2 refers to the solutions of robotic systems that are used in complementary activities often not considered as properly so-called robotic applications since they refer to systems that are developed to support other activities and therefore with a secondary role when compared to their functionality and even structure. Those solutions are often developed ad hoc and even in an artisanal way for specific applications such as, for example, in research activities in other areas. They can be considered ante-litteram service robots since they have been developed as tools and not as autonomous systems while not receiving adequate attention and adequate recognition as robot innovative solutions. To date, in many fields of research, even in disciplines far from the technological fields, use is made of service systems with robotic functions that can be recognized as a further success in the design and use of robots in service areas.

The third field indicated in Fig. 1.2 refers to the traditional industrial robots that, starting from the 1940s, have determined the development of modern Robotics and the start of the success of robots as replacement and support systems for human operators that are still fundamental today in applications in industrial fields with increasingly widespread with developments of generations of increasingly sophisticated and efficient robots in carrying out tasks with increasingly greater performance and complexity. A historical outline of the main events of modern Robotics in terms of industrial robots can be pointed out with the following milestone dates of early days of Robotics:

- 1947: Raymond Goertz built and used an electric-powered teleoperator
- 1954: George C. Devol obtained the first patent for a manipulator with memory
- 1956: Joseph Engelberg and George C. Devol started the first robot builder company Unimation
- 1968: Victor D. Scheinman designed the Stanford Arm
- 1971: Japan Industrial Robot Association JIRA is founded
- 1975: the U.S. Robot Industries Association RIA is founded
- 1975: robots are implemented in a large-scale production at Ford plant in Detroit
- 1981: robots are implemented in a large-scale production at FIAT plant in Cassino
- 1984: IEEE Journal of Robotics and Automation was established

To date, it can be considered that a fifth generation of robots is already being developed considering that the first generation was identified in those robots up to the early 1950s that simply did repetitive operations with adequate precision.

The last field indicated in Fig. 1.2 refers to service robots which, as previously indicated, are those robotic systems developed and applied in fields and services other than the typical industrial areas and therefore they have seen a considerable diffusion in recent years in fields of more and more new dissemination starting from applications in the biomedical fields, exploration of hostile environments such as submarines and space environments, and areas of assistance to human users in operations of various kinds in their non-industrial tasks.

In the next section examples are reported regarding with such historical developments aby indicating technical-historical characterizations of the development of robots and their design and functional concepts in order to also clarify the role of the structure and functionality of the mechanical part in terms of mechanisms that is the subject of this short historical technical examination.

1.4 Illustrative Examples

In this section, illustrative examples are reported which, although they represent very limitedly the great variety of theoretical and constructive solutions of mechanisms in robotic systems, want to emphasize the role of mechanisms in robots both in challenging solutions of the referenced period and in the historical evolutions that have allowed applications still of significant interest today. It should be noted that during historical evolution the centrality of the function of mechanisms has lost its preponderance due to integration with other systems of technologies towards mechatronic solutions and despite this, the versatility and efficiency of the mechanisms for the functionality and success of robots remains fundamental in any context both from technological and historical viewpoints.

Figure 1.3 shows an example of an automaton of Heron [11, 12], in which the structure is centred on automatic functionality due to a series of mechanisms that allow the opening of a door of a temple in an automatic and programmed form as function of the evaporation or condensation of the water in a vessel that generates the necessary actuation energy. This mechanism is typical of the automaton of Greek-Roman Antiquity not only for its structure which can be thought of as already characterized by concepts of Robotics and mechatronics by combining systems of different nature, but mainly for the purpose that is not linked to any production activity. In fact, in ancient times automata were developed mainly for recreational and religious purposes with a general intent of surprising or delighting the users of such systems, even with cultural aims as pointed out in [11]. Obviously, the effects of this design and construction capacity can also be found in the development of the first sophisticated machines for specific applications such as, for example, the automatic saw for cutting materials such as wood and marble. In Fig. 1.3b it is emphasized the aspect of re-programmability of the analogic type that can give these automata the appearance of an ante-litteram robotic solution as previously commented for the fact that the analogic solution can easily be readapted to different regimes and operating laws. The system illustrated in Fig. 1.1b refers to the actuation of pulleys and therefore of rotors by means of adequate winding of the actuating ropes which with their configuration around the cylindrical body, along the rotation axis or with different inclinations on the cylindrical body provide different laws of motion also including periods of stationary operation of the mechanism and of the automaton that is actuated by this system.

Figure 1.4 points out that in ancient times also in other geographical areas there was a considerable development of automata with characteristics of ante-litteram

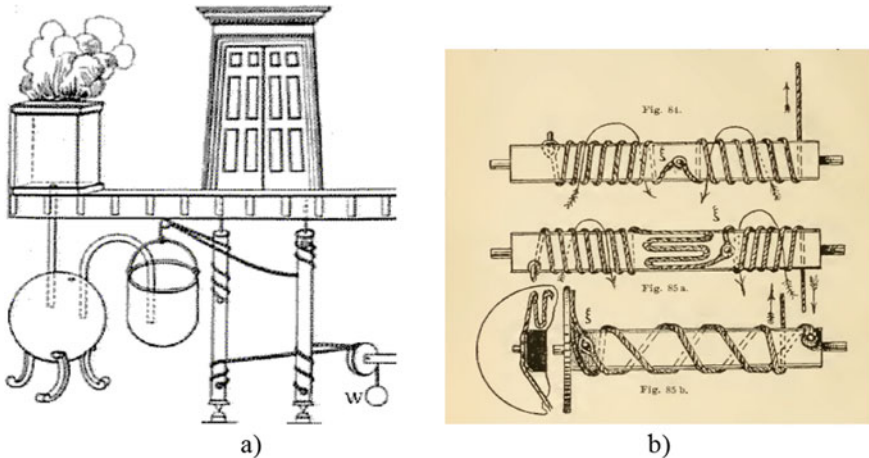


Fig. 1.3 Examples of mechanism designs in robot-like automata in Antiquity [11, 12]: **a** Heron automaton for opening-closing of temple door form third century B.C.; **b** cable wiring as for motion programming

robots both in terms of structure and functionality. In particular, Fig. 1.4 shows the example of the Chinese mechanical cow of the fifth century B.C. in a graphic reconstruction in modern times in which the mechanism structure is emphasized so that allows an implementation with a single degree of freedom, as described in the texts, for the movement of the system that was used in the military field for the transport of heavy material. In Fig. 1.4a the structure of articulated mechanisms is emphasized with a reconstruction kinematic design in [13] and in Fig. 1.4b a modern reconstruction available on the market as a toy by Fenton Inc. in Taiwan is shown, also demonstrating the above considerations that the automata of Antiquity are of considerable interest and still today they have a playful purpose with considerable success and attention from a large public. In toy constructions, a more evident robotic structure of a modern type is frequently created by completing the automaton with electrical actuators and related controls as well as often also with sensors that give it greater flexibility while remaining central the structure and functionality of the mechanical part as highlighted in the toy of Fig. 1.4b.

Figure 1.5 shows examples of solutions developed during the Middle Ages to indicate that even in that period the interest in automatic machines and automata has produced remarkable solutions of high technological significance still based on mechanisms. In particular, Fig. 1.5a represents an automaton produced in the Arab scientific and technological development starting from the solutions in the Greco-Roman world while Fig. 1.5b represents the scheme of an automatic machine for cutting wood, also probably developed starting from ancient solutions with a design of mechanisms. Of particular interest in the machine of Fig. 1.5b is the fact that the structure can even be interpreted as a two-degree-of-freedom system where the actuation coming from a hydraulic flow activates both the advancement of the wood under



Fig. 1.4 Examples of mechanism designs in robot-like automata in Antiquity in Chinese world: **a** a reconstruction of the mechanical wooden cow of fifth century B.C. [13]; **b** a toy reconstruction (photo by Marco Ceccarelli)

cutting and the cutting saw itself. In both cases of Fig. 1.5 great attention is centred on the structure of the mechanisms that provide the typical automata functionality even if, as noted, important details are not completely clear to leave the authorship of the machine in the hands of the designer for its real and efficient construction as a kind of intellectual defence of the illustrated innovation. The robotic aspects can be recognized not only in the complex mechanical versatility of the illustrated functionality but also in the combination of multidisciplinary aspects in terms of mechanics and fluidics with synergistic solutions for efficient system functionality.

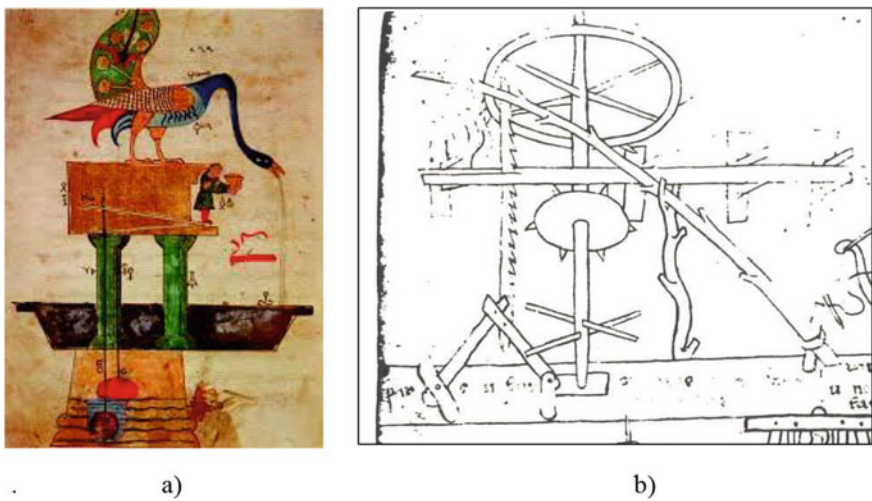


Fig. 1.5 Examples of mechanism designs in robot-like system in Middle Ages [4]: **a** a clock design by Al-Jazari (1136–1206) in twelfth century; **b** the wood saw machine by Villard de Honnecourt (1200–1250) in 13th century

During the Renaissance, with the flourishing of activities and mainly of a renewed interest in science and technology as outlined for example in [14–17], it can be noted a renewed flourishing of projects and the creation of innovative machines to increase and improve the productivity of activities as well as to indicate the high level of theoretical and practical knowledge. The examples of Fig. 1.6 [14–17] show emblematic machine designs that represent the mature interest and ability in the conception and development of automatic and non-automatic solutions with evident aspects of ante-litteram modern Robotics that have been and can still be considered sources of inspiration for further developments. In particular, Fig. 1.6a shows the design of a crane design and used by Filippo Brunelleschi (1377–1446) for the construction of the Florence Cathedral with large dimensions for the time with highly innovative solutions. This can be recognized in the extreme part of the crane with parallel cable architectures that are used to increase the payload capacity and control of the pendular movement of loads. In Fig. 1.6b the study by Mariano di Jacopo on the methods of gripping delicate objects such as a fish with two-finger grippers is noteworthy for the designed finger ends that, in addition to ensuring grip stability, determine suitable contact conditions so as not to damage a grasped object with an attention that today is typical of the most advanced gripping devices. Finally, Fig. 1.6c shows a solution by Francesco di Giorgio (1439–1501) for a vehicle that is equipped with autonomous elements both for steering and driving with solutions which, even if based on gear transmissions, still of considerable novelty in structure application, denote elements and ideas of originality for solutions of considerable interest and a source of design research today yet. Figure 1.6 summarizes the high knowledge and design skills during the Renaissance for innovative machines with the characteristics that can be recognized in modern robots in terms of operating versatility and fields of application in service areas such as today for adapted service robots to specific needs of different nature.

Figures 1.7 and 1.8 show automata that were developed in the periods before to the Industrial Revolution with advanced characteristics as compared to classic automata both in terms of versatile structure and reprogramming capacity with analogue solutions in mechanical designs for playful applications as representative of theoretical and technical skills also coming from other sectors such as mainly the technology of watches and the nascent automatic industrial machinery. In particular, Fig. 1.7 shows one of the most famous automata in which the writing task is performed with a reprogrammable mechanism by means of a cam drum with a humanoid structure and high precision performance. Similarly, Fig. 1.8 from the Japanese Karakuri tradition shows the tea-servant automaton that combines locomotion capabilities through a system of gears and linkages with a manipulation system to offer the cup of tea to a nearby user. Both automata are equipped with an energy source that is created by loading springs so that they present a solution that combines functional autonomy with versatility and programmability in an efficient service operation.

During the Industrial Revolution there was an explosive development of machines also for automatic operations which in many respects can be recognized as the precursors of modern robots. The vastness of solutions and applications does not allow an exhaustive examination in this chapter and therefore only examples are reported

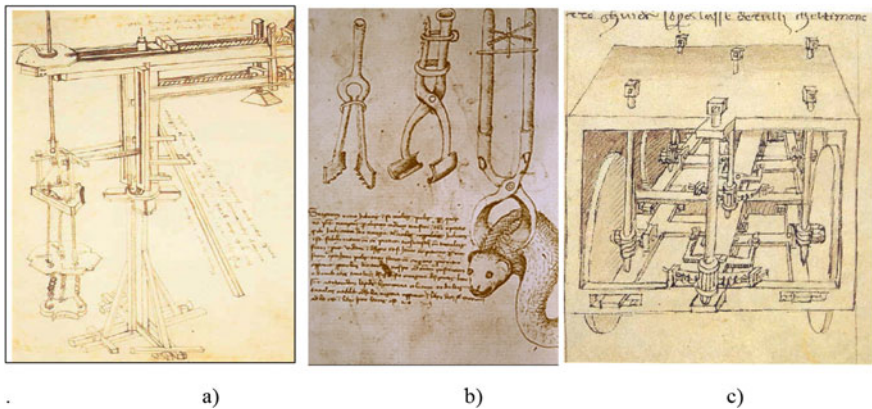


Fig. 1.6 Examples of mechanism designs in robot-like applications in Renaissance [14]: **a** a crane for high payload by Filippo Brunelleschi (1377–1446); **b** a gripper design and analysis by Mariano di Jacopo (il Taccola) (1381?–1458); **c** a self-propelled car by Francesco di Giorgio Martini (1439–1501)

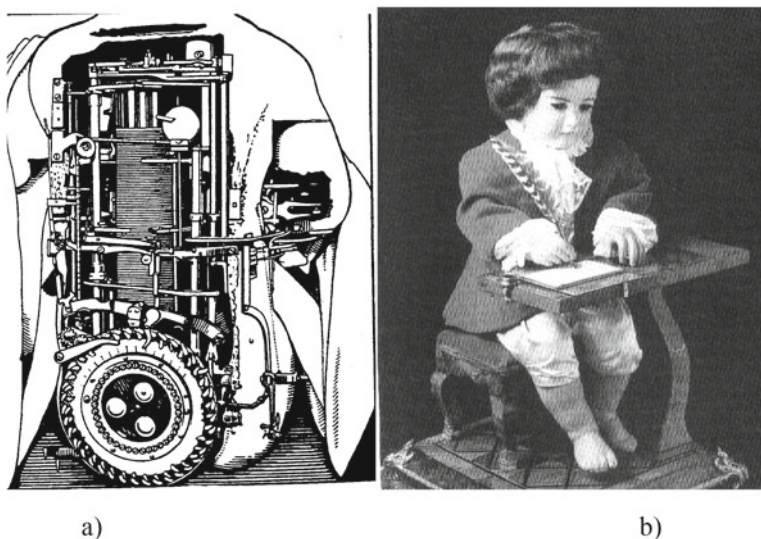


Fig. 1.7 The ‘Drotz writer’ as example of mechanism designs in robot-shaped automata in eighteenth century [4]: **a** the mechanical design; **b** the existing automaton at museum of Neuchatel in Switzerland

as focused on the mechanisms for the perspective adopted in this work. Therefore, Fig. 1.9 shows only two examples with mechanical design schemes of solutions conceived in this period with evident purposes and characteristics typical of modern Robotics. In particular, Fig. 1.9a shows a complex mechanism, however, with one

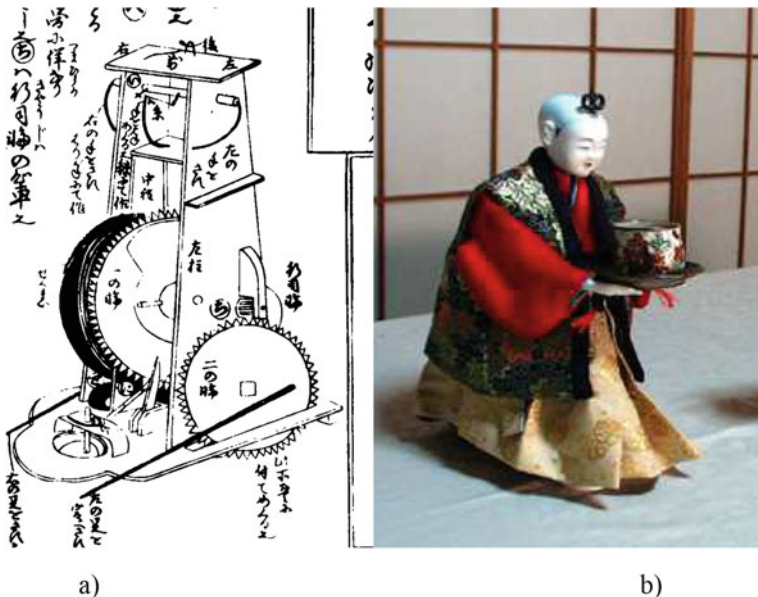


Fig. 1.8 The Japanese tea servant as example of mechanism designs in robot-shaped automata in eighteenth century [4]: **a** the original mechanical design; **b** an existing reconstructed automaton

degree of freedom for the running of a four-legged mobile locomotion system with mechanical structure and robust operation even for unstructured environments as a solution obtained by specifically considering the possibilities of movement and force transmission in articulated mechanisms with several members by Pafnutij L. Chebyshev (1821–1894) as an application of his work on kinematic synthesis of mechanism based on mathematical treatments. In addition, Fig. 1.9b of a USA patent of the end of nineteenth century shows a mechanical system that is shaped even in the form of a horse for a four-legged mobility based on a system of gears as an alternative to articulated mechanisms to have greater load capacity and greater compactness in the design. These two examples show solutions that are based on mechanisms that can still be central today in the development of mobile legged robots and even hybrid systems with robustness and mechanical versatility of considerable efficiency.

Modern Robotics began with tele-manipulators used for the manipulation of radioactive materials during the Second World War and has brought with great speed, also thanks to the technological development of electronics, electrical implementation techniques and sensors, to attractive solutions and indeed also applications in industrial fields with a subsequent rapid diffusion in many other areas. Figure 1.10 shows two examples of these pioneering solutions that can be considered as a reference for the History of Robotics but also for the considerations of this chapter in the role of the mechanical structure and mechanisms, in particular, Fig. 1.10a shows one of the first industrial robots developed by Unimation, the first robot manufacturer as indicated above, in a first industrial application in production lines for the assembly

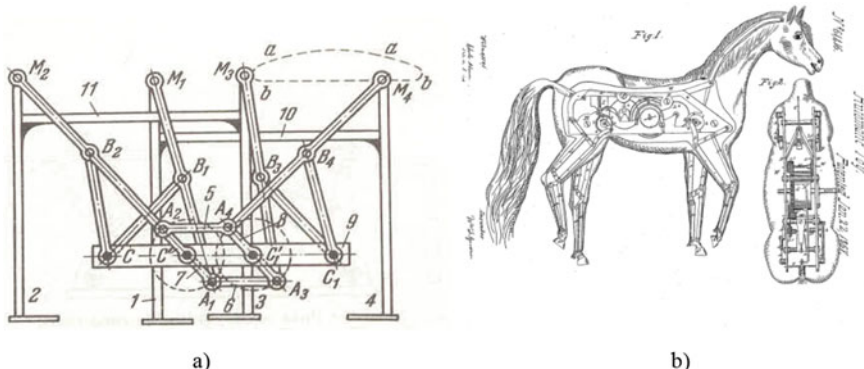


Fig. 1.9 Examples of mechanism designs in robots during the Industrial Revolution: **a** a linkage design for legged mobile system by Pafnutij L. Chebyshev (1821–1894), (available in the handbook by I. I. Artobolevsky on Mechanism in Modern Engineering Design, published in 1975); **b** a geared horse-shaped mobile system from USA patent no. 61416 by W. Farr Goodwin dated Jan. 22, 1867

of automotive vehicles with evident characteristics and functionalities that are based mainly on the mechanics of the structure and mechanical interactions with the object being manipulated. Figure 1.10b shows a historical example of tele-manipulator for the above-mentioned applications with radioactive materials that was developed in the former Soviet Union and now is it stored in a museum collection at the Bauman University in Moscow. It is worth to note how the mechanical structure highly mimics the anatomy of the human arm that it wants to replicate, also in terms of shape and as based on direct-drive mechanics through servo-controlled electric actuators.



Fig. 1.10 Examples of mechanism designs in first robot manipulators in 1950s: **a** a first UNIMATE robot in industrial applications (available at <https://www.youtube.com/watch?v=XI2c91pWGc>); **b** a prototype of the master–slave manipulators arm at Bauman University in Moscow (photo by Marco Ceccarelli)

Figure 1.11 refers to the most representative application field of Robotics as it concerns the development of humanoid robots with functional structures that have the purpose of replacing human operators. Figure 1.11 shows examples of historical development and structures representing the role of mechanical components in these aspects with emulation and replication of the anatomy and functionality of the human limbs. Figure 1.11a shows the first humanoid robot as presented by Professor Ichiro Kato (1925–1994) in 1972 [18], at the Waseda University of Tokyo with a structure clearly based on mechanical solutions and mechanisms for the locomotion and manipulation joints with human analogies. Figure 1.11b shows a Russian prototype developed with a leaner structure but still aimed at replicating the shape of the human anatomy while also maintaining its mechanical structure with mainly serial mechanisms [19]. Figure 1.11c shows the first commercial ASIMO humanoid robot [20], which was mainly used for demonstrations with the solutions of mechanisms completely hidden by a shield. Finally, Fig. 1.11d shows a recent prototype developed by the author's team as based on a parallel structure mechanism that emulate human anatomy considering the synergy of the bone structure with the neuromuscular system interpreted as a mechanism for the movement and transmission of forces [21, 22]. There has been a renewed interest in developing humanoid structures for application in rescue and human servicing with specific mechanical structures and mechanisms that can allow very similar agility and abilities of man in dangerous and structured environments also with the possibility of modes other than simple walk and even able to get up after a fall. An example of such explosive development with many humanoids developed in laboratories all over the world that have seen synergies of hardware and software technologies with additional innovative solutions of mechanical structure also with micro mechanisms can be seen in the development of the humanoid BHR of the Beijing Institute of Technology as reported in [23], as an example of a specific literature on the historical development of humanoid service robots.

Service Robotics has also been developing with updated innovative solutions for specific robot components such as gripping devices essential as an interface for interacting with the external environment and with the objects to be manipulated in both industrial and service applications. Figure 1.12 shows examples of gripping systems referring to a historical-technological development linked both to service applications in the field of medical prostheses and in humanoid Robotics. Figure 1.12a shows the classic hook used as a prosthesis for amputees that allows elementary gripping actions with passively implemented rigid fingers. The need for a better performance of the prostheses has led, thanks also to the development of Service Robotics, to more active solutions such as the one represented in Fig. 1.12b with two fingers to articulated and sensorized mechanisms that create a wider range of configurations of grasp. This need for a reproduction of the human limb and its universal gripping capacity is the problem that is solved with artificial hands with an anthropomorphic structure, especially for humanoid robots using mechanical structures for the fingers with articulated mechanisms or phalanx bodies articulated together with various types of actuators both with cables as in the case of Fig. 1.12c or with rigid mechanisms

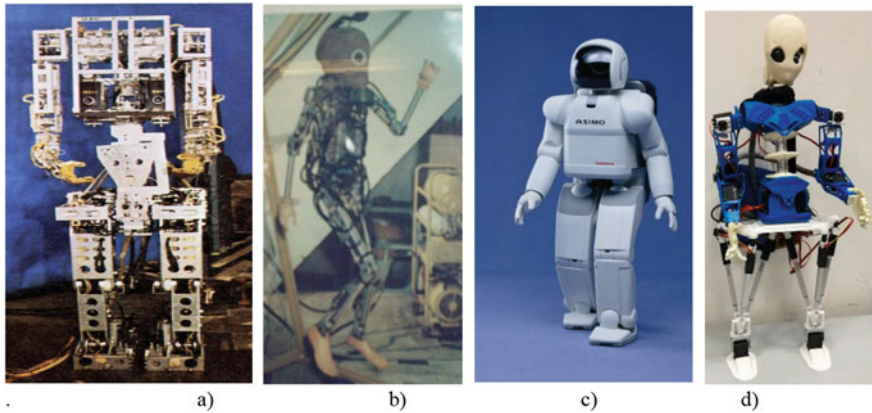


Fig. 1.11 Examples of mechanism designs in humanoid robots: **a** WABOT by Kato in Tokyo in 1972 [18]; **b** humanoid in Moscow in early 1980 as [19]; **c** ASIMO humanoid in 1990s [20]; **d** LARMbot humanoid at University of Rome Tor Vergata [21]

articulated internally to the structure of the fingers as in Fig. 1.12d, to obtain high gripping capacity and operating robustness [27].

However, in Service Robotics, solutions are also developed that are not necessarily sophisticated and made of complex mechanical structures, but they are just aimed at satisfying efficiency in a specific task. This is the case of industrial and non-industrial grippers which are aimed at grasping specific objects or a predetermined family of objects in a way that allows the definition of solutions with adequate mechanisms for robust and easy implementations also in terms of constructive convenience. Figure 1.13 shows two examples of this wide range of cases with reference to a gripper with a planar structure and grasp that is obtained by operating two rigid fingers thanks to a traditional mechanism such as the one shown in the figure with the structure of an internal cam for obtaining a high capacity of force transmission from

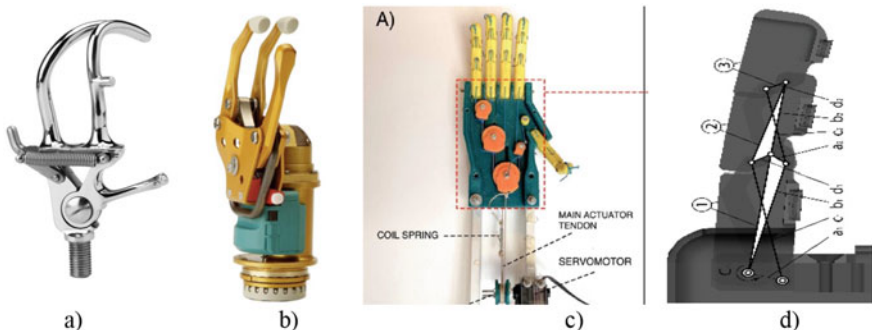
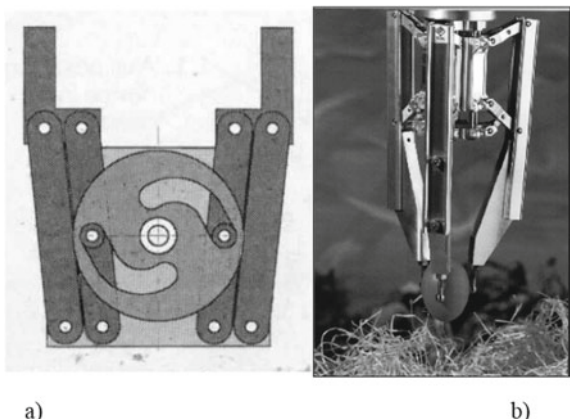


Fig. 1.12 Examples of mechanism designs in artificial hands: **a** the tradition hook [24]; **b** two-finger mechanical prosthesis [25]; **c** tendon-driven robotic hand [26]; **d** a linkage-based finger design [27]

Fig. 1.13 Examples of mechanism designs in robotic grippers [4]: **a** a scheme for an industrial two-finger gripper; **b** a three-finger gripper



a)

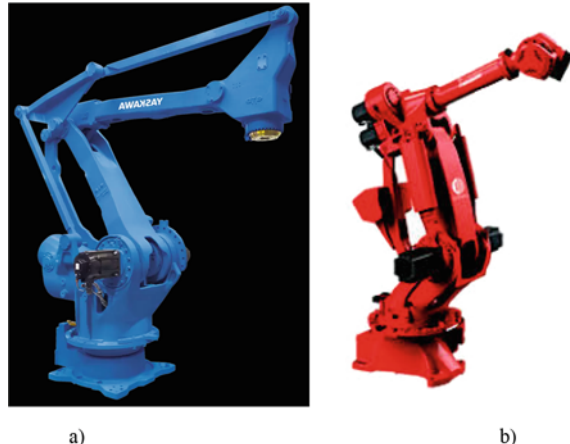
b)

the actuator and performing adequate laws of motion. The mechanism reported is an example of the vast possibilities that can be obtained with the synthesis of articulated and hybrid mechanisms. Figure 1.13b shows the example of a three-finger gripper to indicate how these grippers with suitable mechanisms can also be used in three-dimensional grasps of complex delicate objects. In the figure the three fingers are actuated by corresponding planar pantograph mechanisms with articulated solutions of the traditional type of mechanism mechanics.

Service Robotics has been also developed with other structures for typical functionality of applications in structures and various types of purposes, producing specific categories of robots such as those of locomotors and walking machines and lately also robots for aerial applications such as drones. Mechanisms such as those presented in the previous figures with the structural examples of robots can also be recognized in these robots as well as the use of mechanisms has also been increasingly developed in industrial robots in order to make them more efficient and even less bulky. The examples in Fig. 1.14 refer to the use of mechanisms even of simple structure in industrial robots with the aim of increasing the transmission capacity from the actuator and therefore allowing the location of the actuator so that the structure of the robot can be slim and light as well as can be of help in static and dynamic balancing of an operation with higher and higher performance in motion and load capacity. In Fig. 1.14a it can be seen how the extended use of a planar mechanism such as the articulated parallelogram is implemented to have the actuators on the base of the robot with a greater efficiency also in terms of force transmission for the corresponding actuated joints. Figure 1.14b shows an example of how a mechanism still of the articulated quadrilateral type (but there are also some with a slider-crank mechanisms) are used for static balancing in combination also with balancing masses and for dynamic balancing in operation high performance industrial robots.

The development of increasingly sophisticated mechanisms has brought new structures also in the field of Robotics, as the development of manipulators with

Fig. 1.14 Examples of mechanism designs with serial chain architecture in current industrial robots: **a** a Yaskawa robot [28]; **b** a COMAU robot [29]



parallel architecture that have been conceived and applied in the industrial and service sectors, especially in the last two decades. Figure 1.15 shows examples of how these innovative robots which, although conceived as an alternative to the traditional serial structures of industrial robots of the first generations for their best capabilities in terms of rapid handling and load capacity as well as precision, are characterized by a structure based on the use of mechanisms operating in parallel for the movement of the terminal element which is devoted to a manipulative or service task. Figure 1.15a shows an industrial robot with a Delta structure that was invented in 1988 with immediate success for high speed and acceleration applications, especially in pick and place areas. It can be noted that the structure depends on an assembly of mechanisms that remind articulated linkages and in any case chains of even traditional mechanisms while being assembled in an innovative solution that produces the high performances that characterize it. Figure 1.15b shows an industrial robot used in an innovative way in the field of welding of vehicle bodies with a Gough-Stewart platform structure that was conceived in 1965 as a simulator for testing vehicle tires and immediately implemented as a structure with high potential for innovative unconventional applications where high stiffness, precision and load capacity are required. Finally, Fig. 1.15c shows the CAPaMan prototype that was conceived by the author in 1997 [31] and here it is represented in an earthquake simulator application using the capacity of the structure with only three degrees of mobility to simulate the complex three-dimensional motion of an earthquake. Also, in this parallel manipulator it should be noted the kinematic structure of the legs based on articulated parallelograms suitably employed in a cooperative operation characterizing the kinematics of the parallel manipulator. Lately, in addition to solutions of rigid structure mechanisms, solutions are also used in which the links of the mechanisms are made with cables or with further solutions with flexible components to also have under actuators that create robots with a limited number of active actuators.

In conclusion, the historical-technical development of both industrial and service robots is characterized by an ever-increasing synergy of non-mechanical components

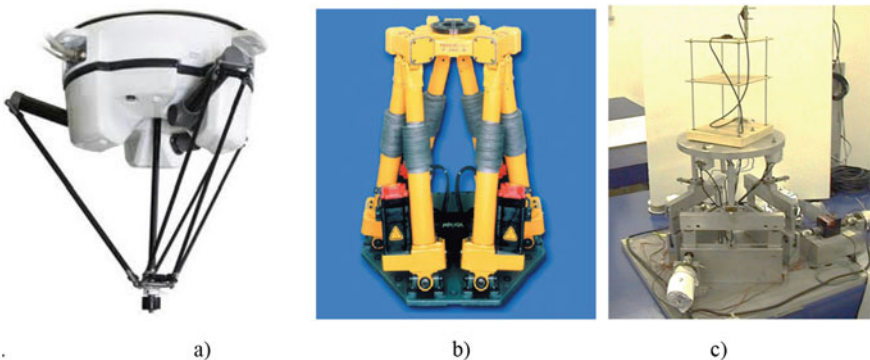


Fig. 1.15 Examples of mechanism designs with parallel chain architecture in current robots: **a** an industrial DELTA robot [30]; **b** an industrial Gough-Stewart platform robot [31]; **c** the earthquake simulator CaPaMan robot [32]

where, however, the role and functionality of mechanics continues to be important as it relates to the purpose of functionality and to the fulfilment of the tasks to which the robot is assigned which are still of a mechanical nature in terms of supporting operations or replacing human operators. Also, in this aspect of improvement of the mechanical structures, an important aspect is the conception and design of the mechanisms with compact and low-cost solutions that have recently seen a considerable use of 3D printing manufacturing with a trend also of miniaturization of the structures according to the tasks for which the robot is designed [33]. The above examples should also be understood in the areas in the above-mentioned historical development for applications that are not necessarily productive in both industrial and non-industrial frames, but they are applied also in ludic and educational and in other areas both for Robotics technology and for an adequate development of an awareness and knowledge of the capabilities of technology and subsequent development which today are essentially recognized in Robotics.

1.5 Conclusions

This chapter is a short account of the History of Robotics looking at the robot evolution in term of mechanism design over time to show not only the role of mechanisms in a modern robot but also to explain the evolution that made the modern robots as advances of the mechatronic systems when their design is well considered with contributions from all the components in a synergic-integrated way with still a central role of the mechanical design with mechanisms for successful tasks with operation based on motion and force. An illustrative approach is used with few emblematic examples to show the central role of the mechanism in the robot designs in terms of historical evolution and task functionalities.

References

1. Singer, C., et al. (eds.): History of Technology. Bollati Boringhieri, Turin (in Italian) (2013)
2. Capocaccia, A.A. (ed.): History of Technique. UTET, Turin (In Italian) (1977)
3. Bautista, P.E., Ceccarelli, M., Echavarri, O.J., Munoz Sanz, J.J.: A Brief Illustrated History of Machines and Mechanisms, Science and Engineering, Book Series on History of Machines and Machine Science, vol. 10. Springer, Dordrecht (2010)
4. Ceccarelli, M.: Evolution and applications of robots. In: Fundamentals of Mechanics of Robotic Manipulation. Kluwer/Springer, Dordrecht (2004)
5. Ceccarelli, M.: A historical perspective of robotics toward the future. *Fuji Int. J. Robot. Mechatron.* **13**(3), 299–313 (2001)
6. Ceccarelli, M.: Notes for a History of grasping devices. In: Carbone, G. (ed.) Grasping in Robotics, pp. 3–17. Springer, Dordrecht (2013)
7. Ceccarelli, M.: An outline of history of mechanism design in servicing science. In: Physics, Astronomy and Engineering: Critical Problems in the History of Science and Society—Proceedings of the SISFA 2012, The Scientia Socialis Press Siauliai (Invited lecture) pp. 1–10 (2012)
8. Ceccarelli, M.: Mechanism design for robots. In: The 11th IFToMM International Symposium on Science of Mechanisms and Machines (SYROM'13), pp. 1–8. Springer, Dordrecht (2013)
9. Ceccarelli, M.: A short account of History of IFToMM and its role in MMS. *Mech. Mach. Theory* **89**, 75–91 (2015). <https://doi.org/10.1016/j.mechmachtheory.2014.09.007>
10. Ceccarelli, M., et al. (eds.): Explorations in the History of Machines and Mechanisms, Book series on History of Machines and Machine Science. Springer, Cham/Dordrecht (2016)
11. Bragastini, R., Ceccarelli, M.: Mechanisms in Heron's automata as technological transfer and cultural means. In: Zhang, B., Ceccarelli, M. (eds.) Explorations in the History and Heritage of Machines and Mechanisms—Proceedings of the HMM2018, pp. 175–186. Springer, Berlin (2019)
12. Aleotti, G.B.: *Gli artifitiosi et curiosi moti spiritali di Herrone hero alexandrinus*. Vittorio Baldini Stam, Ferrara (1589)
13. Yan, H.S.: Reconstruction Designs of Lost Ancient Chinese Machinery. Springer, Dordrecht (2007)
14. Ceccarelli, M.: Renaissance of machines in Italy: from Brunelleschi to Galilei through Francesco di Giorgio and Leonardo. *Mech. Mach. Theory* **43**, 1530–1542 (2008)
15. Ceccarelli, M.: Contributions of Leonardo da Vinci in mechanisms design. In: Proceedings of XXI Spanish National Congress of Mechanical Engineering, Elche, pp. 459–466 (2016)
16. Ceccarelli, M., Molari, P.G.: Francesco di Giorgio (1439–1501). In: Ceccarelli, M., Fang, Y. (eds.) Distinguished Figures in Mechanism and Machine Science-Part 4, pp. 47–66. Springer Nature, Switzerland (2020)
17. Ceccarelli, M.: Contributions of Mariano di Jacopo (il Taccola) in mechanism design. In: Proceedings of XXIII Spanish National Congress of Mechanical Engineering. Universidad de Jaen (2021) (in print)
18. Kobrinski, I., et al. (eds.): First CISM-IFToMM ROMANSY (Udine 5–8 September 1973), Springer, Wien (1974)
19. Institute, R.: Flyer of robotics institute. Bauman State University, Moscow (2008)
20. Honda, ASIMO. <https://asimo.honda.com> (2021)
21. Ceccarelli, M., Cafolla, D., Russo, M., Carbone, G.: LARMBot humanoid design towards a prototype. *MOJ Int. J. Appl. Bionics Biomech.* **1**(2), 00008 (2017)
22. Ceccarelli, M., Russo, M., Morales-Cruz, C.: Parallel architectures for humanoid robots. *Robotics* **9**, 75 (2020). <https://doi.org/10.3390/Robotics9040075>
23. Huang, Q., Yang, T., Liao, W., Zhang, W., Yu, Z., Chen, X., Ceccarelli, M.: Historical developments of BHR humanoid robot. In: Zhang, B., Ceccarelli, M. (eds.) Explorations in the History and Heritage of Machines and Mechanisms—Proceedings of HMM2018, pp. 310–323. Springer Nature AG, HMMS 37 (2019)

24. Ottobock, Hooks. <https://www.ottobock.com.tr/en/prosthetics/products-from-a-to-z/hooks/> (2021)
25. Ottobock, Myoelectric Speed hands. <https://www.ottobockus.com/prosthetics/upper-limb-prosthetics/solution-overview/myoelectric-devices-speedhands/> (2021)
26. Esposito, D., Savino, S., Cosenza, C., Andreozzi, E., Gargiulo, G.D., Polley, C., Cesarelli, G., D'Addio, G., Bifulco, P.: Evaluation of grip force and energy efficiency of the "Federica" hand. *Machines* **9**, 25 (2021). <https://doi.org/10.3390/machines9020025>
27. Carbone, G., Ceccarelli, M.: Design of LARM hand: problems and solutions. *J. Control Eng. Appl. Inform.* **10**(2), 39–46 (2008)
28. Yaskawa, Catalogue of MPL series (2021)
29. COMAU, Catalogue of SMART series (2021)
30. ABB, Catalogue of DELTA series (2021)
31. Fanuc, Catalogue of Hexapod series (2021)
32. Ceccarelli, M.: Historical development of CaPaMan, Cassino parallel manipulator. In: *New Trends in Mechanisms and Machine Science*, pp. 749–747. Springer, Dordrecht (2012)
33. Ceccarelli, M.: Low-cost robots for research and teaching activity. *IEEE Autom. Robot. Mag.* **10**(3), 37–45 (2003)

Chapter 2

Mathematical Formulations for Robot Modelling: Serial Versus Parallel Structures



Lotfi Romdhane, Mohammad Jaradat, and Zouhaier Affi

Abstract This chapter reviews the mathematical formulations of serial and parallel robots. The main objective is to show the complexity of parallel robots models compared to those obtained for serial manipulators. The diversity of designs found in parallel robots makes a standard representation almost impossible. For serial robots, the structure, as the name indicates, is an open kinematic chain and hence all the links have two joints except the first one, the base, and the last one, the end-effector (EE). This type of structure allows a simple and standard geometric description, where the most famous one was introduced by Denavit-Hartenberg in the 50s. This standard geometric description allows a systematic mathematical formulation of the kinematic model, which could be easily automated. However, parallel robots have different structures, specific for each robot, where closed kinematic chains are used to connect the base to the EE. The use of closed kinematic chains made the use of a standard geometric description almost impossible. Each case has its particularity and requires a specific description. Therefore, the resulting kinematic model is also specific to the robot. Moreover, two challenges were added in the case of parallel robots. In their serial counterpart, all the joints are active and limited to Revolute or Prismatic joints. However, parallel robots usually have several passive joints, which adds extra variables in the equations of the resulting geometric model. Due to this complexity, researchers proposed several parallel robots with less than 6 degrees of freedom (DoF) and, in particular, translational ones and purely rotational ones (spherical). In this chapter, examples selected from both types were modelled and the forward and inverse problems were solved analytically, when possible.

L. Romdhane (✉) · M. Jaradat

Mechatronics Program, College of Engineering, American University of Sharjah, Sharjah, UAE
e-mail: lromdhane@aus.edu

Z. Affi

Laboratoire de Génie Mécanique, Ecole Nationale d'Ingénieurs de Monastir, Monastir, Tunisia

2.1 Introduction

So far, developed robot systems or platforms by research or industry can be categorized, based on their configurations, into manipulators also known as robot arms, and mobile robots. Hybrid robot systems are systems consisting of the two categories known as mobile manipulators. The robot manipulators can be further categorized based on their configuration to serial, parallel, cable or soft manipulators. Mobile robots are categorized into wheeled, tracked, legged, flying, underwater and water surface mobile robots. Hybrid robots aim to maximize the benefits from the two main robot systems, for instance increasing the manipulator workspace when augmented with mobility or increasing the manipulation capabilities of mobile robot platforms when augmented with manipulators (Fig. 2.1).

The first main category of manipulators is categorized based on the type of links configurations and geometry of the manipulator. Serial manipulators are made of an open kinematic chain of a series of links connected by active joints. This formation of these connected links and active joints characterizes the manipulator configuration and its degree of freedom (DoF). The manipulator active joints are either linear (prismatic) joints (P) or rotational (revolute) joints (R). For serial manipulators, the joint connects link i with link $i + 1$ of the manipulator, this chain of connections starts from the manipulator base (B) serially to end at the manipulator tooling, called manipulator end-effector (EE). A rotational joint provides rotary motion of the link about the axis z_i by angle (θ). A Prismatic joint provides linear translational motion of the link along the translation axis z_i by a distance (d) [1–3]. Figure 2.2, depicts the classification scheme for most popular serial manipulator systems [4–6].

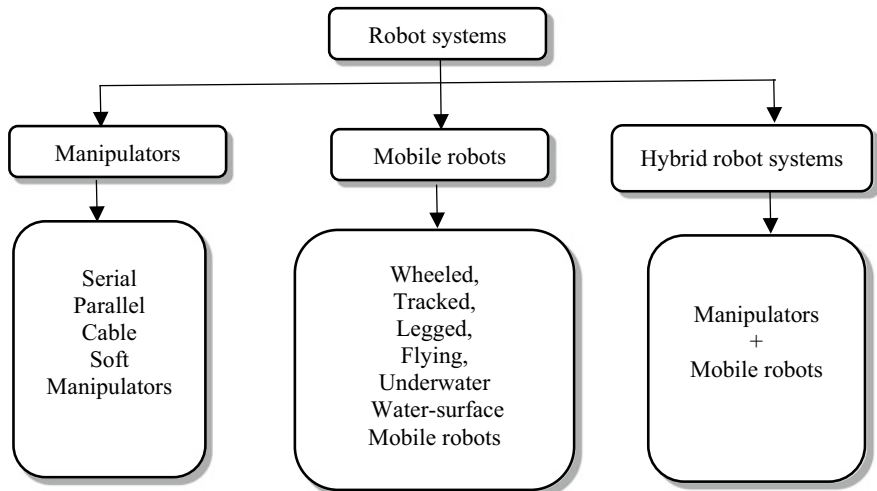


Fig. 2.1 The different types of robot systems [1–3]

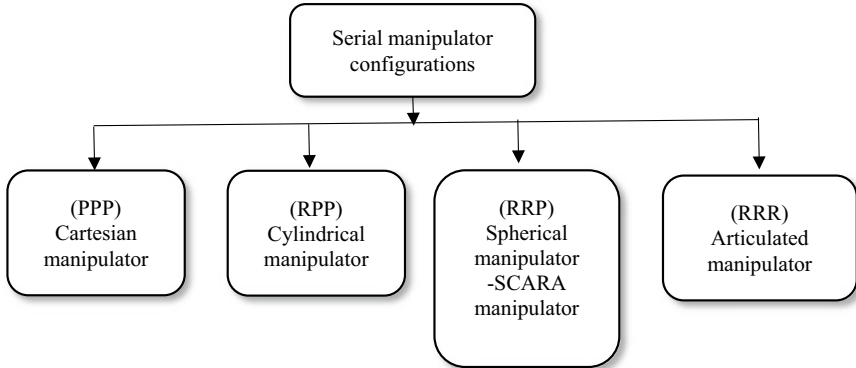


Fig. 2.2 Depicts the classification scheme for most popular serial manipulator systems

In the general sense, each parallel robot consists of two platforms that are connected by several kinematic chains acting in parallel. One of the platforms is defined as the “platform”, it can have up to 6 degrees of freedom relative to the base.

The analysis of this type of mechanisms has been the focus of much recent research. Polard presented the very first parallel robot in 1942 [7]. Gough presented his platform in 1962 [8]. The interest in parallel manipulators (PMs) arises from the fact that they exhibit high Stewart platform was presented by Stewart in 1965 [9]. Since then, several authors [10–15] have proposed a large variety of designs, all based on the same kinematic model proposed originally by Stewart. The interest in parallel manipulators (PMs) arises from the fact that they exhibit high stiffness in nearly all configurations yielding more accuracy.

However, in several applications a six degree-of-freedom mechanism is not required and devices, which have less than six degrees of freedom can be used [16–20]. The most widely known manipulator of this type is the one proposed by Clavel [21] and it has 3 translational DOF and 3 rotational actuators. The delta robot maintains passively its moving platform orientations with respect to the base. In the design proposed by Romdhane [18], two parallel mechanisms are used in series. The first one has 3 translational DOF, whereas the second platform has 3 rotational DOF. Several designs of parallel manipulators with 3-translational degrees of freedom have been developed [22–24].

Since the main objective of this chapter is to present the challenges faced when modelling parallel manipulators, the authors selected the translational and spherical parallel mechanisms to illustrate this issue. The main reason behind this choice, is that the modelling of translational and spherical (only 3 DoFs) parallel mechanisms is still, in some cases, feasible analytically.

However, the main objective, as it was stated above, is to show the complexity of the modelling of these parallel manipulators and the absence of a general notation that can model any type of parallel robot. Indeed, as it will be shown in the next sections, the structure of the parallel robot has a direct effect on the geometric description to

be adopted for the specific case. Moreover, passive joints, which are not present in serial manipulators (except for parallelogram structures) add to the complexity of the model, where the number of variables increases tremendously.

One of the main advantages of parallel robots, and the translational ones, is a high rigidity and a high precision compared to serial robots [25–27].

This chapter is organized as follows: modelling of serial manipulators is presented in Sect. 2. Section 3 presents the modelling of parallel manipulators. Section 4 contains some discussions of the results presented in the previous sections. Some concluding remarks are presented in Sect. 5.

2.2 Modelling of Serial Manipulators

Figure 2.2 shows a 2 DoF manipulator with a spraying tool placed at the end-effector (EE) used for painting applications. The manipulator consists of two-links of lengths (l_1, l_2), link 1 has a prismatic joint, which provides linear translational motion by (d_1), while link 2 has a rotational joint that provides rotary motion of the link by angle (θ_2). The robotic arm can be categorized as a PR manipulator (Fig. 2.3).

The serial manipulator configuration is defined by the number and types of joints (P or R) and links for the first 3 DoF.

a. Forward kinematics

The serial manipulators forward kinematics is based on Denavit-Hartenberg (DH) notation. In this approach the rotational and translation relation between the manipulator joints (i and $i + 1$) are described by a homogenous transformation matrix T for link i [4–6].

Definitions and Notations of DH parameters

A rigid body (i) is assigned a reference frame $R_i(O_i, \mathbf{x}_i, \mathbf{y}_i, \mathbf{z}_i)$, which is defined as follows:

Fig. 2.3 A 2 DoF-PR planar manipulator

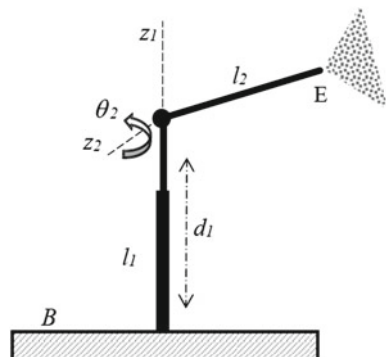
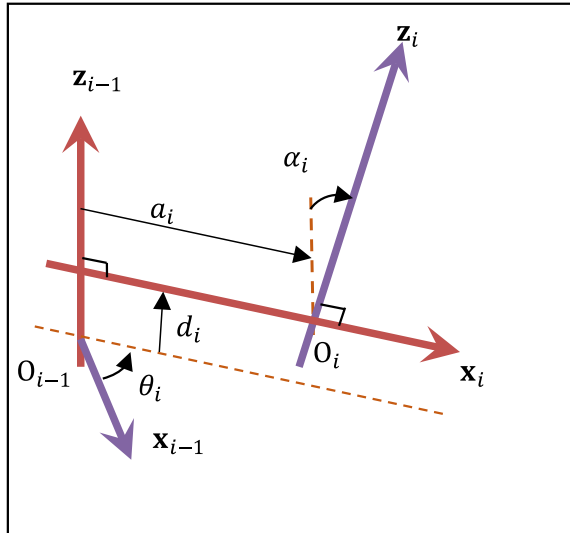


Fig. 2.4
Denavit-Hartenberg
parameters



\mathbf{z}_{i-1} axis of the joints $(i)/(i - 1)$

\mathbf{x}_i common perpendicular of \mathbf{z}_{i-1} and \mathbf{z}_i

$$\mathbf{y}_i = \mathbf{z}_i \times \mathbf{x}_i$$

$${}^{i-1}\mathbf{T}_i = \begin{bmatrix} \cos(\theta_i) & \sin(\theta_i) & 0 & -a_i \\ -\cos(\alpha_i)\sin(\theta_i) & \cos(\alpha_i)\cos(\theta_i) & \sin(\alpha_i) & -d_i \sin(\alpha_i) \\ \sin(\alpha_i)\sin(\theta_i) & -\sin(\alpha_i)\cos(\theta_i) & \cos(\alpha_i) & -d_i \cos(\alpha_i) \\ 0 & 0 & 0 & 1 \end{bmatrix} \quad (2.1)$$

where the parameters of the transformation matrix ${}^{i-1}\mathbf{T}_i$ are defined in Fig. 2.4 [m3, m9, m10, m14].

The multiplication of all the transformation matrices of the serial manipulator links provides the rotational and translation relation between the robot end effector (E) with the respect to its base (B) [4–6].

$$\mathbf{T}_B^E = \prod_{i=1}^n {}^{i-1}\mathbf{T}_i \quad (2.2)$$

Example 1: 2 DoF RR robot The associated joint frames for the 2 DoF-PR planar manipulator of Fig. 2.3 are shown in Fig. 2.5. The manipulator DH parameters are given in Table 2.1. The manipulator input variables are link 1 parameter d_1 and link 2 parameter θ_2 .

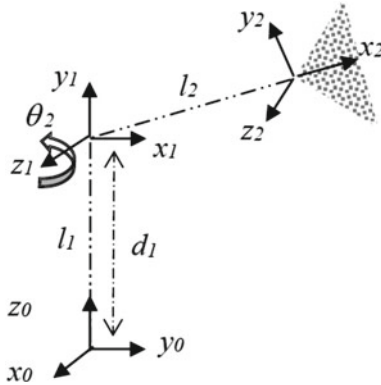


Fig. 2.5 Joints coordinates frames for 2 DoF-PR planar manipulator

Table 2.1 DH parameters for 2 DoF-PR planar manipulator

Link	a_i	α_i	d_i	θ_i
1	0	$\pi/2$	d_1	$\pi/2$
2	l_2	0	0	θ_2

The last column of the resulting transformation matrices $T_{3 \times 1}$ represents the coordinates of the origin of the reference frame fixed on the end effector EE with respect to coordinate frame 0 at the base B . The rotational relation of the end effector EE with respect to coordinate frame 0 at the base B is defined by the rotation part given in the following matrix [4–6]:

$$\mathbf{T}_{EE}^B = \left(\begin{array}{ccc|c} 0 & 0 & 1 & 0 \\ \cos(\theta_2) & -\sin(\theta_2) & 0 & l_2 \cos(\theta_2) \\ \sin(\theta_2) & \cos(\theta_2) & 0 & d_1 + l_2 \sin(\theta_2) \\ 0 & 0 & 0 & 1 \end{array} \right) \quad (2.3)$$

The workspace for the 2 DoF-PR planar manipulator is shown in Fig. 2.6, the workspace defines all possible locations to be visited by the end-effector as joints variables are varied. In Fig. 2.6, the joints variables are changed as: $d_1 \in [0.5, 1]$ and $\theta_2 \in [-\pi/2, \pi/2]$. If the base of manipulator is modified with a rotational joint which rotates about z_0 by θ_1 ($\theta_1 \in [0, 3\pi/2]$) the resulting workspace for the upgraded 3 DoF-RPR manipulator is shown in Fig. 2.7. As demonstrated in the figure, the robot links are shown in black, all possible positions of d_1 are shown in red circles from (0, 0, 0.5) to (0, 0, 1). The workspace surface colour varies from the minimum point along z axis (0, 0, 0.25) to maximum reachable point (0, 0, 1.25) while θ_1 is changed from [0, 3 $\pi/2$] and θ_2 is changed from [- $\pi/2$, $\pi/2$].

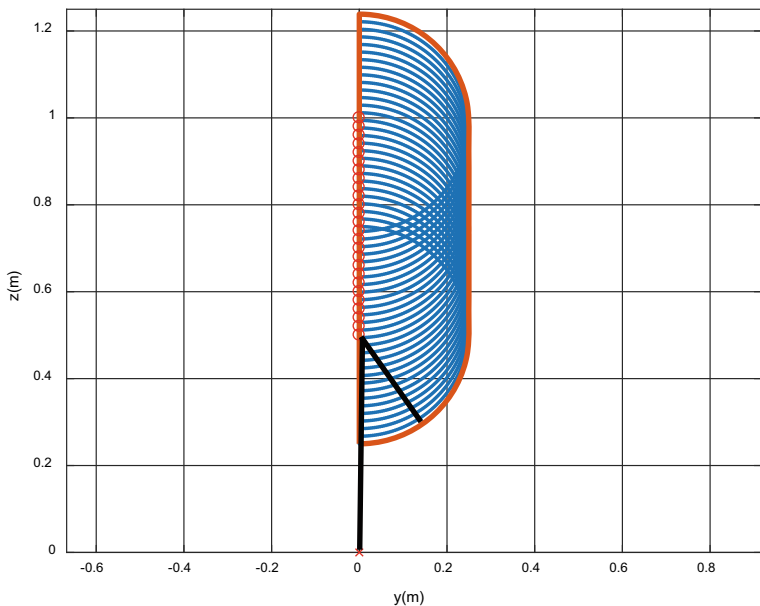
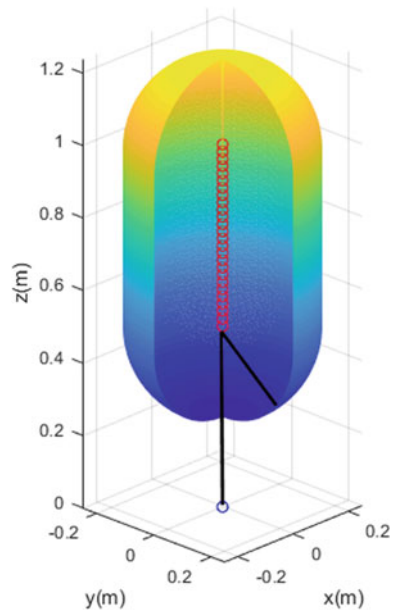


Fig. 2.6 Workspace of 2 DoF-PR planar manipulator ($l_2 = 0.25$)

Fig. 2.7 Workspace of 3 DoF-RPR manipulator ($l_2 = 0.25$)



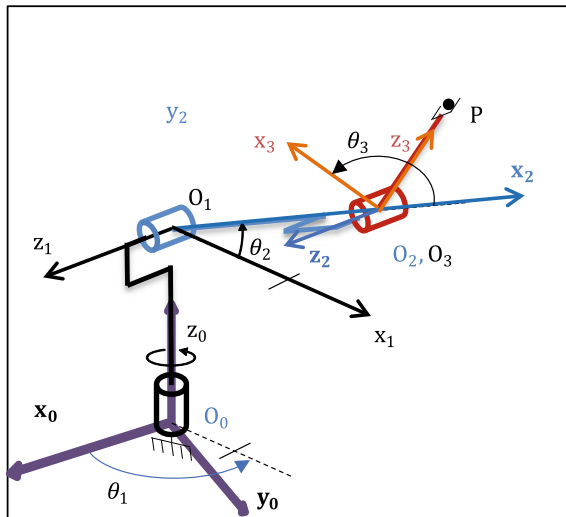


Fig. 2.8 Denavit-Hartenberg parameters for a 3R serial manipulator

Table 2.2 DH parameters for 3 DoF- RRR manipulator

Link	a_i	α_i	d_i	θ_i
1	0	$\pi/2$	l_1	θ_1
2	l_2	0	0	θ_2
3	0	$\pi/2$	0	θ_3

Example 2: 3 DoF-RRR manipulator The DH parameters of the 3 DoF-RRR manipulator are shown in Fig. 2.8, are given in Table 2.2. The manipulator input variables are (θ_1 , θ_2 and θ_3).

The transformation matrix \mathbf{T}_{EE}^B of the manipulator is defined as:

$$\mathbf{T}_{EE}^B = \begin{pmatrix} \cos(\theta_2 + \theta_3) \cos(\theta_1) & -\sin(\theta_2 + \theta_3) \cos(\theta_1) & \sin(\theta_1) & l_2 \cos(\theta_1) \cos(\theta_2) \\ \cos(\theta_2 + \theta_3) \sin(\theta_1) & -\sin(\theta_2 + \theta_3) \sin(\theta_1) & -\cos(\theta_1) & l_2 \cos(\theta_2) \sin(\theta_1) \\ \sin(\theta_2 + \theta_3) & \cos(\theta_2 + \theta_3) & 0 & l_1 + l_2 \sin(\theta_2) \\ 0 & 0 & 0 & 1 \end{pmatrix} \quad (2.4)$$

The coordinates of point O_3 are shown in the 4th column of Eq. (2.4). The position of point $P = [x_p \ y_p \ z_p]$ can be calculated as follows:

$$\mathbf{O}_0\mathbf{P} = \mathbf{T}_{EE}^B * [l_3 \ 0 \ 0 \ 1]^T = \begin{pmatrix} l_2 \cos(\theta_1) \cos(\theta_2) + l_3 \sin(\theta_2 + \theta_3) \cos(\theta_1) \\ l_2 \cos(\theta_2) \sin(\theta_1) + l_3 \sin(\theta_2 + \theta_3) \sin(\theta_1) \\ l_1 - l_3 \cos(\theta_2 + \theta_3) + l_2 \sin(\theta_2) \end{pmatrix} \quad (2.5)$$

Therefore, the forward kinematic problem is simple and systematic thanks to the standard DH representation.

b. Inverse kinematics

The inverse kinematic problem aims at solving for the joints parameters for a given pose of the EE [1–3]. For the known location of the EE of the manipulator shown in Fig. 2.8, the objective is to find the joint angles required to achieve this position, which is given as $\mathbf{O}_0\mathbf{P} = [x_p \ y_p \ z_p]^T$.

Using Eq. (2.5), one can obtain one equation in θ_3 , which yields two solutions:

$$\begin{aligned} \theta_3 &= -\arcsin\left(\frac{l_2^2 + l_3^2 - (x_p^2 + y_p^2 + (z_p - l_1)^2)}{2l_2l_3}\right) \\ \theta_3 &= \pi + \arcsin\left(\frac{l_2^2 + l_3^2 - (x_p^2 + y_p^2 + (z_p - l_1)^2)}{2l_2l_3}\right) \end{aligned} \quad (2.6)$$

For the angle θ_1 , two solutions can be found as:

$$\begin{aligned} \theta_1 &= \arctan\left(\frac{y_p}{x_p}\right) \\ \theta_1 &= \pi - \arctan\left(\frac{y_p}{x_p}\right) \end{aligned} \quad (2.7)$$

For the angle θ_2 , only one solution can be found for a given θ_1 and θ_3 , using the first and last equations of Eq. (2.5):

$$\begin{aligned} x_p &= (l_2 \cos(\theta_1) + l_3 \cos(\theta_1)\sin(\theta_3)) \cos(\theta_2) + l_3 \cos(\theta_1) \cos(\theta_3) \sin(\theta_2) \\ z_p &= l_1 - l_3 \cos(\theta_2 + \theta_3) + l_2 \sin(\theta_2) \end{aligned} \quad (2.8)$$

The solution to these two equations yields a unique solution for θ_2 :

$$\begin{aligned} \sin(\theta_2) &= \frac{l_3 x_p \cos(\theta_3) + l_2 z_p \cos(\theta_1) + l_3 z_p \cos(\theta_1) \sin(\theta_3)}{\cos(\theta_1) (l_2^2 + 2l_2l_3 \sin(\theta_3) + l_3^2 \cos(\theta_3)^2 + l_3^2 \sin(\theta_3)^2)} \\ \cos(\theta_2) &= \frac{l_2 x_p + l_3 x_p \sin(\theta_3) - l_3 z_p \cos(\theta_1) \cos(\theta_3)}{\cos(\theta_1) (l_2^2 + 2l_2l_3 \sin(\theta_3) + l_3^2 \cos(\theta_3)^2 + l_3^2 \sin(\theta_3)^2)} \end{aligned} \quad (2.9)$$

The analytical solution for this 3-axis robot was found analytically. However, for more complex robots, the solution could still be found thanks to the special structure of the wrist. Indeed, most of the serial robots have spherical wrists, which allows the decoupling of the position problem, solved above, and the orientation part, which is usually solved by identifying terms in the matrix obtained based on Euler angles [1–3].

2.3 Parallel Manipulators

Structures of Translational Parallel Manipulators

Since the model for parallel manipulators is structure dependent, in this section we present a non-exhaustive list of 3TPM structures, based on a survey of the literature.

These structures are grouped in 4 groups (Table 2.3), based on selected design for each leg. The first two groups are based on the number of prismatic joints in each leg, the third group uses parallelogram structure, whereas the last one uses extra legs to restrict the rotation.

Table 2.3 Classification of 3TPM

Group	Structure	Geometry
1st group: No prismatic joints	5R	<ul style="list-style-type: none"> • 3-5R [28] • 3-RUU [28–30]
2nd group: with Prismatic joint	4R1P	<ul style="list-style-type: none"> • 3-UPU [31–39] • 3-PUU [26, 40–42] • 3-PRS or 3-RPS [43–46] • 3-URC or 3-CUR or 3-CRU [30, 47–50] • 3-UPS [51] • 3-PRRR [52] • 3-PRRR [22, 53]
	3R2P	<ul style="list-style-type: none"> • 3-PRC or 3-RPC [54–58] • 3-RCC [59, 60] • 3-PRPR [48] • CRC
3rd group: parallelogram structure	Parallelogram	<ul style="list-style-type: none"> • Delta 3-RRPaR [61–63] • Orthoglide 3-PRPaR [26, 64–66] • 3-CRPa [16, 67]
4th group: Compound structure	Compound	<ul style="list-style-type: none"> • RAF [18] • Tricept [33]

In each of the first 3 groups, several designs are presented in the literature, but their equivalent mechanism can always be represented by the one listed in the second column of Table 2.3.

Even though this is not going to be shown in this chapter, we can state that the geometric model of all the designs in each of the first two groups is going to be similar and can be based on the structure shown in column 2 of Table 2.3.

To illustrate the challenges in modelling parallel manipulators, 2 examples were selected for translational parallel robots and one spherical parallel robot. These robots are:

- Delta robot
- Translational UPU robot

Through these 2 examples, the objective is to show the complexity and diversity of the obtained model in each case. The inverse and forward problems are presented and discussed.

Geometric Analysis of the Delta Robot

The Delta robot is a 3-translational-DOF in parallel manipulator. This robot is made of a mobile platform connected to the base by 3 kinematic legs (KL) where the first revolute joint is actuated (Fig. 2.9).

Each KL is made of an arm (2) connected to the base (1) by a revolute joint (Fig. 2.10). Let Δ_1 be the axis of this revolute. Two forearms (3) and (3') follow through two spherical joints centered in points C and C', respectively. The line CC' is chosen to be parallel to the axis of the first revolute joint. Two parallel revolute joints connect each of the forearms to the body (4). The axes of these two revolute joints are chosen to be perpendicular to the line CC'. The architecture of the forearm is made of a parallelogram CC'DD', where D (respectively D') is a point defined

Fig. 2.9 DELTA Robot [68]

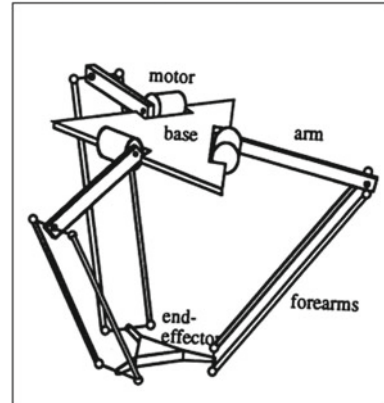
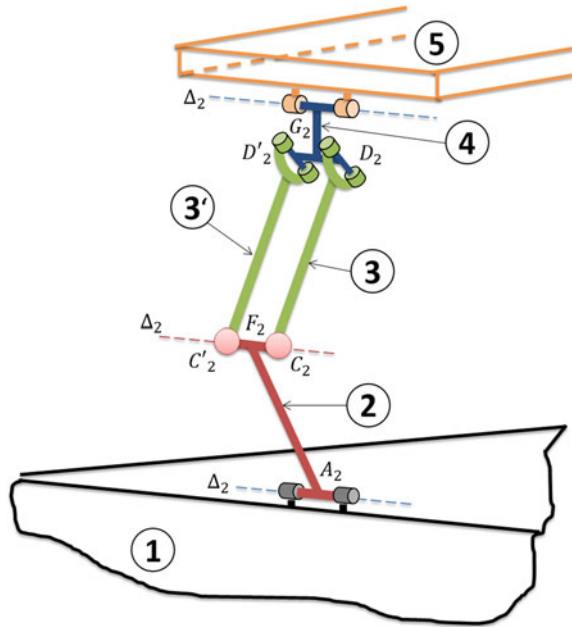


Fig. 2.10 A schematic of the first PKL



by the intersection of the revolute joints axis and a perpendicular line going through C (respectively C'). Body (4) is then connected to the platform by a revolute joint whose axis is perpendicular to the preceding revolute joint axes and parallel to the axis of the first revolute joint (Δ_1). The second PKL is identical to the first one. However, the axis of the first revolute joint in the first PKL has to be nonparallel to the axis of the first revolute joint in the second PKL, in order to eliminate all possible rotations of the platform with respect to the base.

The existence of the two PKLs, with the three extensible legs, leads to an over constrained RAF robot. In order to eliminate this over constraint, the body (4') is added to the first PKL (Fig. 2.10). This body has a vertical revolute joint with the platform (see [18] for more details). The non over constrained version of the mechanism is the one chosen in this study. Indeed, for the static model to be solved in the unknown joint reaction forces, the mechanism has to be non over constrained.

Geometric parameters of the Delta robot

The geometric parameters of the Delta robot are similar to the ones used to describe the passive legs of the RAF. In this case, we have:

- a: the radius of the circle containing points A_i , for $i = 1, \dots, 3$
- g: the radius of the circle containing points G_i , for $i = 1, \dots, 3$
- L_1 : the length of the forearm

L_2 : the length of the arm

(a) Inverse Geometric Problem

In this section, we develop the inverse kinematic model of the KLS. A geometric model of the first KL is presented in Fig. 2.11.

Points F_1 and G_1 are respectively the middle of C'_1C_1 and D'_1D_1 segments (Fig. 2.11). The subscript “ i ” is added since we are modelling leg “ i ”. The position of the platform, represented by the point O_p , is given by:

$$\mathbf{O}_b O_p = \mathbf{O}_b A_i + A_i F_i + F_i G_i + G_i O_p \quad (2.10)$$

We can assume, without loss of generality, that the platform is parallel to the base ($\mathbf{Q} = \mathbf{I}_3$), which yields the following expression:

$$\mathbf{r} = \mathbf{a}_i + \mathbf{R}_{1i}^0 \mathbf{l}_{21} + \mathbf{R}_{2i}^0 \mathbf{l}_{31} + \mathbf{Q} \mathbf{g}_i \quad (2.11)$$

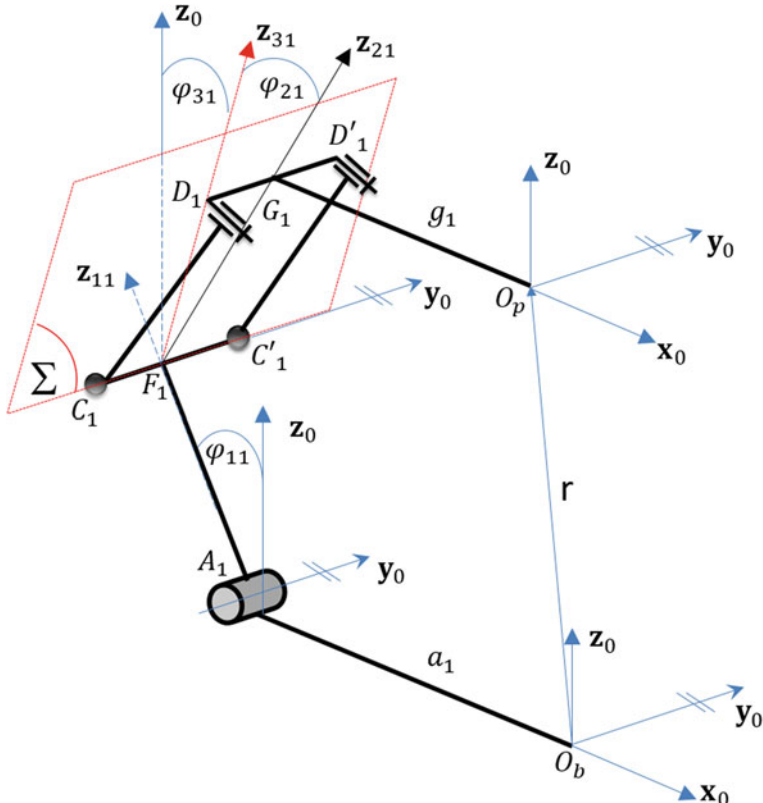


Fig. 2.11 A geometric model of the 1st KL ($\Delta_1 // y_0$)

where:

$$R_{1i}^0 = \begin{bmatrix} \cos\varphi_{1i} & 0 & \sin\varphi_{1i} \\ 0 & 1 & 0 \\ -\sin\varphi_{1i} & 0 & \cos\varphi_{1i} \end{bmatrix} \quad (2.12)$$

$$R_{2i}^0 = R_{3i}^0 R_{2i}^{3i} \quad (2.13)$$

$$R_{3i}^0 = \begin{bmatrix} \cos\varphi_{3i} & 0 & \sin\varphi_{3i} \\ 0 & 1 & 0 \\ -\sin\varphi_{3i} & 0 & \cos\varphi_{3i} \end{bmatrix} \quad (2.14)$$

$$R_{2i}^{3i} = \begin{bmatrix} 1 & 0 & 0 \\ 0 & \cos\varphi_{2i} & \sin\varphi_{2i} \\ 0 & -\sin\varphi_{2i} & \cos\varphi_{2i} \end{bmatrix} \quad (2.15)$$

$$\mathbf{l}_{2i} = L_2 \mathbf{z}_{1i}, \mathbf{l}_{3i} = L_3 \mathbf{z}_{2i} \quad (2.16)$$

$$\mathbf{r} = \overrightarrow{O_b O_p}$$

$\mathbf{a}_i = \overrightarrow{O_b A_i}$ is a vector fixed on the base

$\mathbf{g}_i = \overrightarrow{G_i O_p}$ is a vector fixed on the platform

$$\mathbf{a}_1 = [a, 0, 0]$$

$$\mathbf{a}_2 = \left[-\cos\left(\frac{\pi}{3}\right), \sin\left(\frac{\pi}{3}\right), 0 \right]$$

$$\mathbf{a}_3 = \left[-\cos\left(\frac{\pi}{3}\right), -\sin\left(\frac{\pi}{3}\right), 0 \right]$$

$$\mathbf{g}_1 = [-g, 0, 0]$$

$$\mathbf{g}_2 = \left[g\cos\left(\frac{\pi}{3}\right), -g\sin\left(\frac{\pi}{3}\right), 0 \right]$$

$$\mathbf{g}_3 = \left[g\cos\left(\frac{\pi}{3}\right), g\sin\left(\frac{\pi}{3}\right), 0 \right]$$

The forward kinematic model can be expressed as follows:

$$\begin{cases} x = x_i + \sin\varphi_{1i} L_2 + \sin\varphi_{3i} \cos\varphi_{2i} L_3 \\ y = y_i + \sin\varphi_{2i} L_3 \\ z = z_i + \cos\varphi_{1i} L_2 + \cos\varphi_{3i} \cos\varphi_{2i} L_3 \end{cases} \quad (2.17)$$

where $\mathbf{r} = [x \ y \ z]^T$ and $\mathbf{a}_i + \mathbf{g}_i = [x_i \ y_i \ z_i]^T$ and $z_i = 0$.

$$\mathbf{a}_1 + \mathbf{g}_1 = [a - g, 0, 0]$$

$$\begin{aligned}\mathbf{a}_2 + \mathbf{g}_2 &= \left[-(a-g)\cos\left(\frac{\pi}{3}\right), (a-g)\sin\left(\frac{\pi}{3}\right), 0 \right] \\ \mathbf{a}_3 + \mathbf{g}_3 &= \left[-(a-g)\cos\left(\frac{\pi}{3}\right), -(a-g)\sin\left(\frac{\pi}{3}\right), 0 \right]\end{aligned}\quad (2.18)$$

It is worth mentioning that the configuration of the KL is conditioned by the position vector \mathbf{r} .

Inverse Geometric problem

In this case the position vector \mathbf{r} and the objective is to calculate the three joint angles. It is worth mentioning that the only active parameter in this leg is the angle φ_{1i} , which is motorized. To identify the configuration of the first KL, we should solve the above equations.

Solving these equations yields two possible solutions for φ_{2i} :

$$\varphi_{2i} = \left\{ \arcsin\left(\frac{y - y_i}{L_3}\right), \pi - \arcsin\left(\frac{y - y_i}{L_3}\right) \right\}\quad (2.19)$$

However, due to the limits on the parallelogram only one solution satisfying the condition $-\frac{\pi}{2} < \varphi_{2i} < \frac{\pi}{2}$ is maintained.

For the angle φ_{3i} , we can also have two possible solutions given by:

$$\begin{aligned}\varphi_{3i} &= \left\{ \arccos\left(\frac{C_i}{\sqrt{(x_i - x)^2 + (z_i - z)^2}}\right) + \alpha_i, \right. \\ &\quad \left. -\arccos\left(\frac{C_i}{\sqrt{(x_i - x)^2 + (z_i - z)^2}}\right) + \alpha_i \right\}\end{aligned}\quad (2.20)$$

$$\text{where: } C_i = -\frac{L_2^2 - (x_i - x)^2 - (z_i - z)^2 - L_3^2 \cos^2 \varphi_{2i}}{2L_3 \cos \varphi_{2i}}$$

$$\alpha_i = \arctan\left(\frac{x_i - x}{z_i - z}\right)$$

For a given choice of φ_{3i} , there is only one possible solution for φ_{1i} given by:

$$\varphi_{1i} = \text{atan2}(x - x_i - L_3 \sin \varphi_{3i} \cos \varphi_{2i}, z - z_i - L_3 \cos \varphi_{3i} \cos \varphi_{2i})\quad (2.21)$$

However, we must have $-\frac{\pi}{2} < \varphi_{1i} < \frac{\pi}{2}$ due to the limits on the workspace, which restricts the platform to be on only one side of the base. Moreover, we will keep only the elbow up configuration of the KL, which leads to the condition $\varphi_{3i} \geq \varphi_{1i}$.

Therefore, 4 possible solutions could be found for the inverse problem of the delta robot.

The geometric model of the other two legs can be solved in a similar way, which brings the number of possible solutions to 12, for this case, as the delta robot has 3 legs.

(b) Forward Geometric problem

In this case, the joint angles φ_{1i} are given and we need to find the position given by the vector $\mathbf{r} = [x \ y \ z]^T$. To solve this problem, one can rewrite Eq. (2.17) as:

$$\begin{cases} x - x_i - \sin\varphi_{1i}L_2 = \sin\varphi_{3i}\cos\varphi_{2i}L_3 \\ y - y_i = \sin\varphi_{2i}L_3 \\ z - \cos\varphi_{1i}L_2 = \cos\varphi_{3i}\cos\varphi_{2i}L_3 \end{cases} \quad (2.22)$$

Squaring and adding these 3 equations yields the following three equations ($i = 1, 3$):

$$(x - x_i - \sin\varphi_{1i}L_2)^2 + (y - y_i)^2 + (z - \cos\varphi_{1i}L_2)^2 = L_3^2 \quad (i = 1, 3) \quad (2.23)$$

These equations need to be solved for x , y , and z and the x_i , y_i , and z_i are given by Eq. (2.18).

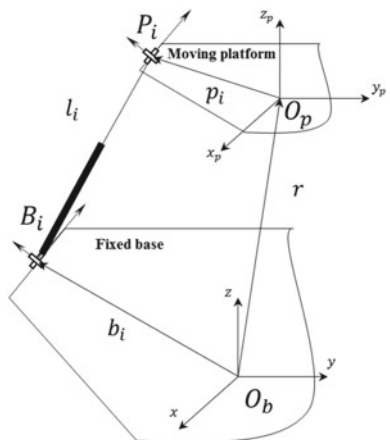
Geometrically, the solution represents the intersection points of 3 spheres with a radius L_3 and centered in the three points $[x_i + \sin\varphi_{1i}L_2 \ y_i \ \cos\varphi_{1i}L_2]^T$ ($i = 1, 3$). By manipulating these 3 equations, one can show that the solution is the intersection of two planes (or a line) and a sphere. Since there are two points of intersection of a line with a sphere, one can conclude that there are two possible solutions for this set of equations. However, these equations are difficult to solve analytically due to their high complexity.

Geometric analysis of the 3-UPU robot

Figure 2.12 shows one limb of a translational 3-UPU parallel manipulator. To facilitate the analysis, we attach two Cartesian coordinate systems $R_b(O_b, x, y, z)$ and $R_p(O_p, x_p, y_p, z_p)$ to the orthocenters of the fixed base and moving platform.

Since each universal joint consists of two intersecting revolute joints, each limb is equivalent to a R-R-P-R-R chain. In order to keep the moving platform from changing

Fig. 2.12 Geometric parameters of one limb UPU



its orientation, it is sufficient for the four revolute joint axes to satisfy the following two geometric conditions.

- The first revolute joint axis is parallel to the last revolute joint axis.
- The two intermediate revolute joint axes are parallel.

In general, the position and orientation of the moving platform with respect to the fixed base can be described by a position vector, $\mathbf{r} = \mathbf{O}_b\mathbf{O}_p$, and a 3×3 rotation matrix, \mathbf{R}^{AB} . However, since the moving platform undergoes pure translation, $\mathbf{Q} = \mathbf{R}^{AB} = \mathbf{I}$ (identity matrix).

Referring to Fig. 2.12, a vector-loop equation can be written for each limb as follows:

$$\mathbf{O}_b\mathbf{O}_p = \mathbf{O}_b\mathbf{B}_i + \mathbf{B}_i\mathbf{P}_i + \mathbf{P}_i\mathbf{O}_p$$

Let

$$\mathbf{p}_i = [\mathbf{O}_b\mathbf{P}_i]_{R_p}$$

$$[\mathbf{O}_p\mathbf{P}_i]_{R_b} = \mathbf{Q}[\mathbf{O}_p\mathbf{P}_i]_{R_p} = \mathbf{Q}\mathbf{p}_i$$

where \mathbf{Q} is a rotation matrix that takes R_p into R_b , and $\mathbf{b}_i = [\mathbf{O}_b\mathbf{B}_i]_{R_b}$

Since \mathbf{Q} is the identity matrix, the above equation yields to, for $i = 1, \dots, 3$:

$$\mathbf{r} = \mathbf{l}_i + \mathbf{b}_i - \mathbf{p}_i \quad i = 1, 2, 3 \quad (2.24)$$

where l_i is the length of the i th limb.

(a) Inverse Geometric problem

In this case the position vector \mathbf{r} is given and the objective is to calculate the three leg lengths l_i .

Squaring the previous equation, yields:

$$l_i^2 = [\mathbf{r} - \mathbf{e}_i]^T[\mathbf{r} - \mathbf{e}_i] \quad i = 1, 2, 3 \quad (2.25)$$

where $\mathbf{e}_i = \mathbf{b}_i - \mathbf{p}_i$. We note that $\mathbf{b}_i, \mathbf{p}_i$ are constant vectors and hence \mathbf{e}_i are constant vectors.

Therefore, in this case the solution of the inverse problem is readily available, and it is one of the main advantages of this type of structures.

(b) Forward Geometric problem

This problem is stated as follows: given the leg lengths l_i 's, find the position of the platform. This problem is much more complex than the previous one.

Equation (2.25) will be used to solve this problem. The left-hand side is given along with the constant vector \mathbf{e}_i . The unknown in this equation is the vector \mathbf{r} . The three components of $\mathbf{r} = [x, y, z]^T$ can be calculated by solving the three equations

given in (2.25). These 3 equations represent the equations of 3 spheres centred in point M_i whose coordinates are given by the vectors \mathbf{e}_i .

We can write Eq. (2.25) as

$$l_i^2 = (x - x_i)^2 + (y - y_i)^2 + (z - z_i)^2 \quad i = 1, 2, 3 \quad (2.26)$$

where $\mathbf{e}_i = [x_i, y_i, z_i]^T$.

The solution of this set of equations is like the one found for the Delta robot. However, the analytical solution is complex to find, and numerical methods pose the problem of selecting the solution out of the 2 possible ones.

Spherical Manipulators

The special case of three DOF spherical PMs have been presented by several works in the literature [69–73]. There are three well known architectures of the spherical manipulator. These PMs provide a pure rotational motion of the platform with respect to the base. In the architecture proposed by [74], the platform and the base are joined by a passive spherical pair and the orientation of the platform with respect to the base is controlled by three UPS legs (U, P and S stand for universal joint, actuated prismatic pair and spherical pair, respectively). The drawback of this architecture is the reduced workspace because of the passive spherical pairs. The architecture proposed by [70], is made out of a platform connected to the base by three RRR legs (R stands for revolute pair) where all the revolute pair axes concurrent in a fixed point. This parallel manipulator is an over constrained mechanism. The drawback of this architecture is that the mechanism jams or high internal loads arise in the links due to geometric errors. The architecture proposed by [75] (called 3-UPU spherical manipulator), has the orientation of the platform with respect to the base controlled by three UPU legs (U and P stand for universal joint and actuated prismatic pair). Each universal pair is made from two revolute pairs with orthogonal axes. For this architecture, the first revolute joint connected to the base and the platform must converge to a fixed point.

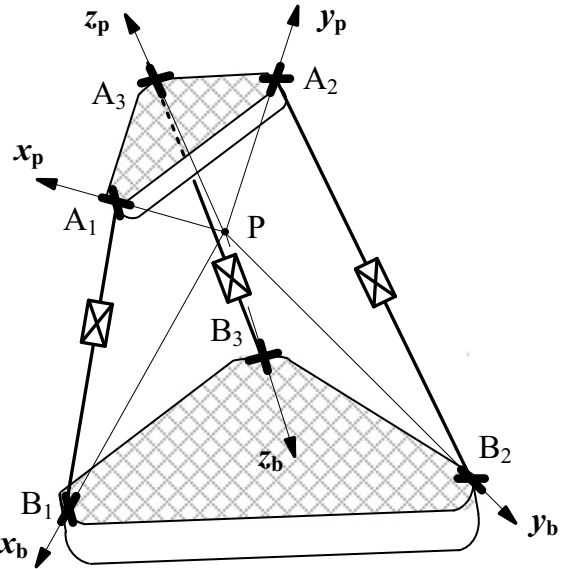
Kinematics of the 3-UPU spherical manipulator

The 3-UPU spherical manipulator is given on Fig. 2.1. The universal pairs U are centred at points B_i , and A_i ($i = 1, 2, 3$) attached respectively in the base platform. In order to have a pure rotational motion of the platform with respect to the base, two conditions have to be fulfilled [71, 76, 77]:

- The first three revolute pair axes fixed in the platform (base) must converge at a fixed point.
- In each leg, the intermediate revolute pair axes must be parallel to each other and perpendicular to the leg axis which is the line through the universal joints' centres.

The first revolute joints connected to the base (platform) are orthogonal and intersect at point P . The frames $S_b(P, x_b, y_b, z_b)$ $S_b(P, x_b, y_b, z_b)$ and $S_p(P, x_p, y_p, z_p)$ are attached to the base and the platform, respectively (Fig. 2.13). The x_b , y_b and z_b

Fig. 2.13 The 3-UPU spherical manipulator



x_b , y_b and z_b axes (x_p , y_p and z_p) (x_p , y_p and z_p) are along the line PB_i , $i = 1, 2, 3$, respectively (PA_i) (PA_i).

Based on the cycle PB_iA_iP , we have:

$$\mathbf{PB}_i + \mathbf{B}_i\mathbf{A}_i + \mathbf{A}_i\mathbf{P} = 0 \quad i = 1, 2, 3 \quad (2.27)$$

Let:

$$\mathbf{b}_i = [\mathbf{PB}_i]_{S_b}$$

$$\mathbf{l}_i = [\mathbf{B}_i\mathbf{A}_i]_{S_b}$$

$$\mathbf{p}_i = [\mathbf{A}_i\mathbf{P}]_{S_p}$$

where \mathbf{b}_i and \mathbf{l}_i , $i = 1, 2, 3$, are two vectors expressed in the fixed reference frame S_b and \mathbf{p}_i , $i = 1, 2, 3$, is expressed in the frame S_p .

The vector \mathbf{p}_i , $i = 1, 2, 3$, expression in the fixed frame S_b is given by:

$$[\mathbf{p}_i]_{S_b} = \mathbf{Q}\mathbf{p}_i \quad i = 1, 2, 3$$

In this case, Eq. (2.28) gives:

$$\mathbf{l}_i = -\mathbf{b}_i + \mathbf{Q}\mathbf{p}_i \quad i = 1, 2, 3 \quad (2.28)$$

where:

\mathbf{Q} be the rotation matrix that takes S_p into S_b , given by:

$$\mathbf{Q} = \begin{bmatrix} c\theta c\psi & -c\varphi s\psi + s\varphi s\theta c\psi & s\psi s\varphi + c\psi s\theta c\varphi \\ c\theta s\psi & c\psi c\varphi + s\psi s\theta s\varphi & -s\varphi c\psi + c\varphi s\theta s\psi \\ -s\theta & s\varphi c\theta & c\varphi c\theta \end{bmatrix} \quad (2.29)$$

c is the cosine and s is the sine of the corresponding angle, respectively.

φ, θ and ψ are, respectively, roll, pitch, and yaw angles.

The vectors \mathbf{b}_i and \mathbf{p}_i , $i = 1, 2, 3$, contain respectively the base and the platform geometric parameters in their local frame.

The vector \mathbf{l}_i , $i = 1, 2, 3$, is a variable vector, which represents the length and the orientation of the i -th leg.

Inverse Geometric problem

For a given orientation of the platform, \mathbf{Q} , Eq. (2.28) gives the vectors \mathbf{l}_i 's, which represent the length and orientation of each leg. In this case, the model is simple, and no solving is needed. The solution is also unique.

Forward Geometric problem

This problem is stated as follows: given the leg lengths l_i 's, find the orientation of the platform. This problem is much more complex than the previous one.

Squaring both sides of Eq. (2.28), gives:

$$l_i^2 = b_i^2 + p_i^2 - 2\mathbf{b}_i^T \mathbf{Q} \mathbf{p}_i \quad i = 1, 2, 3 \quad (2.30)$$

where l_i , b_i and p_i , $i = 1, 2, 3$, are the magnitudes of the vectors \mathbf{l}_i , \mathbf{b}_i and \mathbf{p}_i , respectively.

The base is defined by the three following vectors representing the locations of the three universal joints:

$$[\mathbf{b}_1]_{S_b} = b_1[100]^T; [\mathbf{b}_2]_{S_b} = b_2[010]^T; [\mathbf{b}_3]_{S_b} = b_3[001]^T \quad (2.31)$$

The platform is defined by the three following vectors representing the locations of the three universal joints:

$$[\mathbf{p}_1]_{S_p} = p_1[0 - 10]^T; [\mathbf{p}_2]_{S_p} = p_2[00 - 1]^T; [\mathbf{p}_3]_{S_p} = p_3[-100]^T \quad (2.32)$$

This choice of the locations of the points A_i , $i = 1, 2, 3$, is necessary for a closed form solution to exist [78].

Replacing the expression of the rotation matrix \mathbf{Q} in Eq. (2.8), the following set of equations can be obtained:

$$\begin{cases} -c\varphi s\psi + s\varphi s\theta c\psi = \frac{l_1^2 - p_1^2 - b_1^2}{2b_1 p_1} \\ -s\varphi c\psi + c\varphi s\theta s\psi = \frac{l_2^2 - p_2^2 - b_2^2}{2b_2 p_2} \\ -s\theta = \frac{l_3^2 - p_3^2 - b_3^2}{2b_3 p_3} \end{cases} \quad (2.33)$$

By solving the third equation of the system (2.11) given above, two solutions for the angle θ , can be obtained:

$$\begin{cases} \theta = -\arcsin\left(\frac{l_3^2 - p_3^2 - b_3^2}{2b_3 p_3}\right) \\ \text{or} \\ \theta = -\pi + \arcsin\left(\frac{l_3^2 - p_3^2 - b_3^2}{2b_3 p_3}\right) \end{cases} \quad (2.34)$$

These two solutions can exist, if the following condition is fulfilled:

$$|b_3 - p_3| \leq l_3 \leq b_3 + p_3 \quad (2.35)$$

According to the solutions obtained for the angle θ , the first two equations of the set of Eq. (2.33) can be solved:

$$\begin{aligned} \sin(\psi - \varphi) &= \frac{c_1 - c_2}{c_3 - c_1} \\ \sin(\psi + \varphi) &= \frac{c_1 + c_2}{c_3 + c_1} \end{aligned} \quad (2.36)$$

where $c_i, i = 1, 2, 3$ are given:

$$c_i = \frac{l_i^2 - p_i^2 - b_i^2}{2p_i b_i}, i = 1, 2, 3$$

The solution of the set of Eq. (2.36), which is derived from the two solutions of the angle θ , is given by:

$$\begin{cases} \psi = \frac{1}{2} \left(\arcsin\left(-\frac{c_1+c_2}{c_3+1}\right) + \arcsin\left(\frac{c_1-c_2}{c_3-1}\right) \right) \\ \varphi = \frac{1}{2} \left(\arcsin\left(-\frac{c_1+c_2}{c_3+1}\right) - \arcsin\left(\frac{c_1-c_2}{c_3-1}\right) \right) \end{cases} \quad (2.37)$$

$$\begin{cases} \psi = \pi - \frac{1}{2} \left(\arcsin\left(-\frac{c_1+c_2}{c_3+1}\right) + \arcsin\left(\frac{c_1-c_2}{c_3-1}\right) \right) \\ \varphi = \frac{1}{2} \left(-\arcsin\left(-\frac{c_1+c_2}{c_3+1}\right) - \arcsin\left(\frac{c_1-c_2}{c_3-1}\right) \right) \end{cases} \quad (2.38)$$

$$\begin{cases} \psi = \frac{\pi}{2} + \frac{1}{2} \left(-\arcsin\left(-\frac{c_1+c_2}{c_3+1}\right) + \arcsin\left(\frac{c_1-c_2}{c_3-1}\right) \right) \\ \varphi = \frac{\pi}{2} - \frac{1}{2} \left(\arcsin\left(-\frac{c_1+c_2}{c_3+1}\right) - \arcsin\left(\frac{c_1-c_2}{c_3-1}\right) \right) \end{cases} \quad (2.39)$$

$$\begin{cases} \psi = \frac{\pi}{2} + \frac{1}{2} \left(\arcsin\left(-\frac{c_1+c_2}{c_3+1}\right) - \arcsin\left(\frac{c_1-c_2}{c_3-1}\right) \right) \\ \varphi = -\frac{\pi}{2} + \frac{1}{2} \left(\arcsin\left(-\frac{c_1+c_2}{c_3+1}\right) + \arcsin\left(\frac{c_1-c_2}{c_3-1}\right) \right) \end{cases} \quad (2.40)$$

Thus, eight solutions of the orientation of the platform with respect to the base exist for one given set of l_i 's.

These solutions can exist, if and only if the following conditions are fulfilled:

$$\begin{cases} -1 \leq \frac{c_1+c_2}{c_3+1} \leq 1 \\ -1 \leq \frac{c_1-c_2}{c_3-1} \leq 1 \\ c_3 \neq \pm 1 \end{cases} \quad (2.41)$$

Thus, we can conclude that the orientation workspace of the manipulator is determined by Eqs. (2.35, 2.41), which corresponds to the existence of the solution of the orientation of the platform with respect to the base.

As shown in this example, the main challenge in modelling parallel manipulators is their geometric model. Moreover, based on Eq. (2.30), the inverse geometric problem is strait forward. Indeed, Eq. (2.30) gives the values of the leg length's l_i 's for a given orientation of the platform, represented here by the matrix Q . However, the forward problem is much more complex and can be solved analytically, only in a few special geometries. The example shown in this section, has a special geometry, which allowed the analytical solution of the forward problem. In this case 8 possible solutions are illustrated through Eqs. (2.34), (2.37), (2.38), (2.39), (2.40). This is another difference between the serial and parallel manipulators.

2.4 Discussion

Based on the analysis presented in the previous sections, it was shown that modelling parallel manipulators is much more challenging than their serial counterparts. These difficulties are mainly due to the complexity of the structure of parallel manipulators, compared to serial ones. This parallel structure yields more complex models, in general. In particular, except for parallelogram structures, serial manipulators have only active joints, and their number defines the DoF of the robot. Therefore, the geometric model, in this case, requires as many variable parameters as there are DoFs in the robot. Moreover, there are a handful of different structures for serial manipulators and their geometric description is standardized through DH parameters and their forward models are systematically generated through homogenous matrices. Moreover, the inverse kinematic problem can still be solved analytical, especially in the case of robots with spherical wrists. However, parallel manipulators have much more complex and diverse structures. These structures involve closed loop kinematic chains, which is usually involves a high number of passive joints. This fact makes the geometric model more complex with a high number of variable parameters. The main objective in solving these models is to eliminate these passive parameters to keep only the active ones, which are the controlled ones. Parallel robots with only 3 DoFs, two translators and one spherical, were selected because of their simplicity and for which an analytical solution could be found. These examples were selected to illustrate the

challenges faced when modelling parallel robots. The solutions presented in these examples were facilitated by the special geometry of these structures. However, in some cases up to 8 solutions could exist, which shows the high degree of non-linearity of the model. In other cases, no analytical solution could be found. In more general cases or for parallel robots with more than 3 DoFs, these analytical solutions cannot be obtained, and one has to rely on numerical solutions. It is important to mention that, when comparing the modelling of serial and parallel robots, the geometric description of the structure plays an important role in the complexity of the obtained models. Indeed, the advantage of serial manipulators resides in their standard description, using DH parameter, and their systematic generation of the kinematic models. For this reason, several software programs were developed to generate these models, based on the DH parameters. Two toolboxes under Matlab© are worth mentioning [6, 79].

For parallel robots, no generic software programs exist, due mainly to the diversity of the structures, mentioned above.

2.5 Conclusion

This chapter presented a comparison between the modelling of serial robots and their parallel counterparts. Examples of serial and parallel robots were used to illustrate this comparison. The main difference between the modelling of these two types of robots is their geometric description. Indeed, for serial manipulators, the DH parameters representation offers a standard way to generate systematically all the models. However, in the parallel case, there is no standard in describing the geometry and each structure requires a specific number and type of parameters for its geometric description.

It was shown that for serial robots, the inverse geometric problem is relatively difficult to solve, whereas the direct model is straight forward, and no solving is needed. For parallel robots, in most cases, the forward and inverse problems usually are challenging and require solving nonlinear highly coupled equations. The examples presented in this chapter were selected from parallel robots with only 3 DoFs, either translation or rotation, to illustrate these challenges.

References

1. Borik, A., et al.: Caged quadrotor drone for inspection of central HVAC ducts (May 2019). <https://doi.org/10.1109/ICASET.2019.8714539>
2. Jaradat, M.A., Bani-Salim, M., Awad, F.: A highly-maneuverable demining autonomous robot: an over-actuated design. *J. Intell. Robot. Syst. Theory Appl.* **90**(1–2), 65–80 (2018). <https://doi.org/10.1007/s10846-017-0654-y>
3. Jaradat, M.A., et al.: A fully portable robot system for cleaning solar panels (January 2016). <https://doi.org/10.1109/ISMA.2015.7373479>

4. Ollero, A., Siciliano, B.: Introduction. In: Springer Tracts in Advanced Robotics, vol. 129, pp. 3–11. Springer, Berlin (2019)
5. Orsag, M., Korpeila, C., Oh, P., Bogdan, S.: Aerial Manipulation. Springer International Publishing, Cham (2018)
6. Corke, P.: Robotics, Vision and Control, vol. 118. Springer International Publishing, Cham (2017)
7. 1934-78—Spray-paint robot patents—Pollard Jr, Pollard, Roselund and DeVilbiss Comp. (American)—cyberneticzoo.com. <http://cyberneticzoo.com/early-industrial-robots/1934-78-spray-paint-robot-patents-pollard-jr-pollard-roselund-and-devilbiss-comp-american/>. Accessed 07 Jan 2022
8. Gough, E.: Universal tire test machine. In: 9th International Technical Congress F.I.S.I.T.A, pp. 117–137 (1962)
9. Stewart, D.: A platform with six degrees of freedom. Proc. Inst. Mech. Eng. **180**(1), 371–386 (1965). https://doi.org/10.1243/pime_proc_1965_180_029_02
10. Dietmaier, P.: The Stewart-Gough platform of general geometry can have 40 real postures. In: Advances in Robot Kinematics: Analysis and Control, pp. 7–16. Springer Netherlands (1998)
11. Romdhane, L.: Design and analysis of a hybrid serial-parallel manipulator. Mech. Mach. Theory **34**(7) (1999). [https://doi.org/10.1016/S0094-114X\(98\)00079-2](https://doi.org/10.1016/S0094-114X(98)00079-2)
12. Fichter, E.F., Kerr, D.R., Rees-Jones, J.: The Gough-Stewart platform parallel manipulator: a retrospective appreciation. Proc. Inst. Mech. Eng. Part C J. Mech. Eng. Sci. **223**(1), 243–281 (2009). <https://doi.org/10.1243/09544062JMES1137>
13. Stoughton, R., et al.: A modified Stewart platform manipulator with improved dexterity. ieeexplore.ieee.org. Accessed 08 Jan 2022. Available: <https://ieeexplore.ieee.org/abstract/document/238280/>
14. Dasgupta, B., et al.: The Stewart Platform Manipulator: A Review. Elsevier. Accessed: 08 Jan 2022. Available: <https://www.sciencedirect.com/science/article/pii/S0094114X99000063>
15. Furqan, M., et al.: Studies on Stewart Platform Manipulator: A Review. Springer. Accessed: 08 Jan 2022. <https://doi.org/10.1007/s12206-017-0846-1>
16. Yuan, D., Zhang, Y.: Kinematics analysis of a novel translational parallel manipulator. In: 2009 International Conference on Measuring Technology and Mechatronics Automation, ICMTMA 2009, vol. 3, pp. 785–788 (2009). <https://doi.org/10.1109/ICMTMA.2009.544>
17. Ceccarelli, M., Carbone, G.: A stiffness analysis for CaPaMan (Cassino Parallel Manipulator). Mech. Mach. Theory **37**(5), 427–439 (2002). [https://doi.org/10.1016/S0094-114X\(02\)00006-X](https://doi.org/10.1016/S0094-114X(02)00006-X)
18. Romdhane, L., Affi, Z., Fayet, M.: Design and singularity analysis of a 3-translational-DOF in-parallel manipulator. J. Mech. Des. Trans. ASME **124**(3), 419–426 (2002). <https://doi.org/10.1115/1.1480815>
19. Affi, Z., Romdhane, L., Maalej, A.: Dimensional synthesis of a 3-translational-DOF in-parallel manipulator for a desired workspace. Eur. J. Mech. A/Solids **23**(2) (2004). <https://doi.org/10.1016/j.euromechsol.2004.01.003>
20. Romdhane, L.: Design and Analysis of a Hybrid Serial-Parallel Manipulator. Elsevier. Accessed 08 Jan 2022. Available: <https://www.sciencedirect.com/science/article/pii/S0094114X98000792>
21. Delta robot - Wikipedia. https://en.wikipedia.org/wiki/Delta_robot. Accessed 08 Jan 2022
22. Kim, H.S., Tsai, L.W.: Design optimization of a Cartesian parallel manipulator. J. Mech. Des. Trans. ASME **125**(1), 43–51 (2003). <https://doi.org/10.1115/1.1543977>
23. Gallardo-Alvarado, J., Alici, G., Rodríguez-Castro, R.: A novel three degrees of freedom partially decoupled robot with linear actuators. Robotica **30**(3), 467–475 (2012). <https://doi.org/10.1017/S026357471100083X>
24. Zhang, Y., Xu, H., Wu, X., He, Q.: Kinematics and performances analysis of the 3-CRC translational parallel manipulator. In: 2009 2nd International Conference on Intelligent Computation Technology and Automation, ICICTA 2009, vol. 4, pp. 546–549 (2009). <https://doi.org/10.1109/ICICTA.2009.846>

25. Babu, S.R., Raju, V.R., Ramji, K.: Design for optimal performance of 3-RPS parallel manipulator using evolutionary algorithms. *Trans. Can. Soc. Mech. Eng.* **37**(2), 135–160 (2013). <https://doi.org/10.1139/tcsme-2013-0009>
26. Pashkevich, A., Chablat, D., Wenger, P.: Stiffness analysis of overconstrained parallel manipulators. *Mech. Mach. Theory* **44**(5), 966–982 (2009). <https://doi.org/10.1016/j.mechmachtheory.2008.05.017>
27. Ruggiu, M.: Cartesian stiffness matrix mapping of a translational parallel mechanism with elastic joints. *Int. J. Adv. Robot. Syst.* **9**, 1–8 (2012). <https://doi.org/10.5772/52145>
28. Tanabe, M., Huda, S., Takeda, Y.: Utility workspace of 3-5R translational parallel mechanism. In: 2008 IEEE International Conference on Mechatronics and Automation, RAM 2008, pp. 761–767 (2008). <https://doi.org/10.1109/RAMECH.2008.4690890>
29. Yu, L., Wang, T., Song, H., Wang, Z., Yu, P.: Static analysis for a 3-RUU parallel mechanism. In: 2012 IEEE International Conference on Mechatronics and Automation, ICMA 2012, pp. 749–754 (2012). <https://doi.org/10.1109/ICMA.2012.6283236>
30. Wang, X., Wei, C.: Kinematics and workspace of 3-RUU parallel manipulator. In: 2011 International Conference on Consumer Electronics, Communications and Networks, CECNet 2011—Proceedings, pp. 438–441 (2011). <https://doi.org/10.1109/CECNET.2011.5768973>
31. Walter, D.R.: Kinematic analysis of the TSAI-3UPU parallel manipulator using algebraic methods. *World* **1**, 19–25 (2011)
32. Bhutani, G., Dwarkanath, T.A.: Novel design solution to high precision 3 axes translational parallel mechanism. *Mech. Mach. Theory* **75**, 118–130 (2014). <https://doi.org/10.1016/j.mechmachtheory.2013.11.010>
33. Joshi, S., Tsai, L.W.: A comparison study of two 3-DOF parallel manipulators: one with three and the other with four supporting legs. *IEEE Trans. Robot. Autom.* **19**(2), 200–209 (2003). <https://doi.org/10.1109/TRA.2003.808857>
34. Yang, Y., O'Brien, J.F.: Singularity-free workspace design for the translational 3-UPU parallel robot. In: 2010 IEEE International Conference on Automation Science and Engineering, CASE 2010, pp. 222–227 (2010). <https://doi.org/10.1109/COASE.2010.5584559>
35. Wolf, A., Shoham, M., Park, F.C.: Investigation of singularities and self-motions of the 3-UPU robot. *Adv. Robot Kinemat.*, pp. 165–174 (2002). https://doi.org/10.1007/978-94-017-0657-5_18
36. Qu, H., Fang, Y., Guo, S., Ye, W.: A novel 4-UPU translational parallel mechanism with fault-tolerant configurations. *Proc. Inst. Mech. Eng. Part C J. Mech. Eng. Sci.* **228**(16), 3006–3018 (2014). <https://doi.org/10.1177/0954406214525366>
37. Di Gregorio, R., Parenti-Castelli, V.: Mobility analysis of the 3-UPU parallel mechanism assembled for a pure translational motion. *J. Mech. Des. Trans. ASME* **124**(2), 259–264 (2002). <https://doi.org/10.1115/1.1471530>
38. Hu, B., Yao, Y., Wu, P., Lu, Y.: A comparison study of two 3-UPU translational parallel manipulators. *Int. J. Adv. Robot. Syst.* **10**, 1–9 (2013). <https://doi.org/10.5772/53394>
39. Han, C., Kim, J., Kim, J., Park, F.C.: Kinematic sensitivity analysis of the 3-UPU parallel mechanism. *Mech. Mach. Theory* **37**(8), 787–798 (2002). [https://doi.org/10.1016/S0094-114X\(02\)00021-6](https://doi.org/10.1016/S0094-114X(02)00021-6)
40. Lu, S., Li, Y.: Dimensional synthesis of a 3-DOF translational parallel manipulator considering kinematic dexterity property. In: 2014 IEEE International Conference on Information and Automation, ICIA 2014, vol. 183, no. July, pp. 7–12 (2014). <https://doi.org/10.1109/ICInfa.2014.6932617>
41. Callegari, M., Marzetti, P.: Kinematic characterisation of a 3-PUU parallel robot. In: Proceedings of the Intelligent Manipulation, Grasping IMG04, pp. 377–382 (2004). Available: <http://www.dipmec.univpm.it/meccanica/uk/db/articoli/2004IMG04Genovab.pdf>
42. Li, Y., Xu, Q., Staicu, S.: Kinematics of the 3-PUU translational parallel manipulator. *UPB Sci Bull. Ser. D Mech. Eng.* **73**(4), 3–14 (2011)
43. Yuehua, W., Guan, W., Shiming, J., Jun, L.: A survey on the parallel robot optimization. In: Proceedings - 2008 2nd International Symposium on Intelligent Information Technology Application 2008, vol. 2, pp. 655–659 (2008). <https://doi.org/10.1109/IITA.2008.277>

44. Li, Y., Xu, Q.: Kinematic analysis of a 3-PRS parallel manipulator. *Robot. Comput. Integr. Manuf.* **23**(4), 395–408 (2007). <https://doi.org/10.1016/j.rcim.2006.04.007>
45. Kim, H.S., Tsai, L.W.: Kinematic synthesis of a spatial 3-RPS parallel manipulator. *J. Mech. Des. Trans. ASME* **125**(1), 92–97 (2003). <https://doi.org/10.1115/1.1539505>
46. Schadlbauer, J., Walter, D.R., Husty, M.L.: The 3-RPS parallel manipulator from an algebraic viewpoint. *Mech. Mach. Theory* **75**, 161–176 (2014). <https://doi.org/10.1016/j.mechmачtheory.2013.12.007>
47. Di Gregorio, R.: Kinematics of the translational 3-URC mechanism. *J. Mech. Des. Trans. ASME* **126**(6), 1113–1117 (2004). <https://doi.org/10.1115/1.1814390>
48. Bamberger, H., Wolf, A., Shoham, M.: Architectures of translational parallel mechanism for MEMS fabrication. *J. Mech. Des. Trans. ASME* **130**(8), 0845021–0845028 (2008). <https://doi.org/10.1115/1.2936933>
49. Srivastava, N., Haque, I.: A review on belt and chain continuously variable transmissions (CVT): dynamics and control. *Mech. Mach. Theory* **44**(1), 19–41 (2009). <https://doi.org/10.1016/j.mechmачtheory.2008.06.007>
50. Li, B., Li, Y.M., Zhao, X.H., Ge, W.M.: Kinematic analysis of a novel 3-CRU translational parallel mechanism. *Mech. Sci.* **6**(1), 57–64 (2015). <https://doi.org/10.5194/ms-6-57-2015>
51. Badescu, M., Mavroidis, C.: Workspace optimization of 3-legged UPU and UPS parallel platforms with joint constraints. *J. Mech. Des. Trans. ASME* **126**(2), 291–300 (2004). <https://doi.org/10.1115/1.1667922>
52. Kim, H.S.: Kinematic calibration of a Cartesian parallel manipulator. *Int. J. Control. Autom. Syst.* **3**(3), 453–460 (2005)
53. Kim, D., Chung, W.K.: Kinematic condition analysis of three-DOF pure translational parallel manipulators. *J. Mech. Des. Trans. ASME* **125**(2), 323–331 (2003). <https://doi.org/10.1115/1.1564573>
54. Li, Y., Xu, Q.: Dynamic modeling and robust control of a 3-PRC translational parallel kinematic machine. *Robot. Comput. Integr. Manuf.* **25**(3), 630–640 (2009). <https://doi.org/10.1016/j.rcim.2008.05.006>
55. Callegari, M., Tarantini, M.: Kinematic analysis of a novel translational platform. *J. Mech. Des. Trans. ASME* **125**(2), 308–315 (2003). <https://doi.org/10.1115/1.1563637>
56. Li, Y., Xu, Q.: Kinematic analysis and design of a new 3-DOF translational parallel manipulator. *J. Mech. Des. Trans. ASME* **128**(4), 729–737 (2006). <https://doi.org/10.1115/1.2198254>
57. Babu, S.R., Raju, V.R., Ramji, K.: Design optimization of a 3 DOF translational parallel manipulator. *Int. J. Eng. Adv. Technol.* **3**, 2249–8958 (2015)
58. Li, Y., Xu, Q.: Kinematics and dexterity analysis for a novel 3-DOF translational parallel manipulator. In: Proceedings - IEEE International Conference on Robotics and Automation, vol. 2005, no. July 2015, pp. 2944–2949 (2005). <https://doi.org/10.1109/ROBOT.2005.1570561>
59. Shen, H., Yang, T., Tao, S., Liu, A., Ma, L.Z.: Structure and displacement analysis of a novel three-translation parallel mechanism. *Mech. Mach. Theory* **40**(10), 1181–1194 (2005). <https://doi.org/10.1016/j.mechmачtheory.2004.12.022>
60. Callegari, M., Palpacelli, M.C., Principi, M.: Dynamics modelling and control of the 3-RCC translational platform. *Mechatronics* **16**(10), 589–605 (2006). <https://doi.org/10.1016/j.mechatronics.2006.06.001>
61. Laribi, M.A., Romdhane, L., Zeghloul, S.: Analysis and dimensional synthesis of the DELTA robot for a prescribed workspace. *Mech. Mach. Theory* **42**(7), 859–870 (2007). <https://doi.org/10.1016/j.mechmачtheory.2006.06.012>
62. Stock, M., Miller, K.: Optimal kinematic design of spatial parallel manipulators: application to linear delta robot. *J. Mech. Des. Trans. ASME* **125**(2), 292–301 (2003). <https://doi.org/10.1115/1.1563632>
63. Collard, J.F., Duysinx, P., Fisette, P.: Kinematical optimization of closed-loop multibody systems. *Comput. Methods Appl. Sci.* **12**, 159–179 (2009). https://doi.org/10.1007/978-1-4020-8829-2_9

64. Yan, S.J., Ong, S.K., Nee, A.Y.C.: Optimization design of general triglide parallel manipulators. *Adv. Robot.* **30**(16), 1027–1038 (2016). <https://doi.org/10.1080/01691864.2016.1192063>
65. Caro, S., Wenger, P., Bennis, F., Chablat, D.: Sensitivity analysis of the orthoglide: a three-DOF translational parallel kinematic machine. *J. Mech. Des. Trans. ASME* **128**(2), 392–402 (2006). <https://doi.org/10.1115/1.2166852>
66. Pashevich, A., Wenger, P., Chablat, D.: Design strategies for the geometric synthesis of Orthoglide-type mechanisms. *Mech. Mach. Theory* **40**(8), 907–930 (2005). <https://doi.org/10.1016/j.mechmachtheory.2004.12.006>
67. Zhang, Y., Dang, Y., Wu, X.: Kinematics and singularity analysis of a novel decoupled translational parallel manipulator. In: 2010 IEEE International Conference on Mechatronics and Automation ICMA 2010, No. 1, pp. 622–626 (2010). <https://doi.org/10.1109/ICMA.2010.5587967>
68. Goudali, A.: Contribution à l'étude d'un nouveau robot Parallèle 2-Delta à six degrés de liberté avec découplage (1995). Accessed 12 Mar 2021. Available: <https://www.theses.fr/1995POIT2280>
69. Kong, X., Gosselin, C.M.: Type synthesis of three-degree-of-freedom spherical parallel manipulators. *Int. J. Rob. Res.* **23**(3), 237–245 (2004). <https://doi.org/10.1177/0278364904041562>
70. Gosselin, C., Angeles, J.: The Optimum Kinematic Design of a Spherical Three-Degree-of-Freedom Parallel Manipulator (1989). Accessed 08 Jan 2022. Available: <https://asmedigitalcollection.asme.org/mechanicaldesign/article-abstract/111/2/202/434734>
71. Di Gregorio, R.: The 3-RSS wrist: a new, very simple and not over constrained spherical parallel manipulator. In: Proceedings of the ASME Design Engineering Technology Conference, vol. 5 B, pp. 1193–1199 (2002). <https://doi.org/10.1115/detc2002/mecch-34344>
72. Wu, C., Liu, X.J., Wang, L., Wang, J.: Optimal design of spherical 5R parallel manipulators considering the motion/force transmissibility. *J. Mech. Des. Trans. ASME* **132**(3), 0310021–03100210 (2010). <https://doi.org/10.1115/1.4001129>
73. Wu, G., Caro, S., Bai, S., Kepler, J.: Dynamic modeling and design optimization of a 3-DOF spherical parallel manipulator. *Rob. Auton. Syst.* **62**(10), 1377–1386 (2014). <https://doi.org/10.1016/j.robot.2014.06.006>
74. Innocenti, C., Parenti-Castelli, V.: Direct kinematics of the 6-4 fully parallel manipulator with position and orientation uncoupled. In: *Robotic Systems*, pp. 3–10. Springer Netherlands (1992)
75. Di Gregorio, R.: A new family of spherical parallel manipulators. *Robotica* **20**(4), 353–358 (2002). <https://doi.org/10.1017/S0263574702004174>
76. Karouia, M., Hervé, J.M.: Asymmetrical 3-DoF spherical parallel mechanisms. *Eur. J. Mech. A/Solids* **24**(1), 47–57 (2005). <https://doi.org/10.1016/j.euromechsol.2004.10.001>
77. Ferris, B.D., Stanton, J., Zamora, J.: Kinematics of the wrist. *J. Bone Jt. Surg. - Ser. B* **82**(2), 242–245 (2000). <https://doi.org/10.1302/0301-620X.82B2.9301>
78. Chebbi, A.H., Affi, Z., Romdhane, L.: Modelling and analysis of the 3-UPU spherical manipulator. *Eur. J. Comput. Mech.* **22**(2–4), 157–169 (2013). <https://doi.org/10.1080/17797179.2013.820903>
79. Mathworks, Matlab. Mathworks. Accessed: 08 Jan 2022. Available: https://www.mathworks.com/help/robotics/index.html?s_tid=srchtitle

Chapter 3

Simulating Vibrations of Two-Wheeled Self-balanced Robots with Road Excitations by MATLAB



William Guo and Wei Li

Abstract Complexity is the nature of robotics and also the obstacle for young students to engage with robotic education due to their limited knowledge in mathematics, physics, programming, and engineering. It is logical to use simplified models with less complicated platforms to deliver fundamentals of robotics to young students. A case study of simulating the dynamic motion of a simplified quarter car model in order to better understand the vibrations of the two-wheeled self-balanced robot with different road excitations is reported in this chapter. We employ a numerical method to solve the ODE of the simplified quarter car model. This case study has shown: 1) this approach is more intuitive for students to visually observe the vertical vibrations of slow-moving two-wheeled self-balanced robots over different road excitations; 2) this approach provides an alternative way to conduct simulations for simple models, which overcomes the missed links hidden in a Blackbox such as a Simulink model. Hence, it may potentially become an attractive tool for promoting robotics and STEM education to young students in the future.

3.1 Introduction

In recent years, robotics education for students in primary and secondary schools has been included in education curricula in many countries and innovative approaches have been proposed to make robotics more intuitively understandable for young students [3, 6, 10, 12, 15]. Complexity is the nature of robotics and also the obstacle for young students to further engage with robotic education due to their limited knowledge in mathematics, physics, programming, and engineering. Hence, it is logical to use simplified models with less complicated platforms to deliver fundamentals of robotics to young students so as to motivate them to engage in further studies in STEM. One of the most popular tools suitable for such educational purpose is robotic vehicles [3].

W. Guo (✉) · W. Li

School of Engineering and Technology, Central Queensland University, North Rockhampton,
OLQ 4702, Australia

e-mail: w.guo@cqu.edu.au

Robotic vehicles, or, unmanned vehicles, move on the rolling wheels of the vehicles. The wheels are connected to the vehicle body by various suspension systems. Optimising dynamicity of the suspension system of a vehicle is an important topic for maintaining stability and controllability of the vehicle, and passenger comfortability during the vehicle movement. Logically understanding the dynamic behaviours of such suspension systems is the first step towards the design and implementation of optimal dynamicity for vehicle suspension systems. Computer simulation has been widely used in analysing the dynamic responses of vehicle suspension systems so as to gain better understanding of such systems under different conditions with some well-known models, including the full car suspension model [4, 20], the half car suspension model [1, 8, 17], and the quarter car suspension model [11, 14, 16]. Since most people have had personal experiences in riding with different types of vehicles, using any of these car suspension models to engage with school students in robotics education would be more appealing to young students.

The full car model takes the horizontal and vertical linear motions and the rotational motions of four wheels of a car into consideration. However, the complexity of a full car model in dynamic simulation is increased exponentially, which would be too difficult for most young students to comprehend. In the half car model, both the linear and rotational motions of the front and rear wheels on one-side of a car are considered. As a compromise, the half car model is a fairly good approximation for the full car model. However, simulating the dynamic behaviours of vehicle suspension systems with the half car model is not easy for young students to understand either, particularly when it is implemented by MATLAB Simulink usually presented in the state space through the Laplace transforms. The quarter car model is widely used in analysing the pure linear motions of a wheel and the associated suspension system, particularly incorporating different road excitations due to its simplicity [14, 16]. All these models can be used to analyse the dynamic behaviours of different types of robots. However, for the two-wheeled self-balanced robots that have a pair of parallel wheels only [2, 5, 19, 22], the quarter car model would be an appropriate model for analysing their dynamic behaviours under different road conditions.

Simulink in MATLAB has become a popular choice in simulating the dynamic behaviours of the suspension systems for all three car models [8, 13, 20]. Simulink allows mathematical models for the individual components and the combined subsystems of a car model, and the road excitations to be built as different blocks in a Simulink model by utilising and modifying existing functions in MATLAB. In Simulink, mathematical models represented in time domain, for example as ordinary differential equations (ODEs), are solved by Laplace transforms as blocks in the Simulink model. A Simulink model looks more like a network of logical control units, or a Blackbox, into which various inputs are fed for different responses. For example, the Simulink model for the simplest two-wheeled self-balanced robot with linear controls is shown in Fig. 3.1 [22], in which all *Integrators* are represented in the state-space domain by the Laplace transform. This Simulink model is understandable for experienced electrical or mechanical engineering students in universities but would not be understood by school students.

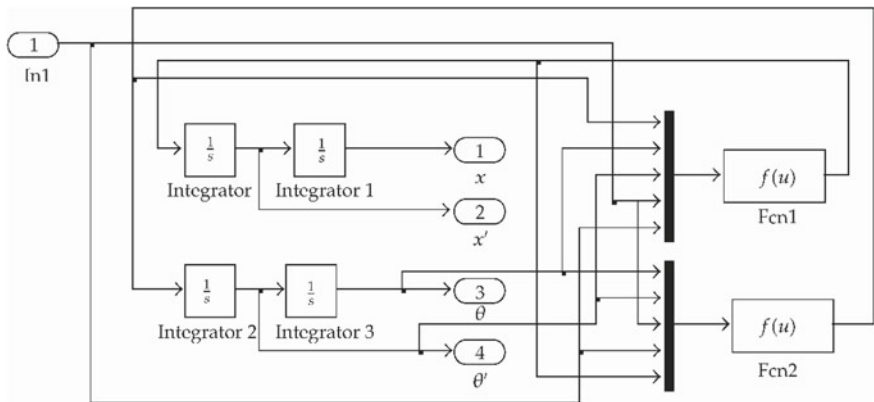


Fig. 3.1 A Simulink model for a simple two-wheeled self-balanced robot (after [22])

The outputs of a Simulink model are usually presented as time-dependent plots. For instance, the vertical movement of the car body connected to the wheel moving on an undulating road is commonly displayed as a curve of time versus the vertical displacement of the car body while the car moves over that section of the road [8, 14, 16, 20], an example shown in Fig. 3.2.

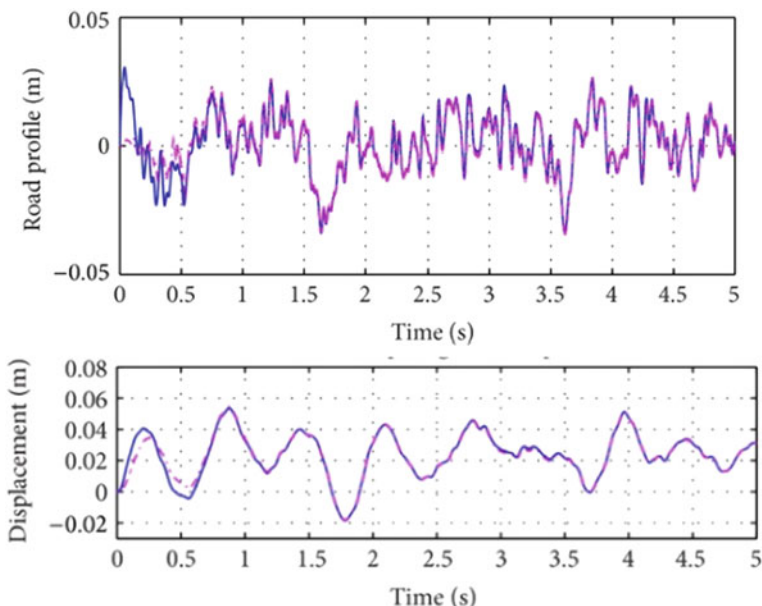


Fig. 3.2 A road profile (top) and the vertical displacements of the car body (bottom) of a quarter car model over the road profile with time (after [14])

However, the road is “static” whereas the car is “dynamic” in such situation. This implies that the time would be different if the car moves with different speeds even though the section of the road is fixed. Or in other words, a fixed section of road will be expressed as a function of time, depending on the speed of individual vehicles when moving over the road. For example, a bump road profile was represented by the following time dependent function by Shao et al. [16].

$$y(t) = \begin{cases} \frac{a}{2}[1 - \cos(\frac{2\pi v}{l}t)], & 0 \leq t \leq l/v \\ 0 & t > l/v \end{cases}$$

In this model, a and l are the height and length of the bump respectively and v is the speed of the vehicle. If choosing $a = 0.1$ m and $l = 0.5$ m, the corresponding bump is the positive half of a cosine function plotted in Fig. 3.3, which peaks at the horizontal point of 0.25 m. This bump is static regardless of how fast vehicles travel. However, such a static bump road is typically presented as a function of time for the simulation outputs, which makes the road look ‘dynamic’ to the readers, such being clearly shown in Fig. 3.4 with three different speeds of 0.1 m/s, 0.2 m/s and 0.5 m/s respectively.

It is obvious that virtually such a time-displacement plot cannot directly reflect the “static” nature of the road. This may be fine for researchers who know the problem well but it would be difficult for young students in primary and secondary schools to virtualise the vertical movement of the car over the road as an educational model. It is illogical to explain to students that ‘the length of a bump is 1 s or 5 s depending on the speed of a car’.

In this chapter, we present a case study of simulating the dynamic motion of a simplified quarter car model in order to better understand the vibrations of the two-wheeled self-balanced robot with different road excitations. The whole mathematical process is described in the time domain and simulation is assisted with conventional

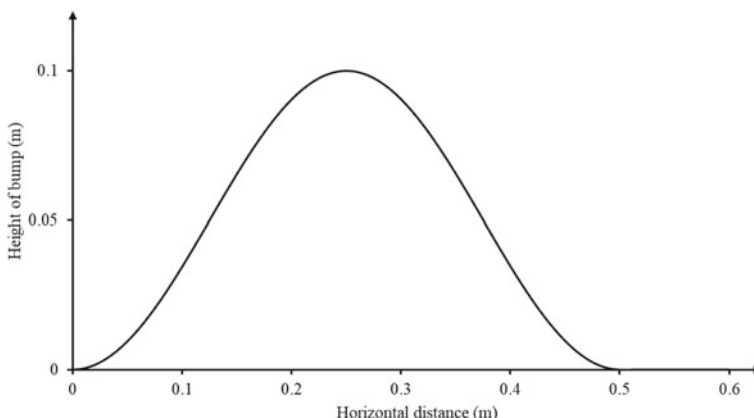


Fig. 3.3 A bump with a height of 0.1 m and a length of 0.5 m

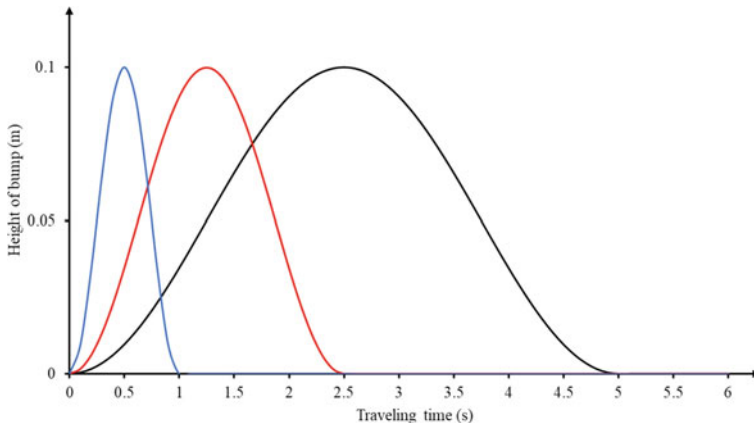


Fig. 3.4 The same bump in Fig. 3.3 represented as a function of time with different traveling speeds black line for 0.1 m/s, red line for 0.2 m/s, and blue line for 0.5 m/s

programming in MATLAB. We employ a numerical method to solve the ODE of the simplified quarter car model, rather than using the state-space blocks by the Laplace transforms available in MATLAB Simulink. This provides an opportunity for the virtual correlation among the model, inputs, and outputs so as to overcome the missed links hidden in a Blackbox such as a Simulink model. This approach not only offers an alternative way to conduct simulations for simple models, but also is useful for the purpose of virtualised STEM education.

In the second section, the quarter car model tailored to the two-wheeled self-balanced robot is described. The third section presents four road excitation profiles that would be commonly encountered for the two-wheeled self-balanced robots. The fourth section outlines the numerical method and solutions to the simplified model with the four road excitations implemented in MATLAB. The fifth section presents and discusses our simulation results of a slow-moving two-wheeled self-balanced robot. A brief summary is presented in the final section.

3.2 The Quarter Car Model and Simplification for the Two-Wheeled Self-balanced Robots

The quarter car model is often drawn from one of the two front wheels of a car. For a conventional vehicle without considering extra in-wheel damping, the mathematical model of the quarter car model (Fig. 3.5) is described by a system of two second-order ODEs as follows.

$$m_s \ddot{y}_s = k_s(y_u - y_s) + c_s(\dot{y}_u - \dot{y}_s)$$

Fig. 3.5 The conventional quarter car suspension model

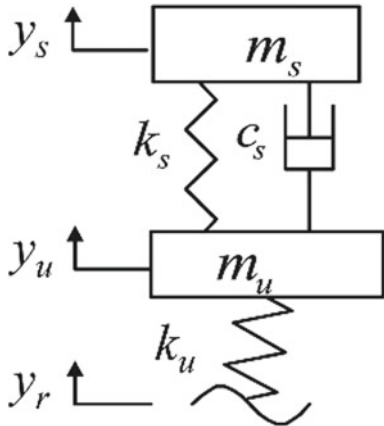
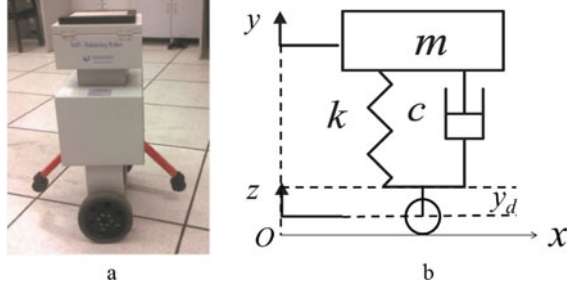


Fig. 3.6 The simplified quarter car suspension model for the simple two-wheeled self-balanced robot **a** a simple two-wheeled self-balanced robot (after [22]), **b** the simplified quarter car mode



$$m_u \ddot{y}_u = k_u(y_r - y_u) - k_s(y_u - y_s) - c_s(\dot{y}_u - \dot{y}_s) \quad (3.1)$$

where m_s is the sprung mass or the vehicle mass; m_u is the unsprung mass or mass of the wheel; c_s is the damping coefficient; k_s is the suspension stiffness; k_u is the tyre stiffness; y_s , y_u , and y_r are the vertical displacements for the vehicle body, wheel and the road disturbance, respectively.

In simple models of the two-wheeled self-balanced robots (Fig. 3.6a), the wheels were rigid without tyre and the mass of the wheels was much smaller than the mass of the robot body [22]. In such a situation, the mathematical model of the quarter car model with road excitation can be simplified by the first second-order ODE in the Eq. (3.1) as follows [18].

$$m \ddot{y} = k(z - y) + c(\dot{z} - \dot{y}) \quad \text{or} \quad \ddot{y} = \frac{k}{m}z + \frac{c}{m}\dot{z} - \frac{k}{m}y - \frac{c}{m}\dot{y} \quad (3.2)$$

where m is the robot mass; k is the suspension stiffness; c is the damping coefficient; y and z are the vertical displacements for the robot body and the road surface where the robot wheels contact with, respectively. The relative vertical displacement between

the robot body and the robot base that is attached to the axis of the wheels (hence the road surface) should be $y_d = y - z$ (Fig. 3.6b).

Equation (3.2) is a second-order constant-coefficient linear ODE that can be solved analytically by conventional characteristic equations or by the Laplace transforms, or other methods [7, 9]. Alternatively, the ODE (2) can be solved numerically by the Runge-Kutta method [7]. The numeric process is to be detailed in the fourth section.

3.3 The Road Excitation Profiles

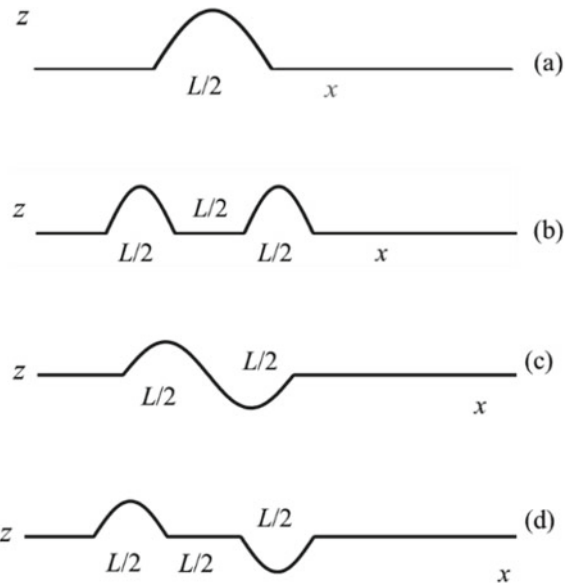
In this study, we use four sinusoidal models to represent four road excitation profiles, each to approximate a common road condition shown in Fig. 3.7.

The first model is a single bump of width $L/2$ represented by the positive half of a sine function (Fig. 3.7a)

$$z = \begin{cases} 0 & 0 \leq x < L/2 \\ -a \sin\left(\frac{2\pi vt}{L}\right) = -a \sin\left(\frac{2\pi x}{L}\right) & L/2 \leq x \leq L \\ 0 & x > L \end{cases} \quad (3.3)$$

where $a (> 0)$ is the height of the single bump; v is the horizontal speed of the vehicle; x is the distance the robot travelled from the beginning ($x = 0$), which correlates to the initial time ($t = 0$). Since the horizontal speed of the vehicle is supposed to be constant, the travelling distance is defined by $x = vt$.

Fig. 3.7 Four road excitation models



The second profile is a double-bump model, each bump with a width $L/2$ and apart by $L/2$ (Fig. 3.7b). In theory, this space can be set to a different value. This double-bump model represents some slow-moving sections near carparks of supermarkets, hospitals, airports and so forth. We approximate this model by two positive halves of a sine function $L/2$ apart as follows

$$z = \begin{cases} 0 & 0 \leq x < L/2 \\ -a \sin\left(\frac{2\pi vt}{L}\right) = -a \sin\left(\frac{2\pi x}{L}\right) & L/2 \leq x \leq L \\ 0 & L \leq x < 3L/2 \\ -a \sin\left(\frac{2\pi vt}{L}\right) = -a \sin\left(\frac{2\pi x}{L}\right) & 3L/2 \leq x \leq 2L \\ 0 & x > 2L \end{cases} \quad (3.4)$$

The third model represents an undulating road surface by a full sine function between $L/2$ and $3L/2$ (Fig. 3.7c). In theory, the widths of the uphill and downhill can be set to different values but we choose a simple sinusoidal for simplicity.

$$z = \begin{cases} 0 & 0 \leq x < L/2 \\ -a \sin\left(\frac{2\pi vt}{L}\right) = -a \sin\left(\frac{2\pi x}{L}\right) & L/2 \leq x \leq 3L/2 \\ 0 & x > 3L/2 \end{cases} \quad (3.5)$$

The fourth model represents a road profile with one uphill and one downhill apart by a distance of $L/2$ (Fig. 3.7d).

$$z = \begin{cases} 0 & 0 \leq x < L/2 \\ -a \sin\left(\frac{2\pi vt}{L}\right) = -a \sin\left(\frac{2\pi x}{L}\right) & L/2 \leq x \leq L \\ 0 & L \leq x < 3L/2 \\ a \sin\left(\frac{2\pi vt}{L}\right) = a \sin\left(\frac{2\pi x}{L}\right) & 3L/2 \leq x \leq 2L \\ 0 & x > 2L \end{cases} \quad (3.6)$$

The third and fourth profiles can be called the full undulation and delayed undulation models respectively. In the delayed undulation model, if the two shapes are far from each other, it simply represents a bump and a dip independent from each other. Therefore, our piecewise road excitation models, though simple but more representative, allow us to include the distances before, between, and after the bumps and/or dips so as to model the vertical movement of the robot body over the specified segment of the road excitation profile, hence closer to real situations.

3.4 Numeric Solutions to the Simplified Model

With the chosen road excitation models defined in the formulae (3.3–3.6), the simplified quarter car model for two-wheeled self-balanced robots described in the Eq. (3.2) can be solved by different methods. All four road excitation models are defined by

piecewise functions as the input to the ODE (3.2), but the solution resulted from the conventional analytical approach would treat the road excitation as continuous periodic function of the same pattern over the time of simulation. For example, given the following second-order ODE with initial conditions $y(0) = 0 \text{ m}$ and $y'(0) = 0 \text{ m/s}$,

$$y'' + 4y' + 4y = 8 \cos 2t,$$

its analytical solution is

$$y = -2te^{-2t} + \sin 2t.$$

If plotting this solution with respect to time as shown in Fig. 3.8 (y_1 in green), it shows that the robot body would go up with the initial bump and then go down during the transient period of the first 3.2 s. Afterwards, the body would settle into the stable status controlled by the cosine undulation excitation periodically. This behaviour is different from the piecewise excitation model that defines a bump in only one section for real situations. If simply cutting the undulation immediately after the cosine excitation in 3.2 s, it does not demonstrate the delayed vertical displacement of the robot body after the road excitation (y_3 in red). The more likely behaviour in this situation is represented by the curve in blue in Fig. 3.8 exhibiting some vertical displacements even after the car exited the bump zone.

However, piecewise functions as the input to the ODE would make solving ODEs more difficult by analytical approaches. The Laplace transforms that convert an ODE to the state-space or the Fourier transforms that transfer an ODE to the frequency domain, become popular to solve ODEs with piecewise functions as the input to the

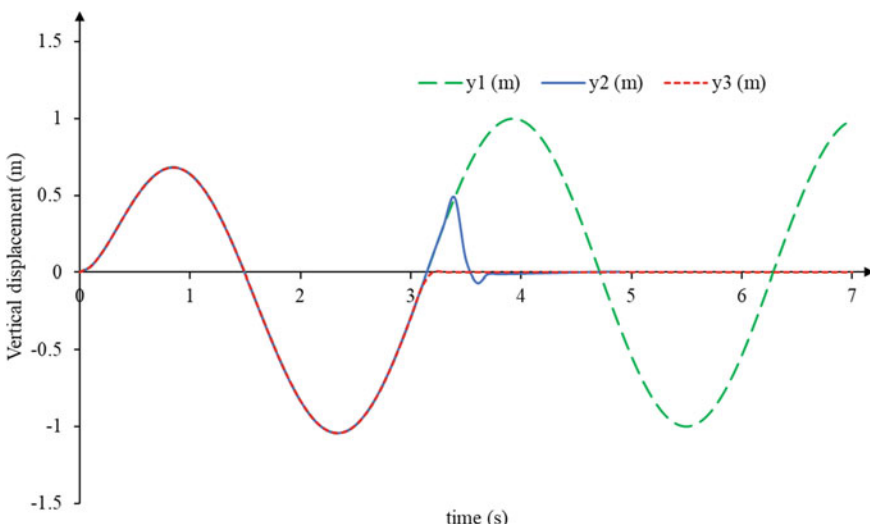


Fig. 3.8 Vertical displacements with a continuous road excitation model

ODEs, which are implemented in some software packages like MATLAB Simulink. As a trade-off, the solution to the ODE in the state-space or frequency domain would be hardly understood by the primary or secondary school students.

As mentioned earlier, we prefer to present features of the vertical movement of our model as close to the real-world situation as possible so MATLAB Simulink is not chosen to solve our problem. Given the fact that our road profiles have stable initial conditions in the first $L/2$ section, we choose the Runge–Kutta method to solve our ODEs numerically in time domain. By converting the second-order ODE into a set of system of first-order ODEs, the Runge–Kutta method solves the system of ODEs by an iterative numerical process only involving arithmetic calculations, which is relatively easier to be understood by the school students.

The Runge–Kutta method has different formulae [7]. If a first-order ODE is defined by

$$\begin{cases} y'(x) = \frac{dx}{dy} = f(x, y) \\ y(x_0) = y_0 \end{cases} \quad (3.7)$$

the classic forth-order Runge–Kutta formula to solve this ODE is expressed as

$$\begin{cases} y_{i+1} = y_i + \frac{h}{6}(k_1 + 2k_2 + 2k_3 + k_4) \\ k_1 = f(x_i, y_i) \\ k_2 = f(x_i + \frac{1}{2}h, y_i + \frac{1}{2}hk_1) \\ k_3 = f(x_i + \frac{1}{2}h, y_i + \frac{1}{2}hk_2) \\ k_4 = f(x_i + h, y_i + hk_3) \end{cases} \quad (3.8)$$

where h is the step size of independent variable (time or spatial interval); $k_1 - k_4$ are values of derivatives at different points. All Runge–Kutta formulae are calculated recursively from previous knowns for the next unknowns.

As the Runge–Kutta method can only be applied to the first-order ODEs whereas the Eq. (3.2) is a second-order ODE, we need to convert the Eq. (3.2) to a system of two first-order ODEs by letting $y_1 = y$ and $y_2 = y'$ as below

$$\begin{cases} y'_1 = y_2 \\ y'_2 = \frac{k}{m}z + \frac{c}{m}z' - \frac{k}{m}y_1 - \frac{c}{m}y_2 \end{cases}, \quad (3.9)$$

with initial conditions $y_1(0) = 0$ and $y_2(0) = 0$. Solving the system (3.9) requires both the road excitation and its derivative with respect to time. The derivatives of the four road excitation models are defined in the formulae (3.10–3.13).

$$z' = \begin{cases} -\frac{2h\pi v}{L} \cos\left(\frac{2\pi vt}{L}\right) = -\frac{2h\pi v}{L} \left(\frac{2\pi x}{L}\right) & L/2 \leq x \leq L \\ 0 & \text{elsewhere} \end{cases} \quad (3.10)$$

$$z' = \begin{cases} -\frac{2h\pi v}{L} \cos\left(\frac{2\pi vt}{L}\right) = -\frac{2h\pi v}{L} \cos\left(\frac{2\pi x}{L}\right) & L/2 \leq x \leq L \text{ or } 3L/2 \leq x \leq 2L \\ 0 & \text{elsewhere} \end{cases} \quad (3.11)$$

$$z' = \begin{cases} -\frac{2h\pi v}{L} \cos\left(\frac{2\pi vt}{L}\right) = -\frac{2h\pi v}{L} \cos\left(\frac{2\pi x}{L}\right) & L/2 \leq x \leq 3L/2 \\ 0 & \text{elsewhere} \end{cases} \quad (3.12)$$

$$z' = \begin{cases} -\frac{2h\pi v}{L} \cos\left(\frac{2\pi vt}{L}\right) = -\frac{2h\pi v}{L} \cos\left(\frac{2\pi x}{L}\right) & L/2 \leq x \leq L \\ \frac{2h\pi v}{L} \cos\left(\frac{2\pi vt}{L}\right) = \frac{2h\pi v}{L} \cos\left(\frac{2\pi x}{L}\right) & 3L/2 \leq x \leq 2L \\ 0 & \text{elsewhere} \end{cases} \quad (3.13)$$

MATLAB provides an implementation of the classic Runge-Kutta method, `ode45`, to numerically solve ODEs [21]. We implement all four models of road excitation for the Eq. (3.2) using MATLAB `ode45`. The first model `simulate_robot_mod_1.m`, is shown as an example below. Note the inputs should have the correct units: m in kg, k in N/m, c in N · s/m, v in km/h, both L and a in metre.

```
% simulate_robot_mod_1.m
function simulate_robot_mod_1(m,k,c,v,L,a)
t_start = 0;
t_end = 4*18*L/(5*v); %final time in seconds.
time_span = linspace(t_start,t_end,400);
x_dist = time_span*(5*v/18);
n = length(time_span);
vertical_pos = zeros(1,n);
for i = 1:n
    vertical_pos(i) = base_z(time_span(i));
end
%*****
% This is to solve system of ODE (9) by ode45 and plot vertical moves.
%*****
initial_position = 0.0;
initial_speed = 0.0;
y0 = [initial_position initial_speed];
[t,y]=ode45(@rhs,time_span,y0);
vertical_disp = y(:,1) - vertical_pos';
plot(x_dist, vertical_pos,'g', x_dist,y(:,1),'r--', ...
      x_dist,vertical_disp,'b-.','LineWidth', 1.2);
xlabel('distance in m');
ylabel ('vertical position in m');
legend('road profile', 'vertical move', 'relative move');
title (sprintf('v = %4.2f km/h', v));
%*****
% This is to define ODE solver for system of ODE (9).
%*****
function zdot=rhs(t,y)
ydot_1 = y(2);
ydot_2 = -(c/m)*y(2) - (k/m)*y(1) ...
          +(k/m)*base_z(t)+(c/m)*base_z_des(t);
ydot = [ydot_1 ; ydot_2];
```

```

end
%*****
% This is the base motion z(t) by road excitation.
%*****
function z = base_z(t)
if ((t>= 9*L/(5*v) ) && (t<=2*9*L/(5*v)))
z = -a*sin(5*pi*v*t/(9*L)) ;
else
y = 0 ;
end
end
%*****
% This is the derivative of base motion z'(t).
%*****
function z_des = base_z_des(t)
if ((t>= 9*L/(5*v) ) && (t<=2*9*L/(5*v)))
z_des = -(5*pi*v*h/(9*L))*cos(5*pi*v*t/(9*L)) ;
else
z_des =0 ;
end
end
end

```

3.5 Simulating Vertical Movement of Slow-Motion Tow-Wheeled Self-balanced Robots

The four excitation models with different values for the speed (v) of the moving robot, the width ($L/2$) of bumps or dips, and the height (a) of the bumps or dips are simulated using our m-files on MATLAB. The robot parameters chosen are the mass of the robot body $m = 50$ kg, the spring constant $k = 1000$ N/m, and the damping coefficient $c = 500$ Ns/m.

In our discussion, we assume a *gap* of 10 cm (or 0.1 m) between the bottom of the robot body and the robot base. The robot base is where the robot body is built on and where the wheels are attached. There should be another space between the robot base and the ground or road surface but we assume this gap is large enough for the wheels to keep moving smoothly. Our focus is on the relative vertical displacement y_d ($= y - z$) between the bottom of the robot body and the robot base linked by a simple suspension system. If y_d is a constant (set to zero here), it implies the robot body and base move forward by keeping the same vertical movement together, being the normal movement of the robot on a flat surface, which signals the stable status of movement for the robot. If y_d is negative and its absolute value is close to the *gap*, it implies the robot body is going to contact the robot base directly, which signals the beginning of the status of instability for the robot movement. If y_d is negative and its absolute value is greater than the *gap*, it implies the robot body has contacted with the robot base, indicating the sharp vibration of the robot or even the fall of the robot, which signals the status of instability for the robot movement. Correspondingly, if

y_d is positive and its absolute value is greater than the *gap*, it implies the robot body moves further away from the robot base with a space of at least double of the *gap* between them, which may destabilise the robot with an elevated centre of the body mass or throw the robot above the ground if the mass of the base is much smaller than the robot body. This may also signal the status of instability for the robot movement.

Hence, we classify the motion status of the robot as: (1) stable if $|y_d| \leq \text{gap}/2$, (5 cm in this case); (2) sub-stable if $\text{gap}/2 < |y_d| \leq \text{gap}$ (5–10 cm in this case); (3) unstable if $|y_d| > \text{gap}$ (> 10 cm in this case). Surely these classifications can be adjusted according to the situations in real applications. By our classification, we will discuss the vertical motion of the robot body under different road conditions based on the simulation outcomes.

3.5.1 Slow Motion Over Narrow Bumps or Dips ($L = 0.5\text{ m}$ and $a = 0.1\text{ m}$)

Narrow bumps are often seen in residential and business areas where a vehicle must significantly reduce speed below 20 km/h commonly. Such bumps are usually about 30–40 cm wide and 5–10 cm high. If a two-wheeled robot moves over similar road surface, the speed would be much slower. Such bumps (similarly dips) are represented by a half-sine shape of 0.25 m wide ($= L/2$) with a height of 0.1 m ($= 10$ cm). If we use the flatness rate $R = a/(L/2) = 2a/L$ to measure the flatness of such bumps or dips, this bump or dip has a flatness rate of $R = 0.4$, not flat by any means. The simulation results over the four road excitation models with such bump or dip or combinations are shown in Fig. 3.9.

Note in all simulation results in this chapter, the green line represents the road excitation; the red line represents the vertical displacement of the robot body; the blue line represents the relative vertical displacement y_d between the robot body and robot base. The vertical displacements are scaled up by MATLAB automatically for clarity whereas the horizontal axis represents the “real” scale of distance the robot moved from the initial position, i.e., $t = 0$ and $x = 0$. Hence, we can see visually every vertical movement of the robot with respect to the variations of the road condition at every location. This is far more intuitive than representing the robot movement by time elapsed shown in Fig. 3.2.

As logically inferred due to inertial, the vertical move of the robot body is always later than that of the robot base that is synchronised with the road excitation. As a result of such temporal delay, the relative displacement between the robot body and robot base appears opposite to and later than the key locations of a road profile. For the single bump model, the robot base moves closer to the robot body while the robot initially moves onto the bump until reaching the top of the bump. The robot base then moves further away from the robot body and reaches the largest space till the robot moves out of the bump. The relative displacement gradually returns to the normal status after the robot completely moves back onto the flat road. The similar

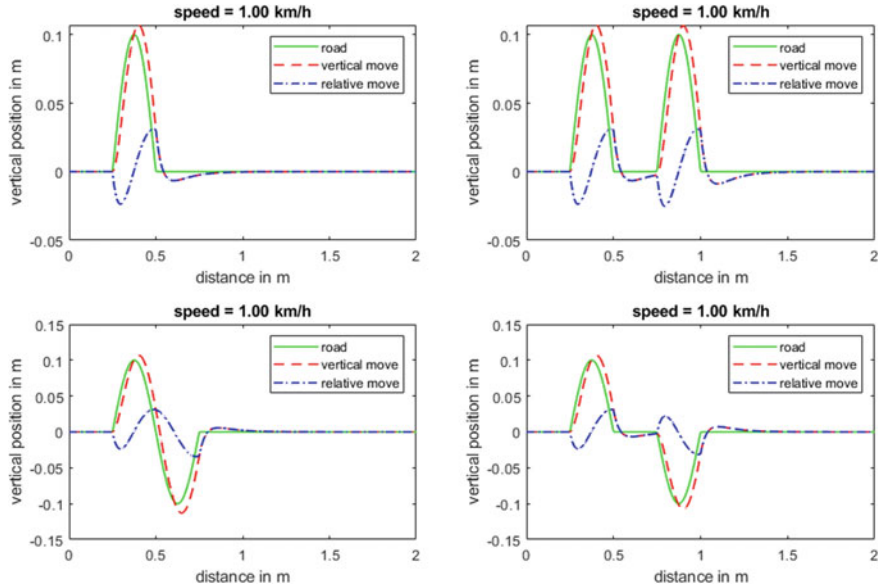


Fig. 3.9 Vertical movements over narrow road excitations ($v = 1 \text{ km/h}$, $L/2 = 0.25 \text{ m}$, $a = 0.1 \text{ m}$, $R = 0.4$)

features also appear to other combinative models with combined disturbances within the transitional section between the two adjacent bumps and/or dips (Fig. 3.9).

With a low speed of 1 km/h (or 28 cm/s), the maximum relative vertical displacement $|y_d|$ looks smaller than 0.05 m or 5 cm for all models. Hence for such a narrow bump/dip or their combinations, a two-wheeled robot moving with a speed of 1 km/h or slower would be stable over such uneven surfaces. If the speed is increased to 2 km/h, the maximum relative vertical displacement $|y_d|$ would be close to or slightly greater than 0.05 m or 5 cm for all models. (Fig. 3.10). Hence for such a narrow bump/dip or their combinations, a two-wheeled robot moving with a speed faster than 2 km/h would see some irregular vibrations over such uneven road surfaces.

3.5.2 Slow Motion Over Shallow Bumps or Dips ($L = 1 \text{ m}$, $a = 0.1 \text{ m}$)

By increasing the width ($L/2$) of the bump or dip to 0.5 m whereas keeping the height to 0.1 m, R becomes 0.2, representing a shallow bump or dip. The simulation results over the four road excitation models with such shallow bump or dip or combinations with a speed of 5 km/h are shown in Fig. 3.11.

The similar features as displayed in the previous simulation also appear to all four models comprised of one or two shallow bumps or dips or their combinations. By

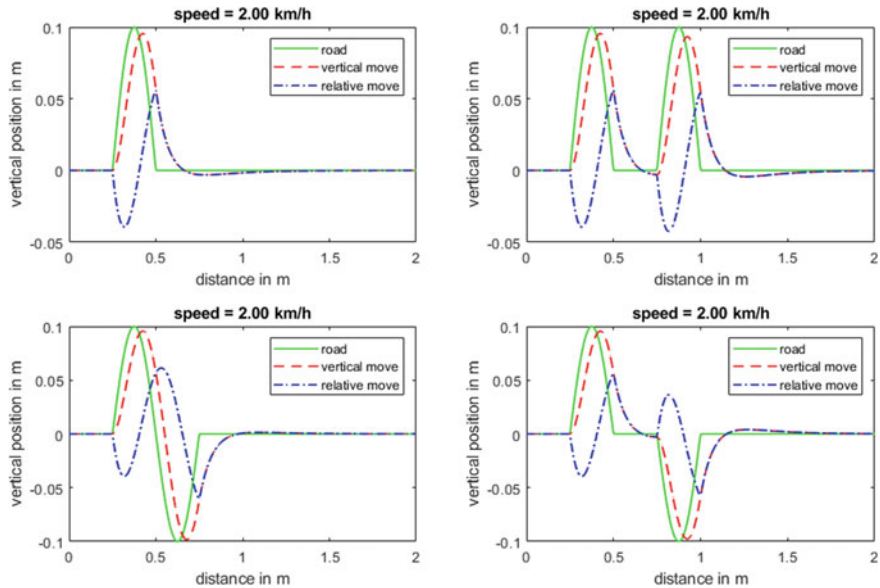


Fig. 3.10 Vertical movements over narrow road excitations ($v = 2 \text{ km/h}$, $L/2 = 0.25 \text{ m}$, $a = 0.1 \text{ m}$, $R = 0.4$)

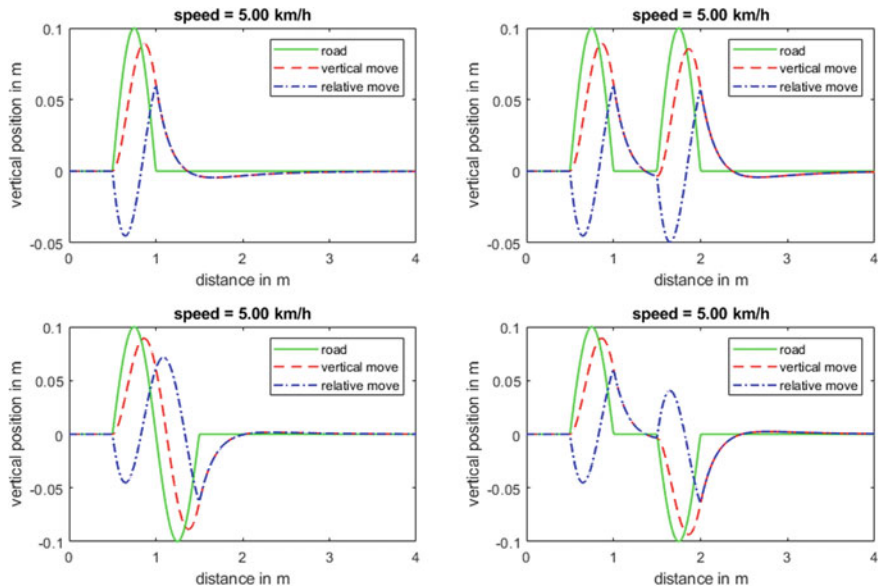


Fig. 3.11 Vertical movements over shallow road excitations ($v = 5 \text{ km/h}$, $L/2 = 0.5 \text{ m}$, $a = 0.1 \text{ m}$, $R = 0.2$)

double the width of the bump or dip compared with the narrow models, the robot moving with a speed up to 5 km/h would be sub-stable over such uneven road surfaces because the maximum relative vertical displacement $|y_{dl}| \geq 5$ cm appears for all four models, particularly the three combinative models where $|y_{dl}| \geq 5$ cm appears at least two times over the key road locations (Fig. 3.11).

Any robot moving with a speed faster than 5 km/h would see more irregular vibrations while moving over such uneven road surfaces. An example of the robot travelling with 10 km/h is shown in Fig. 3.12, in which the maximum relative vertical displacement $|y_{dl}|$ for all models becomes larger than 5 cm at the key points, the full undulation model almost reaching the falling status at the middle point of the undulation where the robot body and robot base are stretched further away at this point of inflection.

These intuitive outcomes are resulted from a simplified quarter car model for the simplest two-wheeled self-balanced robot model for educational purposes. In general, the quarter car model must be modified to take the absorption of the tyre on the wheel and additional damping on the wheel into account, leading to more sophisticated quarter car models. For example, an in-wheel switched reluctance motor was included in the conventional suspension model described by the Eq. (3.1) for electric vehicles [16] shown in Fig. 3.13a. Another suspension model involving active feedback control between the vehicle base and vehicle body studied recently [11] is shown in Fig. 3.13b. These models are better simulated using sophisticated modelling

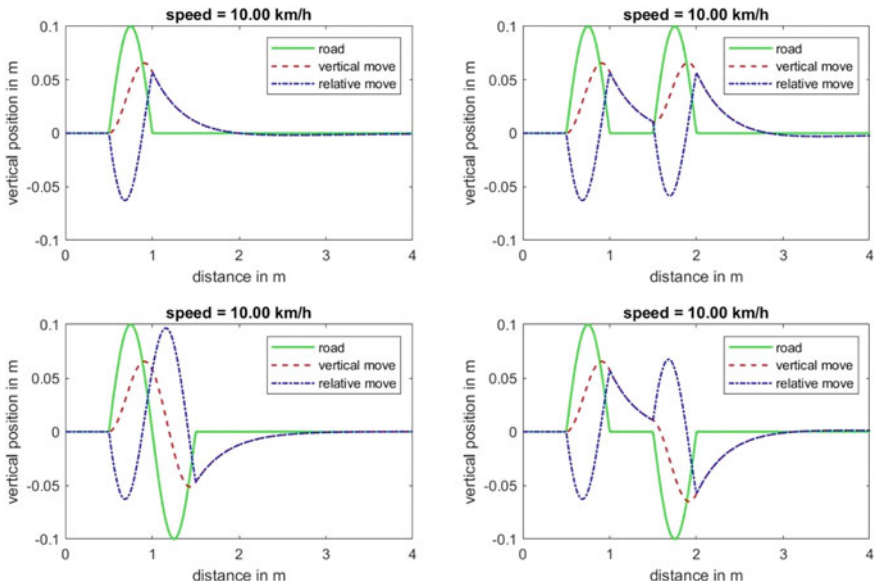
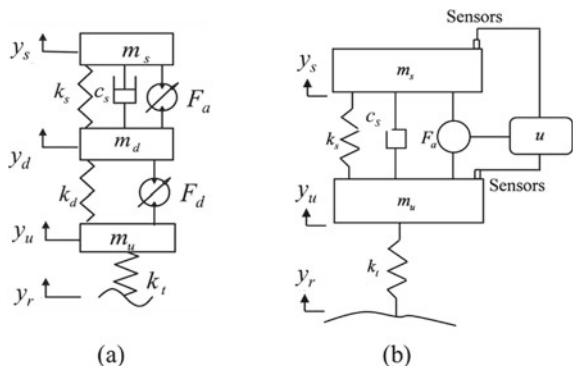


Fig. 3.12 Vertical movements over shallow road excitations ($v = 10$ km/h, $L/2 = 0.5$ m, $a = 0.1$ m, $R = 0.2$)

Fig. 3.13 Sophisticated quarter car suspension models **a** by in-wheel switched reluctance motor (after [16]), **b** by active feedback control (after [11])



packages like MATLAB Simulink. Our intuitive numerical approach would be very difficult to solve such complex models.

3.6 Summary

The case study of simulating the dynamic motion of a simplified quarter car model solved numerically in this chapter has shown: (1) this approach is more intuitive for students to visually observe the vertical vibrations of slow-moving two-wheeled self-balanced robots over different road excitations; (2) this approach provides an alternative way to conduct simulations for simple models, which overcomes the missed links hidden in a Blackbox such as a Simulink model. These make it potentially an attractive tool for promoting robotics and STEM education to young students in the future.

References

1. Al-Ghanim, A., Nassar, A.: Modeling, simulation, and control of half car suspension system using Matlab Simulink. *Int. J. Sci. Res.* **7**(1), 351–362 (2018)
2. Cerezo, J.O., Morales, E.C., Plaza, J.M.C.: Control system in open-source FPGA for a self-balancing robot. *Electronics* **8**, 198 (2019)
3. Chatzopoulos, A., Papoutsidakis, M., Kalogiannakis, M., Psycharis, S.: Innovative robot for educational robotics and STEM. *Lect. Notes Comput. Sci.* **12149**, 95–104 (2020)
4. Chen, X., Zhou, Y.: Modelling and analysis of automobile vibration system based on fuzzy theory under different road excitation information. *Complexity* **2018**, Article ID 2381568 (2018)
5. Chhotray, A., Pradhan, M.K., Pandey, K.K., Parhi, D.R.: Kinematic analysis of a two-wheeled self-balancing mobile robot. *Lect. Notes Electr. Eng.* **396**, 87–93 (2016)
6. Daniela, L., Lytras, M.D.: Educational robotics for inclusive education. *Technol. Knowl. Learn.* **24**, 219–225 (2019)

7. Guo, W.W.: Advanced Mathematics for Engineering and Applied Sciences. Pearson Australia, Sydney (2016)
8. Khan, M.A., Abid, M., Ahmed, N., Wadood, A., Park, H.: Nonlinear control design of a half-car model using feedback linearization and an LQR controller. *Appl. Sci.* **10**, 3075 (2020)
9. Kreyszig, E.: Advanced Engineering Mathematics. Wiley, Hoboken (2011)
10. Laribi, M.A., Zeghloul, S.: Redundancy understanding and theory for robotics teaching: application on a human finger model. *STEM Educ.* **1**, 17–31 (2021)
11. Lee, H.W., Lee, Y.C., Wong, K.-H.: Differential equation approximation and enhancing control method for finding the PID gain of a quarter-car suspension model with state-dependent ODE. *J. Industr. Manage. Optim.* **16**(5), 2305–2330 (2020)
12. Mavrovounioti, V., Chatzopoulos, A., Papoutsidakis, M., Piromalis, D.: Implementation of a 2-wheel educational platform for STEM applications. *J. Multidisciplinary Eng. Sci. Technol.* **5**, 8944–8948 (2018)
13. Perescu, A., Bereteu, L.: Simulation and comparison of quarter-car passive suspension system with Bingham and Bouc-Wen MR semi-active suspension models. *AIP Conf. Proc.* **1564**, 22–27 (2013)
14. Rath, J., Veluvolu, K., Defoort, M.: Adaptive super-twisting observer for estimation of random road excitation profile in automotive suspension systems. *Sci. World J.* **2014**, Article ID 203416 (2014)
15. Romdhane, L., Jaradat, M.A.: Interactive MATLAB based project learning in a robotics course: challenges and achievements. *STEM Educ.* **1**, 32–46 (2021)
16. Shao, X., Naghdy, F., Du, H., Qin, Y.: Coupling effect between road excitation and an in-wheel switched reluctance motor on vehicle ride comfort and active suspension control. *J. Sound Vib.* **443**, 683–702 (2019)
17. Sun, X., Chu, Y., Fan, J., Yang, Q.: Research of simulation on the effect of suspension damping on vehicle ride. *Energy Proc.* **17**, 145–151 (2012)
18. Thomson, W., Dahleh, M.: Theory of Vibration with Applications. Prentice Hall, Upper Saddle River (1998)
19. Unluturk, A., Aydogdu, O.: Adaptive control of two-wheeled mobile balance robot capable to adapt different surfaces using a novel artificial neural network-based real-time switching dynamic controller. *Int. J. Adv. Robot. Syst.* March 2017. 1–9 (2017)
20. Wang, W., Tian, K., Zhang, J.: Dynamic modelling and adaptive control of automobile active suspension system. *J. Européen des Systèmes Automatisés* **53**(2), 297–303 (2020)
21. Wang, Y., Guo, W.W.: Applied Computational Modelling with MATLAB. Pearson Australia, Melbourne (2018)
22. Wu, J., Zhang, W., Wang, S.: A two-wheeled self-balancing robot with the fuzzy PD control method. *Math. Prob. Eng.* **2012**, Article ID 469491 (2012)

Chapter 4

Path Planning for Special Robotic Operations



Paolo Boscariol , Alessandro Gasparetto , and Lorenzo Scalera 

Abstract The problem of robotic path planning has been the focus of countless investigations since the early works of the '70s and, despite the large number of results available in literature, is still a topic that draws a great interest. In virtually all robotic applications it is required to somehow define a feasible and safe path, and such a problem can be cast and solved in many ways, given the several possible combination of robots—industrial robots, Autonomous Guided Vehicles (AGVs), Unmanned Aerial Vehicles (UAVs), underwater vehicles—and scenarios—a production line, a warehouse, an hazardous mountain—and therefore a large number of approaches and solutions have been, and are being, investigated. The aim of this chapter is to provide an overview of such widespread literature, first by briefly recalling some classic and general-purpose methods used in path planning, then by focusing on some application-specific problems, related to AGVs in industry, medical robotics and robotic welding. This choice is motivated by the prominent relevance of the path planning problem in these three applications. Then, a single application of great industrial interest, such as robotic spray painting, is analysed. Its specific features are described, and several techniques for task modelling and path planning are considered. A detailed comparison among these techniques is carried out, so as to highlight pros and cons of each one, and to provide a methodology to choose the most suitable one for the specific robotic spray painting application.

P. Boscariol

Dipartimento di Tecnica e Gestione dei sistemi industriali, Università degli Studi di Padova,
Stradella S. Nicola 3, 36100 Vicenza, Italy

A. Gasparetto  · L. Scalera

Dipartimento Politecnico di Ingegneria e Architettura, Università degli Studi di Udine, Via delle
Scienze 206, 33100 Udine, Italy

e-mail: alessandro.gasparetto@uniud.it

4.1 Path Planning for General-Purpose Applications

Autonomous vehicles, mobile robots and, in general, robots are usually required to move between two- or more-points in space, and solving the path planning problem results in the definition of a feasible and collision-free path to be followed by the robot. Additionally, some metric is usually embedded in the problem solution algorithm to fulfil the improvement of some performance criteria, with the aim of finding an ‘optimal’ solution. This problem is often intertwined with localization, i.e., the problem of understanding where the vehicle actually is [3], and map building [23], i.e., the definition of the map of an unstructured environment during the robot operation. Combining the two problems results in a Simultaneous Localization and Mapping (SLAM) problem [11, 50].

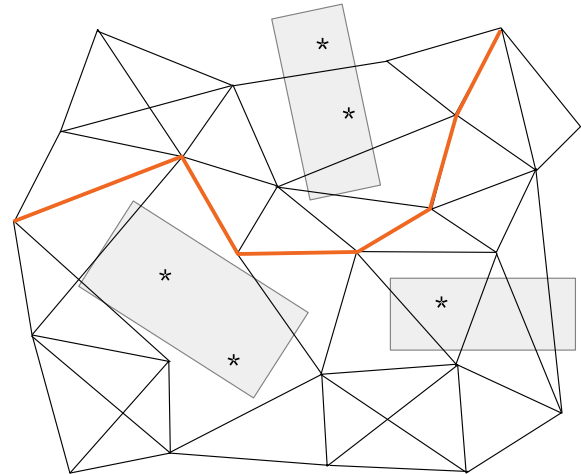
The extremely vast literature on path planning for mobile robots calls for a comprehensive classification of the several methods proposed over the years: one possibility is to classify the available methods among classical methods—such as roadmap planning or artificial potential field method—, heuristic methods—such as genetic algorithms, neural networks—and meta-heuristic methods, among which Ant Colony Optimization and Particle Swarm Optimization are worth of mentioning. A brief overview is presented here before focusing on more application-specific solutions.

4.1.1 Classical Methods

Classical methods refer to the broad range of options that were developed before the introduction of artificial intelligence. The most authoritative reference on such topics is the classic book [90], which focuses on roadmap planning, cell decomposition methods, and artificial potential field methods. Roadmap methods refer to a family of algorithms which share the capability of producing a map composed of one-dimensional curves: once the roadmap is built, the best option among the roadmap is chosen. In practical terms, usually the roadmap can be built as a visibility graph [100], i.e., a graph composed of lines that connect the vertices of the geometric representation of obstacles: the result is the shortest collision-free path, but such path is as close as possible to the obstacles [90]. If the goal is to move as far as possible from obstacles, Voronoi diagrams are a better method to build a roadmap: such diagrams are defined as the locations in space which are equidistant from obstacles. The method based on Voronoi diagrams has found its use not only for mobile robots [49], but for UAVs [41] and underwater vehicles [22] as well.

The artificial potential field method was developed in the eighties [80] as a computationally efficient way to produce a collision-free path. The procedure is divided into two steps: the first one aims at defining a suitable number of potential field functions, that comprise both attractive and repulsive fields. Attractive fields are used to drive the robot to its final goal, repulsive fields are used to represents the areas to be avoided, i.e., the obstacles: their sum produces a total potential that must be

Fig. 4.1 An example of probabilistic roadmap path planning



navigated to seek for an optimal path. Path optimization can be performed either in off-line or on-line fashion. The main strong point of this method lies in its conceptual simplicity, its main drawback is that the total potential field might exhibit local minima in which the robot might be trapped [121]. This difficulty can be however overcome by using navigation functions, i.e., by ensuring that the potential field does not have local minima [38] or by adding procedures to escape local minima.

Another classic method that is worth mentioning is the cell decomposition method [90, 95]. In this method a workspace with obstacles is split into regions, called cells. Each cell is numbered, and then translated into a node of a connectivity graph, which collects the information on the reachability of each node. The best sequence of cells that connects the initial and final cell is found by a simple graph search algorithm. The method can be applied to 2D spaces as well as to higher dimension spaces by simply adjusting the structure of the connectivity graph.

Further developments of the ‘classic’ algorithms have been achieved by introducing random sampling of the workspace, with the aim of boosting the efficiency for large-scale problems. One example is given by the probabilistic roadmap algorithm (Fig. 4.1), which collects random points within the robot workspace, discards the ones that overlap an obstacle, and tries to connect the ones in the free space to produce a feasible path [70, 79]. Random sampling is also used in rapidly-expanding random trees [91]: in this method a tree structure is build by rooting it to the starting point of the path, then a growing algorithm tests the feasibility of a path built by adding ‘branches’ after testing the feasibility and measuring the progress towards the designated goal.

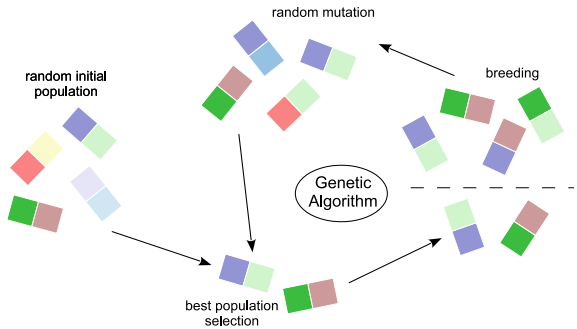
4.1.2 Heuristic and Meta-heuristic Methods

Heuristic methods have been developed since the '90s to circumvent the most common drawbacks sported by classic methods, mainly due to the low efficiency for large-scale problems and local minima trapping [101]. Heuristic methods mainly work by using 'shortcuts' to define a feasible solution, often sacrificing a complete exploration of the possible space of solutions, therefore they often trade off global optimality for speed.

Worth of mention is the use of Genetic Algorithms (GA), which have found an extremely wide field of applications, including path planning. Genetic algorithms work by representing a tentative solution to a general optimization problem by representing it as a population, whose evolution is dominated by selection (elimination of non-fit individuals), propagation of the genes to new generation and gene mutation (Fig. 4.2). This method is of very general application, being suitable to the optimization of virtually every problem, with minimal effort on its mathematical representation, as explicit gradients are generally not needed. One of its main drawback is, however, the possibility that a true optimal solution is not explored, and as such they are incapable of guaranteeing a global optimum. A basic implementation, as the one proposed, for example, in [1], associates a path, represented by a discrete set of point to be visited in sequence, with a chromosome. The initial, necessarily feasible path, is then altered by creating a new generation, according to the crossover mechanism, followed by the evaluation of the fitness function to be minimized. The best chromosome are selected, to improve the quality of the population. This sequence is continued until reaching a pre-defined stopping criteria. Other early examples of application of GA to motion planning include [130, 154]. A path can be also generated by fuzzy logic, which works by combining several fuzzy rules that take into account planning-specific goals such as proximity to the final goal, obstacle avoidance, and direction changes [159]. Alternatively, Particle Swarm Optimization (PSO) has found many applications in path planning: this technique is based on collecting the potential solution of an optimization problem into a swarm of particles. The solution evolves by exploiting the activity of each individual element of the swarm, but as the algorithm progresses, the activity of each particle changes (i.e., it evolves) according to the experience gained by the whole swarm, combining the power of stochastic and evolutionary methods, and exploiting efficiently parallelism [148, 165].

Another popular biologically-inspired method is the Ant Colony Optimization (ACO) [54, 118, 151], which is a meta-heuristic and probabilistic method inspired by the attitude used by ants to forage food. Ants have the capability of finding the best path to a food source by relying on the traces of pheromones left by other ants. The optimization method somehow reflects this behaviour, since the agents, in this case the artificial ants, explore the solution space and leave some long-term memory of the 'trail' run by each ant. The traced are then followed by other 'ants' by exploiting the results of previous explorations, improving gradually the quality of the solution.

Fig. 4.2 Graphical representation of a genetic algorithm optimization procedure.



Ant colony optimization has found its first uses specifically in the field of path planning, being this the actual task performed by real ants. In a basic and typical implementations of a path planning method by Ant Colony Optimization [160], the representation of the navigable space is obtained by a grid map, which contains both free and forbidden grid elements. The task is to find the path from an initial point to the last one with a minimum number of turns and with the shortest possible path. Each ant follows a path that is built iteratively, and each move to another grid is defined by an heuristic that may vary with the implementation. Each ant then ‘marks’ the path depositing the so-called ‘pheromone trace’—leaving an information on the ‘fitness’ of the path that is then used by other ants. Iterations are then stopped when reaching a pre-defined goal. Similar procedures can be applied to a graph, rather than a grid map with minimal alterations to the algorithm.

Similar to the Ant Colony is the Bee Colony method [17, 39], which combines a global search performed by ‘scout bees’, and a local search, performed by ‘forager bees’. Furthermore, the Cuckoo Search Algorithm [107, 133, 150] is also experiencing some applications in the path planning of robotic systems.

4.2 Application-Specific Path Planning

4.2.1 Path Planning for Automated Guided Vehicles

Since their introduction in the mid fifties, Automated Guided Vehicles (AGVs) are an ever increasingly popular solution for material handling and all sort of transports in industry and logistic centres, as well as in transhipment systems [58]. Operating a fleet of AGVs requires to solve two issues: the scheduling and routing problems. While the scheduling problem focuses on the definition of the time frame within which the AGV should move (respecting constraints such as priorities and deadlines), the routing problem focuses on the definition of the route, i.e., the path, that the AGV should move along. Despite being closely related, the two issues are often tackled separately [115]. Each of the problem can be technically challenging, especially

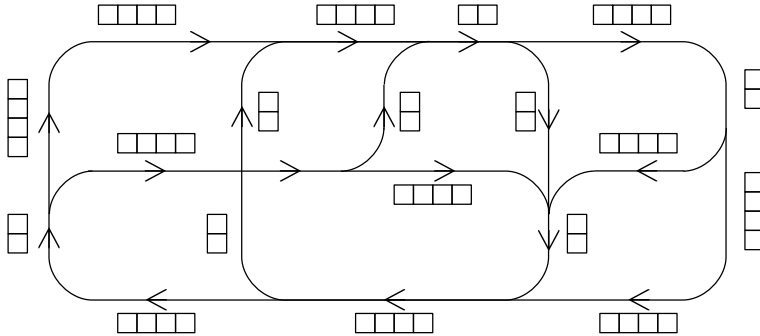


Fig. 4.3 A simple route map for a small warehouse

when the complexity of the scenario is amplified by the numerosity of the fleet of AGVs that in many cases can comprise several hundreds of vehicles (Fig. 4.3).

Routing problems for AGVs, which are briefly reviewed here, are usually split into two groups, by separating static and dynamic routing problems. A static routing problem solves once for all the target of defining, in advance, the route to go from point *A* to point *B*: if the same procedure is then applied to all possible combinations of two arbitrary points, a list of optimal paths can be defined and stored for later use. Once defined, the route between point *A* and *B* is always used. However, these methods are practical only for static scenarios, since every change in the working environment layout requires to re-compute the optimal paths. The most basic formulation of the routing problem is the well-known Travelling Salesman Problem (TSP), in which the distance to be covered for visiting a sequence of ‘cities’ and returning to the starting one must be minimized.

In response to the evident limitation posed by static routing problems, dynamic routing problems can develop. Dynamic routing problems can adapt to time-changing conditions, such as layout changes or traffic [146].

In most cases, the routing problem focuses on defining shorter paths, as is the case of the early work [19]. In that work, the environment is described by a graph over which the quicker path is found by the classic Dijkstra’s algorithm. Moreover, one of the first examples of conflict-free routing on a bi-directional path network is introduced in [40], which exploits a branch and bound algorithm. A method that is commonly used to reach a conflict-free situation is the use of time windows, as introduced in [81, 82]. In the time-window approach each node of the graphs holds the information of free time windows, and an arc connects only the nodes that are not busy by other scheduled jobs.

The literature has evolved over the years striving for computational efficiency and for larger scale scenarios, so the performance sported by the classic Dijkstra’s algorithm has been boosted by switching to other search methods, such as the A* algorithm [147], the branch and price algorithm [123], as well as by using heuristic [10, 87, 103] and meta-heuristic approaches [57, 131, 139]. While most methods of

path planning for AGVs use graphs to represent the path network, grids can be used as well, as in the case of the works [61, 157, 160].

The growing popularity of technology based on the Industry 4.0 paradigm is fostering a new stream of research on AGVs, being those a key element in a smart manufacturing environment with high automation level. Smart factories are required to face the challenges of flexibility and reconfigurability [71, 89], since currently a large part of the commissioning time of a plant is devoted to the generation of collision-free paths. As suggested by the Industry 4.0 paradigm [75], the challenges of decentralization, real-time capability, service orientation, and modularity are all to be faced by AGVs, which can be used in fleets of variable size that can be coordinated either by a centralized system, or by exploiting the on-board sensing and computing capability of AGVs. The work [110], for example, proposes a neural-network based solution to the route-planning problem that is suitable to real-time applications and compliant with the limited computational capability of most AGVs.

4.2.2 *Path Planning for Medical Applications*

The history of surgical robots is now more than 30 years old [21], and currently several medical tasks can be performed, with different shades of autonomy, with the aid of a robot. Common robot-assisted tasks include bone drilling and milling [98], laparoscopy [109] and stereotactic needle placement [88, 92] just to cite a few notable examples. Despite the quite long history of robotics, in general, and of surgical robotics, there are still several issues that need to be solved: one of them is how to fully exploit the capabilities of a surgical robot to their full extent to improve minimally invasive surgery.

One of the key tasks in surgery is needle insertion [52], which is a critical operation since it involves the interaction of a long and flexible element, the needle, with soft tissue, that must be performed with precision while providing minimal tissue damaging. Optimizing the needle-tissue interaction requires also to optimize the needle path: this topic is currently under investigation and thinner needles with a bevel tip, called steering needles [4] are being developed (Fig. 4.4).

When inserted in a patient's tissue, such needles follow an arc: by rotating the needle around its axis, a complex path composed by arc can be defined to reach the target area while avoiding obstacles. Since the needle is clearly not visible during the operation, its motion must be carefully planned ahead: in the work [155], a Rapidly-exploring Random Trees (RRTs) approach is used to perform this task, adding a backchaining mechanism to define the best needle entry point. RRTs are also used in [113], adding a reachability-guided sampling heuristic to alleviate the sensitivity of the algorithm to the choice of the distance metric. In the work [4], the optimal needle path is defined by dynamic programming, using simulations to optimize the performance in a feedback-loop approach. Iterative simulations have been used in [43], using a fast and gradient-free optimization routine that allows the algorithm to compute the optimal needle orientation and insertion point. Some

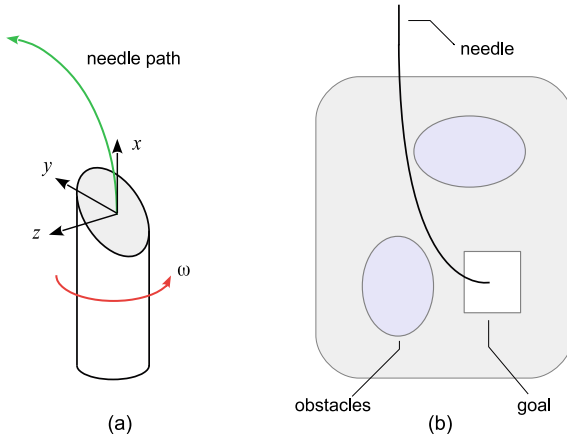


Fig. 4.4 Steering needle: principle of operation (a), a typical insertion path (b)

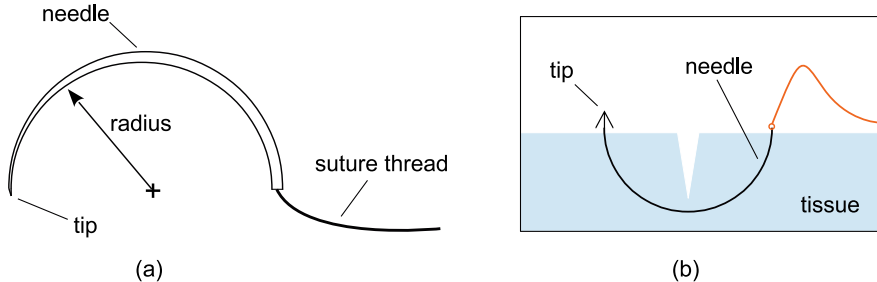


Fig. 4.5 A suturing needle (a), a suturing operation (b)

other steering needle insertion planning methods are based on inverse kinematics of the needle, as in [48], but this method does not ensure solvability for all cases. Alternatively, the classic methods of Roadmaps [119] and Artificial Potential Field [46, 132] have been successfully applied, but such methods trade off the solution speed for global optimality [93]. More recently, also the Particle Swarm Optimization has been proposed as an effective tool for needle steering planning, as in the case of the work [20], showing that a good accuracy can be reached if a proper modelling of the needle-tissue interaction is developed.

Another surgical procedure that can be efficiently performed by robots is suturing (Fig. 4.5), usually performed by specifically shaped needles to join together two tissues by means of a thread [78]. Suturing is a complex operation since its outcome depends on a large number of geometric parameters, such as insertion point, needle orientation, and exit point. Moreover, several constraints must be taken into account, and a rather dexterous manipulator must be used. To cope with these difficulties, in the work [108] the path planning is translated into an optimization problem using the A* solving method [42]. A general-purpose optimization, such as sequential convex

optimization is used for the same task also in [126], which has showcased the first case of a fully autonomous stitching procedure, which however is executed at lower speed than the average surgeon. A sensible speed-up is predicted in the work [143], in which the motion primitives are not defined a-priori, but they are taught to the robot by a human, showcasing a promising ‘teaching by doing’ application in surgery.

4.2.3 *Path Planning for Robotic Welding*

The concurrent developments of welding technology and robotics have fostered a wide usage of welding robots in the manufacturing industry (Fig. 4.6): the most popular and common example is found in the automotive industry. Welding robots have in many cases taken over traditional manual welding, which requires a skilled operator and exposes him to an hazardous environment [138]. The first step to the automation of robotic welding has been performed by introducing the on-line teaching method [45], which is also referred to as teaching and playback, since according to this paradigm the robot just repeats a process learnt after a human-guided teaching process. Such method is however not suited to any change of working conditions, which can significantly affect the outcome of the welding operation [28]. Manually teaching from a teaching pendant is also not suited to small production batches, so in all cases in which flexibility and accuracy are requested, or simply the complexity of the operation is too high, an off-line programming of the welding operation is requested.

Programming a robot for welding essentially requires to generate the welding passes, usually from data extracted from a CAD model, and then to generate the associated robot path [56]. The path is usually developed to enhance productivity, and therefore shorter (i.e., faster) paths are usually sought for, while ensuring obstacle avoidance, which can be obtained using some general-purpose methods [111].

However, welding requires to take into account some specific technical requirements, which mark the difference between general-purpose path planning and welding path planning. In the following, some of these features are recalled and some examples of the related literature are presented.

Joining metal bodies with large gaps requires multiple-pass welding, i.e., the joint must be created by carefully stacking the weld beads according to the best possible geometry. This problem is analysed in [164], by developing an algorithm to produce optimal paths on the basis of an analytic model of the bead deposition process. The planning of multiple-bead passes are investigated also in [2], in which the multiple bead passes are planned according to geometry data extracted from a CAD model, and then the transitions between passes are planned for collision-free motion using the A* algorithm. The minimization of bead number for a faster operation is dealt with in [156], which again uses simple analytical descriptions of the bead geometry to produce optimized welding paths.

Another feature of robotic welding that affects path planning is functional redundancy, which arises from the symmetry of the welding torch. Such redundancy can

Fig. 4.6 A six degrees-of-freedom soldering robot

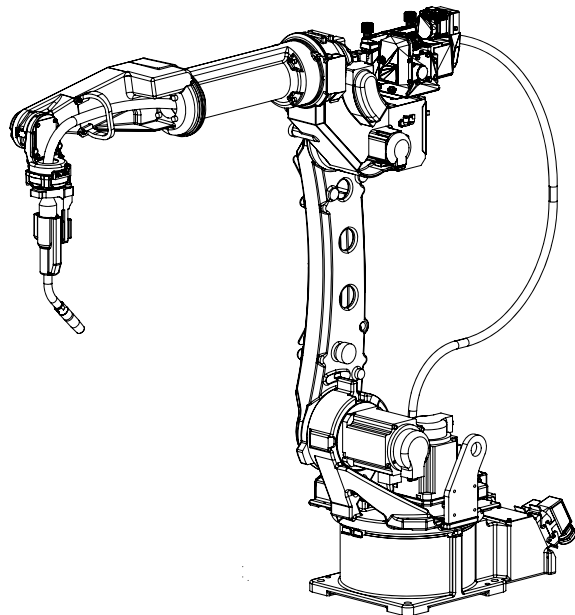
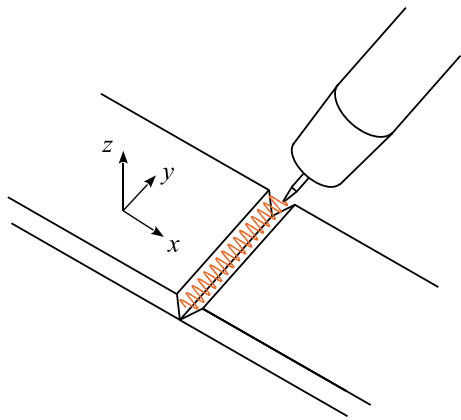


Fig. 4.7 Weave bead welding of a V-groove: planned path



be exploited, as done in the works [60, 74], to ensure task feasibility when coping with singularity avoidance and joint limits, or for fulfilling a secondary goal.

Another task-specific feature is welding weaving [35, 162]: traditionally it is obtained by adding an oscillating device between the robot flange and the welding torch, but such device is not required when weaving is introduced at the motion planning level, simply by adding a sinusoidal displacement to the end-effector path [96, 129] (Fig. 4.7).

A feature than should not be overlooked is that the heat generated during welding introduces some thermal-induced stresses on the material, causing its deformation

[116]. The usual approach is to minimize the overall distortion by carefully sequencing the beads deposition [104], according to the solution of a scheduling optimization problem [84]. The solution to this scheduling problem is generally obtained through general-purpose optimization routines, among which genetic algorithms seems to be quite popular, as in [76, 77], usually defining the fitness function according to a FEM model of the thermal-induced distortions. Alternatively, some heuristics [83, 85] can be used in lieu of a thermo-mechanical model. Some other options for sequencing welding operations are the Ant Colony Optimization and the Particle Swarm Optimization [15, 136].

4.3 Path Planning for Spray Painting Robots

4.3.1 *The Problem of Tool Path Generation*

Nowadays, painting robots are employed in a large number of industrial and manufacturing applications, especially in the automotive, aircraft and furniture manufacturing sectors (Fig. 4.8). The first painting robot was developed by the Norwegian company Tralffa in 1969, and was used for painting wheelbarrows [67]. Since then, the employment of painting machines has been rapidly increasing, thanks to the several advantages of using robots in a paint finishing system [13]. First of all, robots in automation allow to remove humans from hazardous environments, since spray paint particles, if inhaled, can be toxic, carcinogenic, and can lead to chronic neurological problems [97] and pulmonary dysfunctions [36]. Furthermore, the spray painting environment is usually noisy, and requires handling bulky paint guns, while performing repetitive tasks. Another feature of automatic painting is the consistency of the results, since a spray painting robot can ensure better performance in terms of repeatability of the resulting surface, paint uniformity and reliability, than the most skilled technician. Furthermore, robot manipulators afford a greater level of system flexibility, allowing facilities to rapidly adapt to changes in the product design. Robotic painting systems ensure the optimization of cycle time and paint waist, and, as a consequence, a reduction of the amount of gaseous polluting emissions [26].

The tool path planning, i.e., the definition of the sequence of positions and orientations of the robot end-effector during the task to ensure a uniform paint distribution is still a challenge in robotic spray painting. Two main approaches can be adopted for the tool path planning: manual and automatic [24]. In the manual approach an operator manually moves the robot to each desired position, recording the internal joint coordinates corresponding to that end-effector pose [99]. In addition, operations such as activating a spray gun are specified as well. The program is then executed by the robot that moves through the recorded points. This method of robot programming is usually known as *teaching by showing* or *robot guiding*. Similarly, the positions and postures of the robot tool on the processing path against actual work-pieces can be defined by acting on the teaching pendant connected to the robot controller, or by

Fig. 4.8 An industrial spray painting robot



using appropriate external teaching support devices, such as in [134]. Manual tool planning can be very time consuming, since the operators usually adopt a trial-and-error approach. Following this approach, the quality of the results, the cycle time and the paint waist are strictly dependent on the experience and on the skills of the operators. Furthermore, during the execution of the teaching tests the normal production operations must be interrupted.

To overcome these problems, spray painting path and trajectories are usually generated automatically, with an approach called *Computer-Aided Tool Path Planning* (CATP) [24]. This approach is based on the processing of a Computer-Aided Design (CAD) or a point cloud model of the part to be painted, and on the automatic computation of the path and trajectory that the painting robot has to follow. The automatic generation of tool paths avoids trial-and-error operations and reduces the time required to deploy a paint system for a new product, thus reducing production time and costs. However, automatic tool path planning is still a challenging task since the results of the painting process is heavily affected by complex and intertwined factors such as part geometry, the modelling of the spray paint deposition and the flow rate flux of the spray gun. All such information should be included to produce a proper definition of the painting application.

Another important aspect that must be taken into account in the automatic path planning is the compliance with kinematic and dynamic limits of the manipulator. A common approach is to decouple the path definition and the motion law planning into two separate problems [66]. In this way, the sequence of points that the tool has to follow are defined to ensure a proper covering of the target surface without a specific time law. The motion law, i.e., the speed and acceleration profiles, are then designed by taking into account the specifications and the limits of the manipulator.

In the context of robotic spray painting, recent researches include spray modelling and simulation [158], automatic path planning [112] and trajectory planning [140]. Furthermore, robot kinematic and dynamic control [106, 163], methods for optimizing the base position of mobile painting manipulators [120], as well as pose estimation systems [152] are currently being studied. The following subsection introduces the problem of spray painting modelling, which is a prerequisite for the subsequent definition of the path for the spray painting robot.

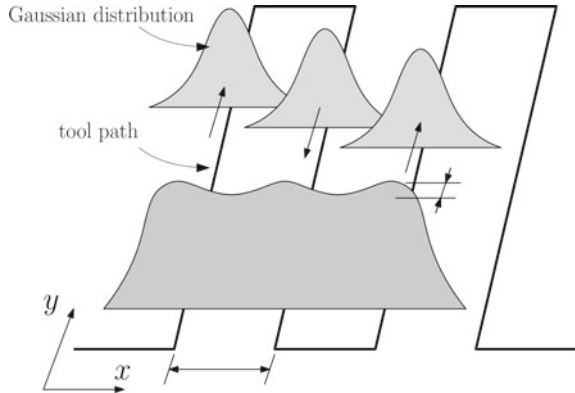
4.3.2 Spray Painting Modeling

Spray painting is a complex process, in which paint is transferred to the object surface for protection or aesthetic using air spray as an atomizing medium. Many factors affect the paint flow rate flux through the spray gun and the distribution of spray within the spray cone, which is generally non-uniform. In particular, the most relevant factors that have to be considered are the technical features of the spray gun and paint nozzle, the air pressure, the amount of thinner in the paint, the temperature of paint and work-piece surface, and the paint viscosity. At present, the mechanism of spray painting is well understood and several models for the flow rate flux and the paint deposition process have been proposed and studied. Most of the paint deposition models consist of analytical functions, which parameters should be determined through fitting repeatable experimental data. These mathematical models usually describe the paint deposition rate on a flat plane with a static spray gun. To account for the painting robot trajectory, the paint thickness is obtained by integrating the paint deposition rate along the path of the spray gun.

Empirical paint deposition models offer a significant advantage over simulation results obtained with numerical methods that usually require complex formulations and high computational costs. Empirical models can also be incorporated into existing simulation tools, providing the user readily available information about the painting process and the characteristics of the resultant coverage path. The main purposes of a deposition model are to capture the structure of the deposition pattern that can be used in a planning system, and to support simulations used to evaluate potential path and trajectory planning algorithms. Indeed, paint deposition models are needed to determine the optimal inter-pass spacing for robotic spray painting, which are the basis of the path planning. These two requirements lead to contradictory criteria, since a deposition model should be accurate enough to predict the paint coverage on different surfaces, but, at the same time, should be mathematically simple and computationally light to be efficiently used within a path planning system. In the deposition process, with *paint coverage* it is usually indicated the total paint thickness on the surface, which depends on the rate of the paint deposition, on the path followed on the surface, and on the speed of the paint gun during the spraying task.

Early approaches to the modeling of spray painting use simplified deposition models, approximating the paint flux of the spray gun with simple analytical functions. These approaches are, in the majority of cases, limited to flat surfaces or make first-

Fig. 4.9 Gaussian paint deposition modeling: evaluation of paint thickness uniformity



order approximations of the surface geometry. For this reason, the utility of these models for the simulation of reliable paint deposition remains limited and restricted to few real applications, such as planar surfaces of automobiles chassis.

Several analytical function are taken into account for the modeling of spray painting. A simple elliptical thickness distribution is considered in the deposition model presented in [135], a parabolic thickness profile with a circular deposition pattern is adopted in [25, 33, 128], whereas in [63] a Gaussian distribution with elliptic cross-section is proposed (Fig. 4.9).

Radially symmetric Gaussian distributions of color intensity within the spray cone are considered in the deposition models for decorative robotic spray painting in [51, 124, 144]. Other examples include the deposition model based on a bi-variate Cauchy distribution for the paint deposition applied to a flat panel presented by Ramabhadran and Antonio [117], and the model proposed by Balkan and Arikán, based on a beta distribution, which uses the shaping parameter β to take the flow-out of the paint into account [14, 122]. Furthermore, Hertling et al. propose in [73] a mathematical model for the paint flux field within the spray cone derived from experimental data on flat plates. Results indicate that deposition patterns are not uniform, and not parabolic, as reported by other researchers, but show a minimum at the center of the spray cone.

In the previously described researches the simplified mathematical formulations are developed for aerosol spray painting only. Nevertheless, nowadays, the modern automotive coating lines are increasingly installing electrostatic rotating bell (ESBR) atomizers, which allow one to obtain high transfer efficiency thanks to the potential difference between the rotating bell and the grounded surface to be painted [37, 53]. ESBR atomizers combine electrostatic and aerodynamic effects to spray the charged particles (with a typical diameter of 10–30 μm) to the target surface. Therefore, the mechanism of paint deposition are complex to be investigated and empirically validated analytic models are needed.

Conner et al. presented in [37] a paint deposition model that accounts for the deposition pattern of ESRB atomizers and the effects of surface curvature. The deposition pattern is modeled with an asymmetric planar deposition function based on a set of



Fig. 4.10 Spray painting application (a), automatic path generation software (b) (image taken from [105])

Gaussians, which globally assumes the shape of an asymmetric volcano. The model is tested on primer coated Ford Excursion doors with good results, but presents some limitations in the predictions of paint deposition on highly curved surfaces. In this case, the paint deposition is under-estimated due to electrostatic effects that actually bend the trajectory of the paint droplets back to the edges of the surface.

A limitation of the analytical approach of paint deposition modeling is that sensible errors can be introduced when dealing with curved surfaces. This is due to the assumption that the streamlines of paint droplets are straight, unlike the real situation in which the streamlines are curved due to the effects of turbulence in the flow field or due to the shape of the workpiece [29]. The problem can be overcome by simulating the paint deposition process with a computational fluid dynamics (CFD) approach, which can precisely describe the flow field and take the turbulence effects into account [47, 59].

4.3.3 Path Planning Approaches

In the context of robotic spray painting, robot paths are frequently planned through self learning programming. The process can start from the CAD model of the workpiece to be painted, described by means of a parametric model, a tessellated mesh [24, 128, 167], or by a point-cloud model acquired by means of vision or proximity sensors [68, 152]. Several examples of path planning starting from CAD models can be found in the present literature. Early examples are given by [72], where a method for accurate simulation of robotic spray application using empirical parameterization is presented, and by [6], where the spray path is first automatically generated on the basis of the CAD data of the work-piece and the spraying parameters, and then converted into robot commands (Fig. 4.10).

The simplest path planning approaches that solve the uniform coverage problem (i.e., to generate a spray path such that the entire surface is completely covered and receives an acceptably uniform layer of paint deposition) take into account single parametric surfaces and are based on the definition of an offset curve. In particular,

a start curve (also termed seed curve [7]) is generated on the target surface, then the subsequent paths are built by offsetting the start curve along a family of curves orthogonal to initial one. This approach is implemented in [9], where the coverage trajectory generation problem is decomposed into three sub-problems: (1) selecting a seed curve, (2) determining a speed profile along each pass, and (3) selecting the spacing between consecutive passes.

The spray deposition can be applied continuously without stopping the paint flow or discontinuously by turning the tool on and off. Several path patterns can be created based on the start curve, such as zigzag, raster, and spiral [18, 24, 161].

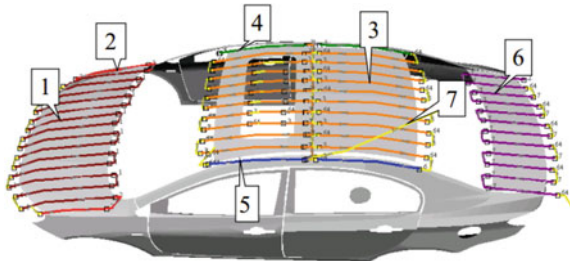
If 3D surfaces are considered instead of planar ones, the path planning becomes more complex. A possible strategy is the referred to as ‘folding’: a 3D model is virtually folded in 2D and treated as a single large surface, then paths are generated in 2D [73]. However, this method introduces higher errors as the surface curvature increases.

The path planning on 3D surfaces can also be solved by means of a feature-based approach: each part to be painted is treated through a set of simple features or elementary surface geometries such as planes, cylinders, cavities (regions with negative curvature) and ribs (parallel narrow regions with high curvature). The paths for the robot are then generated for these features individually using predefined strategies for each region [145]. Another example of path planning on typical regular surfaces including planes, cylindrical, conical and spherical surfaces can be found in [166]. The method is also extended to complex free surfaces with large curvature using hierarchical segmentation to divide the original surface in a number of region to be planned by template programming. The authors in [86] present a general method of offset curve construction with tool-adaptive offsets for free-form surfaces. The offset path is obtained as a family of iso-curves of an anisotropic distance function of a seed curve on the workpiece surface. In [105] a mesh following technique for the generation of tool-paths directly from tessellated models is presented. The technique does not introduce any approximation and allows smoother and more accurate surface following tool-paths to be generated.

Surface segmentation is often used in robotic painting path planning when dealing with complex free-form shapes to divide them into simpler regions (patches). In [8] the authors showcase the segmentation of a complex automotive surfaces into topologically simple surfaces with a hierarchical procedure using the concept of the watershed segmentation of surfaces [114].

In [25, 30–34, 128] the authors adopt a multi-patch approach, in which a CAD model is firstly approximated by a large number of small triangles. The triangles with the nearest locations and directions are then combined into flat patches. For each patch, an approach for flat surface is applied to generate the paths (Fig. 4.11). In [127] tool path planning approach which optimizes the tool motion performance and the thickness uniformity is presented. The method first partitions the part surface into flat patches based on the topology and normal directions, and then determines the movement pattern and the sweeping direction for each patch. Both zigzag and spiral patterns are considered. Zigzag patterns allow the robot to perform simple tool movements, but their non-isotropic nature makes it difficult to achieve thickness

Fig. 4.11 Spray painting paths on a car body (image taken from [30])



uniformity near the patch borders. Spiral patterns have isotropic nature but they may lead to disconnected path segments for some patch shapes.

In [18] a multi-patch approach is considered, where mesh triangles are sorted to define tag points directly, without the need of sorting triangles into a flat or low-curvature patch. In this manner, the spraying path on complex products such as vehicle chassis can be planned. In [153] a surface segmentation based on the determination of the maximum deviation angle of the normal vectors of the vertexes is implemented to generate the patches that are connected and can be covered by paths uniformly. To minimize the cycle time and the material waste, the segmentation also considers as obstacles the holes and the unnecessary painting regions. Furthermore, in [64] a genetic algorithm for surface segmentation is presented and two methods are considered: the first is able to separate the largest patch from the surface, whereas the second is capable of dividing the surface with the smallest number of slices.

In [44], two main methods are identified for the offline path planning of 3D surfaces. In the first approach the CAD mesh file is generated and the robot path is planned by considering the mesh points and the normal vectors to the surface. In the second one, orthogonal planes are used to cut the surface to be coated so as to generate a series of scanning curves. The normal vector is calculated to define the orientation of the torch on every point of the curves. This method is also known as *cutting method* or *marching method* [12]. For example, in [62] radial basis functions are used for surface modeling, and the intersection of surfaces for high-precision trajectory generation. Furthermore, in [55] the cutting method is applied to ensure the uniformity of the distance of two neighbor scanning passes in thermal spraying.

Most of the previously referenced works are based on CAD models to plan the robot tool path. However, the path planning can also be based on point cloud models, obtained by means of vision systems or proximity sensors. In [149] a path planning approach based on point cloud slicing is presented. The authors propose an adaptive method to determine the direction of the slicing plane, use polynomial fitting and uniform interpolation method to obtain smooth spray paths, and introduce an iterative formula to optimize the interval between slicing planes.

Another example of path planning approach in which the model of the object to be painted is acquired through artificial vision is given by [68]. In this work, graph theory and operative search techniques are applied to provide a general and optimal solution to the path planning problem. In particular, the object to be painted is partitioned into primitives that can be represented by a graph and the Chinese

Postman algorithm is run on the graph to obtain the minimum-length path covering all arcs.

More recently, in [152], an image of the target is captured using RGB-D vision sensors. The image is then segmented using a segmentation network and processed to estimate the relative pose between the actual target and the pre-scanned target model.

Besides CAD and point-cloud models, other approaches to automatic path planning for painting robots rely on the processing of digital images for artistic purposes. In this case, the path planning can be based on non-photorealistic rendering techniques [16, 65, 94, 125], which apply user defined algorithms to render an input image into an artwork, or on deep learning approaches that take an input map of a desired texture, and infer robotic paint commands to produce that painting [51].

In most of the previous examples the robot path is planned offline. This is due to the fact that offline path planning allows optimization and repeatability of the robot operation, especially when the same task has to be repeated numerous times for many identical pieces, which is a common scenario in the industrial and manufacturing applications.

However, the offline path planning strategy can lead to a decreasing in the spray quality, for example if large-size elements prone to deformation, such as the hull of ships or parts of buildings, are considered. Indeed, in this case, gravity and mechanical deformation would result in inevitable deformations for large-scale parts and possible discrepancies between the as-built workpieces and their nominal specifications would arise [102]. Thus, the perpendicularity and constancy of distance between subsequent paths computed on the basis of nominal CAD models are not guaranteed, leading to decreased spray quality. Furthermore, in the case of workpiece conveying on the spray-painting pipeline, random pose changes of the part to be painted might occur. To overcome these problems, systems based on the usage of real-time 3-D reconstruction together with online and adaptive path planning techniques are developed. An example of online path planning is given by [27], where the authors adopt a visual feedback based on fringe pattern to control the motion of the robot tool in a closed loop to achieve paint film uniformity. Furthermore, the authors in [69] propose an online modeling approach for automatic spray-painting applications. Specifically, two consumer RGB-D cameras are mounted on the two sides of the pipeline, and the data streams of the moving workpiece are continuously collected for the subsequent trajectory planning. Another example of real-time path planning for spray painting purposes is given by [137], where a stereo camera is used for surface recording via a real-time, appearance-based mapping procedure, as well as to steer the painting robot. However, in the online path planning the difficulty on keeping the camera cleaned from paint arises, and more computational resources are needed with respect to the offline scenario to operate both the image acquisition and the path computation in real-time.

The problem of path planning in spray painting robots is usually decoupled from the definition of the motion law that the manipulator has to follow during the execution of the task. The main objective of the trajectory planning is to ensure constant tool speed to minimize the variation of accumulated film thickness on the surface [5].

An early example of optimization of the speed profile can be found in [117], where two constrained quadratic problems are considered to minimize the painting time subject to lower bounds of speed, and minimize the variation in coating thickness. Nevertheless, these problems do not consider any limit on the end-effector acceleration or any upper bound on end-effector speed. More recently, in [31] not only the spray path defined on a Bezier triangular surface model, but also the end-effector speed along the specified path are optimized to ensure limited variation of the coating thickness.

In [140–142] the authors present a path-constrained trajectory planning strategy that provides feasible motion profiles without resorting to optimization routines and without the need of a dynamic description of the manipulator. The algorithm takes as input an arbitrary description of the end-effector path in the operative space and apply a sequence of look-ahead filtering operations on the speed profile to ensure end-effector speed and joint acceleration limitation.

4.4 Conclusions

In this chapter an overview of the literature on path planning generation in robotics has been presented. The centrality of the problem in robotics is testified by the large number of works written on the topic, which comprises both general-purpose planning methods and application-specific ones. The analysis has been focused on AGVs, medical robots, welding robots and painting robots, as significant examples of the importance of path planning in robotics. In particular, the latter field of application has been analyzed in detail. The analysis has outlined the uttermost importance of path planning in the development of effective robotic operations, as path planning can be used as tool to face the technical challenges of modern industry.

References

1. Achour, N., Chaalal, M.: Mobile robots path planning using genetic algorithms. In: The Seventh International Conference on Autonomic and Autonomous Systems, pp. 111–115 (2011)
2. Ahmed, Y., Wu, C., Pang Ahmed, S.M., Yuan, J., Wu, Y., Chew, C.M., Pang, C.K.: Collision-free path planning for multi-pass robotic welding. In: 2015 IEEE 20th Conference on Emerging Technologies & Factory Automation (ETFA), pp. 1–4. IEEE (2015)
3. Akai, N., Morales, L.Y., Murase, H.: Mobile robot localization considering class of sensor observations. In: 2018 IEEE/RSJ International Conference on Intelligent Robots and Systems (IROS), pp. 3159–3166. IEEE (2018)
4. Alterovitz, R., Branicky, M., Goldberg, K., et al.: Motion planning under uncertainty for image-guided medical needle steering. Int. J. Robot. Res. **27**(11–12), 1361–1374 (2008)
5. Antonio, J.K.: Optimal trajectory planning for spray coating. In: Proceedings of the 1994 IEEE International Conference on Robotics and Automation, pp. 2570–2577. IEEE (1994)

6. Asakawa, N., Takeuchi, Y.: Teachingless spray-painting of sculptured surface by an industrial robot. In: Proceedings of International Conference on Robotics and Automation, vol. 3, pp. 1875–1879. IEEE (1997)
7. Atkar, P.N., Choset, H., Rizzi, A.A.: Towards optimal coverage of 2-dimensional surfaces embedded in \mathbb{R}^3 : choice of start curve. In: Proceedings 2003 IEEE/RSJ International Conference on Intelligent Robots and Systems (IROS 2003) (Cat. No. 03CH37453), vol. 4, pp. 3581–3587. IEEE (2003)
8. Atkar, P.N., Greenfield, A., Conner, D.C., Choset, H., Rizzi, A.A.: Hierarchical segmentation of surfaces embedded in \mathbb{R}^3 for auto-body painting. In: Proceedings of the 2005 IEEE International Conference on Robotics and Automation, pp. 572–577. IEEE (2005)
9. Atkar, P.N., Greenfield, A., Conner, D.C., Choset, H., Rizzi, A.A., et al.: Uniform coverage of automotive surface patches. *Int. J. Robot. Res.* **24**(11), 883–898 (2005)
10. Bae, J., Chung, W.: A heuristic for path planning of multiple heterogeneous automated guided vehicles. *Int. J. Precis. Eng. Manuf.* **19**(12), 1765–1771 (2018)
11. Bailey, T., Durrant-Whyte, H.: Simultaneous localization and mapping (SLAM): part ii. *IEEE Robot. Autom. Mag.* **13**(3), 108–117 (2006)
12. [Bajaj (1988)] Bajaj, C.L., Hoffmann, C.M., Lynch, R.E., Hopcroft, J., et al.: Tracing surface intersections. *Comput. Aided Geometric Des.* **5**(4), 285–307 (1988)
13. Baldwin, S.: Robotic paint automation: the pros and cons of using robots in your paint finishing system. *Metal Finish.* **108**(11–12), 126–129 (2010)
14. Balkan, T., Arikán, M.S.: Modeling of paint flow rate flux for circular paint sprays by using experimental paint thickness distribution. *Mech. Res. Commun.* **26**(5), 609–617 (1999)
15. Beik, V., Marzbani, H., Jazar, R.: Welding sequence optimisation in the automotive industry: a review. *Proc. Inst. Mech. Eng. Part C J. Mech. Eng. Sci.* **233**(17), 5945–5952 (2019)
16. Beltramello, A., Scalera, L., Seriani, S., Gallina, P., et al.: Artistic robotic painting using the palette knife technique. *Robotics* **9**(1), 15 (2020)
17. Bhattacharjee, P., Rakshit, P., Goswami, I., Konar, A., Nagar, A.K.: Multi-robot path-planning using artificial bee colony optimization algorithm. In: 2011 Third World Congress on Nature and Biologically Inspired Computing, pp. 219–224. IEEE (2011)
18. Bi, Z., Lang, S.: Automated robotic programming for products with changes. *Int. J. Prod. Res.* **45**(9), 2105–2118 (2007)
19. Broadbent, A., et al.: Free-ranging agv and scheduling system. *Autom. Guided Veh. Syst.* **43**, 301–309 (1987)
20. Cai, C., Sun, C., Han, Y., Zhang, Q.: Clinical flexible needle puncture path planning based on particle swarm optimization. *Comput. Methods Programs Biomed.*, p. 105511 (2020)
21. Camarillo, D.B., Krummel, T.M., Salisbury, J.K., et al.: Robotic technology in surgery: past, present, and future. *Am. J. Surg.* **188**(4), 2–15 (2004)
22. Candeloro, M., Lekkas, A.M., Hegde, J., Sørensen, A.J.: A 3d dynamic voronoi diagram-based path-planning system for UUVS. In: OCEANS 2016 MTS/IEEE Monterey, pp. 1–8. IEEE (2016)
23. Castellanos, J.A., Tardos, J.D.: Mobile robot localization and map building: a multisensor fusion approach. Springer Science & Business Media
24. Chen, H., Fuhbrigge, T., Li, X.: Automated industrial robot path planning for spray painting process: a review. In: 2008 IEEE International Conference on Automation Science and Engineering, pp. 522–527. IEEE (2008)
25. Chen, H., Sheng, W., Xi, N., Song, M., Chen, Y.: Automated robot trajectory planning for spray painting of free-form surfaces in automotive manufacturing. In: Proceedings 2002 IEEE International Conference on Robotics and Automation (Cat. No. 02CH37292), vol. 1, pp. 450–455. IEEE (2002)
26. Chen, J., Liu, R., Gao, Y., Li, G., An, T.: Preferential purification of oxygenated volatile organic compounds than monoaromatics emitted from paint spray booth and risk attenuation by the integrated decontamination technique. *J. Cleaner Prod.* **148**, 268–275 (2017)
27. Chen, R., Wang, G., Zhao, J., Xu, J., Chen, K., et al.: Fringe pattern based plane-to-plane visual servoing for robotic spray path planning. *IEEE/ASME Trans. Mechatr.* **23**(3), 1083–1091 (2017)

28. Chen, S., Lv, N.: Research evolution on intelligentized technologies for arc welding process. *J. Manuf. Process.* **16**(1), 109–122 (2014)
29. Chen, W., Chen, Y., Zhang, W., He, S., Li, B., Jiang, J., et al.: Paint thickness simulation for robotic painting of curved surfaces based on euler-euler approach. *J. Brazilian Soc. Mech. Sci. Eng.* **41**(4), 199 (2019)
30. Chen, W., Liu, H., Tang, Y., Liu, J., et al.: Trajectory optimization of electrostatic spray painting robots on curved surface. *Coatings* **7**(10), 155 (2017)
31. Chen, W., Liu, J., Tang, Y., Ge, H., et al.: Automatic spray trajectory optimization on b閦ier surface. *Electronics* **8**(2), 168 (2019)
32. Chen, W., Wang, X., Ge, H., Wen, Y.: Trajectory optimization for spray painting robot on bezier-bernstein algorithm. In: 2018 Chinese Automation Congress (CAC), pp. 3389–3394. IEEE (2018)
33. Chen, W., Zhao, D.: Tool trajectory optimization of robotic spray painting. In: 2009 Second International Conference on Intelligent Computation Technology and Automation, vol. 3, pp. 419–422. IEEE (2009)
34. Chen, W., Zhao, D.: Path planning for spray painting robot of workpiece surfaces. *Math. Problems Eng.* (2013)
35. Chen, Y., He, Y., Chen, H., Zhang, H., Chen, S.: Effect of weave frequency and amplitude on temperature field in weaving welding process. *Int. J. Adv. Manuf. Technol.* **75**(5–8), 803–813 (2014)
36. Chen, Y.-C., Lin, C.-H., Lung, S.-C.C., Chen, K.-F., Wang, W.-C.V., Chou, C.-T., Lai, C.-H.: Environmental concentration of spray paint particulate matters causes pulmonary dysfunction in human normal bronchial epithelial beas-2b cell. *Process Safety Environ. Protect.* **126**, 250–258 (2019)
37. Conner, D.C., Greenfield, A., Atkar, P.N., Rizzi, A.A., Choset, H., et al.: Paint deposition modeling for trajectory planning on automotive surfaces. *IEEE Trans. Autom. Sci. Eng.* **2**(4), 381–392 (2005)
38. Connolly, C.I., Burns, J.B., Weiss, R.: Path planning using Laplace's equation. In: Proceedings, IEEE International Conference on Robotics and Automation, pp. 2102–2106. IEEE (1990)
39. Contreras-Cruz, M.A., Ayala-Ramirez, V., Hernandez-Belmonte, U.H.: Mobile robot path planning using artificial bee colony and evolutionary programming. *Appl. Soft Comput.* **30**, 319–328 (2015)
40. Daniels, S.C.: Real time conflict resolution in automated guided vehicle scheduling. Technical Report, AIR FORCE INST OF TECH WRIGHT-PATTERSON AFB OH (1988)
41. Davis, J., Perhinschi, M., Wilburn, B., Karas, O.: Development of a modified voronoi algorithm for UAV path planning and obstacle avoidance. In: AIAA Guidance, Navigation, and Control Conference p. 4904 (2012)
42. Dechter, R., Pearl, J.: Generalized best-first search strategies and the optimality of a. *J. ACM (JACM)* **32**(3), 505–536 (1985)
43. Dehghan, E., Salcudean, S.E.: Needle insertion parameter optimization for brachytherapy. *IEEE Trans. Robot.* **25**(2), 303–315 (2009)
44. Deng, S., Cai, Z., Fang, D., Liao, H., Montavon, G., et al.: Application of robot offline programming in thermal spraying. *Surf. Coatings Technol.* **20**(19–20), 3875–3882 (2012)
45. Dilthey, U., Stein, L.: Robot systems for arc welding-current position and future trends. *Weld. Res. Abroad* **39**(12), 2–6 (1993)
46. DiMaio, S.P., Salcudean, S.E.: Needle steering and motion planning in soft tissues. *IEEE Trans. Biomed. Eng.* **52**(6), 965–974 (2005)
47. Dominick, J., Scheibe, A., Ye, Q.: The simulation of the electrostatic spray painting process with high-speed rotary bell atomizers. part i: direct charging. *Particle Particle Syst. Character.* **22**(2), 141–150 (2005)
48. Duindam, V., Xu, J., Alterovitz, R., Sastry, S., Goldberg, K.: 3d motion planning algorithms for steerable needles using inverse kinematics. In: Algorithmic Foundation of Robotics VIII, pp. 535–549. Springer (2009)

49. Duinkerken, M.B., Ottjes, J.A., Lodewijks, G.: Comparison of routing strategies for agv systems using simulation. In: Proceedings of the 2006 Winter Simulation Conference, pp. 1523–1530. IEEE (2006)
50. Durrant-Whyte, H., Bailey, T.: Simultaneous localization and mapping: part i. *IEEE Robot. Autom. Mag.* **13**(2), 99–110 (2006)
51. El Helou, M., Mandt, S., Krause, A., Beardsley, P.: Mobile robotic painting of texture. In: ICRA 2019-IEEE International Conference on Robotics and Automation (2019)
52. Elgezua, I., Kobayashi, Y., Fujie, M.G.: Survey on current state-of-the-art in needle insertion robots: Open challenges for application in real surgery. *Proc. CIRP* **5**, 94–99 (2013)
53. Ellwood, K.R., Tardiff, J.L., Alaie, S.M., et al.: A simplified analysis method for correlating rotary atomizer performance on droplet size and coating appearance. *J. Coat. Technol. Res.* **11**(3), 303–309 (2014)
54. Englot, B., Hover, F.: Multi-goal feasible path planning using ant colony optimization. In: 2011 IEEE International Conference on Robotics and Automation, pp. 2255–2260. IEEE (2011)
55. Fang, D., Zheng, Y., Zhang, B., Li, X., Ju, P., Li, H., Zeng, C.: Automatic robot trajectory for thermal-sprayed complex surfaces. *Adv. Mat. Sci. Eng.* (2018)
56. Fang, H., Ong, S., Nee, A.: Robot path planning optimization for welding complex joints. *Int. J. Adv. Manuf. Technol.* **90**(9–12), 3829–3839 (2017)
57. Farahani, R.Z., Laporte, G., Miandoabchi, E., Bina, S., et al.: Designing efficient methods for the tandem agv network design problem using tabu search and genetic algorithm. *Int. J. Adv. Manuf. Technol.* **36**(9–10), 996–1009 (2008)
58. Fazlollahtabar, H., Saidi-Mehrabad, M.: Methodologies to optimize automated guided vehicle scheduling and routing problems: a review study. *J. Intel. Robot. Syst.* **77**(3–4), 525–545 (2015)
59. Fogliati, M., Fontana, D., Garbero, M., Vanni, M., Baldi, G., Donde, R., et al.: Cfd simulation of paint deposition in an air spray process. *JCT Res.* **3**(2), 117–125 (2006)
60. Franks, J., Huo, L., Baron, L.: The joint-limits and singularity avoidance in robotic welding. *Ind. Robot Int. J.* (2008)
61. Fransen, K., van Eekelen, J., Pogromsky, A., Boon, M., Adan, I., et al.: A dynamic path planning approach for dense, large, grid-based automated guided vehicle systems. *Comput. Op. Res.* **123**, 105046 (2020)
62. Freitas, R.S., Soares, E.E., Costa, R.R., Carvalho, B.B.: High precision trajectory planning on freeform surfaces for robotic manipulators. In: 2017 IEEE/RSJ International Conference on Intelligent Robots and Systems (IROS), pp. 3695–3700. IEEE (2017)
63. Freund, E., Rokossa, D., Roßmann, J.: Process-oriented approach to an efficient off-line programming of industrial robots. In: IECON'98. Proceedings of the 24th Annual Conference of the IEEE Industrial Electronics Society (Cat. No. 98CH36200), vol. 1, pp. 208–213. IEEE (1998)
64. Fu, Z., Xiao, B., Wu, C., Yang, J.: A genetic algorithm-based surface segmentation method for spray painting robotics. In: 2017 29th Chinese Control and Decision Conference (CCDC), pp. 4049–4054. IEEE (2017)
65. Galea, B., Kia, E., Aird, N., Kry, P.G.: Stippling with aerial robots. In: Proceedings of the Joint Symposium on Computational Aesthetics and Sketch Based Interfaces and Modeling and Non-photorealistic Animation and Rendering, pp. 125–134 (2016)
66. Gasparetto, A., Boscaroli, P., Lanzutti, A., Vidoni, R., et al.: Trajectory planning in robotics. *Math. Comput. Sci.* **6**(3), 269–279 (2012)
67. Gasparetto, A., Scalera, L.: From the unimate to the delta robot: the early decades of industrial robotics. In: Explorations in the History and Heritage of Machines and Mechanisms, pp. 284–295. Springer (2019)
68. Gasparetto, A., Vidoni, R., Saccavini, E., Pillan, D.: Optimal path planning for painting robots. In: ASME 2010 10th Biennial Conference on Engineering Systems Design and Analysis, pp. 601–608. American Society of Mechanical Engineers (2010)

69. Ge, J., Li, J., Peng, Y., Lu, H., Li, S., Zhang, H., Xiao, C., Wang, Y.: Online 3d modeling of complex workpieces for the robotic spray painting with low-cost rgb-d cameras. *IEEE Trans. Instrum. Meas* (2021)
70. Geraerts, R., Overmars, M.H.: A comparative study of probabilistic roadmap planners. In: *Algorithmic Foundations of Robotics V*, pp. 43–57. Springer (2004)
71. Gonzalez, A.G.C., Alves, M.V.S., Viana, G.S., Carvalho, L.K., Basilio, J.C.: Supervisory control-based navigation architecture: a new framework for autonomous robots in industry 4.0 environments. *IEEE Trans. Ind. Inform.* **14**(4), 1732–1743 (2018)
72. Goodman, E.D., Hoppensteradt, L.T.: A method for accurate simulation of robotic spray application using empirical parameterization. In: *Proceedings. 1991 IEEE International Conference on Robotics and Automation*, pp. 1357–1368. IEEE (1991)
73. Hertling, P., Hog, L., Larsen, R., Perram, J.W., Petersen, H.G.: Task curve planning for painting robots. i. process modeling and calibration. *IEEE Trans. Robot. Autom.* **12**(2), 324–330 (1996)
74. Huo, L., Baron, L.: The self-adaptation of weights for joint-limits and singularity avoidances of functionally redundant robotic-task. *Robot. Comput. Integrat. Manuf.* **27**(2), 367–376 (2011)
75. Indri, M., Grau, A., Ruderman, M.: Guest editorial special section on recent trends and developments in industry 4.0 motivated robotic solutions. *IEEE Trans. Ind. Inform.* **14**(4), 1677–1680 (2018)
76. Islam, M., Buijk, A., Rais-Rohani, M., Motoyama, K.: Simulation-based numerical optimization of arc welding process for reduced distortion in welded structures. *Finite Elements Anal. Des.* **84**, 54–64 (2014)
77. Kadivar, M., Jafarpur, K., Baradaran, G., et al.: Optimizing welding sequence with genetic algorithm. *Comput. Mech.* **26**(6), 514–519 (2000)
78. Kapoor, A., Simaan, N., Taylor, R.H.: Suturing in confined spaces: constrained motion control of a hybrid 8-dof robot. In: *ICAR'05. Proceedings., 12th International Conference on Advanced Robotics, 2005.*, pp. 452–459. IEEE (2005)
79. Kavraki, L.E., Svestka, P., Latombe, J.-C., Overmars, M.H., et al.: Probabilistic roadmaps for path planning in high-dimensional configuration spaces. *IEEE Trans. Robot. Autom.* **12**(4), 566–580 (1996)
80. Khatib, O.: Real-time obstacle avoidance for manipulators and mobile robots. In: *Autonomous Robot Vehicles*, pp. 396–404. Springer (1986)
81. Kim, C.W., Tanchoco, J.M.: Conflict-free shortest-time bidirectional agv routeing. *Int. J. Prod. Res.* **29**(12), 2377–2391 (1991)
82. Kim, C.W., Tanchoco, J.: Operational control of a bidirectional automated guided vehicle system. *Int. J. Prod. Res.* **31**(9), 2123–2138 (1993)
83. Kim, D.-W., Choi, J.-S., Nnaji, B.: Robot arc welding operations planning with a rotating/tilting positioner. *Int. J. Prod. Res.* **36**(4), 957–979 (1998)
84. Kim, H.-J., Kim, Y.-D., Lee, D.-H.: Scheduling for an arc-welding robot considering heat-caused distortion. *J. Op. Res. Soc.* **56**(1), 39–50 (2005)
85. Kim, K.-Y., Norman, B., Nnaji, B.: Heuristics for single-pass welding task sequencing. *Int. J. Prod. Res.* **40**(12), 2769–2788 (2002)
86. Kout, A., Müller, H.: Tool-adaptive offset paths on triangular mesh workpiece surfaces. *Comput. Des.* **50**, 61–73 (2014)
87. Kulatunga, A., Liu, D., Dissanayake, G., Siyambalapitiya, S.: Ant colony optimization based simultaneous task allocation and path planning of autonomous vehicles. In: *2006 IEEE Conference on Cybernetics and Intelligent Systems*, pp. 1–6. IEEE (2006)
88. Kwoh, Y.S., Hou, J., Jonckheere, E.A., Hayati, S.: A robot with improved absolute positioning accuracy for ct guided stereotactic brain surgery. *IEEE Trans. Biomed. Eng.* **35**(2), 153–160 (1988)
89. Larsen, L., Kim, J., Kupke, M., Schuster, A.: Automatic path planning of industrial robots comparing sampling-based and computational intelligence methods. *Proc. Manuf.* **11**, 241–248 (2017)
90. Latombe, J.-C.: *Robot Motion Planning*, vol. 124. Springer Science & Business Media (2012)
91. LaValle, S.M.: Rapidly-exploring random trees: a new tool for path planning (1998)

92. Lavallee, S., Troccaz, J., Gaborit, L., Cinquin, P., Benabid, A.-L., Hoffmann, D.: Image guided operating robot: a clinical application in stereotactic neurosurgery. In: Proceedings 1992 IEEE International Conference on Robotics and Automation, pp. 618–619. IEEE Computer Society (1992)
93. Li, P., Yang, Z., Jiang, S.: Needle-tissue interactive mechanism and steering control in image-guided robot-assisted minimally invasive surgery: a review. *Med. Biol. Eng. Comput.* **56**(6), 931–949 (2018)
94. Lindemeier, T., Metzner, J., Pollak, L., Deussen, O.: Hardware-based non-photorealistic rendering using a painting robot. In: Computer Graphics Forum, vol. 34, pp. 311–323. Wiley Online Library (2015)
95. Lingelbach, F.: Path planning for mobile manipulation using probabilistic cell decomposition. In: 2004 IEEE/RSJ International Conference on Intelligent Robots and Systems (IROS)(IEEE Cat. No. 04CH37566), vol. 3, pp. 2807–2812. IEEE (2004)
96. Liu, Y., Zhao, J., Lu, Z., Chen, S.: Pose planning for the end-effector of robot in the welding of intersecting pipes. *Chinese J. Mech. Eng. English Edn.* **24**(2), 264 (2011)
97. Lolin, Y.: Chronic neurological toxicity associated with exposure to volatile substances. *Human Toxicol.* **8**(4), 293–300 (1989)
98. Louredo, M., Díaz, I., Gil, J.J.: Dribon: a mechatronic bone drilling tool. *Mechatronics* **22**(8), 1060–1066 (2012)
99. Lozano-Perez, T.: Robot programming. *Proc. IEEE* **71**(7), 821–841 (1983)
100. Lulu, L., Elnagar, A.: A comparative study between visibility-based roadmap path planning algorithms. In: 2005 IEEE/RSJ International Conference on Intelligent Robots and Systems, pp. 3263–3268. IEEE (2005)
101. Masehian, E., Sedighizadeh, D.: Classic and heuristic approaches in robot motion planning-a chronological review. *World Acad. Sci. Eng. Technol.* **23**(5), 101–106 (2007)
102. Maset, E., Scalera, L., Zonta, D., Alba, I., Crosilla, F., Fusielo, A.: Procrustes analysis for the virtual trial assembly of large-size elements. *Robot. Comput. Integr. Manuf.* **62**, 101885 (2020)
103. Meeran, S., Share, A.: Optimum path planning using convex hull and local search heuristic algorithms. *Mechatronics* **7**(8), 737–756 (1997)
104. Messler, R.W.: Principles of welding: processes, physics, chemistry, and metallurgy. Wiley (2008)
105. Mineo, C., Pierce, S.G., Nicholson, P.I., Cooper, I.: Introducing a novel mesh following technique for approximation-free robotic tool path trajectories. *J. Comput. Des. Eng.* **4**(3), 192–202 (2017)
106. Moe, S., Gravdahl, J.T., Pettersen, K.Y.: Set-based control for autonomous spray painting. *IEEE Trans. Autom. Sci. Eng.* **15**(4), 1785–1796 (2018)
107. Mohanty, P.K., Parhi, D.R.: Optimal path planning for a mobile robot using cuckoo search algorithm. *J. Exp. Theoret. Artif. Intel.* **28**(1–2), 35–52 (2016)
108. Nageotte, F., Zanne, P., Doignon, C., De Mathelin, M., et al.: Stitching planning in laparoscopic surgery: towards robot-assisted suturing. *Int. J. Robot. Res.* **28**(10), 1303–1321 (2009)
109. Nguan, C., Girvan, A., Luke, P.P.: Robotic surgery versus laparoscopy: a comparison between two robotic systems and laparoscopy. *J. Robot. Surgery* **1**(4), 263–268 (2008)
110. Nguyen Duc, D., Tran Huu, T., Nananukul, N.: A dynamic route-planning system based on industry 4.0 technology. *Algorithms*, **13**(12), 308 (2020)
111. Ogbenhe, J., Mpofu, K.: Towards achieving a fully intelligent robotic arc welding: a review. *Ind. Robot Int. J.* (2015)
112. Park, K., Jeon, D.: Optimization of tool path pitch of spray painting robots for automotive painting quality. *Int. J. Control Autom. Syst.* **16**(6), 2832–2838 (2018)
113. Patil, S., Alterovitz, R.: Interactive motion planning for steerable needles in 3d environments with obstacles. In: 2010 3rd IEEE RAS & EMBS international conference on biomedical robotics and biomechatronics, pp. 893–899. IEEE (2010)
114. Pulla, S., Razdan, A., Farin, G.: Improved curvature estimation for watershed segmentation of 3-dimensional meshes. *IEEE Trans. Visual. Comput. Graph.* **5**(4), 308–321 (2001)

115. Qiu, L., Hsu, W.-J., Huang, S.-Y., Wang, H.: Scheduling and routing algorithms for agvs: a survey. *Int. J. Prod. Res.* **40**(3), 745–760 (2002)
116. Radaj, D.: Heat effects of welding: temperature field, residual stress, distortion. Springer Science & Business Media (2012)
117. Ramabhadran, R., Antonio, J.K.: Fast solution techniques for a class of optimal trajectory planning problems with applications to automated spray coating. *IEEE Trans. Robot. Autom.* **13**(4), 519–530 (1997)
118. Rao, A.M., Ramji, K., Rao, B.S.S.: Experimental investigation on navigation of mobile robot using ant colony optimization. In: Smart Computing and Informatics, pp. 123–132. Springer (2018)
119. Reed, K.B., Majewicz, A., Kallem, V., Alterovitz, R., Goldberg, K., Cowan, N.J., Okamura, A.M., et al.: Robot-assisted needle steering. *IEEE Robot. Autom. Mag.* **18**(4), 35–46 (2011)
120. Ren, S., Xie, Y., Yang, X., Xu, J., Wang, G., Chen, K.: A method for optimizing the base position of mobile painting manipulators. *IEEE Trans. Autom. Sci. Eng.* **14**(1), 370–375 (2016)
121. Rimon, E., Koditschek, D.E.: Exact robot navigation using artificial potential functions. *IEEE Trans. Robot. Autom.* **8**(8), 501–518 (1992)
122. Sahir Arıkan, M., Balkan, T.: Process modeling, simulation, and paint thickness measurement for robotic spray painting. *J. Robot. Syst.* **17**(9), 479–494 (2000)
123. Savelsbergh, M., Sol, M.: Drive: dynamic routing of independent vehicles. *Op. Res.* **46**(4), 474–490 (1998)
124. Scalera, L., Mazzon, E., Gallina, P., Gasparetto, A.: Airbrush robotic painting system: Experimental validation of a colour spray model. In: International Conference on Robotics in Alpine-Adria Danube Region, pp. 549–556. Springer (2017)
125. Scalera, L., Seriani, S., Gasparetto, A., Gallina, P., et al.: Non-photorealistic rendering techniques for artistic robotic painting. *Robotics* **8**(1), 10 (2019)
126. Sen, S., Garg, A., Gealy, D.V., McKinley, S., Jen, Y., Goldberg, K.: Automating multi-throw multilateral surgical suturing with a mechanical needle guide and sequential convex optimization. In: 2016 IEEE International Conference on Robotics and Automation (ICRA), pp. 4178–4185. IEEE (2016)
127. Sheng, W., Chen, H., Xi, N., Chen, Y.: Tool path planning for compound surfaces in spray forming processes. *IEEE Trans. Autom. Sci. Eng.* **2**(3), 240–249 (2005)
128. Sheng, W., Xi, N., Song, M., Chen, Y., MacNeille, P.: Automated cad-guided robot path planning for spray painting of compound surfaces. In: Proceedings. 2000 IEEE/RSJ International Conference on Intelligent Robots and Systems (IROS 2000) (Cat. No. 00CH37113), vol. 3, pp. 1918–1923. IEEE (2000)
129. Shi, L., Tian, X., Zhang, C.: Automatic programming for industrial robot to weld intersecting pipes. *Int. J. Adv. Manuf. Technol.* **81**(9–12), 2099–2107 (2015)
130. Shibata, T., Fukuda, T.: Intelligent motion planning by genetic algorithm with fuzzy critic. In: Proceedings of 8th IEEE International Symposium on Intelligent Control, pp. 565–570. IEEE (1993)
131. Shirazi, B., Fazlollahtabar, H., Mahdavi, I., et al.: A six sigma based multi-objective optimization for machine grouping control in flexible cellular manufacturing systems with guide-path flexibility. *Adv. Eng. Softw.* **41**(6), 865–873 (2010)
132. Song, J.S., Zhiyong, Y.: The potential field-based trajectory planning of needle invasion in soft tissue. *J. Biomed. Eng.* **4** (2010)
133. Song, P.-C., Pan, J.-S., Chu, S.-C.: A parallel compact cuckoo search algorithm for three-dimensional path planning. *Appl. Soft Comput.* **106443** (2020)
134. Sugita, S., Itaya, T., Takeuchi, Y., et al.: Development of robot teaching support devices to automate deburring and finishing works in casting. *Int. J. Adv. Manuf. Technol.* **23**(3–4), 183–189 (2004)
135. Suh, S.-H., Woo, I.-K., Noh, S.-K.: Development of an automatic trajectory planning system (atps) for spray painting robots. In: Proceedings. 1991 IEEE International Conference on Robotics and Automation, pp. 1948–1955. IEEE (1991)

136. Tabar, R.S., Wärmejord, K., Söderberg, R.: Evaluating evolutionary algorithms on spot welding sequence optimization with respect to geometrical variation. *Procedia CIRP* **75**, 421–426 (2018)
137. Tadic, V., Odry, A., Burkus, E., Kecske, I., Kiraly, Z., Klincsik, M., Sari, Z., Vizvari, Z., Toth, A., Odry, P.: Painting path planning for a painting robot with a realsense depth sensor. *Appl. Sci.* **11**(4), 1467 (2021)
138. Tarn, T.-J., Chen, S.-B., Zhou, C.: Robotic welding, intelligence and automation, vol. 362. Springer (2007)
139. Tavakkoli-Moghaddam, R., Aryanezhad, M., Kazemipoor, H., Salehipour, A., et al.: Partitioning machines in tandem agv systems based on balanced flow strategy by simulated annealing. *Int. J. Adv. Manuf. Technol.* **38**(3–4), 355 (2008)
140. Trigatti, G., Boscariol, P., Scalera, L., Pillan, D., Gasparetto, A.: A look-ahead trajectory planning algorithm for spray painting robots with non-spherical wrists. In: IFToMM Symposium on Mechanism Design for Robotics, pp. 235–242. Springer (2018)
141. Trigatti, G., Boscariol, P., Scalera, L., Pillan, D., Gasparetto, A., et al.: A new path-constrained trajectory planning strategy for spray painting robots. *Int. J. Adv. Manuf. Technol.* **98**(9–12), 2287–2296 (2018)
142. Trigatti, G., Scalera, L., Pillan, D., Gasparetto, A.: A novel trajectory planning technique for anthropomorphic robots with non-spherical wrist. In: 49th International Symposium on Robotics ISR 2017 (2017)
143. Van Den Berg, J., Miller, S., Duckworth, D., Hu, H., Wan, A., Fu, X.-Y., Goldberg, K., Abbeel, P.: Superhuman performance of surgical tasks by robots using iterative learning from human-guided demonstrations. In: 2010 IEEE International Conference on Robotics and Automation, pp. 2074–2081. IEEE (2010)
144. Vempati, A.S., Khurana, H., Kabelka, V., Flueckiger, S., Siegwart, R., Beardsley, P., et al.: A virtual reality interface for an autonomous spray painting UAV. *IEEE Robot. Autom. Lett.* **4**(3), 2870–2877 (2019)
145. Vincze, M., Pichler, A., Biegelbauer, G., Hausler, K., Andersen, H., Madsen, O., Cristiansen, M.: Automatic robotic spray painting of low volume high variant parts. In: Proceedings of the 33rd ISR (International Symposium on Robotics), vol. 7 (2002)
146. Vivaldini, K.C.T., Galdames, J.P.M., Pasqual, T., Sobral, R., Araújo, R., Becker, M., Caurin, G.: Automatic routing system for intelligent warehouses. In: IEEE International Conference on Robotics and Automation, vol. 1, pp. 1–6. Citeseer (2010)
147. Wang, C., Wang, L., Qin, J., Wu, Z., Duan, L., Li, Z., Cao, M., Ou, X., Su, X., Li, W., et al.: Path planning of automated guided vehicles based on improved a-star algorithm. In: 2015 IEEE International Conference on Information and Automation, pp. 2071–2076. IEEE (2015)
148. Wang, D., Tan, D., Liu, L.: Particle swarm optimization algorithm: an overview. *Soft Comput.* **22**(2), 387–408 (2018)
149. Wang, G., Cheng, J., Li, R., Chen, K.: A new point cloud slicing based path planning algorithm for robotic spray painting. In: 2015 IEEE International Conference on Robotics and Biomimetics (ROBIO), pp. 1717–1722. IEEE (2015)
150. Wang, J., Shang, X., Guo, T., Zhou, J., Jia, S., Wang, C.: Optimal path planning based on hybrid genetic-cuckoo search algorithm. In: 2019 6th International Conference on Systems and Informatics (ICSAI), pp. 165–169. IEEE (2019)
151. Wang, L., Kan, J., Guo, J., Wang, C.: 3d path planning for the ground robot with improved ant colony optimization. *Sensors* **19**(4), 815 (2019)
152. Wang, Z., Fan, J., Jing, F., Liu, Z., Tan, M.: A pose estimation system based on deep neural network and icp registration for robotic spray painting application. *Int. J. Adv. Manuf. Technol.*, pp. 1–15 (2019)
153. Xia, W., Wei, C., Liao, X.: Surface segmentation based intelligent trajectory planning and control modeling for spray painting. In: 2009 International Conference on Mechatronics and Automation, pp. 4958–4963. IEEE (2009)
154. Xiao, J., Michalewicz, Z., Zhang, L., Trojanowski, K.: Adaptive evolutionary planner/navigator for mobile robots. *IEEE Trans. Evol. Comput.* **1**(1), 18–28 (1997)

155. Xu, J., Duindam, V., Alterovitz, R., Goldberg, K.: Motion planning for steerable needles in 3d environments with obstacles using rapidly-exploring random trees and backchaining. In: 2008 IEEE International Conference on Automation Science and Engineering, pp. 41–46. IEEE (2008)
156. Yan, S., Ong, S., Nee, A.: Optimal pass planning for robotic welding of large-dimension joints with deep grooves. *Procedia CIRP* **56**, 188–192 (2016)
157. Yang, X., Wushan, C.: Agy path planning based on smoothing a* algorithm. *Int. J. Softw. Eng. Appl. (IJSEA)* **6**(5), 1–8 (2015)
158. Ye, Q., Pulli, K.: Numerical and experimental investigation on the spray coating process using a pneumatic atomizer: influences of operating conditions and target geometries. *Coatings* **7**(1), 13 (2017)
159. Yen, J., Pfluger, N.: Path planning and execution using fuzzy logic. In: Navigation and Control Conference, p. 2801
160. Yu, J., Li, R., Feng, Z., Zhao, A., Yu, Z., Ye, Z., Wang, J.: A novel parallel ant colony optimization algorithm for warehouse path planning. *J. Control Sci. Eng* (2020)
161. Zeng, Y., Ni, X.H.: Path optimization of spray painting robot for zigzag path pattern. In: Advanced Materials Research, vol. 712, pp. 2260–2263. Trans Tech Publ (2013)
162. Zhan, X., Zhang, D., Liu, X., Chen, J., Wei, Y., Zhou, J., Liu, R.: Comparison between weave bead welding and multi-layer multi-pass welding for thick plate invar steel. *Int. J. Adv. Manuf. Technol.* **88**(5–8), 2211–2225 (2017)
163. Zhang, B., Wu, J., Wang, L., Yu, Z., Fu, P.: A method to realize accurate dynamic feedforward control of a spray-painting robot for airplane wings. *IEEE/ASME Trans. Mechatr.* **23**(3), 1182–1192 (2018)
164. Zhang, H., Lu, H., Cai, C., Chen, S.: Robot path planning in multi-pass weaving welding for thick plates. In: Robotic Welding, Intelligence and Automation, pp. 351–359. Springer (2011)
165. Zhang, Y., Gong, D.-W., Zhang, J.-H.: Robot path planning in uncertain environment using multi-objective particle swarm optimization. *Neurocomputing* **103**, 172–185 (2013)
166. Zhou, B., Fang, F., Shao, Z., Meng, Z., Dai, X.: Fast and templatable path planning of spray painting robots for regular surfaces. In: 2015 34th Chinese Control Conference (CCC), pp. 5925–5930. IEEE (2015)
167. Zhou, B., Zhang, X., Meng, Z., Dai, X.: Off-line programming system of industrial robot for spraying manufacturing optimization. In: Proceedings of the 33rd Chinese Control Conference, pp. 8495–8500. IEEE (2014)

Chapter 5

Robot Design: Optimization Methods and Task-Based Design



Med Amine Laribi, Giuseppe Carbone, and S. Zeghloul

Abstract Practically robots involve in highly dynamic environments to execute specific tasks. To ensure a maximal performance, the optimization of architecture as well as the design parameters are frequently required. This is recurrent and more significant when the task requirements related to safety or other operating conditions must be guaranteed. The present work focuses on two important issues constantly in interaction in robotics, namely optimal robot design and task-based design of robots. The first one deals with optimization approaches and solving methods in order to design robot parts, which includes their dimensioning, according to a number of optimality criteria. The second features a wider set of goals, concerning the selection of the requested number of degrees of freedom as well as the kind of joints to be used, the architecture type, suitable mechanical designs, and control architecture. This step is well known as task-oriented robot design. The main objective of this chapter is to present the most recent research works in the application of optimization and search techniques to task-based robot design.

5.1 Introduction

Robot design is a challenging issue. The robot architecture as well as the important number of parameters contribute to increasing the complexity of the analytical design approach. This impediment is reported in several papers such as [1, 2] which addresses the design of robots for specific task.

Furthermore, the design approach is formulated in terms of multitude criteria to be satisfied that help to select the suitable robot parameters far from internal singular points as reported in [3, 4]. These criteria qualify the performances of the

M. A. Laribi (✉) · S. Zeghloul

Department of GMSC, Pprime Institute, CNRS—University of Poitiers—ENSMA—UPR, 3346 Poitiers, France

e-mail: med.amine.laribi@univ-poitiers.fr

G. Carbone

Department of Mechanical, Energy and Management Engineering, University of Calabria, 87036 Rende, Italy

robot and maximized or minimized to identify the optimal robot parameters. In general, this design approach is formulated as an optimal synthesis problem. Hamida et al. [5] presented a method for the optimal synthesis applied to four translational parallel robots based on the use of power function of a point with a comparative study based on kinematic performances. Russo et al. [6] proposed a task-oriented optimal dimensional synthesis. The proposed methodology combines a path planning algorithm and dimensional synthesis in order to optimize both robot geometry and pose for a given set of points.

The robot structure and its kinematic performance are linked by a close relationship. That is why many researchers focused on the development of approaches to reverse engineer optimal robot geometries based on task requirements. A certain task can be performed by a set of robot architectures, which can be replaced by other architectures more efficient. The experience and intuition of the designer present usually the foundation of the best robot choice for a given task. As consequence, an approach allowing to identify the optimal design from task descriptions with best performances under a set of constraints should be very useful. This approach can be defined as a task-based design.

Constraints deduced from the task description and its operating are used in the identification of the robot kinematics as well as in obtaining the set of optimal parameters. This relation resumes the purpose of the task-based design approach [7]. Researchers interested to task-based design approach explored re-configurable modular manipulator systems which allow high adaptability to a given task. In this context, Valsamos et al. [8] proposed a task-based approach for deciding the optimal configuration for self-reconfigurable manipulators. The task requirements to identify the optimal robot structure is reported by Paredis and Kholsa [9]. They developed a numerical approach for establishing the optimal structure of non-redundant robot. This method does not check for non-singular positions at task points.

Heidari et al. [10] presented a method aimed at developing a task-based methodology for the design of robotic exoskeletons. The procedure of the proposed method, from motion capture to kinematic synthesis to mechanism selection and optimization, is validated with an illustrative example.

The present chapter addresses the paradigm of the design of robots through a description of optimization methods and task-based design. The design problem statement as well as its formulation is detailed. Moreover, the description of optimal criteria is also considered and presented in details. The task specification is pointed through a description and mathematical modelling. Finally, the chapter presents an illustrative example of a robot design, providing the different steps of the task-based design, from the gestures and data analysis, robot architecture study to the optimal design.

5.2 Problem Statement and It's Formulation

In general, robots are characterized by kinematic design variables which consist of:

- Set of geometric parameters, vector: \mathbf{I}_p
- Set of joint variables, vector: \mathbf{I}_v

The geometric parameters include the links dimensions describing the robot defined with a given architecture. These latter can be composed by link twist angles and link lengths. The values of the geometric parameters are determined by dimensional synthesis [5–12]. The joint variables associated usually to an actuation can be an angle or/and a displacement. The values of the joint variables are determined by pose synthesis for a desired motion of the end effector of the robot in the global frame, \mathcal{R}_0 .

The design problem of a robot can consist of establishing relations between the task specifications and the kinematic variables. The task specification can be defined for instance by a given trajectory. However, the kinematic variables can be defined for instance by joint limits, and we speak about kinematic specification. Here, the designer must distinguish between the task space, linked to a given task, and workspace, linked to a reachable space by a robot.

According to these descriptions, the problem statement involving the kinematic design variables can be stated as follow:

Design a robot with a given architecture described by \mathbf{I}_p and \mathbf{I}_v to reach a pose in a global frame, \mathcal{R}_0 .

subject to,

A task specification, kinematic specification and one or more optimality criterion.

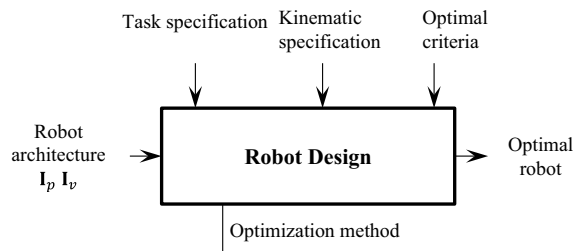
Optimal criteria are used to determine one optimal robot within many alternative solutions that can coexist and satisfy task and kinematic specifications. The problem statement can be summarized in a diagram shown in Fig. 5.1.

Robot design problem formulated as given in Fig. 5.1 is based on the use of optimisation method. This latter decomposes the complexity of the optimisation function, $\mathbf{F}(\mathbf{I}_p)$, in order to drive to a good solution. The optimisation function is composed of highly nonlinear, implicit, and complex functions and involving the kinematic design variables.

Thus, the optimum robot design can be formulated as:

$$\min_{\mathbf{I}_p} [\mathbf{F}(\mathbf{I}_p)] = \min_{\mathbf{I}_p} \{\alpha_i \bar{f}_i(\mathbf{I}_p)\}_{i=1,\dots,N}$$

Fig. 5.1 Flowchart of robot design



Subject to

$$\begin{aligned}\mathbf{A}(\mathbf{I}_p) &= 0 \\ \mathbf{B}(\mathbf{I}_p) &< 0\end{aligned}$$

where *min* is the operator to compute the minimum of a vector with fitness function $\mathbf{F}(\mathbf{I}_p)$. This vector is composed by N sub-functions fitness $\overline{f_i}(\mathbf{I}_p)$ associated to weighing factor α_i ; $\mathbf{A}(\mathbf{I}_p)$ and $\mathbf{B}(\mathbf{I}_p)$ are the vectors of equality constraints and inequality constraints, respectively, that are required to be satisfied (these are also called hard constraints); \mathbf{I}_p represents the set of geometric parameters x_j for $j = 1, \dots, K$. The sub-functions have been defined to be normalised and dimensionless, $\overline{f_i} = \frac{f_i}{\|f_i\|}$. Moreover, the weighting factor allows to give more or less significance to a criterion according to designer purpose. By changing the weighting factor value it's equivalent to moving on the Pareto front in a multi-objective optimisation problem (true in case of problem with only linear terms). As a result, small modification in the factor allow to explore the space of the optimal solutions and change completely the solution but this change depends on the sensitivity of the problem too.

5.3 Optimality Criteria

In the literature, many optimality criteria can be found proposed and investigated by the researchers for evaluating robot performances and perform robot design. The most popular being strong optimality. One notes:

- Kinematic criteria (workspace, dexterity, manipulability, ...),
- Dynamic criteria (dynamic manipulability, ...),
- Load carrying capacity,
- Stiffness criteria,
- Robot configuration,
- Safety, (HIC, ImpF, ...).

In the next, some criteria have been detailed:

5.3.1 Workspace

Robot workspace is the most investigated kinematic property. The workspace of the space robot can be used for trajectory planning. The workspace can be usually classified into three categories, i.e. reachable workspace, dexterous workspace, and

the constant-orientation workspace. The workspace can be obtained by means of discretization, geometric, and numerical methods. The workspace is directly related to the ranges of the joint angles, \mathbf{I}_v .

Figure 5.2 presents the possibility of workspace discretization for the case of pure translational workspace and pure orientation workspace. In fact, this method is used by researchers, [13, 14], to identify the workspace boundaries as well as computation of the workspace volume.

Figure 5.3 presents two examples of robot workspaces obtained by geometric construction. The first workspace of a three translational parallel manipulator, Fig. 5.3a, is a result of the intersection between two workspaces of the two imbricated robots, respectively the passive part and the active part. The active workspace of the manipulator for a given orientation is the intersection of the three volumes delimited by the three pairs of concentric spheres. The passive workspace of the manipulator is the intersection of two torus.

The second example of spherical parallel manipulator (SPM), Fig. 5.3b, is a result of the intersection of three cones, the reachable space of each leg of the SPM.

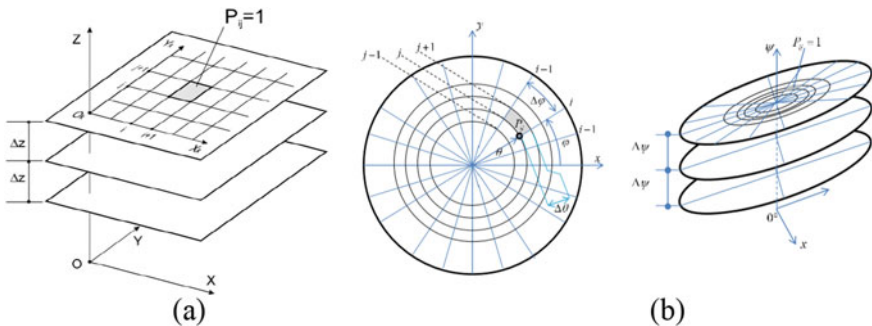


Fig. 5.2 Spatial workspace obtained by discretization method: **a** translation workspace, **b** orientation workspace

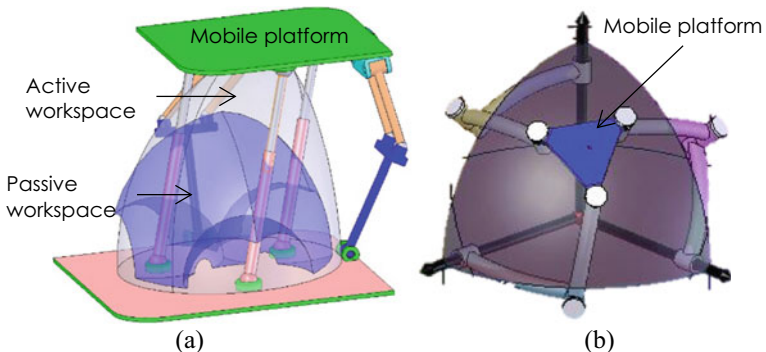


Fig. 5.3 Spatial workspace representation obtained by geometric method

5.3.2 Dexterity

The ability of a robot to reach a point in its workspace from different direction, are known as dexterity. In addition, this kinematic performance informs how far is the end-effector of a robot from the singular configurations.

One of these points are called singularities of the mechanism where the Jacobian matrix \mathbf{J} becomes singular. The Jacobian matrix depends on the instantaneous configuration of the manipulator defined by a joint vector usually called \mathbf{q} , the set joint variables \mathbf{I}_v . In singular configurations the robot loses or gains one or more degree of freedom. Singularities are located at the workspace boundary of the robots and in most cases inside the workspace. Singularity analysis is an important issue and usually performed using the screw theory method [15], Grassmann geometry method [16], differential geometry method [17] or by studying the singularity condition of the Jacobian matrix.

Several methods are proposed to compute the dexterity of a given structure. One of the most used methods is based on the condition number $\kappa(\mathbf{J})$ of the Jacobian matrix \mathbf{J} [18, 19]. The local dexterity:

$$\kappa_L(\mathbf{J}) = \|\mathbf{J}\| \cdot \|\mathbf{J}^{-1}\| \quad (5.1)$$

The global index measure of the dexterity on the whole workspace is computed as given:

$$\eta_G = \frac{\int_{\Omega} \eta_L dw}{\int_{\Omega} dw} \quad (5.2)$$

where the local index, η_L , is the inverse of the condition number, κ_L .

5.3.3 Safety

The evaluation of the safety of physical Human Robot Interaction (pHRI) is quite problematic, e.g. the questions of validity of the considered quantification method and the suitability to the whole-body. In this view, the Abbreviated Injury Scale (AIS) [20] provides a simple medical mapping of different safety criteria to a unified scale with values ranging from 0 (without injury) to 6 (severe injury or death). Based on this scale a pHRI is considered safe with high confidence up to the level 1. Here are some safety criteria that are widely from the literature.

- G: stands for Generalized Model for Brain Injury Threshold was introduced by Newman in Ref. [21]. This index considers both the direction of the impact and the angular accelerations. The G index is valid for 50% of probability of AIS \geq

3, which does not help to evaluate safe and human friendly HR collisions where AIS ≤ 1 .

- NIR: this index is quite similar to Head injury criterion (HIC) formulation. While HIC is generic, NIR is specific to the robot's technical data that are provided in manufacturer catalogues [22, 23]. In our case, HIC is used to include the cover's effect on safety.
- HIC: that quantifies the high accelerations of the brain concussion during blunt shocks even for short amount of time, e.g. HIC_{15} less than 15 ms, which can cause severe irreversible health issues [22, 23].
- ImpF (also known as contact force): this criterion is quite interesting as it can be applied on the whole-body regions. This value is considered for a specific contact surface with minimum 2.70 cm^2 area [22, 23].
- Compression Criterion (CC): reflects damaging effect of Human Robot (HR) collision by means of deformation depth, mainly adopted for the naturally compliant chest and belly regions [22, 23].

5.4 Task Specification

5.4.1 Task Description

The knowledge of application is used by researchers to design the best possible robot ensuring task achievement. This knowledge is represented by the task description and can either be kinematic or dynamic. The task-oriented design focuses on finding robot kinematic design parameters able to ensure the described task. This latter come in different representations, depending on the context, application domain, level of concept considered, tools available, etc.

For instance, task description with a most investigated kinematic property can be given in terms of the set of poses P , as a task, that the robot is supposed to reach with a specific orientation. Let \wp be the set of k task poses that define the robot's performance requirements.

$$\wp = \{P_i; i = 1, \dots, k\} \in T_{WS} \quad (5.3)$$

All these poses belong to the six-dimensional Task's workspace (T_{WS}) that defines both the position and orientation of the robot's end-effector in cartesian space and defined in a global frame. Each pose in the Task's workspace can be given as:

$$P_i = \{x, y, z, \phi_1, \phi_2, \phi_3\} \quad (5.4)$$

5.4.2 Task Modelling

In the context of task description, user is asked to collect the information from a real-life application as well as related specifications and constraints. Currently some relevant ways allow this kind of collect and generate an accurate rendering, namely using: a teleoperation interface in real time, a graphical user interface (GUI) offline and a motion capture system.

5.5 Illustrative Example

This section presents an example to illustrate how to design a robot for a given task. To this end, the motion capture analysis is introduced into the process of task-based design. The final goal is to design a robot, especially for what concern their dimensioning, according to several optimality criteria. The proposed approach is formalized through a practical application in the medical field.

The motion capture analysis is performed on medical gesture for task identification, thus the swept workspace by instruments was defined. In addition to the workspace constraint, the robot must fulfil some requirements.

5.5.1 Analysis of Medical Gestures by Motion Capture

In order to identify the workspace, the surgeon's hand movement is recorded with equipment dedicated to laparoscopy learning techniques, the pelvic-trainer (see Fig. 5.4a). The intended application is the suture-to-end anastomosis which consists in suturing two parts of a ruptured hollow organ. Two tools are used by the surgeon, a clamp, and a needle holder as show in Fig. 5.4b.

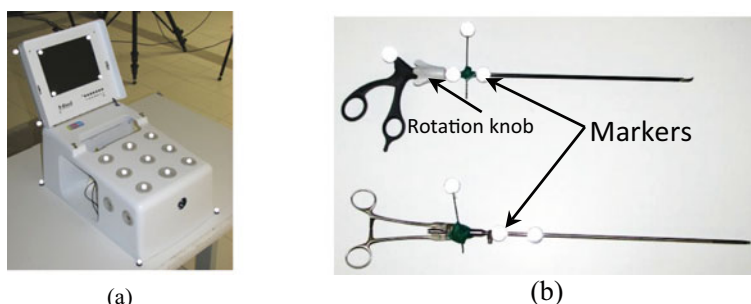


Fig. 5.4 **a** Pelvic trainer and static markers, **b** clamp and needle holder instrumented with reflective markers

In order to track the movement of the surgical tools in three dimensions, three markers are placed on the needle holder, two in the axis of the stem (markers pierced by the stem) and an offset to measure its own rotation. The clamp has four markers since the rod has an additional degree of rotation around the handle. This rotation is controlled by the surgeon with a rotation knob as shown in Fig. 5.4. Three markers are arranged on the stem, two in line (markers pierced by the stem) and another eccentric to measure its own rotation. A marker is placed on the handle to record the relative orientation of the stem.

The aim is to characterize the motion of the expert hands and the tools as well during a surgical act. The motion capture method is based on the experience of the biomechanics community [24] especially for the choice of marker sets and segments reference definition. Computer graphics focus on the use of motion capture and movement synthesis to generate three-dimensional realistic movements for virtual models. Static markers installed on the pelvic training are used only for calibration and positioning of holes (Fig. 5.5). The tools must move through small holes, simulating the skin incisions, within trocar and the movements were basically rotations around the incision point and a translation along the axis of the tool. More than fourteen reflective markers (Fig. 5.5) are placed on the subject (expert hands + instruments). The markers placed on the expert's arms and hands are used to identify the orientation of the arms of the surgeon during operations.

The collected kinematics data are based on the use of the Vicon Nexus motion capture system. The observed volume is about 1 m long, 0.5 m high, and 0.5 m wide. The used Vicon system is a motion capture system based on 10 high speed cameras capable of recording the positions of markers fixed on the tools and the surgeon hands as detailed in Fig. 5.6. Using Nexus software, we identify the three coordinates of each marker at every moment, in the reference coordinates system and when it is visible, by combining coordinates in every camera reference. The data are typically a set of coordinates of each marker as a function of time. More details about measures are given in the next section.

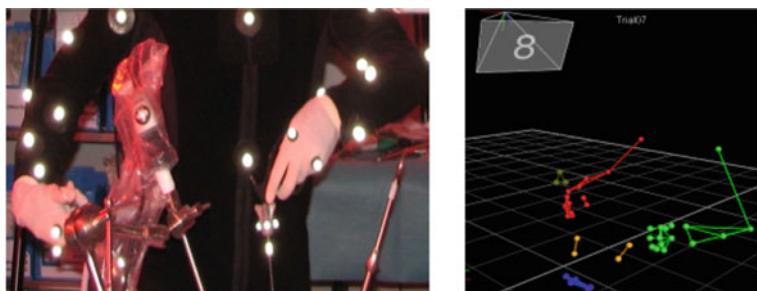
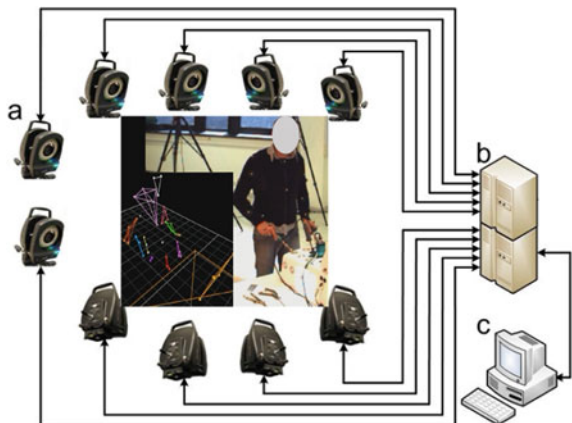


Fig. 5.5 Model reconstruction on Nexus software

Fig. 5.6 A scheme of the used motion capture system:
a 10 MX cameras; **b** MX connectivity units; **c** MX host PC; **d** MX cables



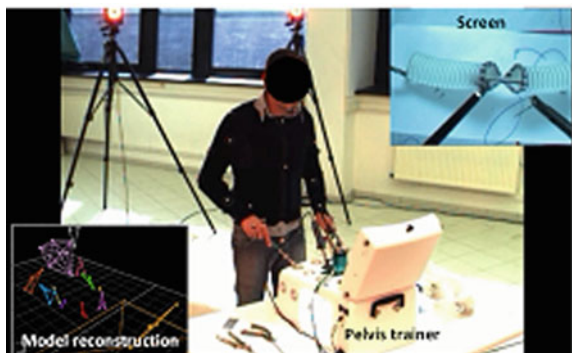
5.5.2 Data Analysis

At the end of the surgical operation, the motion capture system stores all the recorded data. These latter are then analysed to identify the kinematics of the performed movements. Figure 5.7 shows the reconstructed model using the Nexus software and the expert performing the anastomosis.

These data are used to evaluate the size of the workspace within which the tools were moving. This workspace describes the useful workspace (UW). We limit our workspace to the two rotations of the axis of the tools and we discard, as a first analysis, the self-rotation. Since the tool must go always through the hole, we decided to evaluate the workspace size through the calculation of the measured angle of the cone generated by the axis of the tool. This cone is described by an apex angle α . Using these values, a sample of obtained results of motion capture allowed us to represent the UW as illustrated in Fig. 5.8.

A cone is represented for each tool. One corresponds to the clamp with an angle of 17° and the second one is for the needle holder with an apex angle equal to

Fig. 5.7 A surgeon performing an anastomosis technique and the model reconstruction on Nexus software



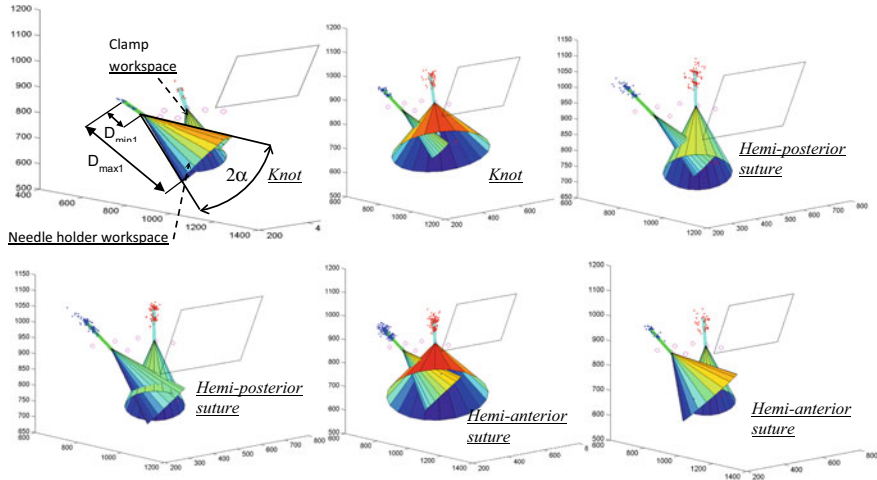


Fig. 5.8 A tool workspace resulting from experiments

26°. These values represent the maximum values recorded on all manipulations performed by 10 surgeons in a MIS environment. Besides the rotations, each tool has also a translation motion along the axis of the cone represented by the maximum and minimum distance, respectively D_{\min} and D_{\max} , between the point of incision and the tool tip.

One note that it can happen that the axes of the tools intersect, which is predictable since they both cooperate to perform the task. This study highlights the complexity of the surgeon movements during anastomosis. The analysis of all these information indicate that the surgical tools (clamp and needle holder) positions encompass a cone with a size parameter 2α (see Fig. 5.8). This value will be considered as an input parameter in the design problem of the slave robot arm for the teleoperation system. The slave robot must fit with the useful workspace of each tool.

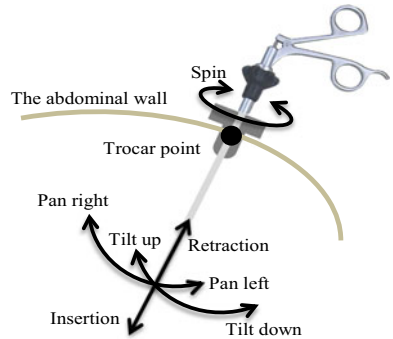
In addition to the information concerning the size of the workspace, these results will give an estimation of the tilt of the workspace with respect to the vertical. This tilt will be defined by the angle, α_T , between the revolution axis of the useful space, \mathbf{z}_T , and the vertical (see Fig. 5.12). The motion capture analysis allowed us to identify this angle. Here, the axis \mathbf{z}_T is located along the surgeon's arm.

The set of parameters identified through the data analysis and will be critical in the design of the slave robot is resumed in Table 5.1. In addition, the necessary degree of freedom for the instrument is four degrees of freedoms (dofs) as shown in Fig. 5.9.

Table 5.1 The identified parameters of useful workspace (UW) by motion capture

Vertex angle	$2\alpha = 52^\circ$
Tilt angle	$\alpha_T = 45^\circ$
Displacement a long \mathbf{z}_T	$D_{\min} = 166.5 \text{ mm}$ $D_{\max} = 278.5 \text{ mm}$

Fig. 5.9 Instrument motions: the mobility is limited due to the insertion site to four dofs



5.5.3 Robot Architecture and Kinematic Model

The mechanism under study, defined in Fig. 5.10, is a member of a class of spherical mechanism in which all the links' rotation axes intersect at a single point located at the centre of the mechanism, called centre of rotation (CoR). This point makes the spherical mechanism a natural candidate for minimally invasive surgical application. Aligning this CoR with the incision point will ensure the three rotations and single translation of the instrument. These 4 dofs comply with requested surgeon motions identified during the motion capture study.

The design challenge is to duplicate the motion of the surgeon hand through the trocar diameter creating one or more output functions at the distal tip inside the body cavity, as follow:

Fig. 5.10 Spherical serial mechanism with the coordinate assignment ($\Re_i(x_i, y_i, z_i)$)

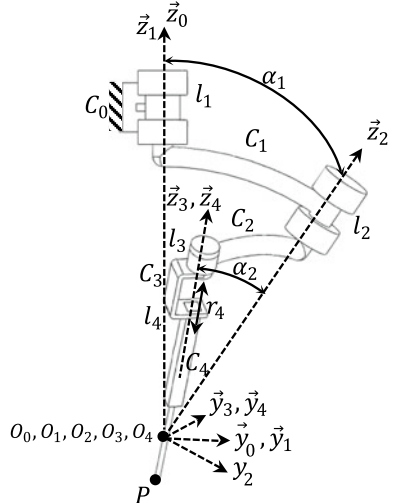


Table 5.2 Serial spherical robot modified D-H parameters

Joint i	σ_i	α_{i-1}	d_{i-1}	θ_i	r_i
1	0	α_0	0	θ_1	0
2	0	$-\alpha_1$	0	θ_2	0
3	0	$-\alpha_2$	0	θ_3	0
4	1	0	0	0	r_4

- Three rotations ($R(\mathbf{z}_1)$, $R(\mathbf{z}_2)$ and $R(\mathbf{z}_3)$) with their respective axes \mathbf{z}_1 , \mathbf{z}_2 , and \mathbf{z}_3 with a remote centre of motion located at the incision point allowing the laparoscopic instrument to sweep a conical space, with a maximum vertex angle of 20° .
- One translation ($T(\mathbf{z}_4)$) of 112 mm along the direction of the tool axis, defined by \mathbf{z}_4 axis, allowing the instrument to reach points inside body cavity.

The proposed serial spherical manipulator with one translation, $3R - T$, is sketched in Fig. 5.10. The kinematic parameters are denoted by the standard modified Denavit and Hartenberg (D-H) [25] notation given in Table 5.2. The rotation angle θ_i defines the angle between the rotation axis $i - 1$ and i . When all joint angles are set to 0, ($\theta_1 = \theta_2 = \theta_3 = 0$), link C₁ lies in a plane defined by \mathbf{z}_0 and \mathbf{y}_0 and link C₂ is unfolded.

Given the mechanism parameters (α_{i-1} , θ_i and r_i) the forward kinematic model (FKM) expresses the position and orientation of the end-effector P in the frame \mathfrak{N}_0 . Using the modified-DH notation defined in Table 5.2, the forward kinematics from the base, \mathfrak{N}_0 , to the end-effector frame \mathfrak{N}_4 is the product of following matrices:

$$\mathbf{T}_0^4 = \mathbf{T}_0^1 \mathbf{T}_1^2 \mathbf{T}_2^3 \mathbf{T}_3^4 \quad (5.5)$$

The position of the point P, located on the end effector (see Fig. 5.10), is expressed by vector that represents the coordinates and the orientation of the axis along which the surgical instrument will point.

The orientation of the instrument axis is defined by the Euler angles (ψ, θ, φ) and the coordinates of the point P is provided by vector \mathbf{P} .

$$\mathbf{P} = \left[\begin{array}{cccc} X_P & Y_P & Z_P & 1 \end{array} \right]^T_{\mathfrak{N}_0} \quad (5.6)$$

That can be expressed using local coordinates in \mathfrak{N}_4 of point P as follows:

$$\mathbf{P} = \mathbf{T}_0^4 \mathbf{P}_{\mathfrak{N}_4} = \left[\begin{array}{cccc} X_P & Y_P & Z_P & 1 \end{array} \right]^T_{\mathfrak{N}_0} \quad (5.7)$$

with,

$$\begin{cases} X_P = r_4(C\alpha_2 S\alpha_1 S\theta_1 + S\alpha_2(C\alpha_1 C\theta_2 S\theta_1 + C\theta_1 S\theta_2)) \\ Y_P = r_4(C\theta_2 S\alpha_0 S\alpha_1 S\alpha_2 - C\alpha_1(C\alpha_2 S\alpha_0 + C\alpha_0 C\theta_1 C\theta_2 S\alpha_2) \\ \quad + C\alpha_0(-C\alpha_2 C\theta_1 S\alpha_1 + S\alpha_2 S\theta_1 S\theta_2)) \\ Z_P = r_4(C\alpha_0(C\alpha_1 C\alpha_2 - C\theta_2 S\alpha_1 S\alpha_2) - S\alpha_0(C\alpha_2 C\theta_1 S\alpha_1 \\ \quad + S\alpha_2(C\alpha_1 C\theta_1 C\theta_2 - S\theta_1 S\theta_2))) \end{cases} \quad (5.8)$$

where, the following notation is considered, $C\theta = \cos \theta$ and $S\theta = \sin \theta$.

From the vector that expresses the position of the point P , the inverse kinematics model aims to express the mechanism joint angles and displacements. The expressions of the joint variables ($\theta_1, \theta_2, \theta_3$) and r_4 are defined in terms of the geometric parameters given by the Euler angles (ψ, θ, φ) and the initial distance c . The value of c is equal to the minimal distance D_{\min} [26].

Throughout this section, we seek a relationship between the three Euler angles and the first joint variable. This relation can be obtained using Eq. (5.5), where the unknown is the joint angle θ_1 to be determined for a given location of the point P . The inverse kinematic model for the branch, RRR, is defined as follows

$$\mathbf{Z}_3 \cdot \mathbf{Z}_2 = C\alpha_2 \quad (5.9)$$

The vectors \mathbf{Z}_3 and \mathbf{Z}_2 are expressed in the reference frame, \mathfrak{N}_0 , and they are function of the geometric parameters, α_0, α_1 and α_2 , and the input variable.

The vector \mathbf{Z}_2 is expressed using the rotation matrix \mathbf{A}_2^0 as

$$\mathbf{Z}_2 = \mathbf{A}_2^0 \cdot \mathbf{z}_2 = \mathbf{A}_2^0 \left[\begin{array}{c} 0 \ 0 \ 1 \end{array} \right]_{\mathfrak{N}_2}^T \quad (5.10)$$

with $\mathbf{A}_2^0 = Rot(X, \alpha_0) Rot(Z, \theta_1) Rot(X, \alpha_1)$.

The vector \mathbf{Z}_3 is expressed in the reference frame using ZXZ Euler angles (ψ, θ, φ) as follows

$$\mathbf{Z}_3 = \mathbf{M}_E \mathbf{z}_3 = \mathbf{M}_E \left[\begin{array}{c} 0 \ 0 \ 1 \end{array} \right]_{\mathfrak{N}_3}^T \quad (5.11)$$

with \mathbf{M}_E is the rotation Euler matrix.

Equation (5.9) can be written as:

$$MS\theta_1 + NC\theta_1 - L = 0 \quad (5.12)$$

with

$$\begin{aligned} L &= -C\theta S\alpha_0 S\alpha_1 + C\psi S\theta C\alpha_0 S\alpha_1 \\ M &= S\psi S\theta S\alpha_1 \end{aligned}$$

$$N = C\alpha_2 - C\psi S\theta S\alpha_0 C\alpha_1 - C\theta C\alpha_0 C\alpha_1$$

Equation (5.12) can have a solution if and only if,

$$\left| \frac{N}{\sqrt{L^2 + M^2}} \right| \leq 1 \Leftrightarrow N^2 - (L^2 + M^2) \leq 0 \quad (5.13)$$

A mathematical description of the workspace of the spherical mechanism is given by Eq. (5.14). Any direction belonging to the workspace must satisfies this equation.

$$\gamma(\psi, \theta, \phi) = N^2 - (L^2 + M^2) \quad (5.14)$$

The workspace of the spherical serial manipulator is defined as a region of the three-dimensional space that can be swiped by the end-effector. The only constraints considered are the ones coming from the spherical serial chain defined by function γ at Eq. (5.14).

5.5.4 Optimal Design

Considering only the first three joints, the reachable workspace of the serial spherical manipulator is a sector of a sphere. It is usually difficult to investigate the workspace of spherical serial mechanisms; the shape of the workspace can be irregular and discontinuous when the physical constraints are considered.

The size and the shape of the workspace are characterized by the mechanism joint lengths (α_1, α_2), joint angles (θ_1, θ_2) and the radius of the sphere swept by the workspace. To ensure that the robot workspace is large enough to contain the UW, the following condition should be verified

$$2\alpha < \alpha_1 + \alpha_2 \quad (5.15)$$

If the fourth prismatic joint is added, defined by the variable r and bounding limits D_{\min} and D_{\max} , the workspace will be a truncated spherical cone. A robot workspace representation is given in Fig. 5.11.

A limitation of the serial spherical topology is the location of the wrist singularities. They are obtained when $\theta_2 = k\pi$. The central one corresponds to the position of the trocar normal to the skin, as shown in Fig. 5.12. However, this position is the most suitable one to obtain good symmetry in the workspace. The surgeon moves more often around this central configuration. Other singularities are located at the edges of the workspace.

In order to avoid the problem of central and edges singularities, a solution has been adopted. Given the geometry of the UW, it is possible to place it within the robot workspace in an area outside singularity. It is sufficient to provide a dipping angle α_D between the axes \mathbf{z}_T and \mathbf{z}_1 as it illustrated in Fig. 5.12. Then, the dipping

Fig. 5.11 Spherical serial mechanism workspace

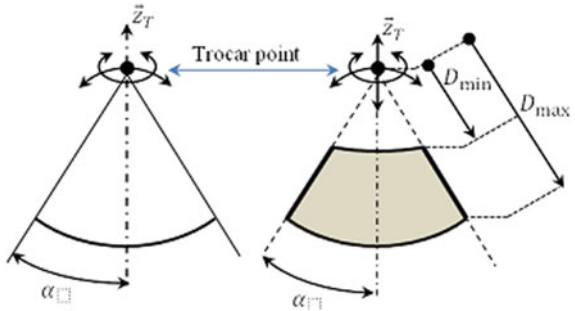
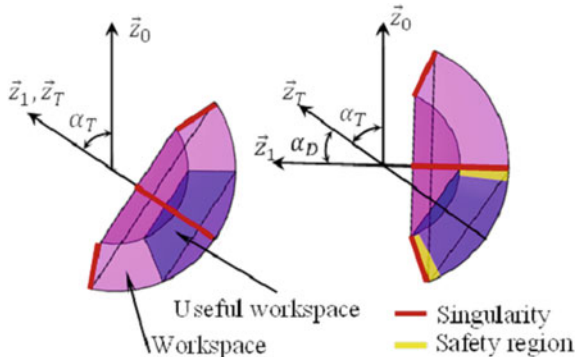


Fig. 5.12 Spherical serial mechanism workspace with singularity locations



angle must meet the following condition:

$$\alpha < \alpha_D \quad (5.16)$$

The optimal design problem can be formulated as follows

- Identify the geometric parameters of the serial spherical manipulator with smallest workspace containing the UW outside singularities (the red regions in Fig. 5.12).
- Identify the geometric parameters in the case where the user defines a safety region (yellow regions in Fig. 5.12).

The selection of the adequate values of geometric parameters for the serial spherical mechanism having a UW inside her workspace can be solved as an optimization problem.

The optimal dimensional synthesis problem can be defined as follows:

Given: A specified volume in space (useful workspace).

Find: The parameters of the serial spherical mechanism having a workspace that includes the specified volume outside singularities.

The associated optimization problem for a suitably chosen objective function $G(\mathbf{I}_p)$ and for a design vector $\mathbf{I}_p = [\alpha_1 \alpha_2 \alpha_D]^T$, can be stated as:

$$\min G(\mathbf{I}_p) = \sum_{i=1}^N \gamma_i(\psi_i, \theta_i, \varphi_i, \mathbf{I}_p)$$

Subject to

$$\begin{aligned} S_i(\psi_i, \theta_i, \varphi_i, \mathbf{I}_p) &< 0 \\ 2(\alpha + \varepsilon) &< \alpha_1 + \alpha_2 \\ \alpha + \varepsilon &< \alpha_D \end{aligned} \quad (5.17)$$

The objective function is constructed as the sum of the distances between the point E_i and the workspace of the serial spherical mechanism. The point E_i is defined by a vector $\mathbf{O}_0 E_i$ belonging to the envelope of the UW as shown in Fig. 5.13. The UW envelope is swept by taking N orientations given by the three Euler angles (ψ , θ and φ). The location and orientation of the useful workspace (UW) are provided by the centre of the sphere, O_0 , and the tilt angle α_T .

The UW is inside the workspace of the serial spherical manipulator if for all orientations $(\psi_i, \theta_i, \varphi_i)$ defining the vectors $\mathbf{O}_0 E_i$, the following condition is approved: $\gamma_i(\psi_i, \theta_i, \varphi_i) < 0$. The inequality is strict to exclude the edges of the workspace.

Optimization process allows finding the suitable solution according to the objective function. The optimal design parameters are given in Table 5.3. The angle values α_1 and α_2 are very close which gives legs with identical lengths.

The collected data and the mathematical framework provided allowed the designer to develop the slave surgical robot satisfying the problem requirements as shown in Fig. 5.14.

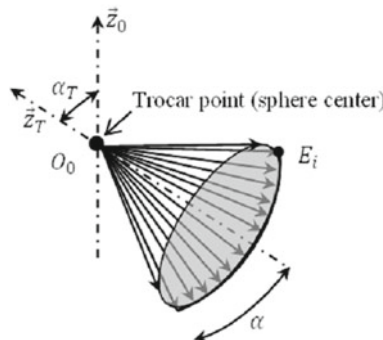


Fig. 5.13 The vector $\mathbf{O}_0 E_i$ on the useful workspace (UW)

Table 5.3 The optimal design parameters for the serial spherical mechanism

Design parameters		α_1	α_2	α_D
Values		31°	29°	31°

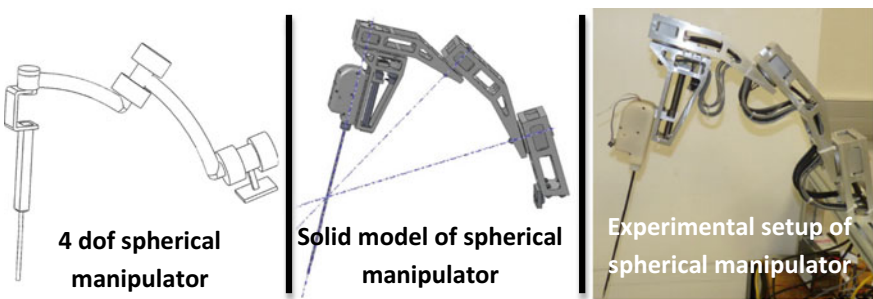


Fig. 5.14 The different design steps of serial spherical manipulator (slave surgical robot)

References

1. Seidmann, A., Arbel, A., Shapira, R.: A two-phase analytic approach to robotic system design. *Robot. Comput.-Integr. Manuf.* **1**(2), 181–190 (1984)
2. Tsai, Y., Soni, A.: Workspace synthesis of 3R, 4R, 5R, and 6R robots. *J. Mech. Mach. Theor.* **20**(6), 555–563 (1985)
3. Ceccarelli, M., Lanni, C.: A multi-objective optimum design of general 3R manipulators for prescribed workspace limits. *J. Mech. Mach. Theor.* **39**, 119–132 (2003)
4. Laribi, M.A., Carbone, G., Zeghloul, S.: On the optimal design of cable driven parallel robot with a prescribed workspace for upper limb rehabilitation tasks. *J. Bionic Eng.* **16**, 503–513 (2019). <https://doi.org/10.1007/s42235-019-0041-4>
5. Ben, H.I., Laribi, M., Mlika, A., Romdhane, L., Zeghloul, S.: Dimensional synthesis and performance evaluation of four translational parallel manipulators. *Robotica* **39**(2), 233–249 (2021)
6. Russo, M., Raimondi, L., Dong, X., Axinte, D., Kell, J.: Task-oriented optimal dimensional synthesis of robotic manipulators with limited mobility. *Robot. Comput.-Integr. Manuf.* **69** (2021)
7. Tabandeh, S., Melek, W., Biglarbegian, M., Won, S., Clark, C.: A memetic algorithm approach for solving the task-based configuration optimization problem in serial modular and reconfigurable robots. *Robotica* **34**(9), 1979–2008 (2016). <https://doi.org/10.1017/S0263574714002690>
8. Valsamos, C., Moulianitis, V., Aspragathos, N.: Index based optimal anatomy of a metamorphic manipulator for a given task. *Robot. Comput. Integr. Manuf.* **28**(4), 517–529 (2012)
9. Paredis, C.J.J., Khosla, P.K.: Kinematic design of serial link manipulators from task specifications. *Int. J. Robot. Res.* **12**(3), 274–287 (1993)
10. Heidari, O., Wolbrecht, E.T., Perez-Gracia, A., Yihun, Y.S.: A task-based design methodology for robotic exoskeletons. *J. Rehabil. Assistive Technol. Eng.* (2018). <https://doi.org/10.1177/2055668318800672>
11. Laribi, M.A., Romdhane, L., Zeghloul, S.: Analysis and dimensional synthesis of the DELTA robot for a prescribed workspace. *Mech. Mach. Theor.* **42**(7), 859–870 (2007)
12. Carbone, G., Ottaviano, E., Ceccarelli, M.: An optimum design procedure for both serial and parallel manipulators. *Proc. Inst. Mech. Eng. C J. Mech. Eng. Sci.* **221**(7), 829–843 (2007)
13. Ceccarelli, M.: Fundamentals of Mechanics of Robotics Manipulation. Kluwer, Dordrecht (2004)
14. Essomba, T., Laribi, M.A., Zeghloul, S., Poisson, G.: Optimal synthesis of a spherical parallel mechanism for medical application. *Robotica* **34**(03), 671–686 (2016). <https://doi.org/10.1017/S0263574714001805>
15. Davidson, J.K., Hunt, K.H.: Robots and Screw Theory. Oxford University Press, Oxford (2004)

16. Wu, X.Y., Bai, S.P.: Analytical determination of shape singularities for three types of parallel manipulators. *Mech. Mach. Theor.* **149**, 103812 (2020)
17. Park, F.C.: Optimal robot design and differential geometry. *ASME J. Mech. Des.* **117**(B), 87–92 (1995)
18. Merlet, J.-P.: Jacobian, manipulability, condition number, and accuracy of parallel robots. *ASME J. Mech. Des.* **128**(1), 199–206 (2006)
19. Li, C.Y., Angeles, J., Guo, H.W.: Mobility and singularity analyses of a symmetric multi-loop mechanism for space applications. *Proc. Inst. Mech. Eng. C. J. Mech. Eng. Sci.* (2021)
20. Friedl, W., Chalon M.: FAS A flexible antagonistic spring element for a high performance over. In: IEEE/RSJ International Conference on Intelligent Robots and Systems, pp. 1366–1372 (2011). <https://doi.org/10.1109/IROS.2011.6094569>
21. Newman, J.A.: A generalized acceleration model for brain injury threshold (GAMBIT). In: Proceedings of the International IRCOBI Conference on the Biomechanics of Impact, Zurich (1986)
22. Cordero, C.A., Carbone, G., Ceccarelli, M., Echávarri, J., Muñoz, J.L.: Experimental tests in human–robot collision evaluation and characterization of a new safety index for robot operation. *Mech. Mach. Theor.* **80**, 184–199 (2014)
23. Fosch-Villaronga, E., Mahler, T.: Cybersecurity, safety and robots: Strengthening the link between cybersecurity and safety in the context of care robots. *Comput. Law Secur. Rev.* **41** (2021). <https://doi.org/10.1016/j.clsr.2021.105528>
24. Strandberg, J., Pini, A., Häger Charlotte, K., Schelin, L.: Analysis choices impact movement evaluation: a multi-aspect inferential method applied to kinematic curves of vertical hops in knee-injured and asymptomatic persons. *Front. Bioeng. Biotechnol.* **9** (2021). <https://doi.org/10.3389/fbioe.2021.645014>
25. Siciliano, B., Khatib, O.: Handbook of Robotics. Springer, Berlin, Heidelberg (2008)
26. Nouaille, L., Laribi, M.A., Nelson, C.A., Essomba, T., Poisson, G., Zeghloul, S.: Design process for robotic medical tool guidance manipulators. *Proc. Inst. Mech. Eng. Part C J. Mech. Eng. Sci.* **230**(2), 259–275. <https://doi.org/10.1177/0954406215590639>

Applications

Chapter 6

Review: Robots for Inspection and Maintenance of Power Transmission Lines



Rogério Sales Gonçalves , Frederico Costa Souza,
Rafael Zimmermann Homma, Daniel Edgardo Tio Sudbrack,
Paulo Victor Trautmann, and Bruno Cordeiro Clasen

Abstract This chapter deals with the state of the art on the application of robots for inspection and maintenance of power transmission lines. Inspection activities generally involve filming lines with high-resolution cameras and/or infrared cameras and sensors. On the other hand, maintenance activities require direct contact of the robots/equipment with the lines, in order to carry out activities related to their components. Numerous studies have been found addressing the theme, regarding models and prototypes development to be used for the inspection and maintenance. After the review presentation related to power transmission line inspection/maintenance robots, a discussion about the area's main problems and the future researches is carried out.

6.1 Introduction

Mankind depends on electricity for its comfort and better survival, allowing the accomplishment of several daily tasks and saving lives in several cases. To supply this need, thousands of kilometers of power transmission lines are required, which must undergo inspections and maintenance that minimize failures in this power supplying. New transmission lines are also constantly being built to supply the growing demand for electricity.

In this sense, this chapter deals with the state of the art on the application of robots for inspection and maintenance of power transmission lines. Inspection activities generally involve filming lines with high-resolution cameras and/or infrared cameras and sensors to identify the corona effect. On the other hand, maintenance activities require direct contact of the robots/equipment with the lines, in order to carry out

R. S. Gonçalves (✉) · F. C. Souza
Federal University of Uberlândia, Av. João Naves de Ávila, 2121, Santa Mônica, Uberlândia,
MG 38408-100, Brazil
e-mail: rsgoncalves@ufu.br

R. Z. Homma · D. E. T. Sudbrack · P. V. Trautmann · B. C. Clasen
CELESC, Av. Itamarati, 160, Itacorubi, Florianópolis, SC CEP: 38408-100, Brazil

activities related to their components. To date, numerous studies have been found addressing the theme, regarding models and prototypes development to be used for the discussed purposes.

As advantages, these robots can reduce costs related to maintenance and inspection operations, which involve human labor; considerably increase the tasks efficiency and reduce the human being integrity risks, since it would decrease the work need involving operators in direct contact with the lines.

However, we can enumerate some limitations in the robots use, such as adverse climatic conditions susceptibility, operational instabilities, sensitivity to electromagnetic interference from the power lines and limitations in the robots autonomous functioning.

After the review presentation related to power transmission line inspection/maintenance robots, a discussion about the area's main problems and the future researches is carried out.

6.2 Robots for Power Lines Inspection

Monitoring of electricity distribution systems is one of the most significant tasks for energy utilities, since knowledge of cables and components estimated lifetime could prevent the concessionaires' revenue compromise of millions of dollars. The efforts spent on monitoring the distribution system status are justified by the reduction of the failures occurrence due to the electricity supply interruption, equipment damage and repair costs [1].

There are countless tasks for power lines maintenance/inspection such as cables detailed inspection, the physical and mechanical integrity visualization regarding defects and atmospheric discharges, proving the need for emergency or scheduled maintenance; visual inspection of the conductor cables; spacers; porcelain, glass or polymeric insulators; towers; installation or removal of aircraft warning spheres; cable splice services; cleaning; repairs and installations of new lines, vegetation management, identifying objects that may put the line integrity at risk, soil erosion, among others.

Due to climatic factors exposure, such as sun, rain, wind and snow; natural aging; vandalism or human beings' improper activities the components used in the energy transmission system lose their electrical properties over time, requiring maintenance to correct possible failures in such components before they can compromise the energy distribution or solve problems that interrupted the power supply. In addition to the natural aging factors, most of the components used in distribution networks are not subjected to strict quality controls during their manufacturing process, allowing the appearance of imperfections in them. Therefore, it is necessary to carry out periodic inspections to detect possible failures in such components before they can compromise the energy distribution.

Transmission line inspection is performed by operators who visually inspect the conductors. Thus, in addition to economic motivation, the reduction in human risks

associated with inspection and maintenance operations on high voltage cables (such as exposure to intense electromagnetic fields) is also a problem.

The commonly used inspection/maintenance methods are:

- In a helicopter operators perform a visual inspection. One of them makes a visual inspection with a binocular, observing the network physical structure, checking the towers and the conductors' connection. The other operator uses a thermal imager and other sensors to check for overheating in conductors and connectors;
- In a helicopter, an operator, dressed in an insulating suit, is suspended on a platform. As the helicopter approaches the line, the operator uses a stick to equalize the platform potential with the transmission line potential. With the equalized potential, the operator places the safety equipment and the necessary inspection/maintenance devices hanging from the line. Then he passes to the line, sitting or crouching over it. The helicopter moves away and the operator performs the inspection and/or maintenance by dragging on the line.
- Another way is to suspend the operator on a platform with the aid of a vehicle. The platform is electrically isolated from the vehicle so that there is no risk of short circuit. To perform any activity on the line, the operator equalizes the platform potential with the transmission line potential. In this case, the operator remains on the platform while carrying out the inspection/maintenance and the vehicle moves towards the line. There are also platforms that are placed on the cables themselves and the technicians carry out its movement.
- Inspection of high voltage cables by UAVs (Unmanned Aerial Vehicles). These have cameras with high zoom capacity, thermal camera and other sensors to identify the problem points in the high voltage lines.
- Another common strategy used regularly in these operations is the use of boom trucks. These trucks usually house a cab installed at its end, enabling an operator to control manipulator arms. However, problems such as low mobility, controllability, and accessibility are constant. This means that this strategy is limited to being used to maintain elements at low heights.

New approaches are in research worldwide to automate the inspection and maintenance process on power transmission lines. Main advances include the identification and mapping through GPS (Global Positioning System) equipment of places where there may be cable failures; use of sophisticated cameras to visualize problems; use of sensors; data acquisition equipment and computers (used for processing data obtained from sensors and images to identify problem locations); the application of mobile robots that act on lines in inspection and/or maintenance activities and Unmanned Aerial Vehicles (UAVs) for inspection [2, 3]. Chen [4] presents a review of works involving different techniques for environment recognition by inspection robots.

As advantages, the use of UAVs to inspect transmission lines present a significant reduction in the time spent on inspection operations and a considerable increase in their efficiency, in addition to decreasing risks with employees [5, 6]. When compared to the use of suspended mobile robots, the use of UAVs provides much faster inspection [7].

It is possible to list several advantages related to the use of UAVs for inspection application, which are [7]:

- Wide overcoming of terrain restrictions;
- The same UAV can inspect transmission lines of different voltage levels;
- Fast inspection, with quick automated defect detection;
- Low cost of use and maintenance compared to the usage of helicopters;
- Can identify a variety of transmission lines defects;
- Greater approximation of lines and towers when compared to the use of helicopters.

Among the problems of using UAVs, we can highlight:

- Low autonomy when compared to the use of helicopters;
- Flight limitations due to bad weather, rain and strong winds;
- Regulatory problems in several countries that prevent UAVs from operating outside of human sight;
- Problems with electromagnetic interference that can affect the behavior of UAVs.

Currently, the problem of high voltage cables inspection is practically solved with the use of UAVs that can carry high-resolution cameras with great zoom capability, infrared cameras and sensors to identify the corona effect. Corona discharges are ultraviolet emissions in ionized air caused by increasing in electrical fields, these generally triggered by defective components [8]. Current research has focused on the development of software to optimize the acquired data analysis in order to carry out the necessary maintenance and in research to increase the UAV's autonomy, recharging its batteries by landing or in proximity to high-voltage cables [9–12].

Within this perspective, recent works can be mentioned. Bhola et al. [9] developed a method for detecting power lines in images captured by an UAV. The image processing approach is based on spectral-spatial methods. Erdelj et al. [13] presented an algorithm that automates the replacement of UAVs used in inspection operations, so that the service becomes uninterrupted. The MAVLink communication protocol was used to implement the algorithm, which is a standard protocol for commercial UAVs.

Nguyen et al. [10] present an automatic vision system linked to an inspection UAV, based on a deep learning algorithm. This algorithm is capable of automatically detecting and classifying components present in the lines, in addition to detecting significant failures that require maintenance, through the images captured by the UAV during inspection operations. Takaya et al. [14] also present an inspection system that can be widely adapted to commercial UAV models.

Within the technology of sensors and image capture devices applied to inspection, Teng et al. [15] proposed the use of a LIDAR sensor. The sensor is coupled to an UAV and was used to map mountains. They cite as advantages of using the sensor embedded in the UAV its lower cost of implementation and greater inspection speed compared to the application of LIDAR sensors based on the ground, besides providing high resolution (0.125° angle resolution and 4 cm range resolution), which allows the sensor application widely in the field of high voltage lines inspection.

Fig. 6.1 Inspection UAV landed on a power line [17]



Still using LIDAR sensor technology, Pu et al. [16] introduced an approach to scanning transmission line corridors that is capable of automatically detecting important characteristics of the lines such as soil types on which the lines are based, cable types, towers, surrounding vegetation and construction type.

Within the inspection UAVs area, we can cite the work of Miralles et al. [17]. In this work, the construction of a UAV with semiautomatic landing capacity in a transmission line carrying a payload is described (Fig. 6.1). This UAV is being developed by the company MIR Innovation linked to Hydro-Québec and has a LIDAR sensor to carry out detailed inspections on high voltage cables allowing to identify flaws in the cable sheath. The authors enumerated contributions as: introduction of a new UAV that lands on a transmission line and then walks along it to perform an inspection; description of a vision system and two algorithms for calculating the position of the UAV relative to the line; results of large-scale outdoor tests, showing that the proposed UAV with the vision system is able to land on a transmission line safely in moderate wind conditions.

Another study found that presents a UAV built for landing on transmission lines is that of Chang et al. [18]. The UAV has hybrid operating modes, being able to land on an overhead ground wire and move over the line like a wheeled robot. It also has an adaptive algorithm that allows obstacles around the lines to be automatically recognized and then effectively circumvented by the UAV. No information is given on how the system deals with the electromagnetic interference issue, coming from magnetic fields induced by high voltage power lines.

6.3 Robots for Power Lines Maintenance

Also, in the subject of robot's performances in high voltage power lines, the need to develop robots to maintain the transmission lines components is highlighted. These robots come in different formats and models, such as mobile robots and UAVs. Many recent works have focused on finding solutions in this area.

Maintenance on energized lines started with the use of hot sticks repair to turn energized switches on and off. In these sticks, various tools can be adapted for different tasks. With the use of these sticks, the need to disconnect a line for maintenance becomes rarer [19].

The live line operators work in direct contact with the lines' energized parts at voltages up to 34.5 kV, being in a neutral position and isolated from the ground by safety devices such as gloves, sleeves and covers. The distance maintenance method is used for voltages up to 230 kV using hot sticks repair. Above 230 kV the use of the hot sticks is difficult due to their weight and size. At voltages greater than 230 kV, maintenance is made using the potential method where the electrician is isolated from the earth and uses a conductive suit, with the service being performed at the same potential as the line [19]. As an example, we can mention the Brazilian electric sector, which uses lines that operate in 230 kV, occupying an extension of more than 100,000 km, which demands continuous inspection/maintenance operations.

Figure 6.2 shows some examples of maintenance made by the energy company CELESC, Brazil.

Motivated by the difficulties and risks due to the human workers operating on the high voltage power lines, new investigations have been developed in the mobile robotics field, to be used in maintenance tasks in direct contact with the transmission lines. We can cite the recent work of Disyadej et al. [20], Miller et al. [21] and Yan [22].

Overall, the advantages of maintenance robots' application are:

- Can fulfill maintenance tasks dismissing operators influence;
- Reduces the risks for power line workers;
- Reduces costs;

In the other hand, the disadvantages are:

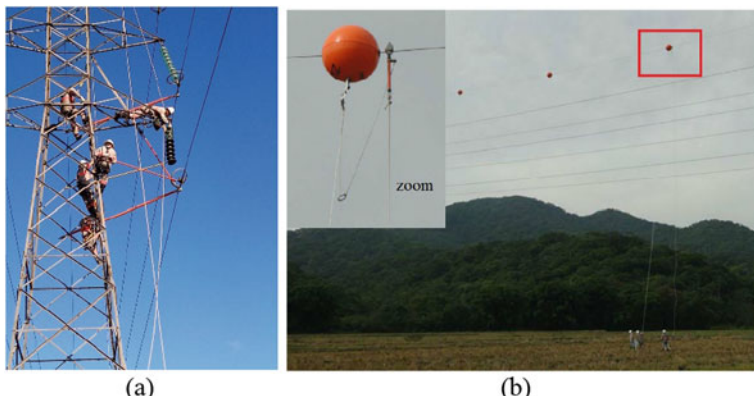


Fig. 6.2 Maintenance procedures made by energy company CELESC, Brazil. **a** Maintenance of insulator chain using hot sticks; **b** install of aircraft warning spheres

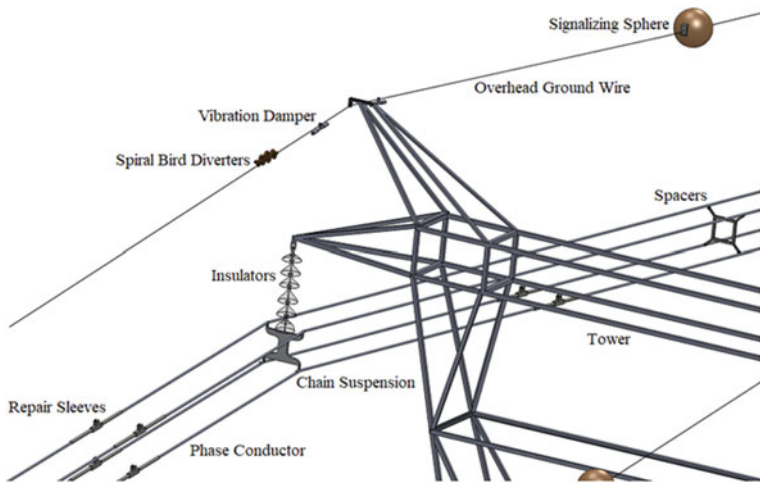


Fig. 6.3 Obstacles present in the power lines distribution system

- Low controllability;
- Very restricted obstacle surpassing capacity;
- Great mass and low portability.

In power transmission lines there are several elements that become obstacles for mobile robots such as aircraft warning spheres, suspension chains, insulators, gloves, spacers, clamps, preformed vibration dampers or stockbridge vibration dampers, spiral bird diverters, amendments (Fig. 6.3), and different tower types. Thus, the solutions found in literature that use mobile robots suspended by cables cannot easily overcome all types of existing obstacles, are complex and difficult to be placed on the cables. UAVs have been proposed as alternatives, so that these obstacles can be more easily overcome.

In literature are solutions that address specific problems related to the maintenance of high voltage power lines, such as installation of aircraft warning spheres, vibration dampers, line spacers and cable and isolator chains cleaning operations.

6.3.1 Installation of Aircraft Warning Spheres on Overhead Ground Wire

The aircraft warning spheres are spherical shaped equipment, usually orange colored, installed on the overhead ground wire of the transmission towers in order to serve as daytime signaling for airplanes, helicopters, balloons, etc. These spheres can reach about 60 cm diameter with an average mass of 5 kg.

The aircraft warning spheres installation by electricians involves a team of at least 6 people and has the risk of the electrician falling, materials falling, tools falling and

risk of shock by induction and even the improper equipment operation by the team. The average time to install an aircraft warning sphere is 30 min without considering the time to access and assemble the equipment to reach the overhead ground wire [23].

The installation of these spheres can also be done with the aid of helicopters. In this case, the electrician stays on a platform outside the helicopter and performs the installations with small synchronized movements using special tools. It should be noted that the use of helicopters represents falling risk, proximity risks to the propeller, excessive proximity or collision with the cables, malaise of the electrician or pilot and possibility of aircraft crash.

Due to the risks that this aerial signaling maintenance/installation task represents, solutions are being researched to automate these maintenance processes with the use of mobile robots [2, 3] or drones.

In [24] a device is presented for the installation of several aircraft warning spheres using a helicopter. It positions the device on the overhead ground wire to install the sphere automatically by the proposed mechanism. The disadvantage of this application is the high cost of using the helicopter and accidents risk involving its use.

The work [25] presents a device for settling an aircraft warning sphere developed to be installed with the aid of cables. The device disadvantage is that its use is not allowed at great heights.

A remote-control robot for the installation/removal of signaling spheres has also been presented in [26]. This has the disadvantage of not crossing obstacles and having to be positioned on the cable by operators. Robots similar to the presented in this work, for spheres installation with a rotating tool, are presented in [27, 28].

In [29] the aircraft warning sphere installation from a UAV is presented. The UAV takes the sphere developed for this application to the point of installation, fixes it on the cable and returns to the ground to repeat the operation (Fig. 6.4).

Works [30, 31] show mobile robots suspended by wires for installation of aircraft warning spheres adapted with a closing mechanism on the lower part of the sphere. These robots were developed specifically for spheres with a lever-type closing mechanism positioned at the bottom of the sphere. These robots cannot overcome the cable obstacles and pass the towers. These robots also have the disadvantage that they need to be placed on the cable by the technicians that climb the towers and must be lifted by ropes.

The work [32] presents a mobile robot suspended by cable that allows locomotion along the cable and the installation of several spheres stored in the robot's body. The robot is not able to overcome the cable obstacles and the existing towers. Its disadvantage is also the great mass and the need to be taken to the cable by climbing the tower and lifting the robot by ropes.

In the case of robots suspended by cables, these have the great disadvantage of requiring operators/technicians to climb the tower to position these.

It should also be noted that solutions using mobile robots suspended by cable make adaptations to the existing aircraft warning spheres or serve a specific sphere model. There are several commercial aircraft warning spheres that can be grouped

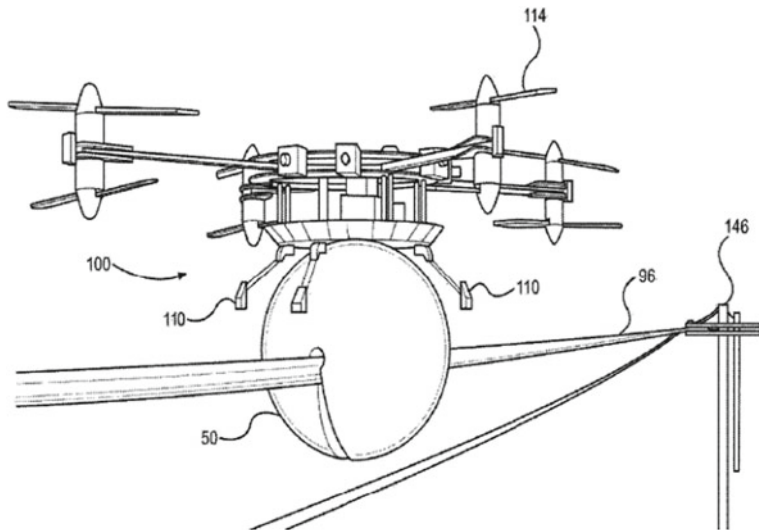


Fig. 6.4 UAV used to install signaling spheres in transmission line [29]

according to the cable fixing mechanism. The first group are spheres that have a closing mechanism (by turning) that is positioned at the top of the spheres. These are developed specifically for installation using a maneuver stick from the fixed platform in helicopters. The second group are spheres that have the rotation closing mechanism positioned at the bottom of the spheres. The third group are spheres that also have the closing mechanism at the bottom of the spheres, but the closing of the sphere in the cable is done from a mechanism with an attached lever. The fourth group are spheres formed by two halves that are attached to the cable by screwing their ends.

6.3.2 Cleaning High Voltage Cables and Insulator Chains

The insulators cleaning is essential to avoid failures in the electricity transmission system due to the various pollution types that are impregnating in them. These failures can cause the flashover phenomenon.

To accomplish the high voltage power lines isolation from the towers, devices known as insulators are required. The insulators must have, in addition to good dielectric characteristics, excellent mechanical characteristics, in view of the severe nature work that will be performed. The insulator must withstand high compression stresses, must be hard and have a highly polished surface. The insulators become dirty due to birds, dust, salt and chemicals from various smokes [33]. These dirt deposits form a conductive layer on the insulator's surface and can cause the flashover

phenomenon. Most flashovers are unpredictable, leading to the need for maintenance operations that take hours to complete.

Traditional cleaning of insulator chains is usually carried out by operators on the live line (called “hot line washing”), or when are disconnected. This cleaning can be performed by technicians using tissues, high pressure washers positioned in the towers, or carried by technicians. Cleaning can also be performed using trucks associated with platforms, or trucks associated with robotic devices in the case of low voltages in applications within cities. In the case of high voltage power lines in the transmission system, helicopters are also used.

The cleaning of insulators presents to the electricians falling risks, personal injury or allergies, electric shock, cuts by damaged insulator, injury by crushing limbs and equipment collision with the structure and/or accessories and personal injury due to tools falling. The average time to perform this task is 1.5 h per structure [23].

These insulator cleaning processes can be extremely dangerous, due to the high voltage passing through the transmission lines and any accident type can be fatal. In order to reduce the accident risk with live line operators, several solutions have been proposed, such as the use of robots and drones.

The cleaning of insulators with the use of robots follows the same format, using complex devices that move along or around the insulators discs to perform their mechanical cleaning. There is a robot for cleaning insulators based on the caterpillar’s movement as the locomotion principle along the insulators chain [34]. These robots’ models follow the same locomotion principle and have similar mechanisms [35].

Works [36, 37] presented robots for insulators cleaning and inspecting, with the robots being able to move along the insulator chain. Among the operations performed, one is the cleaning of the insulator chain disks with brushes.

The great difficulty in using these robots concerns the maintenance of complex prototypes and the need to place them in the insulators by technicians, which ends up being risky in the same way, as technicians have to climb to place the robots, suffering with ergonomic problems due to the robots’ high mass.

The insulators cleaning with a high-pressure washer using a helicopter was first described in 1984 [38].

In [39] an apparatus for insulators cleaning is presented. The apparatus consists of rotating brushes for cleaning. A helicopter is used to position the apparatus.

There are some applications of UAVs for insulators cleaning. In [40] a UAV with three nozzles for cleaning insulators is presented. One spout is responsible for the cleaning product, another for clean water and the third for a high-pressure spray. The cleaning process is monitored by a camera with images sent to a station on the ground, where the operator determines whether the cleaning has been carried out completely.

Aerones enterprise has developed a similar UAV that can be applied to insulators cleaning. French energy company Engie is developing UAVs to be used to clean insulators. The use of a moss cleaning solution (the same product used for cleaning roofs) is being tested. The UAV sprays the product on the insulators and after a few days, it dries out from the discs. In Brazil the company CELESC is working on a solution for cleaning insulator chains also using UAVs.

It is also mentioned the use of a model helicopter or UAV, to perform the cleaning of insulators with the use of an external water source such as a tank truck [41].

Regarding the removal of foreign objects in the high voltage power lines, the simplest way to perform these cleaning operations is from an UAV with a flamethrower adaptation. There are already ready solutions on the market. The use of UAVs with adapted flamethrowers has led to discussions as to whether this would be the most efficient and correct way to clean power lines. The use of these raises environmental questions about the material incineration that causes fumes that contaminate the environment and do not allow the recycling of these materials. In addition, the removal of trash in many cases not being complete with debris in the cable and the possibility of fires in the vicinity due to the large amount of fuel used in the flamethrower.

A robot for cleaning foreign objects in high voltage cables using cutting tools and electric heating (by resistance and without fuel) coupled to the robot was presented in [42]. The robot is a mobile platform that allows movement along the cable.

There are also solutions for mobile robots applied to de-icing high voltage cables [43, 44]. Other work [45] presents a mechanism for removing ice from high voltage cables in which it is positioned and moved along the cable using an UAV. Zhang [46] proposed a new method for enhancing the obstacle-surpassing capability of existing robots for removing ice from the lines.

In [47] a robot with a blade is presented to remove foreign objects in the high voltage lines. The blade is attached to the wheel.

New tools have been adapted in the LineROVer robot, including a tool for removing foreign objects in high voltage lines. This tool has a claw to hold the object and an articulated arm with a cutting disc [48].

A robot for inspection and maintenance of high voltage cables was also presented, which has a rotating brush tool for cleaning the cables [21].

In [49] was presented a mobile robot for cleaning and inspecting high voltage cables remotely operated by radio control. The inspection is performed manually by sending the images to a station on the ground. The robot can adapt one tool for pruning trees and another for cutting objects using scissors.

6.3.3 Installation of Vibration Dampers

The transmission lines cross great distances with diverse environmental conditions that are unfavorable to maintain the conducting cables and overhead ground wire (non-energized cables) useful life.

Power transmission lines are subject to the action of winds that generate vibrations in them. These vibrations can cause damage to the cables. To reduce vibrations and reduce damage, vibration dampers are used. There are two main types of vibration dampers: preformed and stockbridge type.

As the preformed vibration dampers are installed close to the towers/hardware, this operation is usually performed by technicians who need scale the towers to place

them. When replacing the vibration damper in conductor cable or overhead ground wire, a team of at least three people is usually required and there is a risk of the electrician falling, injury from falling tools or materials. Insects and animals in the tower are also risks. The average execution time of this task is 20 min per damper without considering the time for access, equipment assembly to reach the cable and the electricians' descent [23].

The installation of preformed vibration dampers can also be done with the aid of helicopters, but this activity is extremely dangerous due to the proximity to the high voltage towers. In this case the electrician is on a platform outside the helicopter and with small synchronized movements performs the installations using generally only the movement of his hands by wrapping the pre-formed vibration damper on the cable.

The installation of new preformed vibration dampers is necessary due to the aging or damage they suffer over time and the construction of new power lines. Due to the risks that the preformed vibration dampers maintenance/installation task represents, solutions are being researched to automate this maintenance process using mobile robots [2, 3].

In [50] a remotely operated robot is presented on the overhead ground wire to individually install bird signals. These aim to scare the birds away. This robot allows the installation of a bird scarer and is not able to overcome the obstacles in the cables and towers. This cable-suspended robot has the great disadvantage of requiring operators/technicians to climb the tower to position it.

The choice of the stockbridge type vibration damper model is based on studies that consider the diameter, mass, traction, climatic and topographic conditions and the span between the towers. Usually, these dampers are applied to transmission lines that use only one cable per phase [51]. These dampers can reach approximately 600 mm in length and mass between 1 and 7 kg.

The installation of stockbridge vibration dampers is made in the same way of the installation of preformed vibration dampers, including all the risks mentioned. Thus, several researchers have studied automated solutions, usually with the use of robots to perform this maintenance task [2, 3].

In the literature there is a complex robot capable of overcoming obstacles and some types of towers and having a tool capable of installing stockbridge.

type vibration dampers. This robot is heavy and needs several operators to position it on the high voltage cable [52].

A work was also found that presents a mobile robot suspended by cable capable of carrying out the task of installing stockbridge type vibration dampers from robotic mechanisms. This robot can overcome some obstacles present in the high voltage cables and needs operators to place it on the cable [53]. Other robot specific to install stockbridge vibration dampers is presented in [54] (Fig. 6.5).

Chen [55] proposed and constructed a pneumatic robotic gripper to improve maintenance capabilities of maintenance robots. The author ensures that it can lift over 21 times its self-weight and a variety of components, such as a stockbridge vibration damper. Successful electromagnetic resistance tests have also been carried out at voltages from 500 to 1000 kV with a robot with this grip.

Fig. 6.5 Robot for installing stockbridge vibration damper [54]



6.3.4 Installation of Spacers at High Voltage Cables

The energy transmission above 138 kV over long distances presents the problem of corona discharge that causes significant energy loss and interference in the communication circuits. To reduce the corona effect, it is preferable to use more than one conductor per phase or grouped conductors. These bundled conductors also increase the amount of current that can be carried compared to a single conductor. Spacers, Fig. 6.3, are used to separate these cables. Spacers must withstand the forces due to wind and magnetic forces, avoiding a short circuit between the cables.

The installation of spacers can also be done with the aid of helicopters. In this case, the electrician stands on a platform outside the helicopter and, with small synchronized movements, performs the installations using special tools, usually of the type screwdrivers, for fixing the spacers on the cables.

From the research carried out, no specific robots were found to install spacers between the high voltage cables, the installation of which was carried out by operators placed on the cables or with the use of an operator on a platform coupled to a helicopter.

6.3.5 Electromagnetic Interference in the Robots Applied to Inspection/Maintenance of Power Transmission

Electromagnetic interference (EMI) is cited by many authors [56, 57] as being one of the engineering challenges related to the implementation of autonomous inspection robots/UAVs for high voltage lines. To mitigate its effects, it is necessary to implement protection techniques and electromagnetic shielding to the robots' structure.

During inspection and maintenance operations using human labor in transmission lines, it is essential that safety procedures are adopted to avoid any risks to the operators' physical integrity, which would be caused by the electromagnetic interference influence or direct contact with the lines. One of the strategies used for protection is to equalize the electrical potential of the helicopter or tower-operator system with that of the line to be repaired. This precaution type extends to ensure the integrity of robots and UAVs that can meet lines through which high potentials permeate.

Cameron et al. [58] investigated the “incomplete Faraday cage” effect that appears in the helicopter used in the transmission line inspection, due to the fact that the line operator is effectively surrounded on three sides (top, rear and bottom) by metallic walls. These walls would be the rotating propeller blades of the helicopter, the helicopter cabin and the work platform, all with the same electrical potential. This configuration would assist in the operators shielding from the electromagnetic fields influence coming from the lines.

Electromagnetic interference in UAVs can lead to partial or complete loss of the information signals transmitted to these aircraft controller, and consequently, to the improper equipment functioning on board the UAV. This phenomenon can even lead to a complete loss of aircraft controllability [59].

Wang and Wang [34] claim that it is necessary to implement an equivalent potential zone in the entire robots' structure, when they are used in contact with high voltage lines. Therefore, all robot components must be connected with low contact resistance. In addition, the authors suggest that cables, sensors, batteries and circuits should be protected by conductive objects.

Fang and Wang [59] highlight the fact that all conductive parts of maintenance/inspection robots must be interconnected with cables so that the same electrical potential permeates the entire robotic structure. In addition, certain embedded circuits must be protected with electromagnetic interference shielding.

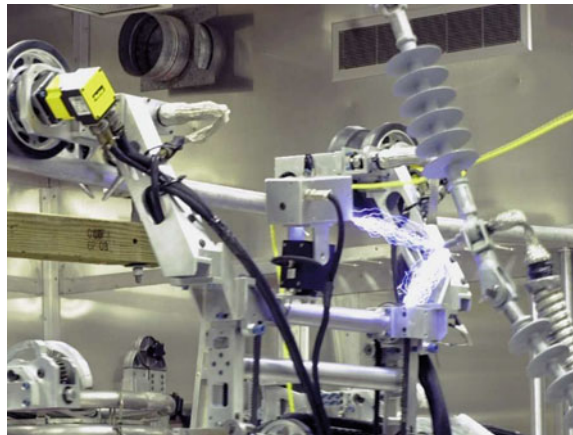
Liu et al. [53] tested different methods of electromagnetic shielding on inspection robots. The authors pointed out that the copper-based conductive coating with anti-oxidation component addition is the best electromagnetic shielding method in these applications. Montambault and Pouilot [56] developed a wheeled robot for inspection on lines with voltages up to 735 kV. The authors ensured that the entire robotic structure conducts electricity to avoid potential differences in its structure. Shields and protection systems have been installed around batteries and embedded circuits to ensure such behavior (Fig. 6.6).

In a study on the direct influence of an electrical discharge on UAVs, Gaynudinov and Chermoshentsev [60] highlighted the evaluation of the embedded electronics immunity in UAVs as an important aspect to be considered.

The triggering mechanisms of electromagnetic fields around transmission lines can be divided into [58]:

- (1) Presence of currents and voltages in the operational mode;
- (2) Presence of currents and voltages in the short circuit mode;
- (3) Presence of external sources of over voltage, for example, an electric shock impact.

Fig. 6.6 Line inspection robot shielded for voltages up to 735 kV [56]



Due to the electromagnetic fields random formation caused by the second and third mechanisms, difficulties arise in the large-scale experimental study of UAVs over high voltage transmission lines [58].

Barnett et al. [61] discuss the attenuation of electromagnetic interference in robots for maintenance, and present shielding strategies based on calculations for attenuation of electric and magnetic fields incident on the robots. It is one of the few works that deal with the subject in a more comprehensive way.

Permata et al. [62] tested aluminum foils shielding with thickness of 0.15 and 0.30 mm involving the fuselage of an unmanned aerial vehicle. The experiments aimed to evaluate the shields resistance to the electrical discharges effect and the electromagnetic induction effect inside the vehicle's fuselage. The authors concluded that the induced voltages and electric fields measured in the shielded UAV are much lower than those obtained without the shield. The physical damage caused by discharges into the vehicle's fuselage can be eliminated by using a 0.30 mm thick aluminum shield.

Few works exist that develop solutions to the problem of electromagnetic interference on UAVs applied in maintenance, so that they can work in contact with the lines. In [63] was described a UAV model that allows contact with high voltage lines, as it has an electrically conductive shield that encapsulates the vehicle. This protective layer is energized in order to electrically shield the vehicle, in the same way as the energized stick technique, known as bonding-on. In addition, anti-thermal materials are used to protect the UAV, which are already in use in the protective suit of operators who carry out maintenance on the lines.

Recently Feng and Zhang [64] presented an almost completely autonomous maintenance robot which able to work on 10 kV overhead lines. It consists of an insulated bucket vehicle and a working platform, with its basis on earth.

From that presented, the maintenance of high voltage lines using mechanisms, whether mobile robots or UAVs, is still a complex problem.

6.4 Discussion

In 2013, Pagnano et al. [8] suggested as an object of future research in the inspection area the imperative to develop robust aircraft control algorithms, thus guaranteeing high flight stability and accurate inspections in situations where there is the influence of strong side winds. In addition, they indicate the importance of implementing obstacle detection and avoidance systems, as well as the insertion of a trail/line tracking mechanism in robots, as a complement to the already used GPS system. Technologies for line tracking already exist [65, 66] but the problem of the winds influence on UAVs remains a technical challenge. Most UAV commercial manufacturers do not recommend operating the equipment with winds greater than 8 m/s.

In 2010, Montambault and Pouliot [67] suggested the use of robots for inspection/maintenance tasks with the collaboration of robotic devices and said that part of the solution to the problem of automated transmission lines inspection would come from the collaboration of various platforms, such as, between multiple UAVs, or between UAVs and robots with wheels in rows. After ten years, there are already studies and initial applications among several UAVs such as the one presented in [13].

The use of helicopters with operators, even in the case of the use of automated mechanisms, presents falling and greater risks accidents with operators, in addition to the high associated costs. Maintenance operations performed are usually corrective, that is, to remedy a problem that has already occurred.

Maintaining electricity transmission systems is a significant task for electric utilities. While the inspection processes of the elements of the transmission systems are at an advanced stage with the use of semi-automated systems using UAVs, maintenance activities are still carried out with live line operators with hand tools.

There are indisputable difficulties in maintaining the power lines, whatever the method used. This is motivated by the fact that the transmission lines, with their emission of intense electric and magnetic fields, are complex and dangerous environments. In addition, the devices used in the transmission lines have very variable configurations, in diversity and size. The most common obstacles to be overcome by robots are vibration dampers, aircraft warning spheres and the towers themselves (Fig. 6.1), the latter being the biggest obstacle to be overcome.

The robots that move around the cables, despite the various configurations already proposed, do not fully meet the needs. Each model has advantages and disadvantages, but its application has been practically unfeasible. Some devices are capable of mounting/dismounting an aircraft warning sphere. For this, the device must be placed and removed from the cable for each assembly/disassembly operation.

Other systems are equipped with wheels. In this case, with each repair sleeve cable, aircraft warning spheres or vibration dampers, they cannot overcome the obstacle. To surpass this problem, systems are used in which the robot is composed of various parts, but connected in series. This configuration makes the control unit extremely complex, making the system unviable.

Based on the mobility of animals endowed with legs, one can imagine the development of a robot with legs, that is capable of walking on the cable, that is able to overcome obstacles of different dimensions and arranged at random and that, in addition, has a simple structural design and, consequently, enables a simplified control unit. If the robot walks hanging from the cable, its own weight assists in its balance. However, the difficulties for the robot to satisfy these qualities are great because, in addition to obstacles such as warning spheres, vibration dampers and spacers, it must be able to pass through the cable support towers, overcome the various insulator types as well as change the movement direction, following the cable.

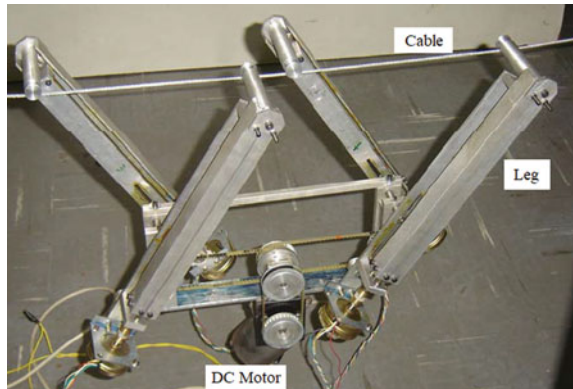
Figure 6.7 shows a robot with legs of varying lengths suspended by a wire proposed in [68]. Mobile robot suspended by cable have been studied since the 1980s and despite the difficulties listed above in their use, they are still under development and represent solutions for punctual maintenance problems, reducing the risks of technicians in contact with cables.

For the presented reasons, the development of a mobile robot that simultaneously performs all the mentioned activities is an extremely complex task and whose immediate results are questionable. Various researches in this sense ended up, many times, in the construction of a prototype, with the investment of high sums in equipment and personnel, without further work continuation.

Another problem identified in the development of mobile robots applied to power lines is the impossibility of having a compact multitasking robot that can carry out inspections and different maintenance tasks.

There is also the problem of electromagnetic interference on the robots, which is a major obstacle to the wide application of maintenance robots on the lines, because they must operate in contact or very close to the lines. The existence of embedded electronic devices that operate at low voltage in these robots makes the issue even more complex, since these devices are very sensitive to small variations in voltage, which can completely compromise their functions related to remote communication, image capture, actuators and other devices.

Fig. 6.7 Robot with legs to be applied in power lines inspections/maintenance



Due to the risks arising from the maintenance operations on the power lines, and the limitations pointed out to the automated methods described, the use of robots to perform/automate this maintenance task in conjunction with UAVs can be considered [2, 3].

Based on the state of the art presented, considering all the limitations of the methods and research described, in 2013 Gonçalves and Carvalho [3] suggested the use of drones in conjunction with mobile robots. This invention can be called a drone-robot because it is formed by an UAV that allows the coupling of different robotic modules to be applied in maintenance activities. Each module has a specific function, within the context of operationalizing the transmission lines. Elements such as aircraft warning spheres, line spacers, vibration dampers, etc., can be transported and coupled to the lines to develop autonomous operations. The robotic module is left on the cable and after performing automated maintenance, the drone removes the robotic module from the cable and is ready for new maintenance task. The focus on modular robots is justified by the difficulty of building a lightweight robot with a size compatible with the lines that manages to aggregate all the necessary maintenance operations on the power lines.

Robots can collect information during the inspection process, for later analysis or real-time analysis, which can involve various operations related to high voltage cables. The use of sensors and other embedded communication and action devices will assist in fulfilling the function that the modules were designed to perform.

The main objective of the drone-robots is to reduce the possibility of accidents with technicians who carry out this type of maintenance. The coupling of these robotics modules to the UAV allows the transposition of all obstacles present in the high voltage cables and overhead ground wire, in addition to allowing the movement of the drone-robot between the towers.

The drone-robots also reduces the risks to technician, as it is not necessary to install/place these on the cables by climbing on the high voltage towers. In this way, the drone-robots device aims to reduce the human risks associated with maintenance operations on high voltage cables and overhead ground wire, such as exposure to intense electromagnetic fields, falls and risks of electric shock.

The use of the drone-robots also allows maintenance activities to be carried out without the need to switch off the electric power, impacting equipment, industrial consumers and homes to a minimum. Therefore, with the increase of use of the drone-robots, there is an increase in the efficiency of the energy system.

In 2013, when the idea of using UAV coupled with robotic modules was presented [3], it ran up against the acquisition costs of UAVs and their limited carrying capacity. Currently, you can buy commercial UAVs for less than US \$10,000 with a useful load capacity of 10 kg and an autonomy of around 15 min. Thus, these parameters can be used in the design of maintenance tasks with drone-robots. It should be noted that commercial UAVs are not developed for applications directly or close to high voltage cables, which is necessary to develop controller protection as cited in this chapter.

Figure 6.8 represents the idea of using a robotic module to wash insulator chains. The drone is adapted to be used close to the high voltage cables with the controller

being inside in a Faraday cage and its entire structure covered with aluminum foil in such a way as to satisfy the 0.3 mm thickness. A high-pressure washer and a tank with demineralized water are used. A sensor allows maintaining a safe and effective distance for high-pressure washing. A unit on the ground supplies both the water source and the electricity. It must be ensured that the water jet is not continuous, it must be in the form of a spray to avoid the formation of potential difference. Finally, UAVs are still limited to inspection activities. Their applications in maintenance are rare and expected to increase in the coming years.

According to Haoyang [69], the UAV technology is heading to a new stage of intelligence, with the advent of new technologies such as 5G, BeiDou, Internet of Things, artificial intelligence and big data, optimizing its capabilities and increasing the systems efficiency. Recent works that present novelties in image processing techniques and artificial intelligence are in development by Zhang et al. [70], Yu [71] and Silano [72].

Possible future developments in the field will involve overcoming the limitations cited in this chapter. In general, robots will have robust shielding that virtually nullifies unwanted electromagnetic effects. With the development of energy storage technologies, there will be greater operating autonomy. The advent of 5G and the Internet of Things (IoT) will allow wide controllability, allowing robots to be commanded over long distances, remotely. The rolling on wire robots will be more compact, with lesser mass and greater ability to overcome obstacles, but not absolute capacity of overcoming. The use of UAVs will also be expanded, especially in maintenance operations. These operations may take place through the cooperation between robots and UAVs, to meet the demand for the various maintenance operations required in the lines.

6.5 Conclusions

In this chapter, the main research that seek solutions in power lines maintenance and inspection were reported and analyzed. According to the papers found, it can be said that the area of power lines inspection by UAVs and robots is already consolidated, while the maintenance area still has significant problems, which prevent its wide implementation. Among them, we can mention, to mobile robots, the difficulty of overcoming the electromagnetic interference problem, low operation autonomy, low capacity to overcome obstacles and inefficient robot's controllability, being the most frequent problems related to the latter two.

Latest researches have gradually shown advances in the maintenance area, mainly in the flying robots, which are able to overcome obstacles more effectively and clean insulators chains. However, even with the advances achieved in the last decades, many problems persist, so there are still few robots developed for maintenance that can be applied in practice without suffering from any of the reported problems.

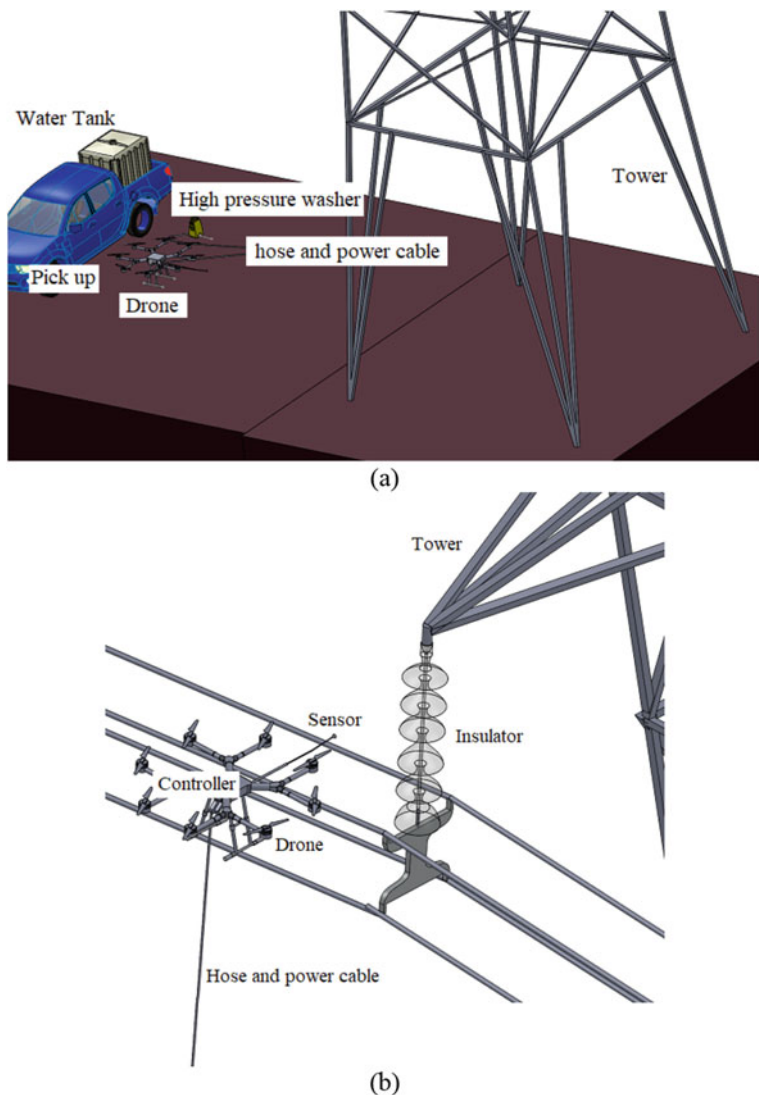


Fig. 6.8 **a** Scheme of drone-robot solution for washing insulator chain. **b** Detail of washing procedure

The development of a reliable, lightweight and autonomous robot with high capacity to overcome obstacles and protected against electromagnetic interference is still open to specific applications at power transmission lines maintenances.

The idea of autonomous modular robots working together with UAVs is a promising proposal to solve most of the reported problems involving inspection

and maintenance of power lines. As a next step, we are developing modules for inspection and/or maintenance to be coupled to the drone.

Acknowledgements The authors thank Universidade Federal de Uberlândia (UFU), Centrais Elétricas de Santa Catarina (CELESC R&D Program) and Agência Nacional de Energia Elétrica (ANEEL) for the financial support to this work.

References

1. Pinheiro, M.J.C., Lins, E.A.: Robotized system for fault detection in transmission line cables by digital radiography with energized installation. In: 19th National Seminar on Electricity Production and Transmission, p. 8, Rio de Janeiro, RJ (2007)
2. Rubin, L.: The Future of Power Line Inspection. Electrical World T&D (2000)
3. Gonçalves, R.S., Carvalho, J.C.M.: Review and latest trends in mobile robots applied in power transmission lines. *Int. J. Adv. Robotic Syst.* (2013)
4. Chen, M. et al.: Environment perception technologies for power transmission line inspection robots. *J. Sensors* **2021** (2021)
5. Zhu, X., Li, X., Yan, F.: Design and implementation for integrated UAV multi-spectral inspection system. *IOP Conf. Ser. Earth Environ. Sci.* **133**(1), 012006 (2018)
6. Li, Z. et al.: Transmission line Intelligent Inspection Central Control and Mass Data Processing System and Application Based on UAV, pp. 1–5. IEEE (2016).
7. Li, L.: The UAV Intelligent Inspection of Transmission Lines. Atlantis Press, Paris, France (2015)
8. Pagnano, A., Höpf, M., Teti, R.: A roadmap for automated power line inspection. Maintenance and repair. *Proc. CIRP* **12**, 234–239 (2013)
9. Bhola, R., et al.: Detection of the power lines in UAV remote sensed images using spectral-spatial methods. *J. Environ. Manage.* **206**, 1233–1242 (2018)
10. Nguyen, V.N., Jenssen, R., Roverso, D.: Intelligent monitoring and inspection of power line components powered by UAVs and deep learning. *IEEE Power Energy Technol. Syst. J.* **6**(1), 11–21 (2019)
11. Simic, M., Bil, C., Vojisavljevic, V.: Investigation in wireless power transmission for UAV charging. *Proc. Comput. Sci.* **60**(1), 1846–1855 (2015)
12. Simic, M., Bil, C., Vojisavljevic, V.: Design of a Recharge Station for UAVs using Non-contact Wireless Power Transfer, pp. 1–11. American Institute of Aeronautics and Astronautics, Reston, Virginia, 4 Jan 2016
13. Erdelj, M. et al.: UAVs that fly forever: uninterrupted structural inspection through automatic UAV replacement. *Ad Hoc Netw.* **94** (2019)
14. Takaya, K. et al.: Development of UAV system for autonomous power line inspection. In: 2019 23rd International Conference on System Theory, Control and Computing, ICSTCC 2019—Proceedings, pp. 762–767 (2019)
15. Teng, G.E. et al.: Mini-UAV Lidar for power line inspection. *Int. Arch. Photogramm. Remote Sens. Spatial Inf. Sci.* **42**(2W7), 297–300 (2017)
16. Pu, S. et al.: Real-time powerline corridor inspection by edge computing of UAV Lidar data. *Int. Arch. Photogramm. Remote Sens. Spatial Inf. Sci.* **42**(2/W13), 547–551 (2019)
17. Miralles, F. et al.: Linedrone technology: landing an unmanned aerial vehicle on a power line. In: Proceedings—IEEE International Conference on Robotics and Automation, pp. 6545–6552 (2018)
18. Chang, W. et al.: Development of a power line inspection robot with hybrid operation modes. In: IEEE International Conference on Intelligent Robots and Systems, pp. 973–978 (2017)
19. CELESC, ELVT Maintenance Course on Energized Transmission Lines (2019)

20. Disyadej, T. et al.: High voltage power line maintenance inspection by using smart robotics. In: 2019 IEEE Power and Energy Society Innovative Smart Grid Technologies Conference, ISGT 2019, pp. 1–4 (2019)
21. Miller, R., Abbasi, F., Mohammadpour, F.: Power line robotic device for overhead line inspection and maintenance. *Ind. Robot Int. J.* **44**(1), 75–84 (2017)
22. Yan, Y., et al.: Research on mechanism configuration and coordinated control for power distribution network live working robot. *Ind. Robot.* **47**(3), 453–462 (2020)
23. COPEL: Maintenance on High Voltage Distribution Lines with Dead Line (2015)
24. Jans, D.: Device for Installing Markerballs on Overhead Cables, Particularly Live Power Cables, US 5038465 (1991)
25. Zhenhua, Y.: High-Voltage Transmission Line Aviation Warning Ball and Installation Method Thereof, CN 103489284 B (2015)
26. Campos, M.F.M., Pereira, G.A.S., Vale, S.R.C., Bracarense, A.Q., Pinheiro, G.A., Oliveira, M.P.: A robot for installation and removal of aircraft warning spheres on aerial power transmission lines. *IEEE Trans. Power Del.* **18**(4) (2003)
27. Yonggang, J., Liang, Z., Rui, G., Lei, C., Juan, J., Feng, Z.: Automatic Handling Device for Aviation Mark Balls, CN 203045255 U (2013)
28. Rui, G., Yonggang, J., Feng, Z., Lei, C., Liang, Z., Juan, J.: Robot for Automatically Loading and Unloading Aviation Marker Balls, CN 102975192 B (2014)
29. McNally, J.: Method for Installing an Object Using an Unmanned Aerial Vehicle, US 9932110 B2 (2018)
30. Horn, H.E., Scheuner, J., Petermann, D.: Device and Method for Positioning Flight Warning Balls on Lines, in Particular on the Earth Lines of High Voltage Power Lines, EP 2916404 B1 (2014)
31. Souza, C.F., Santos, E.R.: Robot for Installation and Removal of Aerial Signaling Sphere, BR 102013013343-4 A2 (2015)
32. Park, Y., Jae, J., Han, Y.: Airplane Warning Sphere Installation Robot and Control Method for the Same, KR 10-2017-0045975 (2015)
33. Hadipour, M., Shiran M.A.: Various pollutions of power line insulators. *Majlesi J. Electr. Eng.* **6**(1) (2017)
34. Wang, L., Wang, H.: A survey on insulator inspection robots for power transmission lines. In: 4th International Conference on Applied Robotics for the Power Industry (CARPI) (2016)
35. Wang, L., Wang, H., Song, Y., Pan, X.: Development of a bio-inspired live cleaning robot for suspension insulator strings (2016)
36. Park, J.Y., Song, S.I., Cho, B.H., Byun, S.H., Kim, J.B.: Robot Mechanism for Cleaning and Inspection of Live-Line Insulators, US 7797781 B2 (2010)
37. Jiang, B., Bao, R., Jia, J., Zhongshiyu, L., Fu, M.: Robot for Cleaning Insulators, RU 2659252 C1 (2015)
38. Kurtgis, M.P.: Method for Washing Voltage Transmission Line Insulators, US4477289 (1984)
39. Jans, D.: Apparatus for Cleaning the Insulators of Live Power Lines by Means of Helicopters, EP0479181A2 (1991)
40. Tengfei, S., Ronghai, L., Xin, Z., Zhangqin, W., Xinliang, G., Yingchun, Y., Hongwei, X.: Electrified Insulator Cleaning Method Based on Unmanned Aerial Vehicle, CN105170523A (2015)
41. Hadipour, M., Aberomand, N., Jameii, M.S.: A New approach for live line insulator washing with unmanned autonomous mobile helicopter (UAMH). In: International Conference NESEFF (2016)
42. Cao, Y., Wang, H., Chang, Y., Zhang, L.: An entanglement-clearing robot for power transmission line with composite clearing tool. In: The 5th Annual IEEE International Conference on Cyber Technology in Automation, Control and Intelligent Systems (2015)
43. Montambault, S., Pouliot, N.: The HQ LineROVer: contributing to innovation in transmission line maintenance. In: IEEE 10th International Conference on Transmission and Distribution Construction, Operation and Live-Line Maintenance (2003)

44. Gongping, W., Yingsong, L., Hua, X., Yu, Y.: Robot for De-Icing of Power Transmission Lines, CN101728803A (2011)
45. Ying, P., Hongwei, L., China, X., Li, G., Yong, L., Jianglu, H.: Power Line Deicing Robot, CN206820434U (2017)
46. Zhang, X.: Research on the method of transmission line deicing robot overcoming obstacles with inclined angle. *J. Phys. Conf. Ser.* **4**, 2021 (1881)
47. Cheng, W., Yongdong, J., Jianjun, W., Jiangshen, S., Yucun, W., Chunlai, L., Yao, L.: A Kind of Power Transmission Line Cleaning Plant, CN205846575U (2016)
48. Zhang, F., Cao, L., Guo, R., Zhong, L., Jia, J., Jia, Y., Chi, X.: Extended applications of LineROVer technology. In: 10th IEEE International Conference on Control and Automation (ICCA) (2013)
49. Thomazini, D., Gelfuso, M.V.: Device for Cleaning and Inspecting Cables and Insulators from the Power Supply at a Distance, BR 102014020138-6 A2 (2016)
50. Marcelo, R.S.: Robot for Signaler Installation on a Lightning Rod. BR 102017015379-7 A2 (2019)
51. Marchi, M.E., Merino V.J.Z.: Dynamic Analysis of Stockbridge Shock Absorbers, Course Conclusion Paper, Federal Technological University of Paraná (2014)
52. Pouliot, N., Richard, P.-L., Montambault, S.: LineScout technology opens the way to robotic inspection and maintenance of high-voltage power lines. *IEEE Power Energy Technol. Syst. J.* **2**(1) (2015)
53. Jiang, W., Yan, Y., Yu, L., Peng, M., Li, H., Chen, W.: Research on dual-arm coordination motion control strategy for power cable mobile robot. *Trans. Inst. Measur. Control* **41**(11), 3235–3247 (2019)
54. Jiang, W., Zuo, G., Zuo, D.H., Li, H., Yan, J.J., Ye, G.C.: Autonomous behavior intelligence control of self-evolution mobile robot for high-voltage transmission line in complex smart grid. *Complexity* **2020**, 17 (2020)
55. Chen, Y. et al.: A soft-robotic gripper for ultra-high-voltage transmission line operations. In: 2020 IEEE 4th Conference on Energy Internet and Energy System Integration: Connecting the Grids Towards a Low-Carbon High-Efficiency Energy System, EI2 2020, pp. 788–793 (2020)
56. Liu, J. et al.: The Research on Electromagnetic Compatibility of the Autonomous Inspection Robot for Power Transmission Line. IFEESD, pp. 1091–1094 (2016)
57. Montambault, S., Pouliot, N.: Design and validation of a mobile robot for power line inspection and maintenance. *Springer Tracts Adv. Robot.* **42**, 495–504 (2008)
58. Cameron, G.W., Bodger, P.S., Woudberg, J.J.: Incomplete faraday cage effect of helicopters used in platform live-line maintenance. *IEE Proc. Gener. Transmiss. Distrib.* **145**(2), 145 (1998)
59. Nuriev, M.G., Gizatullin, Z.M., Gizatullin, R.M.: Physical modeling of electromagnetic interferences in the unmanned aerial vehicle in the case of high-voltage transmission line impact. *Russian Aeronaut.* **60**(2), 292–298 (2017)
60. Fang, L.J., Wang, H.G.: Research on the motion system of the inspection robot for 500 kv power transmission lines. In: 2010 1st International Conference on Applied Robotics for the Power Industry, Carpi 2010, no. 11, pp. 1–4 (2010)
61. Barnett, S.B. et al.: Electromagnetic Interference Mitigation in a High Voltage Inspection Robot, pp. 331–341, 2020. Available at https://doi.org/10.1007/978-3-030-31676-1_32
62. Gaynutdinov, R.R., Chermoshentsev, S.F.: Study of Lightning Strike Impact on Unmanned Aerial Vehicle, pp. 428–432. IEEE, June 2016
63. Permata, D., et al.: Electromagnetic interference shielding in unmanned aerial vehicle against lightning strike. *Telkommika (Telecommun. Comput. Electron. Control)* **17**(2), 915–919 (2018)
64. Feng, J., Zhang, W.: Autonomous live-line maintenance robot for a 10 kV overhead line. *IEEE Access* **9**, 61819–61831 (2021)
65. Tian, F., Wang, Y., Zhu, L.: Power Line Recognition and Tracking Method for UAVs Inspection, pp. 2136–2141. IEEE (2015)
66. Zhou, G. et al.: Robust Real-Time UAV Based Power Line Detection and Tracking, pp. 744–748. IEEE (2016)

67. Montambault, S., Pouliot, N.: About the future of power line robotics. In: 2010 1st International Conference on Applied Robotics for the Power Industry, pp. 1–6, Carpi (2010)
68. Gonçalves, R.S., Carvalho, J.C.M.: A mobile robot to be applied in high-voltage power lines. *J. Br. Soc. Mech. Sci. Eng.* **1**, 1/11 (2014)
69. Haoyang, L.: Application of 5G in electric power inspection UAV. *J. Phys. Conf. Ser.* **1920**(1), 012048 (2021). Available at <https://doi.org/10.1088/1742-6596/1920/1/012048>
70. Zhang, F. et al.: OTL-classifier: towards imaging processing for future unmanned overhead transmission line maintenance. *Electronics (Switzerland)* **8**(11) (2019)
71. Yu, C. et al.: Design of the transmission line inspection system based on UAV. In: 2020 10th International Conference on Power and Energy Systems, ICPES 2020, pp. 543–548 (2020)
72. Silano, G., et al.: Power line inspection tasks with multi-aerial robot systems via signal temporal logic specifications. *IEEE Robot. Autom. Lett.* **6**(2), 4169–4176 (2021)

Chapter 7

Towards Human Activity Recognition Enhanced Robot Assisted Surgery



Hang Su and Elena De Momi

Abstract Medical robotics have drawn increasing research interests in the past years. The potential of employing intelligence techniques is still not yet fully utilized to improve the capabilities of medical devices for assisting human beings during surgical operations. This book chapter presents a novel human activity recognition enhanced robot-assisted surgery to promote human enhancement with AI techniques. Novel-designed multisensory fusion systems can be used to provide more knowledge to boost the recognition rate and robustness. Then the identification results in the complex environment using deep learning can be used to determine the machine behavior using a hierarchical control framework. A detailed explanation is introduced in this chapter.

7.1 Recap of the Development of Medical Robots

During the past few decades, medical robots have experienced rapid development and have been widely applied in various fields, from open surgery to invasive surgery, including rehabilitation training, Orthopaedic Surgery, and Minimally Invasive Surgery. The rapid development of medical robots has benefited from the interdisciplinary integration of robots, biotechnology, and computer technology. Dating back to 1985, a PUMA 200 robot equipped with a CT scanner was introduced for accurate positioning during CT-guided brain tumour biopsy surgery [1]. This application of robotic technology in medical surgery is considered to represent the origin of the development of medical robot applications. Medical robots have demonstrated the unparalleled advantages of traditional surgery procedures in dealing with high-precision, delicate, and complex surgical procedures, and postoperative training. Basically, according to their function and application scenarios, they can be mainly

H. Su · E. De Momi
Building 32.2, Via Giuseppe Colombo, 40 20133 Milano, Italy
e-mail: hang.su@polimi.it

E. De Momi
e-mail: elenade.momi@polimi.it

classified into three types, namely exoskeleton rehabilitation robots, Surgical robots, and Micro- and nanorobots [2]. In this section, the typical medical robot system in the market and research institute are introduced according to the above classification.

(1) Exoskeleton rehabilitation robots: Robot-assisted rehabilitation has recently attracted more and more attention for its advantages in high precision, good repeatability, and various training modes over traditional manual therapy [3]. Exoskeleton rehabilitation robots are usually wearable on the patient's limbs. The robot drives the affected limb by generating joint force or torque. Such exoskeletons are usually rigid structures that can carry out effectively cognitive and physical interaction with patients. The research contents of exoskeleton rehabilitation robots include multi-modal cognitive interaction between human behaviour and robot, safe and reliable physical human-robot interaction, wearability and portability, and user comfort [4]. In the 1960s, the United States began to study human exoskeleton devices [5]. The original intention of this study was for military use, and the main purpose was to enhance the movement load capacity of soldiers in the battlefield. And then, researchers began to explore the value of exoskeletons in the rehabilitation and functional compensation field. Lokomat is a famous rehabilitation exoskeleton representative [6], which is the first robot to carry out comprehensive rehabilitation training for patients with lower-limb paralysis. It can help patients recover from the decline of body function caused by a variety of causes. Sawicki and Ferris developed a knee ankle foot orthosis (KAFO) robot using pneumatic muscle as the driving unit of the exoskeleton robot [7]. Pneumatic muscle has the advantages of a large output force weight ratio and internal flexibility and safety. This robot can provide flexion and extension moments to realize exercise rehabilitation training. Israel's medical technology company has launched Rewalk exoskeleton, which is expected to help paraplegic patients get rid of wheelchairs in their daily life [8]. The Rewalk robot is equipped with a large number of sensors. These sensors can sense the change of the wearer's body posture in real-time and use the corresponding control strategies to assist the wearer in all kinds of movements. At present, it can help patients achieve various actions such as walking, standing, and even climbing stairs. The robot still needs to be used with crutches to keep the balance of paraplegic patients when they walk. Cybernetics Laboratory of the Tsukuba University of Japan has developed a HAL wearable power-assisted robot system [9]. HAL robots are widely used, not only for the disabled but also for the elderly in the decline of function and workers who work hard. There are mainly two control modes used in HAL: control strategy based on EMG signal, a control strategy based on gait pre-learning and gait pattern generation. The combination of biological muscle electrical signal technology and exoskeleton robot control greatly improves the adaptive ability and the wearing comfort of an exoskeleton. It can also assist multiple joints of the whole body and be welcomed by more and more groups.

(2) Surgical Robots: Surgical robots have significant potential in terms of improving accuracy and dexterity, reducing trauma, and shortening the surgery period while compared with conventional surgical procedures. Meanwhile, surgical robots can enhance the capability of clinicians, for example, eliminate the tremor, allow the body to keep flexibility during surgical operations. Besides, since the clinicians and the patient do not need to directly in contact, the cross-infection rate when conducting

surgical operations can be significantly reduced, which is also of great significance in dealing with infectious operations such as SARS and COVID-19 [10]. According to Allied Market Research in 2018, the global market for surgical robots has been valued at USD 56,294.9 million in 2017 and is expected to reach USD 98,737.0 million by 2024. Generally, surgical robots can be divided into four types, namely, laparoscopic robots, neurosurgical robots, orthopaedic robots, and vascular intervention robots.

Laparoscopic surgery is considered a revolutionary surgical method when compared with the traditional open surgery method since it only requires several small incisions in the patient's body, and this is helpful for the patient's surgery. Surgical robots have been introduced to gastrointestinal surgery, hepatobiliary and pancreatic surgery, and urinary system surgery [11]. At present, the Da Vinci series surgical robots (Intuitive Surgical, U.S) are considered the most widely used in commercialized laparoscopic robot systems. Since 1999, the Da Vinci surgical robot has been updated for five generations, and the latest model released is the Xi (2014), which includes three modules: the surgeon console, the robotic arm, and the imaging system [12]. Besides, the FreeHand surgical robot [13] was designed to fix and support the camera during abdominal surgery. Senhance, NeoGuide colonoscopy, etc., robotic platforms are proved by the FDA [13]. Universal robots are also gradually being studied for application in laparoscopic surgery, considering the low cost and strong applicability. For example, the serial redundant KUKA robot LWR4+ is adopted to conduct the surgical operation during robot-assisted minimally invasive surgery procedures [14].

In neurosurgery, the NeuroMate stereotactic robot [15] was utilized to perform functional neurosurgery with an accuracy of 1.29 mm. A neurosurgical robot called Pathfinder was introduced to complete conventional brain surgery stereotactic surgery. The clinicians set the target position and the trajectory. Besides, medical robots also have been introduced to assist clinicians in completing surgical tasks in an orthopaedic surgical operation. For example, Navio [16] is a hand-held knee replacement robot without the need to perform CT scan planning before surgery. The ROBODOC surgical system [15] proposed in 1992 can complete a series of orthopaedic operations. In 1997, the CASPAR surgical system [17] launched by OrtoMaquet (Germany) was used for bone grinding in THA and TKA with an accuracy of 0.1 mm. Compared with laparoscopy and orthopaedic robots, research in the field of vascular intervention robots is relatively backward. Recently, some mature vascular intervention robot systems have emerged. The Sensei X systems [13] and CorPath systems [18] represent the typical vascular interventional robots.

(3) Micro- and nanorobots: The application of robotics in the medical field not only covers the macro level but also extends to the micrometer- and nanometer scale and derives a unique robotic branch micro- and nanorobotics. Micro- and nanorobots are small in size and can be accurately guided and controlled by endogenous or exogenous stimulation. That makes them have broad application prospects in the medical field. For example, under precise guidance and control, micro- and nanorobots can be used as drug carriers for targeted drug delivery [19]. After surface functionalization, micro- and nanorobots even can be used for in vivo interventional diagnosis and treatment [20]. Not only that, but nanorobots also show significant advantages in

assisted minimally invasive surgery [21], which has higher surgical accuracy, meanwhile, reduce surgical complexity. Except for using the typical non-contact physical methods such as light, electricity, and magnetism, the action methods based on chemical reactions and biological motors have also been rapidly developed. Furthermore, micro-and nanorobots can obtain the advantages of multiple action modes to deal with more complex working environments [22]. The control mode of the micro-and nanorobots is closely related to the action method. Although some studies have revealed the possibility of intelligent control [23] and three-dimensional control [24], the current control level of Micro- and nanorobots is still at a relatively low stage. Therefore, the realization of high-precision intelligent three-dimensional motion is still the important research direction of micro- and nanorobots in the future.

Except for the robots mentioned above, some other types of robots, such as model robots and helpmate robots [25], also have been used to varying degrees in the field of medicine and health. With further development and popularization of the medical robots, both medical staff and patients will be able to gain more benefits (Fig. 7.1).

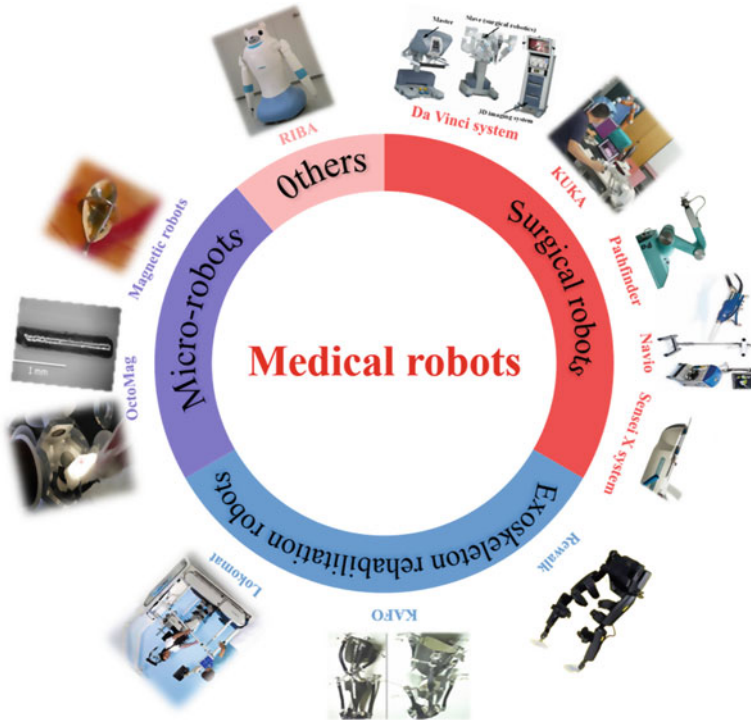


Fig. 7.1 Types of medical robots and typical representatives

7.2 Development and Challenges in Surgical Robots

In particular, surgical robots have drawn various attention, such as robot-assisted minimally invasive surgery (RAMIS). RAMIS was developed to overcome the limitations of existing minimally invasive procedures and improve the surgeon's ability to perform open minimally invasive surgery. The benefits of minimally invasive robotic surgery compared to traditional minimally invasive surgery include smaller cuts, fewer pains, lower risk of infection, faster recovery, less scarring and blood loss. Nowadays, more and more national governments, enterprises and research institutions are engaged in the research and development of RAMIS systems and have also obtained various research results. Among them, the more famous minimally invasive surgical robots include the Da Vinci surgical robot, DLR-MiroSurge, and KUKA surgical robots, which is shown in Fig. 7.2.

Da Vinci surgical robot was designed and manufactured in 1995 by Intuitive Surgical company in the United States and was mainly used for clinical, surgical treatment and diagnosis. In 2000, FDA completed its safety verification and began to promote it [26]. It consists of the surgeon console system, bedside manipulator system and imaging system. Surgeons can use the console to operate patients remotely; the bedside manipulator system can filter out the hand vibration of the chief surgeon with its unique vibration elimination and motion positioning functions; the imaging system is used to provide a high-definition three-dimensional stereoscopic image. Da Vinci surgical robot can magnify three-dimensional vision compared with traditional laparoscopic surgery, which provides surgeons with more clear operation vision and



Fig. 7.2 Surgical robots

more intuitive operation distance. Also, its manipulator has seven degrees of freedom, enabling surgeons to control it and increase the dexterity of operation accurately. It can be seen that Da Vinci surgical robot has a wide application in MIS, including cardiothoracic surgery, gynaecology, urology, and abdominal surgery. Especially for some complex surgeries that require a long time and accurate operation, such as pancreaticoduodenectomy, the high stability and precision of the Da Vinci surgical robot determine its unique role [27].

In 2009, the German Aerospace Center (DLR) designed and developed a minimally invasive surgical robot system called MiroSurge [28]. MiroSurge mainly includes the main console and three MIRO robotic manipulators [29]. The main console integrates a 3D display and two 7-DoFs main hands, which contains force feedback (now upgraded to Sigma.7). Two MIRO manipulators are used to install surgical instruments with a six-dimensional force sensor, and the third manipulator is applied to install an endoscope. Before the operation, the manipulator could automatically position the instrument or endoscope to the planned incision position, and during the operation, the position of the manipulator can be manually adjusted while it is moving without affecting the operation. It is worth mentioning that MiroSurge is also specially designed for heart surgery. That is, the motion of the surgical instrument can be controlled according to the rhythm of the heartbeat to keep the surgical instrument still relative to the heart, thereby reducing the risk of heart surgery.

KUKA has developed various medical robots to meet the requirements of different medical application areas. Among which, due to their high precision and the capability of human-robot collaboration, LWR 4+ and LBR Med has been widely used in minimally invasive surgery [30–35], where the LBR Med is designed specifically for medical applications. In contrast to Da Vinci surgical robot, KUKA lightweight robots are open-chained manipulators. Thanks to its high-performance servo controller, the KUKA LBR Med can achieve precise path following and tool positioning. In RAMIS, one important issue is to maintain the Remote Center of Motion (RCM) constraint [36]. The KUKA LBR has integrated the ability to define and use trocar kinematics to maintain the RCM constraint through hand-guided motion constrained by trocar kinematics. The LBR Med is also equipped with redundant integrated torque sensors, which endows it with strong haptic capabilities, the ability to perceive external influences, and collision detection, making the RAMIS more flexible and safer. More and more research works have been developed with the application of KUKA medical robots, such as surgical skills acquisition [34] and human-like control [31, 33].

Despite these superiorities of surgical robotics, their application in the operating room is still hindered by several drawbacks:

- The first challenge of the high cost of surgical robots, the high purchase and maintenance cost of surgical robots leads to the higher price of robotic surgery compared with traditional surgery, which is unaffordable for many patients.
- The complexity of surgical robots may bring longer operating room setup time and would disturb the surgical plan. Furthermore, a significant challenge can be

posed by complex surgical robots for surgeons; that is, it may take lots of training for surgeons to learn how to use the surgical instruments.

- Another challenge in minimally invasive surgery is that the current position of the surgical tool within the tissue should be known by the surgeon, and it is still a difficult problem due to the complex environment with the human body and the required high positioning performance. Therefore, multiple sensors should be fused to improve the positioning performance of the surgical tool.

7.3 Theoretical Potentials for Surgical Robot Development

It should be mentioned that the theory for robot control and advanced sensing has achieved a huge process.

7.3.1 *Advancement of Control Technology in Surgical Robots*

In RAMIS, the necessary surgical tool and camera need to pass through a small abdominal incision to execute the surgical operation. To protect the patient from external, injure caused by the surgical tool, all the surgical tools and the cameras must be limited inside the wound. Therefore, the small incision will bring a kinematic constraint at the far point called the remote centre of motion (RCM). Satisfying the RCM constraint without affecting operation accuracy is a challenge. In addition, the RAMIS system should be safe and accurate in human-robot interaction. Therefore, in RAMIS systems utilizing serial robotic redundancy, there are three main control goals that can be defined at three levels based on priority: surgical operation, RCM constraints, and ensuring interaction with the user and environment [37]. Many novel control schemes and methods have been implemented to achieve these three levels of goals.

Hierarchical control framework

Hierarchical control is an efficient strategy to manage the above three levels of control objectives in a prioritized sequence. The corresponding control diagram is shown in Fig. 7.3, in which the tasks were divided into three priority levels: surgical operation, RCM constraint and interaction behaviour. By introducing hierarchical operational space, the 7-DoF serial robot can achieve whole-body impedance control. That provides an effective method to avoid force overshoot and rigid interaction in the robot operation. In addition, the RCM constraint also can be achieved by taking appropriate constraint rules in the null space of the Jacobian matrix. Meanwhile, applying the RCM constraint and safe constraint in null-space can guarantee the robot's compliant behaviour in the interactive progress and enhance surgical safety [32, 33]. Furthermore, we can introduce other control modules such as disturbance

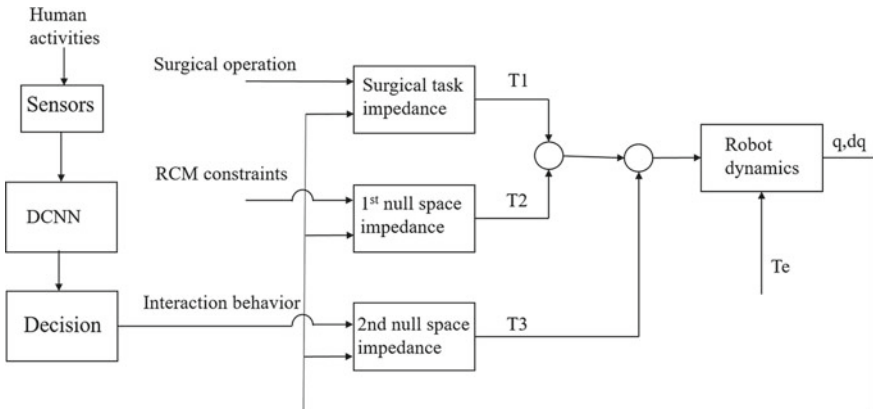


Fig. 7.3 The proposed hierarchical control framework

observers to compensate for the disturbance while maintaining the RCM constraint and improving surgical accuracy.

The human activity recognition system

It is important to recognize the operator's intentions and act appropriately. In the past decade, the rapid development of artificial intelligence (AI) [38] technology offers an efficient way to build HAR classifiers based on machine learning (ML) [39] and deep learning (DL) (Huang et al.) algorithms. As shown in Fig. 7.3, multiple sensors can perceive human activities, and then the deep convolutional neural networks (DCNN) [40] model be used to identify the human's activity for further operation decisions [30]. The Recurrent Neural Network (RNN) [41] is another sensitive method to time-varying sequences. Long-Short Term Memory (LSTM) neural networks are applied in human-robot collaboration to predict and classify cooperative trajectory based on a serial of pre-set objectives in the workspace and model-based generated data of human motion, as shown in Fig. 7.4. After Combining multiple sensors, this technology can generate a new research direction; human activity recognition enhanced robot-assisted minimally invasive surgery (HAR-RAMIS), and we will discuss it in Sect. 7.5.

Passivity control implementation

Transparency of the robotic MIS system is important for enhancing the compliant human-robot interaction. Haptic feedback is the most promising method to improve the transparency of the surgical robotic system, especially for bilateral teleoperation. With haptic guidance, the system can exert forces on the user's interface, then influencing the input signal through force interactions with the operator [42]. Therefore, the system should be safe and accurate according to surgical task requirements. However, the system should also be robust during the interaction with the variable environment, such as non-rigid contacts in insertion surgery, which has been one of

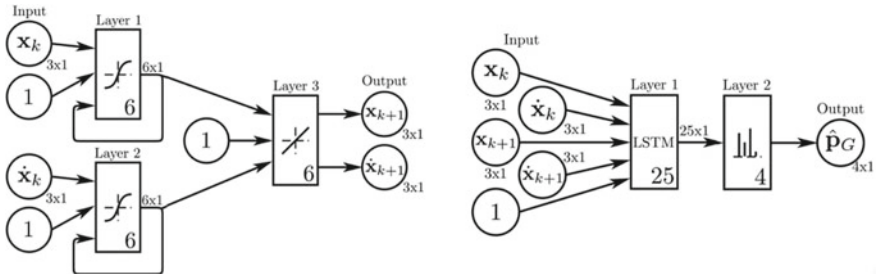


Fig. 7.4 RNNs and LSTM for human activity recognition

the main challenges faced by researchers. Admittance control is one of the possible solutions [43]. As shown in Fig. 7.5, A passive bilateral teleoperated controller for redundant surgical robotic systems satisfying RCM constraints is discussed [24]. The controller is composed of two modules: One is a bilateral teleoperation controller based on a two-layered approach; The other method is taking decoupled Cartesian Admittance Control to meet the RCM kinematic constraints.

Shared control-further development

Surgical tasks which contain significant dynamics variation, interaction with operators and environment, model uncertainties and time delay all have an adverse effect on the performance of the system. To solve these problems, the monitoring concept was introduced. Supervisory control will allow high-level autonomy to the robot system. However, the supervisory control obviously cannot be used for complex and variable surgical tasks [44]. Most of the existing commercial surgical robot

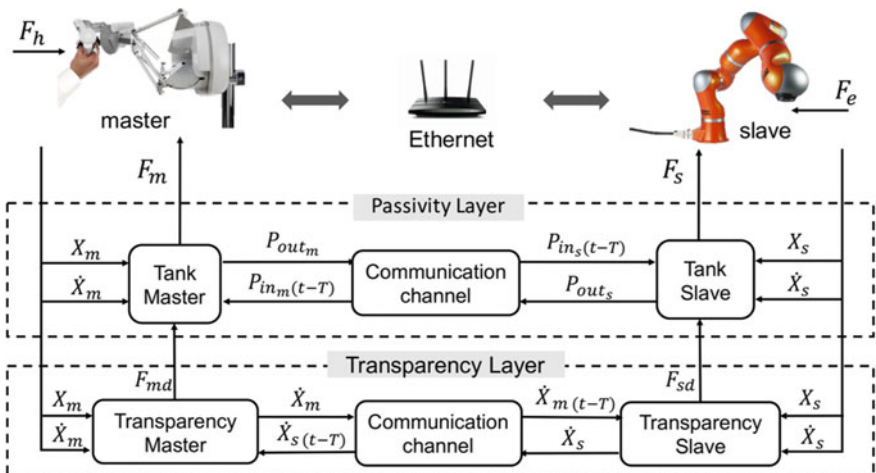


Fig. 7.5 The bilateral teleoperation framework with a passivity control module (“tank master” and “tank slave” are the energy tank)

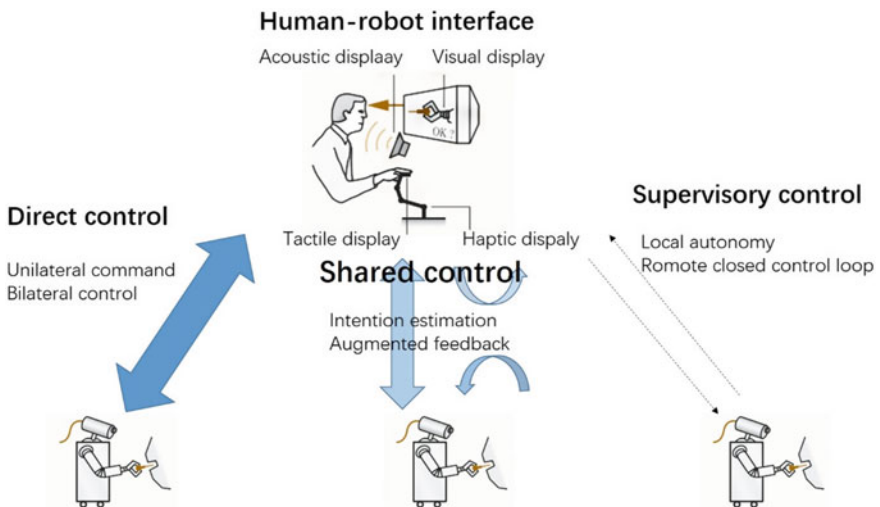


Fig. 7.6 Different concepts for telerobotic control architectures

systems use direct control. The remote robots strictly execute the received operator's even wrong or inaccurate orders [45]. Therefore, in the face of complex and high precision surgical tasks, direct control requires a high level of operator's operation, fatigue resistance, system stability and low time delay. Autonomous task execution and cognitive decision-making capabilities are the trends for remote robots. The NearLab of Politecnico di Milano introduced shared control into surgical robot systems to improve human-robot interaction and achieved high operation accuracy. The shared control allows the remote robot to estimate humans' intention and modify wrong or inaccurate orders (Fig. 7.6).

7.3.2 Advancement of Sensor Technology in Surgical Robots

Except for mechanical design and control systems, sensing and estimation are fundamental phases of the application of any robots. For example, dozens of sensors are required for a surgical robot to function and respond to its environment: force and tactile sensors for contact sensing [46, 47] inertial sensors for estimating moving parts [37], and visual sensors for image feedback [48], sEMG sensors [35], and ultrasonic sensors [49], etc. Among these, force and tactile sensing, inertial sensing, and image-based visual sensing are most important. In some complex surgical scenarios, multiple sensors are often used to obtain the feedback information of the surgical operations. Thus, sensor fusion technology could be applied to integrate information from various heterogeneous sensors, as shown in Fig. 7.7.

(1) Sensors

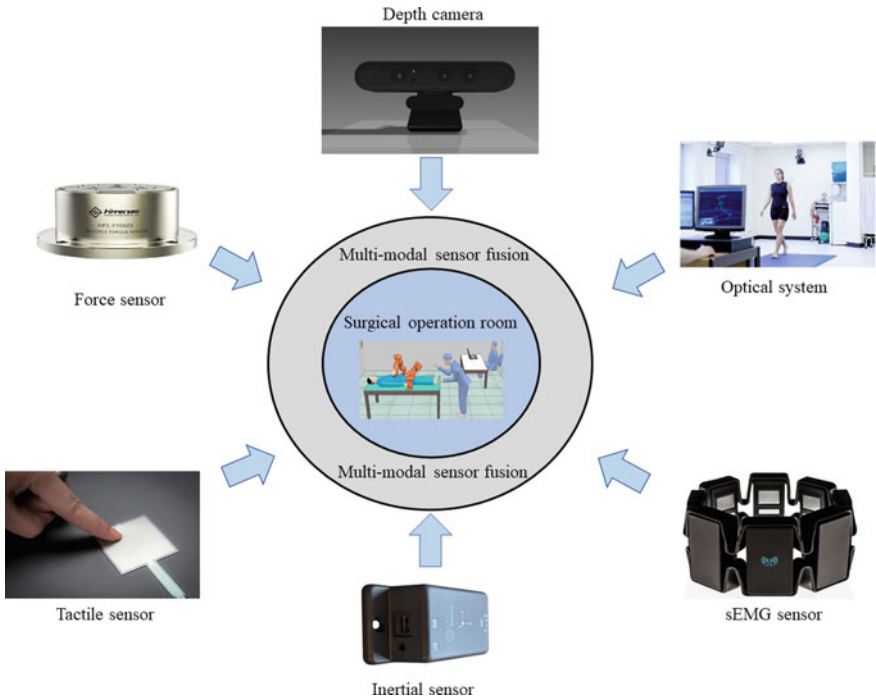


Fig. 7.7 Typical sensors used in robot-assisted surgical operations and multi-modal sensor information can be fused together to support surgical operation

In traditional surgery, the surgeon often uses the hand to estimate the force that should be applied in order not to injure the patient (Fig. 7.8). Nowadays, the haptic feedback integrates the sense of both tactile and force [46], which makes it possible to allow sawbones to feel the patients' tissues from a completely separate place. In the da Vinci Surgical System (Intuitive Surgical Inc., USA), although force feedback is used to compensate for the absence of haptic sensors, the use of haptic sensors can enhance the assessment of pathological conditions and tissue characteristics. Similarly, force sensors typically mounted on the end of a robot can be used to detect collisions of rigid targets. However, they cannot prevent soft tissue injuries or suture tears. After combining force and haptic perception, the above limitations could be addressed with a haptic feedback system. Haptic sensing has become an important research area with the advancement of teleoperated minimally invasive surgery since it could enhance a surgeon's sense of telepresence, which could expectedly lead to upgraded performance (Fig. 7.9).

In minimally invasive surgery, inertial sensors can be applied to two aspects, firstly, they can be used to estimate the pose of surgical instruments [50, 51], and secondly, they can be utilized to estimate human operators' motion [52, 53]. Recent progress in MEMS inertial sensors make the sensors miniature enough to be installed into surgical instruments, and thus, the sensors can be a promising replacement to



Fig. 7.8 Haptic device, force feedback dimension and 6-D force sensor

Fig. 7.9 Inertial sensor



optical systems since optical systems are limited by the line-of-sight constraint. Different from optical sensors, inertial sensors can achieve precise pose estimation without the limitation of line-of-sight. In addition to the estimation of surgical instruments, inertial sensors-based human activity recognition (HAR) is a widely used technology that helps robots understand what people are doing by extracting features from human action data. It is an important part of the effective interaction between humans and robots. It is a method that enables the robot to make reliable decisions by understanding human semantics (Fig. 7.10).

Image-based visual sensing could provide a wealth of information for humans, and eyes obtain nearly 80–90% of the information in our daily life. Therefore, vision is also very important for surgical robots, and visual sensors play a vital role in robot-assisted surgery. Firstly, in surgical operations, the visual feedback to the surgeon is commonly provided by endoscopic imaging [54]. In robot-assisted suturing, image-based visual sensing can also be applied since it provides a clear sight of the tissue, either by supporting the alignment of the surgical tool with the position of the incision or by controlling the laparoscopic tools, e.g., in tying a knot [55, 56]. Besides, direct camera vision, e.g., stereo cameras and depth cameras, can also be used for visual sensing in medical robotic applications.

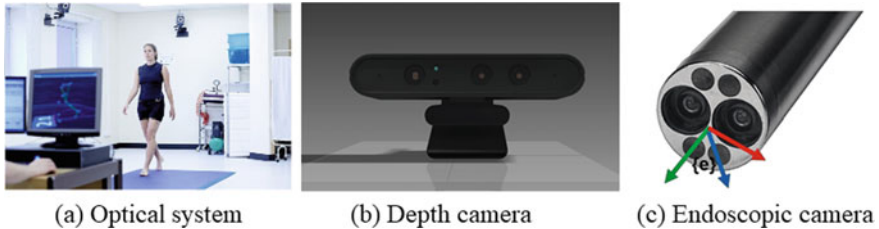


Fig. 7.10 Common-used visual sensors in surgical operations

(2) Sensor fusion methods

As mentioned above, single kind of sensor sometimes is insufficient in complex surgical operations. Therefore, multiple sensors are often fused to obtain the feedback information of the surgical operations. Figure 7.11 shows the information interaction between surgical robot and patient. The feedback information includes two parts; one is the response information to the robot action, and the other is the environment information. For example, visual sensors and inertial sensors are combined for robust estimation of the pose of a freely moving target in surgical operations [37], electromagnetic and inertial sensors are fused to estimate the position and orientation of the surgical instrument [51]. In this subsection, the main sensor fusion methods are reviewed, such as Kalman filters [57] and optimization-based fusion methods [58], etc.

Kalman filters

Given the observation of the state, The Kalman filter is a recursive linear estimator that sequentially determines an estimate of the state of the system. Given the following discrete-time statistical model about the state x_k and the observation z_k :

$$\begin{aligned} x_k &= F_{k-1}x_{k-1} + G_{k-1}v_k \\ z_k &= H_{k-1}x_k + D_{k-1}w_k \end{aligned} \quad (7.1)$$



Fig. 7.11 Information interaction between surgical robot and human

Random series represent process noise and observation noise which are both Gaussian, time uncorrelated, and zero mean. Then, the classical Kalman filter proceeds recursively as follows

$$\begin{aligned}\hat{x}_{k|k-1} &= F_{k-1}\hat{x}_{k-1|k-1} \\ P_{k|k-1} &= F_{k-1}P_{k-1|k-1}F_{k-1}^T + G_{k-1}Q_{k-1}G_{k-1}^T \\ K_k &= P_{k|k-1}H_k^T(N_{k|k-1})^{-1} \\ \hat{x}_{k|k} &= \hat{x}_{k|k-1} + K_k e_{k|k-1} \\ P_{k|k} &= (I - K_k H_k)P_{k|k-1}\end{aligned}\tag{7.2}$$

where $e_{k|k-1} = z_k - H_k \hat{x}_{k|k-1}$ is the innovation and its covariance matrix is given by $N_{k|k-1} = H_k P_{k|k-1} H_k^T + R_k$. It is noted that when the state mode and/or the observation are nonlinear, the extended Kalman filter (EKF) [50] or unscented Kalman filter (UKF) [37] can be applied.

Optimization-based fusion methods

For optimization-based sensor fusion methods [59], the following optimization model can be established:

$$\begin{aligned}\min \theta \\ s.t. \sum_k |z_k - \hat{z}_k| = \sum_{k \in N} |z_k - f(\theta_k)|\end{aligned}\tag{7.3}$$

where z_k is the observation obtained by various sensors, θ is the objective state that we should estimate, $f(\theta_k)$ is a linear or nonlinear function, minimizing the above loss function leads to the optimal estimation of the state θ . For the above optimization problem, traditional optimization methods, such as the Gradient descent method, interior-point method, quadratic programming method, could be used every timestep to obtain the optimal estimation. In addition, if the approximation function is chosen as $f(\theta) = \omega^T \phi(\theta) + \varepsilon(\theta)$, $\forall \theta \in R^l$, $\varepsilon(\theta) \in R$ and $\phi(\theta)$ denote the weights vector, estimation error, and basis function. By defining the approximation function like this, various advanced approaches could be used to solve this problem, e.g., fuzzy approximation [36], RBFNN [60], and deep learning [53].

7.3.2.1 Theory of Machine Learning in Surgical Robots

Machine learning (ML) is a subject that contains statistics, probability theory, approximation theory and various complex algorithms, and its purpose is to learn relevant models from various kinds of empirical data and complete the specified requirements. There are many ML algorithms, including support vector machine, neural network, decision tree, Bayesian classifier, etc. Among them, support vector machine (SVM) is one of the most typical algorithms, and it is also the most common algorithm in the field of robot learning. It is a classifier with the largest interval defined in the feature

space, which is essentially a binary classification model. Through the idea of interval maximization, various sample data are divided to solve the optimization problem of convex quadratic programming. According to whether the training samples are linear and separable, SVM can be divided into linear separable SVM and nonlinear SVM, which fully demonstrates its universal adaptability. The general expression of SVM is as follows:

$$\begin{cases} \min_{w,b,\xi_i} \frac{1}{2} w^2 + C \sum_{i=1}^m \xi_i \\ s.t. y_i (w^T \phi(x_i) + b) \geq 1 - \xi_i \\ \xi_i \geq 0, i = 1, 2, \dots, m \end{cases} \quad (7.4)$$

where w, b is the model parameter of SVM, C is the scale factor, ξ_i is the soft interval distance, and $\phi(x)$ is the kernel function used to map samples in high dimensions, such as polynomial kernel function, Gaussian kernel function and string kernel function.

In the field of medicine, SVM is applied in surgical robots to relieve the pressure of surgeons and improve surgical accuracy. For instance, hand physiological tremor is a common phenomenon for surgeons, which will cause potential risks for surgery. To solve this problem, [61] presents a novel SVM method to track hand tremor. It utilizes the method of small-scale sampling signal and high-dimensional feature mapping to filter the external interference signal, and the hybrid kernel is applied to improve the generalization ability of the model. Furthermore, when the surgical robot completes the operation, the analysis of the surgical video is essential. Volkov et al. [62] presents an automated real-time laparoscopic video segment system with minimal computing resources. SVM and Hidden Markov Model are utilized to capture video stream variability with an augmented feature space. It can be well integrated into the surgical robot system and enhance the autonomy and adaptability of the robot.

Considering that reinforcement learning (RL) [63] has excellent performance for uncertain factors, such as Google's Alphago, Google's robotic manipulator, some scholars also propose to apply the RL technology to the RAMIS. RL aims to establish the mapping relationship between environment state space and action set. It does not rely on the environment model and prior knowledge and has autonomous learning and online learning characteristics. Therefore, it has gradually become the research hotspot of surgical robot in a complex environment. The application principle of reinforcement learning in surgical robots is as follows.

According to whether the state transition probability is known, RL can be divided into model-based and model-unknown algorithms. The model-based RL algorithm can use the learned learning experience to construct the environment model and find out the optimal strategy through learning value function, including Dynamic programming, Dyna-Q algorithm, etc. The model-unknown method directly learns the value function through the continuous interaction between the robot and the environment and obtains the corresponding strategies. The typical algorithms include Q-learning, Sarsa, and Monte Carlo. Table 7.1 shows the general flow chart of the

Table 7.1 General flow chart of Q-learning algorithm

Input: Environment E; Action Space A; Initial State x_0 ;
Reward Discount ρ ; Update Step α .

Process:

1. $Q(x,a)=0, \pi(x,a)=\frac{1}{|A(x)|};$
2. $x=x_0;$
3. **for** $t=1,2,\dots$ **do**
4. r, \bar{x} represent the generated reward and transferring state produced by action $a=\pi(x)$ in the environment;
5. $\bar{a} = \pi(\bar{x});$
6. $Q(x, a) = Q(x, a) + \alpha(r + \rho Q(\bar{x}, \bar{a}) - Q(x, a));$
7. $\pi(x) = \text{argmax}_a Q(x, a);$
8. $x = \bar{x};$
9. **end for**

Output: strategy π

Q-learning algorithm, and the flow of other typical algorithms is similar to it. The direct strategy search method does not need to consider the value function but directly parameterizes the strategy and finds an optimal decision. It studies the way of animal thinking, thus enhancing the intelligence of the system.

Compared with supervised learning, RL pays more attention to the long-term benefits, which makes it more suitable for solving the global optimal solution problem. It has also been proposed to control surgical robots in order to complete various minimally invasive surgeries. Su et al. [34] designs an approach of motor skill transferring based on improved RL optimization to help robot carry out various minimally invasive surgeries. After multiple operation demonstrations by surgeons, the KUKA LWR4+ robot can generate motion trajectories autonomously and respect the remote center of motion (RCM) constraints of abdominal wall, even if the RCM is unknown, which shows that RL can enhance the autonomy and adaptive ability of surgical robot and improve the safety of surgery.

In 2016, NVIDIA released a new Pascal architecture based on in-depth optimization of Artificial Intelligence (AI), and the entire Tesla series of graphics cards as well as embedded chip NVIDIA Jetson TX1, providing massive computing power for the field of AI. At the same time, Google released open source TensorFlow code to visualize the training system of DL, which greatly promotes the progress of AI. Since then, the field of deep learning (DL) has gradually become mainstream. At present, the convolutional neural network is the most popular image processing algorithm. It can directly take the image data as the input, without pre-processing and extra feature extraction, and realize end-to-end learning. It mainly consists of the convolutional layer, pooling layer, and full connection layer. The convolution layer can greatly reduce the network parameters; the pooling layer can further reduce the model capacity and enhance the robustness of features; the full connection layer at the end of the network is responsible for connecting all deep features. Figure 7.12 shows

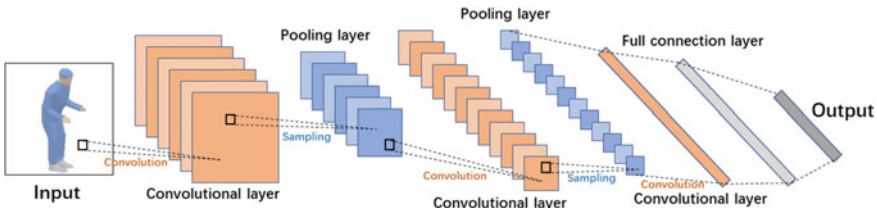


Fig. 7.12 The general structure of convolutional neural network

the general flow of a convolution neural network in processing image data. It can be applied to image and video processing related to minimally invasive surgery, such as human activity recognition, in order to enhance the interaction between surgeons and surgical robots.

The algorithm structure of ML is relatively simple and occupies fewer computer resources, so it is more suitable for feature analysis and classification of some small data sets. Due to the expansion of data, the improvement of algorithms and the enhancement of computing power, the advancement of DL is also rapid. Especially, convolution neural network, recurrent neural network, and other characteristic deep network architecture, further exert their unique advantages and potential [64, 65].

7.4 Current Limitations of RAMIS

Although RAMIS has significant superiorities compared with conventional surgical procedures, including improving accuracy, minimizing trauma, and shortening post-operative recovery time, however, the high cost of specially customized surgical robots and the lack of intelligence of surgical robot systems are the two main critical limitations that need to be solved urgently.

Firstly, the high price of surgical robots is considered the key factor restricting large-scale promotion. Currently, most surgical robots are customized for specific surgical scenarios, such as orthopaedic robots, neurosurgery robots, etc., which determines their poor versatility. The specialized custom-developed surgical robots are usually expensive, limiting their acquisitions among hospitals. Recently, industrial robots with redundant manipulators (KUKA robot) have meanwhile been successfully adopted and further developed for several decades in precise automation processes [31, 32, 36]. Their characteristic of low cost has generated people's interest in using them in medical applications, especially in RAMIS.

Furthermore, the lack of intelligence of current robotic systems is another issue that limits its development. And, it has raised great attention from both academia and the industrial area [66]. During surgical operations, the surgical robot is required to collaborate with the clinicians to complete surgical tasks, such as cutting, sewing, and knotting, etc. To enhance safety and reduce the workloads of clinicians, the control framework should be well designed to provide the robotic surgical systems

with the capacity of knowledge of human activity recognition in the operating room. Except for recently published scientific works [47, 67], the European Commission has also financed related research projects such as the recent ARS (Autonomous Robotic Surgery) under the H2020 ERC “Excellence Science” program. The ARS project aims to establish a framework for the autonomous execution of robotic tasks by analysing robotic surgery data to extract the action and knowledge models of a specific intervention (heart surgery).

7.5 Human Activity Recognition Enhanced Robot-Assisted Minimally Invasive Surgery (HAR-RAMIS)

The proposed HAR-RAMIS in Fig. 7.13 aims to develop a novel framework to provide robotic surgical systems with the knowledge of human activity recognition. In this framework, the multimodal sensor fusion systems are used to acquire and pre-process human activity data. Then the classifier based on the deep learning technology is introduced to understand human behaviour and intentions by analysing the sensors’ data. Finally, according to the task and human activity recognized by the classifier, the robot control strategies will be switched automatically.

HAR-RAMIS will use AI methods and numerous sensor fusion to assess and interpret the surgeons’ activity in the operating room. This paper collects the multimodal qualitative-quantitative information (including the surgeon and surgical environment) from different sensors (e.g., motion, force, IMU, IoTs, and depth vision)

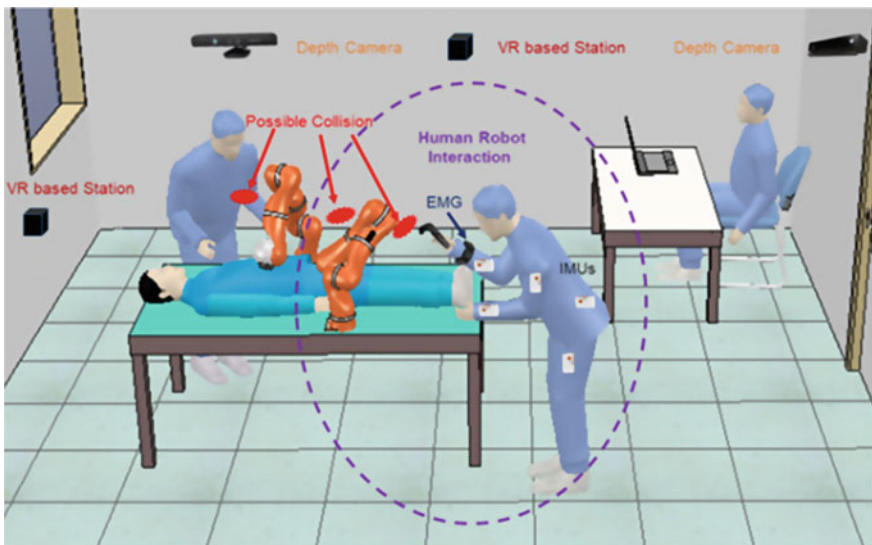


Fig. 7.13 The scenario of human activity recognition based on multi-sensor fusion

and analyse it with the AI techniques in order to understand human activities and to provide intelligent assistance to the robotic system. It would enable the robotic surgical system to provide real-time semi/fully autonomous assistance to the surgeons and more user-friendly robot arm behaviour.

To this end, research efforts through this paper will focus on the development of a novel cognitive framework where its **main objectives** include:

- Multimodal signal measurement/pre-processing system for human activity acquisition
- Deep learning enabled human activity recognition
- Event-driven hierarchical control of KUKA IIWA robot for RAMIS.

Compared with complicated measurement procedures, multi-modal information from multiple sensor systems can be integrated for Human Activity Recognition (HAR) during specific application cases, using the Kinect camera, the Inertial Measurement Unit (IMU), and deep learning algorithms. To enhance the accuracy and safety performance during surgical operations, multiple information, including position, vision, and velocity data are collected and processed. To further improve robot performance during RAMIS operations and enhance the autonomy of robotics, the activities recognition of surgeons during RAMIS are critical to be measured and understood. To handle the collision issue and avoid causing damage to the organs and tissues of the patient, EMG sensors and depth vision cameras are adopted to obtain the data for DNN model training. Besides, the intention and force of the surgeons can be predicted and regulated during surgical operations using the data collected from multi-sensor systems.

The details of data processing and modelling are described in Fig. 7.14. Experimenters demonstrate various scenarios during surgery and record scene data using a multisensory system. To deal with the multimodal data and extract features from the collected information, several classical signal processing methods can be utilized, such as the Kalman filter, the wavelet denoising, and the Particle filter. The collected raw data and original signals can be processed and then can be provided to the surgeons and robot. In addition, to improve the accuracy, depth vision information can be calibrated to obtain the movement and velocity of the surgeons. Furthermore, to smooth the data and enhance the stability, the sliding window method is adopted for the segmentation of the collected data into several phases. And DL method is demonstrated to have great potential for enhancing the robustness of data regression and classification. Then, as shown in Fig. 7.15, the recognition and classification of surgeons' activities can be achieved using the DL-based approach after the labelling step is completed. To deal with the various requirements in different medical applications, detailed control strategies should be developed. The specific types of scenes can be identified by the multimodal data, and then the predefined control algorithm using the hierarchical control strategy can be executed. For example, the DL-based classification method is adopted to identify the activities using both depth vision and IMU data, including the position, velocity, and acceleration. In the corresponding scenario, the operator carries more sensors mounted in different parts, which aim

to provide more information for identifying the complicated surgical operations, activities and even predict the intention of the surgeon.

The main contributions of the proposed multisensory fusion powered HAR using DL algorithm for RAMIS can be summarized as follows:

- Novel designed multisensory fusion system provides more information for HAR to enhance the recognition rate.
- A DL-based technique will be implemented to identify human activities in the complex environment.

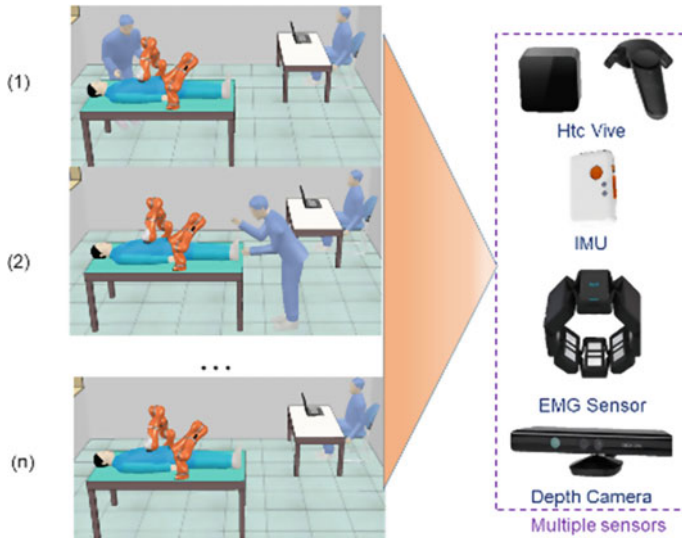


Fig. 7.14 Human activity recognition using multiple sensors

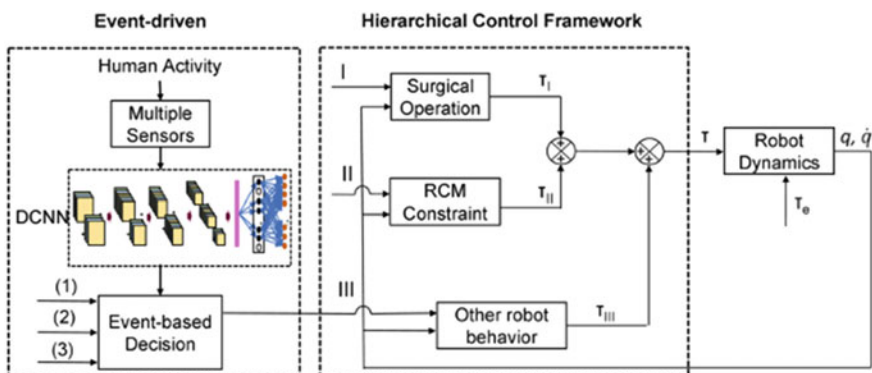


Fig. 7.15 The proposed event-driven control framework for HAR-RAMIS

- Event-driven hierarchical control of KUKA IIWA robot for RAMIS based on the human activities.

In addition to the perception and rearrangement of priority tasks, the smoothness and stability of task switching also are essential to guarantee surgical safety. A continuous adaptive control method was proposed to realize this goal, as shown in Fig. 7.15. There are two major modules in the continuous adaptive control method called the event-driven model and hierarchical control architecture. The DCNN based event-driven model is used to identify human activity for further event-based decision-making. While the hierarchical control module is responsible for using redundant degrees of freedom to achieve different control objectives such as human-like behaviour, manipulability optimization and compliance with security enhancement policies. In RAMIS, control goals can be defined in three levels according to priority, as follow:

Surgical Operation: The priority task in the RAMIS is the surgical operation, which is vital for the success of the surgery.

RCM Constraint: During surgery, the surgical tool should be confined within the surgical incision, which creates a kinematic constraint known as the remote centre of motion (RCM).

Other robot behaviours: Use the redundancy of the robot arm to achieve additional tasks. For example:

- I Human-like behaviour to improve the performance of human-robot cooperation and improve the interactive experience.
- II A compliant enhanced null-space behaviour is utilized to enhance the safety of the surgical operation.
- III A novel manipulability optimization control approach has been proposed to maximize the robot manipulability with its redundancy of a redundant serial robot for real-time RAMIS.

Hierarchical operational control is an efficient strategy to manage the above three different levels of manipulation tasks in a prioritized sequence, as shown in Fig. 7.15.

7.6 Conclusions

This chapter introduced the common robots in the medical field and discussed the critical technical challenges and current research advances in surgical robotics. The hotspots of the surgical robot can be summarised into the following three themes.

Multimodal signal measurement/pre-processing system for human activity acquisition: In particular, a multiple depth vision system can detect human activities even in the operating room by utilizing signal processing techniques, like Kalman filters. Different from the existing solutions, the multimodal signal provides more information and characterization of the surgeons' motion, which can improve the recognition quality and accuracy.

Improving recognition quantity and accuracy with a multisensory fusion-powered HAR framework using deep learning: In the literature, although both ML and DL methods have been adopted to train several models for HAR, they are limited by the single-modal information, which is not applicable in a complex environment. In this solution, the generality and robustness of DL enabled HAR is strengthen. The novel implemented DL approaches can automatically extract features from the processed data automatically, e.g., recurrent neural network (RNN), by integrating a specific layer that can remove noises from the raw signal, such as a rectified linear unit (ReLU) and convolutional neural network (CNN).

Event-driven hierarchical control of KUKA IIWA robot for RAMIS: Different robot behaviours will be defined according to the operating room's surgeons' activities. Different from the pre-programmed solution in the existing works, our solution can automatically switch the robot behaviour based on the human activities in the operating room so that the future robot systems will be able to work with humans in complex and unstructured environments.

References

1. Kwok, Y.S., Hou, J., Jonckheere, E.A., Hayati, S.: A robot with improved absolute positioning accuracy for CT guided stereotactic brain surgery. *IEEE Trans. Biomed. Eng.* **35**(2), 153–160 (1988)
2. Buettner, R., Alena, R., Boos, A.: A systematic literature review of research in the surgical field of medical robotics. In: IEEE 44th Annual Computers, Software, and Applications Conference (COMPSAC), Madrid, Spain, pp. 517–522 (2020)
3. Ren, Y., Wu, Y.N., Yang, C.Y., Xu, T., Harvey, R.L., Zhang, L.Q.: Developing a wearable ankle rehabilitation robotic device for in-bed acute stroke rehabilitation. *IEEE Trans. Neural Syst. Rehabil. Eng.* **25**(6), 178–185 (2017)
4. Okamura, M., Mataric, M.J., Christensen, H.I.: Medical and health-care robotics. *IEEE Robot. Autom. Mag.* **17**(2), 26–37 (2010)
5. Bosecker, C.J., Krebs, H.I.: “MIT-Skywalker”. In: IEEE International Conference on Rehabilitation Robotics, pp. 542–549 (2009)
6. Jezernik, S., Colombo, G., Keller, T., et al.: Robotic orthosis lokomat: a rehabilitation and research tool. *Neuromodul. Technol. Neural Interf.* **6**(2), 108 (2003)
7. Sawicki, G., Ferris, D.: A pneumatically powered knee-ankle-foot orthosis (KAFO) with myoelectric activation and inhibition. *J. Neuroeng. Rehabil.* **6**(1), 23 (2009)
8. Esquenazi, A., Talaty, M., Packel, A., et al.: The ReWalk powered exoskeleton to restore ambulatory function to individuals with thoracic-level motor-complete spinal cord injury. *Am. J. Phys. Med. Rehabil.* **91**(11), 911–920 (2012)
9. Sankai, Y.: HAL: hybrid assistive limb based on cybernics. *Robot. Res.* 25–34 (2010)
10. Khan, Z.H., Afifa, S., Chang, W.L.: Robotics utilization for healthcare digitization in global COVID-19 management. *Int. J. Environ. Res. Publ. Health* **17**(11), 1–23 (2020)
11. Omisore, O.M., Han, S., Xiong, J., Li, H., Li, Z., Wang, L.: A review on flexible robotic systems for minimally invasive surgery. *IEEE Trans Syst Man Cybernet Syst.* <https://doi.org/10.1109/TSMC.2020.3026174> (2020)
12. Wilson, T.G.: Advancement of technology and its impact on urologists: release of the da Vinci xi, a new surgical robot. *Eur. Urol.* **66**(5), 793–794 (2014)
13. Peters, B.S., Armijo, P.R., Krause, C., Choudhury, S.A., Oleynikov, D.: Review of emerging surgical robotic technology. *Surg. Endosc.* **32**, 1636–1655 (2018)

14. Su, H., Enayati, N., Vantadori, L., Spinoglio, A., Ferrigno, G., De Momi, E.: Online human-like redundancy optimization for tele-operated anthropomorphic manipulators. *Int. J. Adv. Rob. Syst.* **15**(6), 1729881418814695 (2019)
15. Zhou, J., Ma, X., Xu, Z., Qi, Z.: Overview of medical robot technology development. In: 37th Chinese Control Conference (CCC), Wuhan, China, pp. 5169–5174 (2018)
16. Smith, J.R., Riches, P.E., Rowe, P.J.: Accuracy of a freehand sculpting tool for unicondylar knee replacement. *Int. J. Med. Robot. Comp. Assisted Surg.* **10**(2), 162–169 (2014)
17. Meister, D., Pokrandt, P., Both, A.: Milling accuracy in robot-assisted orthopaedic surgery. In: Proceedings of the 24th Annual Conference of the IEEE Industrial Electronics Society, vol. 4, pp. 2502–2505 (2018)
18. Weisz, G., Metzger, D.C., Caputo, R.P., Delgado, J.A., Marshall, J.J., Vetrovec, G.W., Reisman, M., Waksman, R., Granada, J.F., Novack, V., Moses, J.W., Carrozza, J.P.: Safety and feasibility of robotic percutaneous coronary intervention: PRECISE (percutaneous robotically enhanced coronary intervention) study. *J. Am. Coll. Cardiol.* **61**(15), 1596–1600 (2013)
19. Singh, A.V., Ansari, M.H.D., Laux, P., Luch, A.: Micro-nanorobots: important considerations when developing novel drug delivery platforms. *Expert Opin. Drug Deliv.* **16**(11), 1259–1275 (2019)
20. Chatupniak, A., Morales-Narváez, E., Merkoçi, A.: Micro and nanomotors in diagnostics. *Adv. Drug Deliv. Rev.* **95**, 104–116 (2015)
21. Ullrich, F., Bergeles, C., Pokki, J., Ergeneman, O., Erni, S., Chatzipirpiridis, G., Pané, S., Framme, C., Nelson, B.J.: Mobility experiments with microrobots for minimally invasive intraocular surgery. *Invest. Ophthalmol. Vis. Sci.* **54**(4), 2853–2863 (2013)
22. Yang, J., Zhang, C., Wang, X., Wang, W., Xi, N., Liu, L.: Development of micro-and nanorobotics: a review. *Sci. China Technol. Sci.* **62**(1), 1–20 (2019)
23. Medina-Sánchez, M., Xu, H., Schmidt, O.G.: Micro-and nano-motors: the new generation of drug carriers. *Ther. Deliv.* **9**(4), 303–316 (2018)
24. Su, H., Schmirander, Y., Li, Z., Zhou, X., Ferrigno, G., De Momi, E.: Bilateral teleoperation control of a redundant manipulator with an RCM kinematic constraint. In: 2020 IEEE International Conference on Robotics and Automation (ICRA) (2020)
25. Mukai, T., Hirano, S., Nakashima, H., Kato, Y., Sakaida, Y., Guo, S., Hosoe, S.: Development of a nursing-care assistant robot RIBA that can lift a human in its arms. *IEEE/RSJ Int. Conf. Intell. Robots Syst.* 5996–6001 (2010)
26. Gomes, P.: Surgical robotics: reviewing the past, analyzing the present, imagining the future. *Robot. Comp. Integrat. Manuf.* **27**(2), 261–266 (2011)
27. Allan, M., Ourselin, S., Hawkes, D.J., Kelly, J.D., Stoyanov, D.V.: 3-D pose estimation of articulated instruments in robotic minimally invasive surgery. *IEEE Trans. Med. Imaging* **37**(5), 1204–1213 (2018)
28. Hagn, U., Konietzschke, R., Tobergte, A., Nickl, M., Jörg, S., Kübler, B., Passig, G., Gröger, M., Fröhlich, F., Seibold, U., Le-Tien, L., Albu-Schäffer, A., Nothelfer, A., Hacker, F., Grebenstein, M., Hirzinger, G.: DLR MiroSurge: a versatile system for research in endoscopic telesurgery. *Int. J. Comput. Assist. Radiol. Surg.* **5**(2), 183–193 (2010)
29. Troccaz, J., Hagn, U., Nickl, M., Jörg, S., Passig, G., Bahls, T., Nothelfer, A., Hacker, F., Le-Tien, L., Albu-Schäffer, A., Konietzschke, R., Grebenstein, M., Warup, R., Haslinger, R., Frommberger, M., Hirzinger, G.: The DLR MIRO: a versatile lightweight robot for surgical applications. *Ind. Robot.* **35**, 324–336 (2008)
30. Sandoval, J., Su, H., Vieyres, P., Poisson, G., Ferrigno, G., De Momi, E.: Collaborative framework for robot-assisted minimally invasive surgery using a 7-dof anthropomorphic robot. *Robot. Auton. Syst.* **106**, 95–106 (2018)
31. Su, H., Enayati, N., Vantadori, L., Spinoglio, A., Ferrigno, G., De Momi, E.: Online human-like redundancy optimization for tele-operated anthropomorphic manipulators. *Int. J. Adv. Robot. Syst.* **15**(6) (2018b)
32. Su, H., Yang, C., Ferrigno, G., De Momi, E.: Improved human-robot collaborative control of redundant robot for teleoperated minimally invasive surgery. *IEEE Robot. Autom. Lett.* **4**(2), 1447–1453 (2019)

33. Su, H., Qi, W., Yang, C., Aliverti, A., Ferrigno, G., De Momi, E.: Deep neural network approach in human-like redundancy optimization for anthropomorphic manipulators. *IEEE Access* **7**, 124207–124216 (2019)
34. Su, H., Hu, Y., Li, Z., Knoll, A., Ferrigno, G., De Momi, E.: Reinforcement learning based manipulation skill transferring for robot-assisted minimally invasive surgery. In: Proceedings of the 2020 IEEE International Conference on Robotics and Automation (ICRA) (2020b)
35. Su, H., Schmirander, Y., Li, Z., Zhou, X., Ferrigno, G., De Momi, E.: Bilateral teleoperation control of a redundant manipulator with an RCM kinematic constraint. In: IEEE International Conference on Robotics and Automation (ICRA), pp. 4477–4482 (2020c)
36. Su, H., Qi, W., Schmirander, Y., Ovur, S. E., Cai, S., & Xiong, X.: A human activity-aware shared control solution for medical human–robot interaction. *Assembly Autom.* **42**(3), 88–934 (2022)
37. Enayati, N., De Momi, E., Ferrigno, G.: A quaternion-based unscented Kalman filter for robust optical/inertial motion tracking in computer-assisted surgery. *IEEE Trans. Instrum. Meas.* **64**(8), 2291–2301 (2015)
38. Qian, Y., Qiao, H., Xu, J.: Understanding deep neural network by filter sensitive area generation network. In: International Conference on Neural Information Processing, pp. 192–203, Springer, Cham (2018)
39. Huang, X., Nie, X., Qiao, H., Zhang, B.: Supervised PolSar image classification by combining multiple features. In: 2019 IEEE International Conference on Image Processing (ICIP), pp. 634–638. <https://doi.org/10.1109/ICIP.2019.8803812> (2019)
40. Qi, W., Liu, X., Zhang, L., Wu, L., Zang, W., Su, H.: Adaptive sensor fusion labeling framework for hand pose recognition in robot teleoperation. *Assem. Autom.* (2018)
41. Qi, W., Su, H.: A cybertwin based multimodal network for ecg patterns monitoring using deep learning. *IEEE Trans. Ind. Informat.* **18**(10), 663–6670 (2022)
42. Haidegger, T., Autonomy for surgical robots: concepts and paradigms. *IEEE Trans. Med. Robot. Bionics.* **1**(2), 65–76 (2019)
43. Li, Z., Liu, J., Huang, Z., Peng, Y., Pu, H., Ding, L.: Adaptive impedance control of human–robot cooperation using reinforcement learning. *IEEE Trans. Industr. Electron.* **64**, 8013–8022 (2017)
44. Marescaux, J., Leroy, J., Rubino, F., Vix, M., Simone, M., Mutter, D.: Transcontinental robot assisted remote telesurgery: feasibility and potential applications. *Ann. Surg.* **235**, 487–492 (2002)
45. Sheridan, T.B.: Teleoperation, telerobotics and telepresence: a progress report. *Control. Eng. Pract.* **3**(2), 205–214 (1995)
46. Puangmali, P., Althoefer, K., Seneviratne, L.D., Murphy, D., Dasgupta, P.: State-of-the-art in force and tactile sensing for minimally invasive surgery. *IEEE Sens. J.* **8**(4), 371–380 (2008)
47. Su, H., Qi, W., Yang, C., Sandoval, J., Ferrigno, G., De Momi, E.: Deep neural network approach in robot tool dynamics identification for bilateral teleoperation. *IEEE Robot. Autom. Lett.* **5**(2), 2943–2949 (2020)
48. Li, P., Yang, Z., Jiang, S.: Needle-tissue interactive mechanism and steering control in image-guided robot-assisted minimally invasive surgery: a review. *Med. Biol. Eng. Comp.* **56**, 931–949 (2018)
49. Stoll, J., Novotny, P., Howe, R., Dupont, P.: Real-time 3D ultrasoundbased servoing of a surgical instrument. In: Proceedings of 2006 IEEE International Conference on Robotics and Automation (ICRA), pp. 613–618 (2006)
50. Ren, H., Kazanzides, P.: Investigation of attitude tracking using an integrated inertial and magnetic navigation system for hand-held surgical instruments. *IEEE/ASME Trans. Mechatron.* **7**(2), 210–217 (2012)
51. Ren, H., Rank, D., Merdes, M., Stallkamp, J., Kazanzides, P.: Multisensor data fusion in an integrated tracking system for endoscopic surgery. *IEEE Trans. Inf. Technol. Biomed.* **16**(1), 106–111 (2012)
52. Qi, W., Su, H., Yang, C., Ferrigno, G., De Momi, E., Aliverti, A.: A fast and robust deep convolutional neural networks for complex human activity recognition using smartphone. *Sensors* **19**(17), 3731 (2019)

53. Qi, W., Su, H., Aliverti, A.: A smartphone-based adaptive recognition and real-time monitoring system for human activities. *IEEE Trans. Human Mach. Syst.* **50**(5), 414–423 (2020)
54. Azizian, M., Khoshnam, M., Najmaei, N., Patel, R.V.: Visual servoing in medical robotics: a survey. Part I: endoscopic and direct vision imaging—techniques and applications. *Int. J. Med. Robot. Comp. Assisted Surg.* **10**(3), 263–274 (2014)
55. Aghajani Pedram, S., Ferguson, P., Ma, J., Dutson, E., Rosen, J.: Autonomous suturing via surgical robot: an algorithm for optimal selection of needle diameter, shape, and path. In: Proceedings of 2017 International Conference on Robotics and Automation (ICRA) (2017)
56. Zhong, F., Wang, Y., Wang, Z., Liu, Y.-H.: Dual-arm robotic needle insertion with active tissue deformation for autonomous suturing. *IEEE Robot. Autom. Lett.* **4**(3), 2669–2676 (2019)
57. Zhang, J., Li, P., Jin, C.-C., Zhang, W.-A., Liu, S.: A novel adaptive Kalman filtering approach to human motion tracking with magnetic-inertial sensors. *IEEE Trans. Industr. Electron.* **67**(10), 8659–8669 (2019)
58. Wang, J., Song, S., Ren, H., Lim, C.M., Meng Max, Q.-H.: Surgical instrument tracking by multiple monocular modules and a sensor fusion approach. *IEEE Trans. Autom. Sci. Eng.* **16**(2), 629–639 (2018)
59. Zhang, J., Li, P., Zhu, T., Zhang, W.-A., Liu, S.: Human motion capture based on kinect and IMUs and its application to human-robot collaboration. In: Proceedings of the 2020 5th International Conference on Advanced Robotics and Mechatronics (ICARM) (2020)
60. Su, H., Qi, W., Chen, J., Zhang, D.: Fuzzy Approximation-based Task-Space Control of Robot Manipulators with Remote Center of Motion Constraint. *IEEE Trans. Fuzzy Syst.* **30**(6), 1564–1573 (2022)
61. Luo, J., Yang, C., Dai, S., Liu, Z.: Tremor attenuation for surgical robots using support vector machine with parameters optimization. In: 2018 Tenth International Conference on Advanced Computational Intelligence (ICACI). <https://doi.org/10.1109/ICACI.2018.8377539> (2018)
62. Volkov, M., Hashimoto, D.A., Rosman, G., Meireles, O.R., Rus, D.: Machine learning and coresets for automated real-time video segmentation of laparoscopic and robot-assisted surgery. *IEEE Int. Conf. Robot. Autom. (ICRA)* (2017). <https://doi.org/10.1109/ICRA.2017.7989093>
63. Fang, J., Sun, Q., Chen, Y., Tang, Y.: Quadrotor navigation in dynamic environments with deep reinforcement learning. *Assem. Autom.* (2021)
64. Shvets, A.A., Rakhlis, A., Kalinin, A.A., Iglovikov, V.I.: Automatic instrument segmentation in robot-assisted surgery using deep learning. In: 17th IEEE International Conference on Machine Learning and Applications (ICMLA) (2018)
65. Su, H., Hu, Y., Karimi, H.R., Knoll, A., Ferrigno, G., De Momi, E.: Improved recurrent neural network-based manipulator control with remote center of motion constraints: experimental results. *Neural Netw.* **131**, 291–299 (2020)
66. Yang, G.-Z., Cambias, J., Cleary, K., Daimler, E., Drake, J., Dupont, P.E., Hata, N., Kazanzides, P., Martel, S., Patel, R.V., Santos, V.J., Taylor, R.H.: Medical robotics—regulatory, ethical, and legal considerations for increasing levels of autonomy. *Sci. Robot.* **2**(4), eaam8638 (2017)
67. Su, H., Ovur, S.E., Li, Z., Hu, Y., Li, J., Knoll, A., Ferrigno, G., De Momi, E.: Internet of things (IoT)-based collaborative control of a redundant manipulator for teleoperated minimally invasive surgeries. In: IEEE International Conference on Robotics and Automation (ICRA), pp. 9737–9742 (2020f)
68. Li, T., Chang, X., Wu, Z., Li, J., Shao, G., Deng, X., Qiu, J., Guo, B., Zhang, G., He, Q., Li, L., Wang, J.: Autonomous collision-free navigation of microvehicles in complex and dynamically changing environments. *ACS Nano* **11**(9), 9268–9275 (2017)
69. Morgan, P.S., Carter, T., Davis, S., Sepehri, A., Punt, J., Byrne, P., Moody, A., Finlay, P.: The application accuracy of the Pathfinder neurosurgical robot. *Int. Congr. Ser.* **1256**, 561–567 (2003)
70. Zhong, S., Zhou, J., Qiao, H.: Bioinspired gain-modulated recurrent neural network for controlling musculoskeletal robot. *IEEE Trans. Neural Netw. Learn. Syst.* (2021)
71. Huang, X., Yang, Q., Qiao, H.: Lightweight two-stream convolutional neural network for SAR target recognition. *IEEE Geosci. Remote Sens. Lett.* **18**(4), 667–671 (2021). <https://doi.org/10.1109/LGRS.2020.2983718>

72. Su, H., Yang, C., Ferrigno, G., De Momi, E.: Improved human-robot collaborative control of redundant robot for teleoperated minimally invasive surgery. *IEEE Robot. Autom. Lett.* **4**, 1447–1453 (2019)
73. Su, H., Sandoval, J., Vieyres, P., Poisson, G., Ferrigno, G., De Momi, E.: Safety-enhanced collaborative framework for tele-operated minimally invasive surgery using a 7-DoF torque-controlled robot. *Int. J. Control. Autom. Syst.* **16**(6), 2915–2923 (2019)
74. Nicolis, D.: Human intention estimation based on neural networks for enhanced collaboration with robots. In: 2018 IEEE/RSJ International Conference on Intelligent Robots and Systems (IROS) Madrid, Spain, October 1–5 (2018)
75. Sin, Y.J., Chen, Y.L., Ko, T.H., Kai, T.S.: Shared control design of a walking-assistant robot. *IEEE Trans. Control Syst. Technol.* **25**(6), 2143–2150 (2017)

Chapter 8

Metamorphic Manipulators



Charalampos Valsamos, Nikolaos Stravopodis, Vassilis Moulianitis,
and Nikos A. Apsragathos

Abstract Metamorphic robotic manipulator systems have been proposed in the relevant literature as a design paradigm able to enhance multiple aspects of robotic manipulator systems, such as adaptability to task requirements and performance during task execution. The present chapter presents the main design considerations for such robotic systems, examining the need for such systems and the proposed design concept. Furthermore, the modelling of metamorphic manipulator systems is presented, as well as the process of determining the analytical solution to their kinematic problems utilizing a modular kinematic approach. The chapter also presents methods for the dynamic structuring and design of metamorphic manipulator systems.

8.1 Introduction

Robotic systems are gaining an increasing role and use in all areas and aspects of human life and work. Whether used in manufacturing, space, health, scientific research, service or even entertainment, robots provide the ability to perform tasks in conditions that would be very difficult or impossible. Currently, most of the utilized robotic systems have a fixed anatomy, i.e., their structure is non changeable. They are designed to be able to perform a set of similar tasks presenting high performance during execution, and although the anatomies of some of these systems may be complex, they usually cannot perform a completely different task with the same high performance. Certain anatomies are uniquely suited to different types of tasks, such as for example a SCARA (Selective Compliance Assembly Robot Arm) anatomy is extremely well suited for performing assembly tasks but is not such well performing

C. Valsamos · N. Stravopodis · V. Moulianitis (✉)

Product and System Design Engineering Department, University of the Aegean,
Konstantinoupoleos 1, Ermoupolis, 84100 Syros, Cyclades, Greece
e-mail: moulianitis@aegean.gr

N. A. Apsragathos

Mechanical Engineering and Aeronautics Department, University of Patras, Rio, 26500 Patras,
Western Greece, Greece

in tasks requiring complex tool motions where an articulated anatomy is better suited. As such, in order to increase task flexibility, most robotic systems use intelligent sensors and advanced control systems. Therefore any attempt to improve task flexibility for fixed anatomy robots is mostly aimed at improving the control software, as opposed to improving their structure and alleviating any restrictions it presents to task execution. Such being the case, a fixed anatomy robot can be used to perform more different tasks, though their variety remains relatively low.

The need to increase task flexibility requires a new approach in robot design, allowing the robot to be adapted to the new environment or the new task requirements by the reshaping of its anatomy and/or structure. Configurability and reconfigurability has been identified as one of the key technological aspects that will enable the evolution of robotics in the future in the Multi-Annual Roadmap (MAR) for Robotics in Europe [1]. Configurability may be defined as the ability to configure a system that is structured using different components so as for it to be able to meet the end user's needs. Reconfigurability, implies a system composed of various interchangeable components that the end user may use to structure and restructure the system's anatomy to meet different needs that may arise.

Reconfigurable robots are structured from various autonomous parts (modules), providing the ability to the end user to change their anatomy and functionality according to the requirements of the environment or the task to be performed. As such, significant research on the design of new robotic systems is bend on the implementation of the reconfiguration paradigm to robotic systems. It is expected that in most future robotic systems this paradigm will be implemented for higher configurability and adaptability. According to MAR this is a direct result of the increased complexity and diversity of the tasks to be performed by robots as they are integrated into more application domains.

However, still some important issues remain for the implementation of this new robotic design. First and foremost, the developed systems are extremely complex in most of their aspects as opposed to the fixed anatomy robots in use today. Their modular structure, although allowing for a significant increase in task flexibility also presents drawbacks such as the required down times for reconfiguration of the system, complex control strategies and schemes, increased complexity to their kinematics and dynamics (since each new anatomy is in fact a different robot) etc. As such, efforts have been made in research in the field to alleviate such issues, and the most promising new paradigm is the introduction of metamorphic manipulators. Metamorphic manipulators segregate the terms structure and anatomy, that in the case of fixed anatomy and reconfigurable manipulators are essentially the same. As such a single structure may be altered to various anatomies. The metamorphic manipulators in fact present aspects of both fixed anatomy and reconfigurable robots: the modular structure of reconfigurable manipulators allowing the end used to created different structures and the operation as a fixed anatomy robot once the desired anatomy of a structure is defined. As such, metamorphosis may be defined as the process of changing a structure's anatomy without altering the structure itself.

The present chapter addresses the paradigm of metamorphic manipulators, providing a thorough representation of their structure and metamorphosis capabilities. Moreover, the notion of modular kinematics is presented along with a generalized analytical solution to the inverse kinematics of metamorphic manipulators are also presented. The dynamics of metamorphic manipulators are also considered and presented in detail. Finally, the chapter presents several indices and methods for the determination of the optimal topology, structure, anatomy, and task placement for metamorphic manipulators considering both kinematic and dynamic optimization.

8.1.1 The Application of the Metamorphosis Paradigm to Manipulators

The notion of metamorphic robots is not as novel as it may sound. The description of metamorphic robotic systems was provided by Gregory Chirikjian [2]:

What separates metamorphic systems from other reconfigurable robots is that they possess all of the following properties: (1) self-reconfigurability without outside help, (2) a large number of homogeneous modules, (3) physical constraints ensure contact between modules. (p. 1)

However, for a person to fully grasp the definition provided by Chirikjian, several key aspects such as modularity and reconfigurability, as well as self-reconfigurability must first be briefly defined.

8.1.2 The Beginning—The Notion of Modularity and Reconfigurability

The main driving force behind the implementation of the modularity and reconfigurability paradigms in robotics stem from the earlier work on reconfigurable manufacturing systems [3]. These new system configurations were the result of the foreseen requirements for manufacturing systems able to adapt to rapid and unpredictable changes that the new global market impresses on production. One of the first manufacturing system design paradigms that resulted by this realization was the well-known Flexible Manufacturing System (FMS). However, although them being more adaptable than the current dedicated systems, researchers moved on to further increase the systems adaptability and such research led to the Reconfigurable Manufacturing Systems (RMS) and the implementation of the modularity and reconfiguration paradigm.

At the core of RMS is the reconfiguration approach through the design and integration of modular machines and open architecture controllers. The key points in an RMS are the following [4, 5]:

- **Modularity.** The term is used to describe the use of common units for building variants of various devices or machines. In RMS, all the basic elements are modular. The benefits of modularity include expansion savings, increased expediency in changing products / parts, increased product variety, minimizing system design and development time, and easier diagnosis, maintenance, repair, and system removal.
- **Integrability.** The information, power and engine interfaces in RMS are paramount. These are analysed and designed at three levels, system, machine, and module. System-level interfaces include those between different machine tools. The interfaces at the machine level include those between the machine parts and their subdivisions, defining their cooperation, while the interfaces at the module level refer to the connectivity at the lower level and the forming of the basis of system coherence. The hierarchical structure allows for rapid and accurate integration that increases the performance of the entire system.
- **Customization.** One of the main differences between FMS and RMS is the ability of the latter to be configured in terms of flexibility and control. Flexible configuration means that machines are built around the product families they will produce. Accordingly, control configuration is achieved by completing control components using an open architecture, which provides exactly as many control functions as required reporting.
- **Convertibility.** The short system change times between the production of different batches of products are a maximum requirement. In order to achieve this, a rapid adjustment of the system and its parts takes place.
- **Diagnosability.** Using modularity, detecting, and identifying the reasons for incompatible behaviours in the system is relatively easy.

It wasn't long before many robotics researchers and providers realized that the above-mentioned paradigms were inadvertently suited for robots as well, both parts of manufacturing systems but most importantly due to their applications to different fields. A robot encompassing these paradigms and key aspects would present a greater flexibility and variability in the different tasks that it could be utilized for regardless of the sector of its application. As such in the latter decades of the past century more and more different designs of modular and reconfigurable robots ranging from single multi-purpose manipulators [6–18] to integrated systems [19] were presented. Published research results were positive to say the least and as such research in the field bloomed. An example of the different fields that a robotic system could be utilized when encompassing these paradigms was the emergence of the self-reconfigurable systems [20]. Although most of these systems were mostly applicable in exploration of unknown and obstacle cluttered environments where their reconfiguration ability was performed automatically to address obstacles through form changing, and lacked the ability of manipulation, still they represent the pinnacle of the implementation of the modularity and reconfiguration paradigm to robots. It was upon such research that Chirikjian provided the definition for metamorphosis which now is a common factor in similar designs [21–24].

8.1.3 The Need for a Metamorphic Manipulator

The emergence of modular reconfigurable robots created two distinct classes of robotic manipulators (whether of serial, parallel or hybrid serial parallel configurations), fixed anatomy and modular reconfigurable robots.

The first class (Image 8.1) is quite widespread and many years in active use in various fields of human activity (industry, construction, medicine, aerospace, energy production, etc.), while steadily, with their further development, they gradually gain ground in new work areas (help at home, cooperation with humans, etc.). The main qualification of this class is first of all the accumulated experience from the long period of time in use as well as the fact that it still occupies a large number of researchers in terms of improving its operation, in areas that have already been established as a dominant tool, but also in terms of improving its capabilities to penetrate areas that until now was not possible. The big disadvantage of manipulators of fixed structure is their very structure. The different structures provided for these robots are usually well fitted for a range of similar robotic tasks, while their utilization in different tasks is usually conducted via altering their control and providing further sensor capabilities.

The second class of serial robotic arms is relatively new (Image 8.2), and therefore is still in its early stages, where most of the applications that have been presented so far are experimental installations or demonstration systems. Nevertheless, its main qualification is the adaptability that characterizes it, as it allows the user to build any type of arm required to perform the task to be undertaken. This way of designing them allows the user to occasionally build the required arm type from the set of basic structural elements (modules). In addition to the disadvantage of non-commercial mass use at this level of development, reconfigurable manipulators also present some

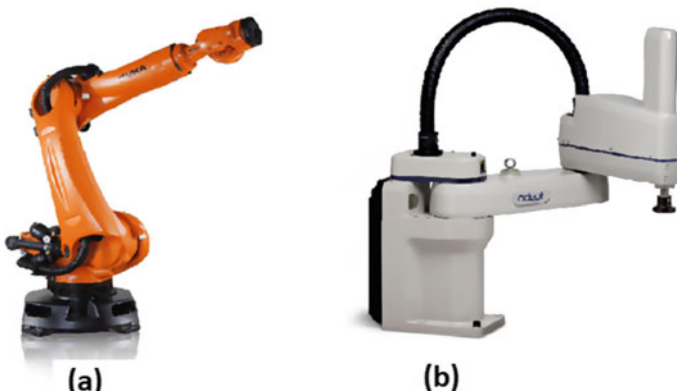


Image 1 Examples of fixed anatomy manipulators: **a** an articulated manipulator and **b** a SCARA type manipulator. *Images courtesy of Kuka and Adept respectively*

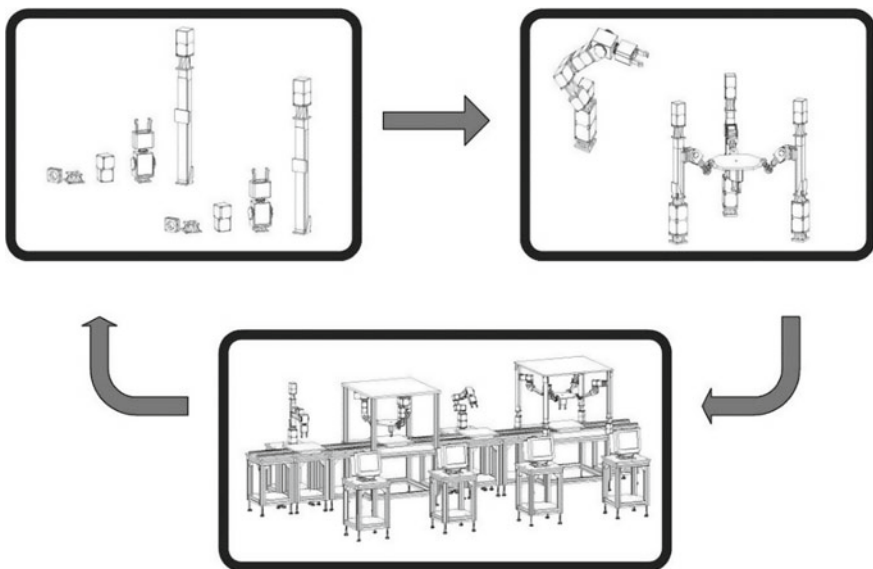


Image 2 Examples of reconfigurable robots utilized for different tasks in an assembly work cell (adapted from [19])

disadvantages, the main one being the requirement of significant downtime in order to structure and plan the new layout and operation and control.

In addition to the above, both classes have another disadvantage in terms of available structures, as both lead to manipulators with the same structural characteristics. These characteristics mostly refer to the position of axis orientation of the joints axes within the manipulator where it is “preferred” that the consecutive axes are either perpendicular to each other (even in case of skewness where their projection at the same plane results in them being perpendicular) or parallel. This arrangement arises due to the need to simplify the kinematics of the arm [25], while in the case of reconfigurable manipulators an additional reason for this is the way of connecting the available structural elements [6–19].

Technical issues aside, the core reason for the implementation of reconfigurability and/or metamorphosis to robots is the need for higher flexibility of robotic systems. As robots become ever more utilized in different applications, there is a definite requirement for high performance and greater flexibility in the types of tasks a given system may be utilized for. For example, due to their increased importance as tools in the manufacturing industry, robots are increasingly utilized not only in the case of mass production but also by small manufacturers and SMEs. Since a robotic system corresponds to a quite large investment in the case of an SME, it should provide the user with the flexibility to utilize it for different tasks in the manufacturing process, which due to the high probability of change in the range of products manufactured by an SME are constantly changing. As such, while a fixed anatomy robot will perform very well for an initial task, in the case the task is altered, significant cost and time are

required to re-program and adapt the robot to the new requirements. A reconfigurable robot in this case presents the advantage that the SME may simply adapt the structure of the robot to better suit the new task demands, limiting the required cost and time required for the process, albeit not to such a large degree as expected, due to the complexity of resetting the system to perform the new task. Therefore, the main goal of the implementation of either the reconfigurability or the metamorphosis paradigm to robotic manipulators is the increase in task flexibility with a subsequent reduced cost and time requirements between the utilization of the robot to different tasks, so as that it presents a viable and advantageous investment for the end user.

Metamorphic manipulators were presented as an interim class of manipulators that encompass characteristics from both classes in a “*best of all worlds*” fashion. They implement the modularity and reconfigurability paradigms as the reconfigurable robots but also provide a fixed anatomy during task performing simplifying the requirements for planning and control of the systems. Furthermore, their kinematics are also modular, allowing the rapid derivation of forward and inverse kinematic problems solutions for different possible anatomies, as it will be presented further on.

8.1.4 The Concept of Metamorphosis on Manipulators

Metamorphic manipulators were first presented in [26–28]. Their main structure is modular, composed of different basic building blocks of three main categories:

- **Active modules.** In basis, these are the joints of the robotic manipulator. They are self-contained mechatronic devices with actuation, control and sensing capabilities and provide the necessary actuation for the robot structure.
- **Pseudo joints.** These are 1 rotational D.o.F. manually operated modules that facilitate the metamorphosis of the systems via the alteration of a structure’s Denavit-Hartenberg parameters leading to different anatomies without the requirement for dismantling the structure.
- **Passive modules.** These are peripheral modules, lacking actuation, computing power and sensors, providing connectivity and specific parameter values (such as link lengths) as required.

One of the main goals of the pseudo-joint is to increase the homogeneity of the metamorphic arm system, i.e., to reduce the elements required to form a structure. The second goal fulfilled through the pseudo-joint is the immediate transformation of a metamorphic structure from one anatomy to another, without the requirement to disassemble it into its basic parts and reassemble it into the new anatomy. This results in a significant reduction in the downtime required to change the anatomy of the arm to the new one as determined by the work to be performed. With the introduction of the pseudo-joints in the structure of the metamorphic arm, it is possible to change its anatomical features easily and quickly such as link lengths and twist angles. The possibility for transformation of the mechanism arises from

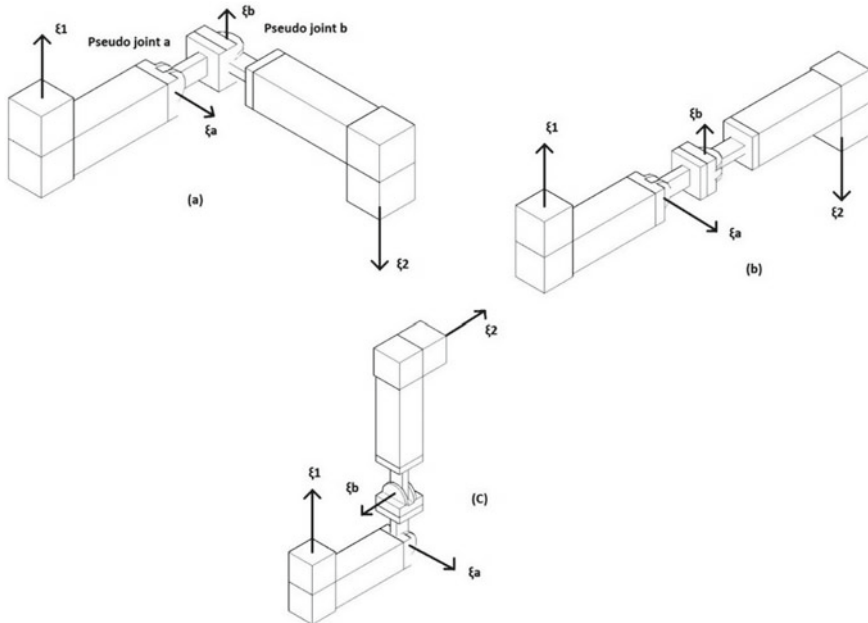


Fig. 8.1 Alteration of a link structure via the utilization of pseudo joints

the introduction of the rotation axes of the pseudo-joints in the structure of the mechanism. Figure 8.1 shows a relevant example.

The reference anatomy and final (desired) anatomy show significant differences. The first and foremost is the relative position and orientation of the twists of the active joints. In the reference anatomy, they are parallel, while in the desired anatomy they are perpendicular. The two anatomies are shown in Fig. 8.2.

Figure 8.2 presents the two anatomies with their respective geometric characteristics, the system of the base of the mechanism defined $\{B\}$ and the system of the working end $\{T\}$. It is evident from the comparison of the two, that:

1. In the reference configuration the twists of the active joints of the mechanism ξ_1 and ξ_2 are parallel. Also, the coordinates of the centre of $\{T\}$ in relation to $\{B\}$ (in the reference configuration with $\theta_1 = \theta_2 = 0^\circ$) are given as:

$$Bp_T = [L_3 L_1 + L_2 L - L_4] \quad (8.1.1)$$

2. In the final configuration, the twists of the active joints of the mechanism ξ_1 and ξ_2 are now perpendicular, while the coordinates of the centre of $\{T\}$ in relation to $\{B\}$ (in the reference configuration with $\theta_1 = \theta_2 = 0^\circ$) are given as:

$$Bp_T = [0 L_1 + L_4 L + L_2 + L_3] \quad (8.1.2)$$

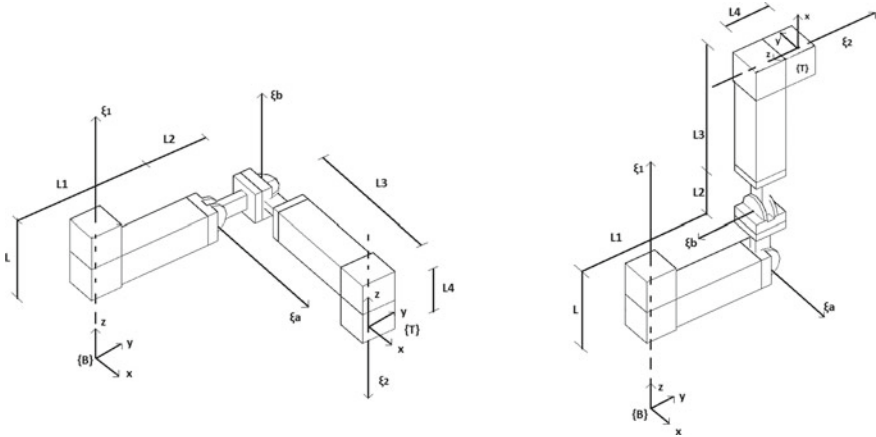


Fig. 8.2 The parameters of the reference and final anatomy of the link in Fig. 8.1

3. If the maximum possible length of the mechanism is considered at the $x - y$ plane, for the reference anatomy that is $L_{x-y,max} = \sqrt{L_3^2 + (L_1 + L_2)^2}$ and for the final $L_{x-y,max} = L_1 + L_4$.

One of the major aspects of metamorphic robots is the separation of the notion of anatomy and structure which for the other two classes are identical. Both in the case of a fixed anatomy robot as well as for a reconfigurable robot, the (current in the case of the latter) anatomy is also their structure. Through the usage of the pseudo joints, these notions for a metamorphic manipulator are inadvertently connected but significantly different to each other. A structure is the form of the manipulator, composed by the various modules and depended on the connective relations and sequence of them. However, the anatomy is defined by the current configuration of the pseudo joints within the structure. Therefore, one structure may present a multitude of different anatomies.

More formally, the definition of the main aspects of a metamorphic manipulator are the following [27]:

Metamorphic Parameters - Anatomy: A metamorphic anatomy is described by the vector θ_p of pseudo-joint angles θ_p . For a metamorphic structure comprising m pseudo-joints, the vector θ_p is defined as:

$$\underline{\theta}_p = [\theta_{p1} \theta_{p2} \cdots \theta_{pj} \theta_{pm}]^T \in V^m, \theta_{pj} \in V, j = 1, 2, \dots, m$$

$$V = \left\{ \theta_{pj} = \theta_{pj}^L + k \cdot \frac{|\theta_{pj}^L| + |\theta_{pj}^U|}{12} : k = 0, 1, 2, \dots, 12, j = 1, 2, \dots, m \right\} \quad (8.1.3)$$

where θ_{pj}^L and θ_{pj}^U the minimum and maximum possible value of the angle of jth pseudo-joint respectively. Considering all possible combinations of the quantized values of the angles of the pseudo-joints in a structure, the probable number of anatomies into which it can be transformed is N^m , where N is the total number of the quantized values of the angles of the pseudo-joint (set to 13 as an example in Eq. 8.1.3).

- **Metamorphic Topology:** An open kinematic chain formed by a combination of the three available basic elements, and the connections between them. A metamorphic topology does not include the geometric characteristics of the arm (lengths, positions, and orientations of torsional joints) and can therefore be implemented in several metamorphic structures. All the metamorphic structures produced from a given metamorphic topology present the same number of different anatomies in which they can be transformed (N^m).
- **Metamorphic Structure:** It is the materialized physical form of a metamorphic topology, where the basic elements from which it is structured are placed as defined by the topology but considering the geometric characteristics of them and their whole.
- **Reference anatomy:** It is the anatomy of a specific metamorphic structure, defined by the designer, which is considered as the initial anatomy of this structure. The designer can either use the adjustments of the angles of the pseudo-joints as they are or consider that in the reference anatomy it $\boldsymbol{\theta}_p^{\text{Ref}} = \mathbf{0}$, adjusting the range of values of (Eq. 8.1.3) for each respective pseudo-joint.
- **Reference configuration:** As in any open chain kinematic arm, the configuration of the ith anatomy $\boldsymbol{\theta}_p^i$ is determined by the values $\boldsymbol{\theta} = [\theta^L, \theta^U]$ of the variables of its active joints, where n is the number of D.o.F. of the anatomy and θ^L, θ^U the minimum and maximum value of the joint variables. The reference configuration is defined as $\boldsymbol{\theta} = \mathbf{0}$.

8.1.5 Modelling Metamorphic Manipulators

Screw and Lie group theory allows for user-friendly modelling of multi body systems. In the case of Serial Metamorphic Manipulators (SMM) a special issue should be addressed regarding their modelling when considering their kinematics and dynamics. The impact of anatomy metamorphosis should be integrated in the analytic formula used to describe the kinematic and dynamic model of the manipulator. Although the operation of the pseudo-joints greatly differs from the active joints' modules, both belong to the same lower Reuleaux pair of zero pitch subgroups (rotation about a line) and can be identically parameterized. In robotics the group of rigid transformations induced by the mechanical joints is called $SE(3)$, which is a Lie Group. As such, one-parameter subgroups of this group are utilized to parameterize the motion generated by the joints [29]. Each subgroup represents the restricted rotation induced by each joint to the adjacent robot links and is also a Lie Group. In

order each of these groups to be generated, the Algebra of the corresponding group should be defined. This can be achieved in various ways [30].

The Lie Algebra of $SE(3)$, denoted as $se(3)$, can be identified with the matrices $\hat{\xi} \in R^{4 \times 4}$. An element of $se(3)$ is referred to as a *twist*. Twists can be parameterized to 6-dimensional vectors $\xi \in R^6$ using the *vee* operator. Each passive and active joint is associated with a corresponding twist, which “generates” the rotation about the joint axis. This action can be interpreted geometrically using the theory of screws. In order to map the twist with the transformation matrix representing the generated motion the *exponential map* is utilized. That is, given $\xi \in se(3)$ and $q \in R$, the exponential of $\hat{\xi}q$ is an element of $SE(3)$. This exponential map gives the relative motion of the link attached to the joint with respect to the spatial reference frame. As a result, it allows a *global* description of rigid body motion, which doesn’t suffer from singularities due to the use of body-fixed coordinates. In conclusion, using these tools, an intuitive modelling can be achieved.

Here, Modular Structure Representation (MSR) presented in [27] and the modifications proposed in [15] will be used to define the special characteristics that a serial metamorphic manipulator introduces. The definitions of *Active Joint*, *Pseudo joint*, Metamorphic Anatomy and Configuration, with the corresponding statements and the string notation formulated for the establishment of MSR remain intact. However, the metamorphic topology and structure definitions will be expanded somewhat. The key definitions introduced are, Assembly Sequence, Metamorphic Structure and Synthetic Assembly. The first refers to the sequence of the basic components (active and passive modules) that form the structure of the manipulator. The second designates the setting of the assembly parameters. The latter relates to the connectivity surfaces and the corresponding parameters given for the interconnection of passive and active modules of the manipulator chain. Each connectivity surface is designated with a number that precedes the number that specifies the following active (0) or passive (1) module. Assembly parameters consist of the three independent rotation variables about the axes of the preceding link frame and the corresponding position variables. This local parameterization, despite of not being optimal, facilitates a user-friendly depiction of the assembly. In order to shape the metamorphic structure, the following statements are established:

- A chain starts with an active module with a \hat{z} direction of the rotation axis.
- Pseudo joints have two connectivity surfaces.
- Between two adjacent modules of the structure an interconnection is formed using a synthetic assembly.
- Adjacent modules inside a metamorphic link must be orthogonal at reference anatomy of each structure.

The three types of distinct connections between adjacent modules (perpendicular, parallel, skew) are parameterized by the assembly parameters of the synthetic assembly. The synthetic assembly is assigned the “&” symbol to simplify the string notation of the corresponding structure. For each “&” symbol in the structure string the 6 parameters $\{R_s, P_s\}$ of the synthetic assembly should be also given. These local parameters define the transformation between the preceding active module of

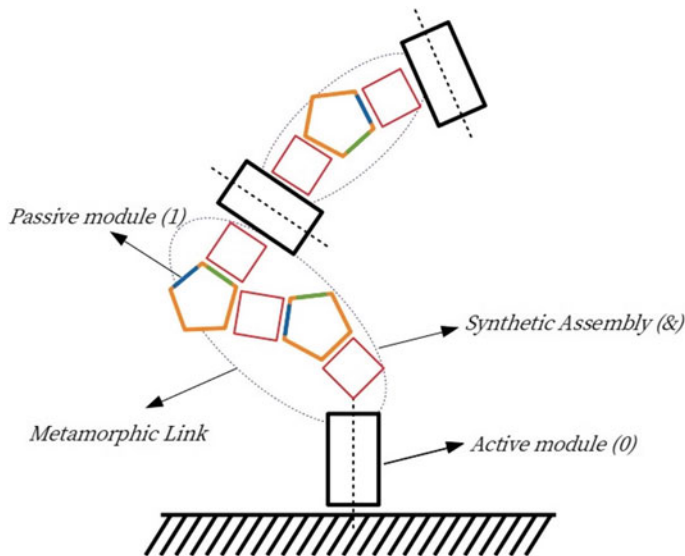


Fig. 8.3 Basic components of a metamorphic structure

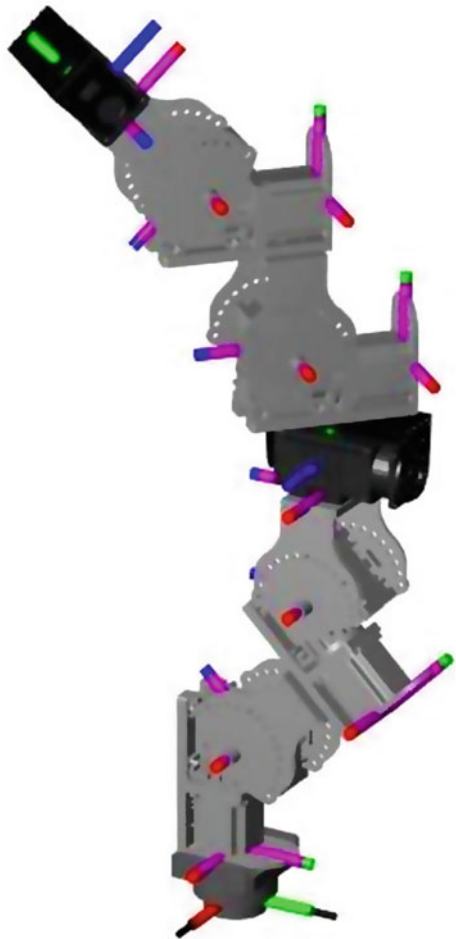
link i and the pseudo joint of the next link $i + 1$. Finally, for string notation purposes, active and passive modules are assigned with 0 and 1 respectively. The modified MSR notation given above, and the basic components of a metamorphic structure are presented in Fig. 8.3. An example structure produced is illustrated in Fig. 8.4.

8.2 Metamorphic Robot Kinematics

Due to the complexity of the structure of reconfigurable robots in most cases of proposed systems in the relevant literature, two different approaches are met, when addressing their forward and inverse kinematics problems solving. The first, involves utilizing the well-known and established analytical methods used in typical fixed anatomy systems, while the second involved utilizing computational iterative methods for solving the kinematic problems of the proposed systems.

However, the added complexity of metamorphic robots i.e., the segregation of the concepts of structure and anatomy, that are usually the same for both fixed anatomy and reconfigurable robots, presents additional challenges with respect to both their kinematics and dynamics problems. In this sense, most iterative methods would present an obvious solution due to the capability of soft AI solving techniques in coping with highly complex problems. However, iterative techniques usually provide sub-optimal solutions and, in most cases, with respect to the inverse kinematics problem will provide a single solution of the robot's configuration. The importance of having all configurations of the robot at different postures allows for a better path

Fig. 8.4 Structure example
(0-&21-&31-0-&31-&31-0)



and task design. Additionally, they require increased time and computational power with respect to analytical solutions.

As such the notion of a method that allows the analytical solution of the inverse kinematics problem of metamorphic manipulators has already been addressed in the relevant literature. Utilizing Lie algebra and Screw theory, along with the Paden-Kahan subproblems method, it is possible to modularize the analytical solution of the inverse kinematics of a metamorphic manipulator, so as for it to be able to provide the solution for most, if not all, possible anatomies of a given metamorphic structure.

8.2.1 A Modular Parametric Analytical Solution for the Kinematics of Metamorphic Serial Manipulators

A parametric analytical solution of the inverse kinematic problem capable of producing solutions for any possible anatomy of a metamorphic arm as it transforms into a new one could prove very useful especially in designing its optimal anatomy, as it will produce accurate solutions with minimal requirement, both in computing power and in time. At the same time, the use of pseudo-joints to facilitate and accelerate the metamorphic process in metamorphic arms, allows the modularization of the parametric solution for each emerging anatomy during the metamorphic process.

Using pseudo-joints, parameters of the anatomy of the manipulator and more specifically the twist angles between the axes of the joints of the active can be introduced in such a way in the algebraic processes of solving the inverse kinematic problem, so that it can produce a solution for any value of them. This is achieved by considering the twist angle as a parameter of a pseudo-joint in the same way as with a normal joint. In this way, the resulting transformation table for the pseudo-joint can be considered as predefined, which can be easily introduced into algebraic calculations to produce the analytical expression of the direct kinematic problem.

Since this transformation is known, it can be used algebraically in the process of producing inverse kinematic solution equations to significantly reduce the complexity induced by any change in the manipulator's anatomy.

A combination of the POE (Product of Exponentials Formula) methods [29] and operations on the proper Euclidean Group [29, 30] is used to generate closed-ended equations for the solution of inverse kinematics. The POE method is preferred over the others known as that of the Denavit Hartenberg (DH) parameters as it is simpler to use and develop, while showing significantly reduced complexity during the production of the equations of the inverse kinematic solution, due to the use of the Paden—Kahan [29, 32]. In addition, the use of the DH parameters for the expression of the kinematic equations of the arm requires the expression of the joint-imposed transformations of the anterior joint coordinate system, whether active or pseudo-joint, thus introducing additional complexity to the algebraic calculations. The POE method on the other hand allows the expression of the transformations imposed by the joints with respect to a fixed point, greatly facilitating the calculations. The modelling procedure presented may still be applied however in the case of determining the kinematic problem solutions of a given structure, it is broken down to its main basic elements, i.e., active joints and pseudo joints. This allows the full implementation of the POE method as well as the exploitation of the operation of the pseudo joints in the structure to formulate a modular kinematics solution approach.

The following sections present the solution process of the analytical parametric solution for metamorphic structures of 3, 4, 5 and 6 DoF, as well as the conditions under which this solution is feasible.

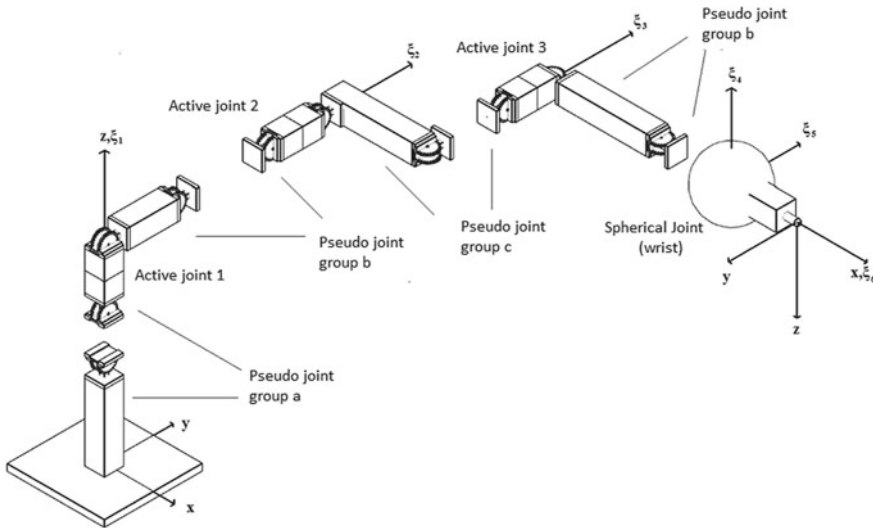


Fig. 8.5 A generic 6 D.o.F. metamorphic structure

A 6 D.o.F. general structure of a metamorphic serial manipulator is considered, structured by 6 active joints and 4 groups of pseudo-joints through which the metamorphic links of the structure are formed. The pseudo-joint groups may contain one or two pseudo-joints.

The general form of such a manipulator is in Fig. 8.1. The figure shows the groups a, b, c, d of the pseudo-joints, the active joints, and their twists, as well as a spherical joint at the end of the arm (wrist). The modular analytical kinematics solution presented, is structured according to the degrees of freedom of the given structure. In the following, the solution is categorized as such (Fig. 8.5).

8.2.1.1 3 D.o.F. Metamorphic Structures

In the case of a 3 D.o.F. metamorphic structure, the wrist presented in Fig. 8.1 is omitted, along with pseudo joint group d. As such the respective expression for the structure's forward kinematics problem is given as:

$$e^{\xi_a \theta_a} e^{\xi_1 \theta_1} e^{\xi_b \theta_b} e^{\xi_2 \theta_2} e^{\xi_c \theta_c} e^{\xi_3 \theta_3} e^{\xi_d \theta_d} g_{st}(0) = g_d \quad (8.2.1)$$

where $e^{\xi_a \theta_a}$, $e^{\xi_b \theta_b}$, $e^{\xi_c \theta_c}$, $e^{\xi_d \theta_d}$, are the corresponding transformations induced by the respective pseudo joint groups (considered as parametrically expressed transformations) and $e^{\xi_1 \theta_1}$, $e^{\xi_2 \theta_2}$, $e^{\xi_3 \theta_3}$ the corresponding transformations induced by the active joints in the structure.

The twists of the active joints of the manipulator are considered to be in a randomly relative position to each other (they may be intersecting, parallel or even skew).

As a first step, Eq. (8.2.1) is reconfigured to isolate the transformation tables:

$$e^{\xi_1 \theta_1} e^{\xi_b \theta_b} e^{\xi_2 \theta_2} e^{\xi_c \theta_c} e^{\xi_3 \theta_3} = e^{-\xi_a \theta_a} g_d \cdot g_{st}^{-1}(0) \cdot e^{-\xi_d \theta_d} = g_1 \quad (8.2.2)$$

Since the introduced transformations from the pseudo-joints of groups a and d are known. Applying both members of Eq. (8.2.2) at a point \mathbf{p} located on the twist of the third active joint results to:

$$e^{\xi_1 \theta_1} e^{\xi_b \theta_b} e^{\xi_2 \theta_2} e^{\xi_c \theta_c} e^{\xi_3 \theta_3} \cdot p = g_1 \cdot p \quad (8.2.3)$$

However, since \mathbf{p} lies on the twist of the third joint, it stands that $e^{\xi_3 \theta_3} \cdot p = p$. Moreover, since the induced transformation from the third pseudo joint group is known, it also stands that $e^{\xi_c \theta_c} \cdot p = p_1$. As such, Eq. (8.2.3) becomes:

$$e^{\xi_1 \theta_1} e^{\xi_b \theta_b} e^{\xi_2 \theta_2} \cdot p_1 = g_1 \cdot p \quad (8.2.4)$$

Subtracting a point \mathbf{q} located on the twist of the first joint from both members of Eq. (8.2.4) yields:

$$e^{\xi_1 \theta_1} e^{\xi_b \theta_b} e^{\xi_2 \theta_2} \cdot p_1 - q = g_1 \cdot p - q \quad (8.2.5)$$

Moreover, since \mathbf{q} lies on the twist of the first active joint and the induced transformation be the pseudo joint group b are parametrically expressed (i.e., known) Eq. (8.2.5) may be rewritten as:

$$e^{\xi_1 \theta_1} e^{\xi_b \theta_b} \cdot (e^{\xi_2 \theta_2} \cdot p_1 - e^{-\xi_b \theta_b} \cdot q) = g_1 \cdot p - q \quad (8.2.6)$$

The transformation of the point \mathbf{q} through the inverse induced transformation of the pseudo-joint group b provides a new point \mathbf{q}_1 . Since the transformations maintain the distances between points, taking the norms of the two members of Eq. (8.2.6) yields,

$$\|e^{\xi_2 \theta_2} \cdot p_1 - q_1\| = \|g_1 \cdot p - q\| \quad (8.2.7)$$

Equation (8.2.7) is an expression of the third sub-problem Paden Kahan and can be solved to produce the displacement of the second joint [29]. The solution is obtained by assuming that point \mathbf{p}_1 rotates at an angle θ_2 about twist ξ_2 so that its distance from the point \mathbf{q}_1 is given and equal to the known distance of the second member of Eq. (8.2.7). Depending on the final position of the point \mathbf{p}_1 , the twist and the location of point \mathbf{q}_1 , the solution of the equation can provide either one, none or two solutions.

Knowing the value of the variable θ_2 , and returning to Eq. (8.2.4), it stands that:

$$e^{\xi_1 \theta_1} (e^{\xi_b \theta_b} e^{\xi_2 \theta_2} \cdot p_1) = g_1 \cdot p \quad (8.2.8)$$

where Eq. (8.2.8) can be solved to find the solution for the variable θ_1 if a new point $e^{\xi_b \theta_b} e^{\xi_2 \theta_2} \cdot p_1 = p_2$ is considered since all these transformations are now known. In essence in this case the problem corresponds to that of rotation of the point \mathbf{p}_2 about the twist ξ_1 at an angle of θ_1 until it coincides with point $g_1 \cdot p$, which is the respective expression of the first Paden Kahan sub-problem [29]. Solving this problem provides one or no solutions for the value of the variable θ_1 for each value of the variable θ_2 calculated in Eq. (8.2.7).

Since the values of the two variables θ_1 and θ_2 are known Eq. (8.2.3) can be rearranged as:

$$e^{\xi_3 \theta_3} \cdot p = e^{-\xi_c \theta_c} e^{-\xi_2 \theta_2} e^{-\xi_b \theta_b} e^{-\xi_1 \theta_1} g_1 \cdot p = p_r \Rightarrow e^{-\xi_3 \theta_3} p_r = p \quad (8.2.9)$$

In Eq. (8.2.9), subtracting a point \mathbf{r}_3 lying anywhere except the twist of the third joint, and taking the norm of both parts yields:

$$\|e^{-\xi_3 \theta_3} p_r - \mathbf{r}_3\| = \|p - \mathbf{r}_3\| \quad (8.2.10)$$

Equation (8.2.10) is an expression of the third Paden Kahan sub-problem [29] and the equation can provide one, none or two solutions, solved just like Eq. (8.2.7) to produce the value of the variable θ_3 . At the end of the solution process, the parametric solution produces a maximum of four possible solutions to the inverse kinematics, ensuring the necessary multiplicity.

8.2.1.2 4 D.o.F. Metamorphic Structures

For a general 4 D.o.F. metamorphic structure, pseudo joint groups d and e are reinstated as shown in Fig. 8.1 while a fourth active joint with corresponding twist ξ_4 is connected as the last joint of the structure.

The respective expression of the structure's forward kinematics is then:

$$e^{\xi_a \theta_a} e^{\xi_1 \theta_1} e^{\xi_b \theta_b} e^{\xi_2 \theta_2} e^{\xi_c \theta_c} e^{\xi_3 \theta_3} e^{\xi_d \theta_d} e^{\xi_4 \theta_4} e^{\xi_e \theta_e} g_{st}(0) = g_d \quad (8.2.11)$$

Isolating the transformation tables results in:

$$e^{\xi_1 \theta_1} e^{\xi_b \theta_b} e^{\xi_2 \theta_2} e^{\xi_c \theta_c} e^{\xi_3 \theta_3} e^{\xi_d \theta_d} e^{\xi_4 \theta_4} = e^{-\xi_a \theta_a} g_d \cdot g_{st}^{-1}(0) \cdot e^{-\xi_e \theta_e} = g_2 \quad (8.2.12)$$

Applying the two parts of Eq. (8.2.12) to a point \mathbf{p} lying on the twist of the fourth joint results in:

$$e^{\xi_1 \theta_1} e^{\xi_b \theta_b} e^{\xi_2 \theta_2} e^{\xi_c \theta_c} e^{\xi_3 \theta_3} p_1 = q \quad (8.2.13)$$

where, $g_2 \cdot p = q$ and $e^{\xi_d \theta_d} e^{\xi_4 \theta_4} p = p_1$ since the fourth joint twist does not affect point \mathbf{p} , and, if the transformation of the pseudo-joints is known. From Eq. (8.2.13)

the following relations [30] may be defined:

$$e^{\xi_3 \theta_3} p_1 = a \quad (8.2.14)$$

$$e^{-\xi_1 \theta_1} q = b \quad (8.2.15)$$

$$e^{\xi_2 \theta_2} e^{\xi_c \theta_c} a = e^{-\xi_b \theta_b} b \quad (8.2.16)$$

Since points **a** and **b** lie in circles that are configured from the variables of the third and first joint respectively, it stands that:

$$a = p_1 + \sin \theta_3 \cdot \omega_3 \times (p_1 - r_3) + (1 - \cos \theta_3) \cdot \omega_3 \times (\omega_3 \times (p_1 - r_3)) \quad (8.2.17)$$

$$b = q + \sin \theta_1 \cdot \omega_1 \times (q - r_1) + (1 - \cos \theta_1) \cdot \omega_1 \times (\omega_1 \times (q - r_1)) \quad (8.2.18)$$

where ω_1 , ω_3 are the unit vectors of the twists of the two joints and r_1 , r_3 points lying on each twist.

The $e^{\xi_c \theta_c} a$ points and $e^{-\xi_b \theta_b} b$ due to Eq. (8.2.16) lie in a plane perpendicular to the twist of the second active joint and therefore the dot products of their vectors with the unit vector of the twist of the second joint are equal. Also, the distances of the points from the twist of the second active joint should be equal. Therefore, it stands that:

$$e^{\xi_c \theta_c} a \omega_2 = e^{-\xi_b \theta_b} b \omega_2 \quad (8.2.19)$$

$$(e^{\xi_c \theta_c} a - r_2)^2 = (e^{-\xi_b \theta_b} b - r_2)^2 \quad (8.2.20)$$

The second equation after mathematical manipulation becomes a linear equation of $\cos \theta_1$, $\sin \theta_1$, $\cos \theta_3$, $\sin \theta_3$ [18]. Together with Eq. (8.2.19) two linear equations for the four variables ($\cos \theta_1$, $\sin \theta_1$, $\cos \theta_3$, $\sin \theta_3$) are obtained, where the known trigonometric identity $\cos^2 \theta + \sin^2 \theta = 1$ can be used to omit the two (for example $\cos \theta_3$, $\sin \theta_3$). The process ultimately yields two quadratic equations for the other two variables ($\cos \theta_1$, $\sin \theta_1$), one of which is the trigonometric identity. By applying the relations of the tangent of the half-angle $\cos \theta = \frac{1-t^2}{1+t^2}$, $\sin \theta = \frac{2t}{1+t^2}$ to the two equations, the identity is automatically satisfied while the second one is now transformed into a quadratic equation with respect to t . By finding t the values of the variables $\cos \theta_1$, $\sin \theta_1$ may be determined. Based on the above, 4 solutions are obtained as the maximum number of solutions for the value of θ_1 . Through the linear Eqs. (8.2.19) and (8.2.20) the solutions for the angle θ_3 are obtained. Knowing now θ_1 and θ_3 Eq. (8.2.16) can be solved for θ_2 .

Since the angles of the first three active joints are known, Eq. (8.2.12) is transformed into:

$$e^{\xi_4 \theta_4} = e^{-\xi_d \theta_d} e^{-\xi_3 \theta_3} e^{-\xi_c \theta_c} e^{-\xi_2 \theta_2} e^{-\xi_b \theta_b} e^{-\xi_1 \theta_1} g_2 \quad (8.2.21)$$

Equation (8.2.21) can be solved to find the values of the variable θ_4 by applying both sides of the equation to a point \mathbf{p}_r that does not lie on ξ_4 . Finally, the proposed methodology produces a maximum of 4 solutions for metamorphic structures of 4 D.o.F.

8.2.1.3 5 D.o.F. Metamorphic Structures

An additional active joint with twist ξ_5 and an additional group of pseudo joints are considered to be serially connected to pseudo joint group e from the 4 D.o.F. structure. The expression of the forward kinematics of the structure is given as:

$$e^{\xi_a \theta_a} e^{\xi_1 \theta_1} e^{\xi_b \theta_b} e^{\xi_2 \theta_2} e^{\xi_c \theta_c} e^{\xi_3 \theta_3} e^{\xi_d \theta_d} e^{\xi_4 \theta_4} e^{\xi_e \theta_e} e^{\xi_5 \theta_5} e^{\xi_f \theta_f} g_{st}(0) = g_d \quad (8.2.22)$$

The isolation of transformation matrices yields:

$$e^{\xi_1 \theta_1} e^{\xi_b \theta_b} e^{\xi_2 \theta_2} e^{\xi_c \theta_c} e^{\xi_3 \theta_3} e^{\xi_d \theta_d} e^{\xi_4 \theta_4} e^{\xi_e \theta_e} e^{\xi_5 \theta_5} = e^{-\xi_a \theta_a} g_d \cdot g_{st}^{-1}(0) \cdot e^{-\xi_f \theta_f} = g_3 \quad (8.2.23)$$

Equation (8.2.22) is a problem with 5 variables. In order for a solution to be obtained, it must be broken down into problems with three or fewer variables. The basic premise for this to happen is that there is an intersection between the first active joint twist and second active joint transformed twist or between the fourth active joint twist and the transformed fifth active joint twist. The two solution cases are presented below.

Condition A. Twists ξ_4 and ξ'_5 (transformed twist ξ_5 due to the pseudo-joints in group e induced transformation) intersect. The intersection of the two twists must first be calculated. Twist ξ_5 is given as [29]:

$$\hat{\xi}_5 = [\hat{\omega}_5 - \hat{\omega}_5 \cdot r_5] \quad (8.2.24)$$

where $\hat{\omega}_5$ is the skew-symmetric array of the unit vector ω_5 of the twist and \mathbf{r}_5 a point on ξ_5 . The transformed twist ξ'_5 due to induced transformation by the pseudo-joint group is given as:

$$\hat{\xi}'_5 = Ad_{e^{\xi_e \theta_e}} \hat{\xi}_5 = e^{\xi_e \theta_e} \hat{\xi}_5 e^{-\xi_e \theta_e} \quad (8.2.25)$$

From Eq. (8.2.25) the unit vector of the transformed twist may be calculated. Also point \mathbf{r}_5 is transferred to a new position as:

$$r'_5 = e^{\xi_e \theta_e} r_5 \quad (8.2.26)$$

Given ω'_5 , r'_5 , ω_4 , r_4 (the last two corresponding to twist ξ_4) it is easy to geometrically determine the point of intersection \mathbf{q} of $e^{\xi_4\theta_4}$ and $e^{\xi_e\theta_e}e^{\xi_5\theta_5}$.

The procedure for finding the point is as follows:

A line along each twist can be defined as:

$$\frac{x - x_0}{a} = \frac{y - y_0}{b} = \frac{z - z_0}{c} \quad (8.2.27)$$

where $\omega = \{\alpha, b, c\}^T$, $\mathbf{r} = \{x_0, y_0, z_0\}^T$. The common point should satisfy the expression of Eq. (8.2.27) in each principal direction, and thus the following equations arise:

$$\begin{aligned} \frac{x * -x_{05}}{a_5} &= \frac{x * -x_{04}}{a_4} \frac{y * -y_{05}}{b_5} \\ &= \frac{y * -y_{04}}{b_4} \frac{z * -z_{05}}{z_5} = \frac{z * -z_{04}}{z_4} \end{aligned} \quad (8.2.28)$$

The solution of Eq. (8.2.28) provides the coordinates of the point of intersection $\mathbf{q} = [x^*, y^*, z^*]$ of the two twists.

Applying the two members of Eq. (8.2.23) to point \mathbf{q} it yields:

$$e^{\xi_1\theta_1}e^{\xi_b\theta_b}e^{\xi_2\theta_2}e^{\xi_c\theta_c}e^{\xi_3\theta_3}e^{\xi_d\theta_d}q = g_3q \quad (8.2.29)$$

since $e^{\xi_4\theta_4}e^{\xi_e\theta_e}e^{\xi_5\theta_5}q = \mathbf{q}$. Equation (8.2.29) is similar to Eq. (8.2.13) used in solving the kinematics for structures 4 D.o.F. and can be solved using the same procedure for the values of $\theta_1, \theta_2, \theta_3$. Given these, Eq. (8.2.23) is transformed into:

$$e^{\xi_4\theta_4}e^{\xi_e\theta_e}e^{\xi_5\theta_5} = e^{-\xi_d\theta_d}e^{-\xi_3\theta_3}e^{-\xi_c\theta_c}e^{-\xi_2\theta_2}e^{-\xi_b\theta_b}e^{-\xi_1\theta_1}g_3 = g_4 \quad (8.2.30)$$

Equation (8.2.30) can be solved by applying both of its parts to a point \mathbf{p} lying on ξ_5 , resulting in:

$$e^{\xi_4\theta_4}p' = g_4p = \quad (8.2.31)$$

where $p' = e^{\xi_e\theta_e}e^{\xi_5\theta_5}p$. Equation (8.2.28) can be solved to find θ_4 . With known θ_4 Eq. (8.2.30) becomes:

$$e^{\xi_5\theta_5} = e^{-\xi_e\theta_e}e^{-\xi_4\theta_4}g_4 \quad (8.2.32)$$

Equation (8.2.32) can be solved for θ_5 by applying both parts of the equation to a point \mathbf{p}_5 that does not lie on ξ_5 .

Condition B: Intersection of the twists ξ_1 and ξ'_2 (transformed twist ξ_2 due to the pseudo-joints group b induced transformation) First the intersection point of the two twists must be calculated. The twist ξ_2 is given as [29]:

$$\hat{\xi}_2 = [\hat{\omega}_2 \widehat{\omega_2} \cdot r_2 00] \quad (8.2.33)$$

where $\hat{\omega}_2$ is the antisymmetric array of the unit vector ω_2 of the twist and \mathbf{r}_2 a point on ξ_2 . The transformed twist ξ'_2 is given as:

$$\hat{\xi}'_2 = Ad_{e^{\xi_b \theta_b}} \hat{\xi}_2 = e^{\xi_b \theta_b} \hat{\xi}_2 e^{-\xi_b \theta_b} \quad (8.2.34)$$

From Eq. (8.2.34) the unit vector of the transformed twist ξ'_2 may be determined. Additionally point \mathbf{r}_2 is transferred to a new position as:

$$r'_2 = e^{\xi_b \theta_b} r_2 \quad (8.2.35)$$

Given $\omega'_2, \mathbf{r}'_2, \omega_1, \mathbf{r}_1$ (the last two concern the twist ξ_1) it is easy to geometrically determine the intersection point \mathbf{q} of $e^{\xi_1 \theta_1}$ and $e^{\xi_b \theta_b} e^{\xi_2 \theta_2}$.

To solve Eq. (8.2.35) for the joint variables, first its two parts are applied to a point \mathbf{p}_5 lying on ξ_5 , resulting in:

$$e^{\xi_1 \theta_1} e^{\xi_b \theta_b} e^{\xi_2 \theta_2} e^{\xi_c \theta_c} e^{\xi_3 \theta_3} e^{\xi_d \theta_d} e^{\xi_4 \theta_4} p'_5 = g_3 p_5 \quad (8.2.36)$$

where $p'_5 = e^{\xi_c \theta_c} e^{\xi_5 \theta_5} p$. Subtracting from both parts of Eq. (8.2.36) the point of intersection \mathbf{q} of $e^{\xi_1 \theta_1}$ and $e^{\xi_b \theta_b} e^{\xi_2 \theta_2}$ yields:

$$\begin{aligned} & e^{\xi_1 \theta_1} e^{\xi_b \theta_b} e^{\xi_2 \theta_2} e^{\xi_c \theta_c} (e^{\xi_3 \theta_3} e^{\xi_d \theta_d} e^{\xi_4 \theta_4} p'_5 - e^{-\xi_c \theta_c} e^{-\xi_2 \theta_2} e^{-\xi_b \theta_b} e^{-\xi_1 \theta_1} q) \\ &= g_3 p_5 - q \Rightarrow e^{\xi_1 \theta_1} e^{\xi_b \theta_b} e^{\xi_2 \theta_2} e^{\xi_c \theta_c} (e^{\xi_3 \theta_3} e^{\xi_d \theta_d} e^{\xi_4 \theta_4} p'_5 - q') \\ &= g_3 p_5 - q \end{aligned} \quad (8.2.37)$$

where $e^{-\xi_c \theta_c} e^{-\xi_2 \theta_2} e^{-\xi_b \theta_b} e^{-\xi_1 \theta_1} q = e^{-\xi_c \theta_c} q = q' =$. Since the transformations retain the lengths, taking the measures of its two members of Eq. (8.2.37) yields:

$$\|e^{\xi_3 \theta_3} e^{\xi_d \theta_d} e^{\xi_4 \theta_4} p'_5 - q'\| = \|g_3 p_5 - q\| \quad (8.2.38)$$

Equation (8.2.38) can be solved for θ_3, θ_4 under the following prerequisites [32]:

Prerequisite B1. The twists ξ_3 and ξ'_4 intersect. The intersection of the two is calculated by the same procedure used to find the intersection of $e^{\xi_1 \theta_1}$ and $e^{\xi_b \theta_b} e^{\xi_2 \theta_2}$. The solution process is presented in detail in [32].

Prerequisite B2. The twists ξ_3 and ξ'_4 are parallel. The solution process is also presented in detail in [32].

Case of no possible solution: In the case that ξ_3, ξ'_4 are skew, Eq. (8.2.38) results in an 8th degree equation, which has no analytical solution [32].

In case either of the prerequisites B1 and B2 are satisfied, Eq. (3.38) may be analytically solved and providing the values of θ_3, θ_4 . Given these, Eq. (8.2.36) is transformed into:

$$e^{\xi_1 \theta_1} e^{\xi_b \theta_b} e^{\xi_2 \theta_2} p''_5 = g_3 p_5 \quad (8.2.39)$$

where $e^{\xi_c \theta_c} e^{\xi_3 \theta_3} e^{\xi_d \theta_d} e^{\xi_4 \theta_4} p'_5 = p''_5$. Equation (8.2.39) may be solved for θ_1, θ_2 following the same procedure utilized in solving Eqs. (8.2.29) and (8.2.30). Given the values of the variables of the first joints, Eq. (8.2.23) is transformed into:

$$e^{\xi_5 \theta_5} = e^{-\xi_e \theta_e} e^{-\xi_4 \theta_4} e^{-\xi_d \theta_d} e^{-\xi_3 \theta_3} e^{-\xi_c \theta_c} e^{-\xi_2 \theta_2} e^{-\xi_b \theta_b} e^{-\xi_1 \theta_1} g_3 = g_4 \quad (8.2.40)$$

Equation (8.2.40) is resolved as Eq. (8.2.32) to find the value of θ_5 . Finally, the proposed methodology produces a maximum of 8 solutions for the inverse kinematics problem of a metamorphic structure of 5 D.o.F.

8.2.1.4 6 D.o.F. Metamorphic Structures

The considered general metamorphic structure is presented in Fig. 8.1.

An expression of the forward kinematics of the structure is the following:

$$e^{\xi_a \theta_a} e^{\xi_1 \theta_1} e^{\xi_b \theta_b} e^{\xi_2 \theta_2} e^{\xi_c \theta_c} e^{\xi_3 \theta_3} e^{\xi_d \theta_d} e^{\xi_4 \theta_4} e^{\xi_5 \theta_5} e^{\xi_6 \theta_6} g_{st}(0) = g_d \quad (8.2.41)$$

The analytical solution of the inverse kinematic for a structure 6 D.o.F. is possible only if three consecutive joints have twists that intersect at the same point, as Pieper proved [25]. In the presented solution this is considered to take place at the last three joints, as shown in Eq. (8.2.41). Here they intersect at the same point forming the wrist of the structure. If the transformation on both parts of Eq. (8.2.41) are isolated and applied to the point of intersection of the twists of the last three joints, \mathbf{p}_{wrist} , yields:

$$\begin{aligned} & e^{\xi_1 \theta_1} e^{\xi_b \theta_b} e^{\xi_2 \theta_2} e^{\xi_c \theta_c} e^{\xi_3 \theta_3} e^{\xi_d \theta_d} e^{\xi_4 \theta_4} e^{\xi_5 \theta_5} e^{\xi_6 \theta_6} p_{wrist} \\ &= e^{-\xi_a \theta_a} g_d g_{st}^{-1}(0) p_{wrist} \Rightarrow e^{\xi_1 \theta_1} e^{\xi_b \theta_b} e^{\xi_2 \theta_2} e^{\xi_c \theta_c} e^{\xi_3 \theta_3} p = \mathbf{q} \end{aligned} \quad (8.2.42)$$

where $\mathbf{q} = e^{-\xi_a \theta_a} g_d g_{st}^{-1}(0) p_{wrist}$, $e^{\xi_4 \theta_4} e^{\xi_5 \theta_5} e^{\xi_6 \theta_6} p_{wrist} = p_{wrist}$ because point \mathbf{p}_{wrist} lies in the twists ξ_4, ξ_5, ξ_6 and, $e^{\xi_d \theta_d} p_{wrist} = p$ since the transformation introduced by the pseudo-joints group d is known. Equation (8.2.42) is the same as Eq. (8.2.12) used for the solution of the inverse kinematics problem for structures of three D.o.F. Therefore, following the same methodology it can be solved for the values of the variables $\theta_1, \theta_2, \theta_3$.

Knowing the values of the variables of the first three joints Eq. (8.2.42) may be transformed as:

$$e^{\xi_4 \theta_4} e^{\xi_5 \theta_5} e^{\xi_6 \theta_6} = e^{-\xi_d \theta_d} e^{-\xi_3 \theta_3} e^{-\xi_c \theta_c} e^{-\xi_2 \theta_2} e^{-\xi_b \theta_b} e^{-\xi_1 \theta_1} e^{-\xi_a \theta_a} g_d g_{st}^{-1}(0) \quad (8.2.43)$$

Equation (8.2.43) is a simpler expression of Eq. (8.2.2) and can be solved by applying the method presented for 3 D.o.F. structures. At the end of the above operations, a total of 8 solutions to the inverse kinematic problem for structures 6 D.o.F.

8.3 Metamorphic Manipulator Dynamics

8.3.1 Lagrange Formulation of the Dynamic Model for a Serial Metamorphic Manipulator

The dynamic model of a manipulator provides a description of the relationship between the joint actuator torques and the motion of the structure. Definitions and string notation presented in Section definitions are utilized to describe the structure of a SMM. The key coordinate systems attached to a metamorphic manipulator are illustrated in Fig. 8.6.

Here, the metamorphic structure's dynamic model is extracted through the Lagrange formulation. This choice stems from two key reasons. Firstly, it is systematic and can be adapted to the characteristics of a metamorphic serial structure. Secondly, it provides the equations of motion in a compact analytical form, alongside with the matrices that are necessary for control design. In order to extract the

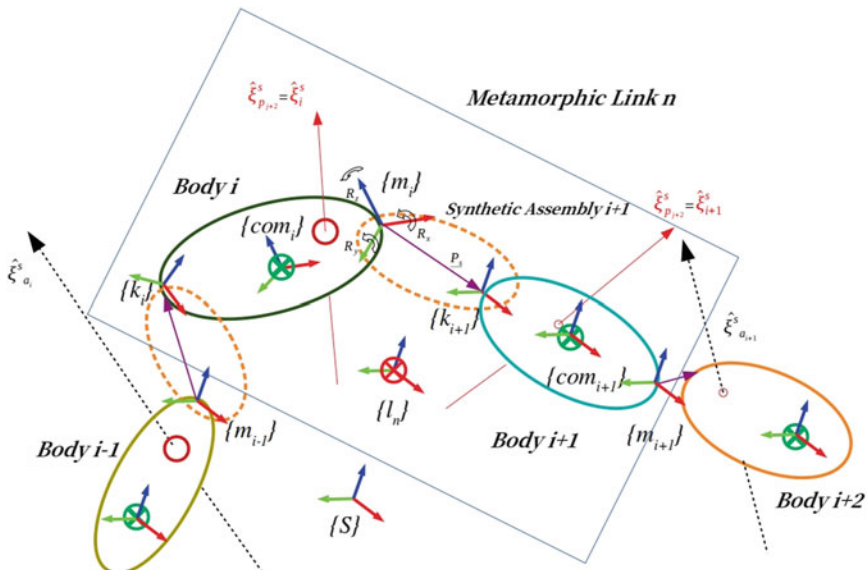


Fig. 8.6 Coordinate frames for the modelling of a Serial Metamorphic Manipulator

Inertia and Coriolis matrices of a serial metamorphic structure, the structure's kinematics are developed using the Product of Exponentials (POE) formula as shown previously in the chapter.

8.3.1.1 Generalized Inertia Matrix

In metamorphic manipulators, structure assembly parameters $s \in R^{6 \times n_s}$ and metamorphic parameters $\theta_p \in V^m$ should be integrated the calculation of the Generalized Inertial Matrix. The key attribute that should be taken into consideration is that mass distribution of the links is not predetermined. Therefore, the Link Inertia Matrix (LIM) should be extracted after the assembly of a metamorphic structure.

The individual tasks for metamorphic structure assembly and Generalized Inertial Matrix computation are presented in Fig. 8.7.

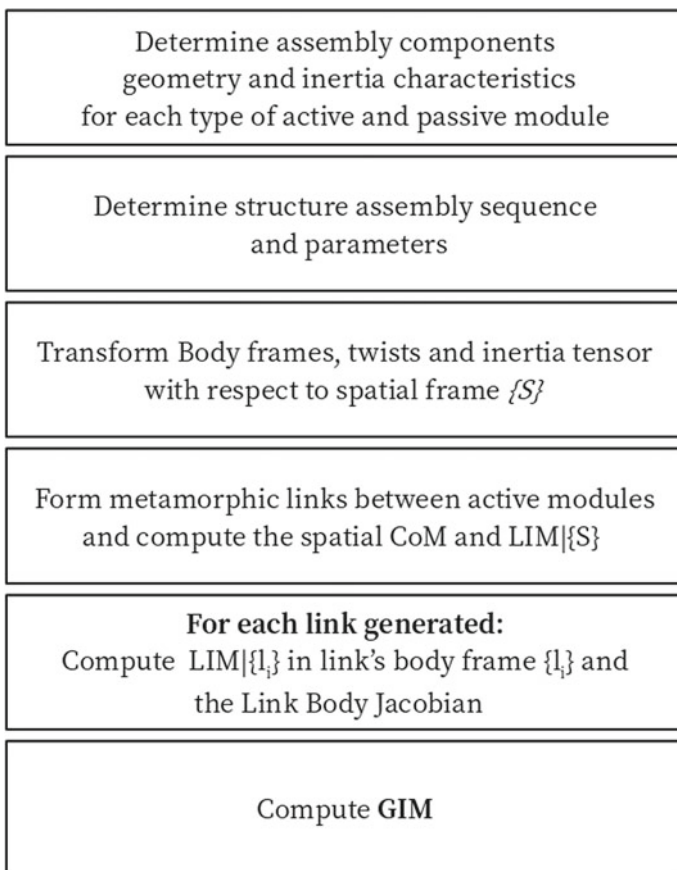


Fig. 8.7 Generalized inertia matrix calculation steps

First, the bodies that will be assembled inside the metamorphic structure must be defined. For the active modules and pseudo joints, used to structure the metamorphic structure, the following aspects are provided:

- the reference transformation between two connection frames $g_{k_{i+1}m_{i+1}}$
- the body twist with relation to the rotational motion generated by the module's axis $\hat{\xi}_{i+1}^b$
- the Centre of Mass of each body's $g_{COM_{i+1}}$ with respect to the body's connecting frame m_i and
- the body inertia matrix M_i^b with respect to the body's Center of Mass.

Next the desired assembly of the metamorphic structure is introduced with the corresponding assembly parameters s . The local parameterization defined by a set of 6 parameters $s = \{R_s, P_s\} \in R^6$ for the synthetic assembly $i + 1$ corresponds to a homogeneous transformation matrix $g_{syn_{i+1}} \in SE(3)$. After the assembly of a body, the new spatial transformation of the last connecting frame $g_{sm_{i+1}}$ is determined as:

$$g_{sm_{i+1}} = g_{sm_i} \cdot g_{syn_{i+1}} \cdot g_{k_{i+1}m_{i+1}} \quad (8.2.47)$$

Utilizing the adjoint transformation the twist and the inertia matrix of the last assembled body is expressed with respect to spatial frame as:

$$\hat{\xi}_{i+1}^s = g_{sk_{i+1}} \cdot \hat{\xi}_{i+1}^b \cdot g_{sk_{i+1}}^{-1} = Ad_{g_{sk_{i+1}}} \cdot \hat{\xi}_{i+1}^b \quad (8.2.48)$$

$$M_i^s = Ad_{g_{sk_{i+1}}}^T \cdot M_i^b \cdot Ad_{g_{sk_{i+1}}}^{-1} \quad (8.2.49)$$

Anatomy metamorphosis can be integrated in the assembly calculations, given the reference pseudo joint twists and the desired anatomy $\theta_P \in Q^{n_p}$. The only difference between the reference and a desired anatomy assembly is that when the j th pseudo joint module is assembled the reference passive twist is transformed due to the rotation induced by the change of preceding pseudo joints' angles setting given in θ_P .

$$\hat{\xi}_{p_j}^{s'} = Ad_{e^{\hat{\xi}_{p_1}\theta_{p_1}} \cdot e^{\hat{\xi}_{p_{j-1}}\theta_{p_{j-1}}}} \cdot \hat{\xi}_{p_j}^s \quad (8.2.50)$$

and the spatial transformation of the pseudo joint calculated for reference anatomy in Eq. (8.2.47)

$$g'_{sm_{i+1}} = e^{\hat{\xi}_{p_j}^{s'}\theta_{p_j}} g_{sm_{i+1}} \quad (8.2.51)$$

A metamorphic link m is constructed, for each desired structure and anatomy, by all the intermediate bodies (pseudo joints) m_i between two active modules. Since all spatial transformations for the Centre of Mass and inertia of the link's bodies are extracted, the spatial transform of the link's Centre of Mass g_{sm_n} and Inertia Matrix

M_m^s can easily be determined as:

$$M_m^s = \sum_{x=1}^{m_i} M_x^s \quad (8.2.52)$$

As presented earlier in the chapter, the reference anatomy of a metamorphic structure is defined by setting all the metamorphic parameters equal to zero. At this anatomy and for each link generated, the Link Inertia Matrix with respect to the link's Centre of Mass M_n^b and the Body Jacobian of each link required for dynamic modeling may be determined. Given the extracted M_n^s it stands that:

$$M_n^b = Ad_{g_{s_{l_n}}}^T \cdot M_n^s \cdot Ad_{g_{s_{l_n}}} \quad (8.2.53)$$

Next, the Link Body Jacobian matrices must be determined utilizing the method presented in [29]. Given the total number of active modules and the number of the intermediate pseudo-joints, the structure assembly sequence is determined. First the adjoint transformation $A_{ln} \in R^{6x6}$ is computed. The coordinates for each link's Center of Mass frame are expressed with respect to the spatial frame given the exponentials that relate to the relative rotation induced by the active and pseudo modules of the structure. Given a metamorphic structure, with z pseudo joints between active joints $n + 1$ and $n + 2$, then for the l^{th} active joint the adjoint transformation of the n th column is given by:

$$\begin{aligned} A_{ln} = & \{Ad_{e^{\hat{\xi}_{a_{n+1}} \cdot q_{a_{n+1}}} \cdot e^{\hat{\xi}_{p_1} \cdot q_{p_1}} \cdots e^{\hat{\xi}_{p_z} \cdot q_{p_z}} \cdot e^{\hat{\xi}_{a_{n+2}} \cdot q_{a_{n+2}}} \cdots e^{\hat{\xi}_{a_l} \cdot q_{a_l}}}^{-1} \\ & nI \quad l = \\ & n0 \quad l < n \end{aligned} \quad (8.2.54)$$

Therefore, the l th Link Body Jacobian is given as:

$$J_l^b = Ad_{g_{s_{l_n}}}^{-1} \cdot \left[A_{l1} \hat{\xi}_l^{-1} \dots A_{ll} \hat{\xi}_l^{-1} 0 \dots 0 \right] \quad (8.2.55)$$

Finally, the elements of the GIM of a metamorphic manipulator are calculated as:

$$M_{ln}(\Theta, \Theta_p, s) = \sum_{x=\max(l,n)}^{n_a} \hat{\xi}_l^{sT} \cdot A_{xl}^T \cdot M_x^s \cdot A_{xl} \cdot \hat{\xi}_l^s \quad (8.2.56)$$

As in the case of serial manipulators with only active joints, the dynamic attributes can be determined directly from active $\hat{\xi}_{a_i}$ and pseudo joint $\hat{\xi}_{p_i}$ twists, the link's Center of Mass extracted only for the reference anatomy of each structure and the link inertia matrices with respect to body frame. Kinematic complexity introduced by the additional coordinate frames of the pseudo joints and the abstract synthetic assembly is reduced to additional exponential terms in the forward kinematic mapping. The

powerful effect of applying screw theory, is portrayed in the simplification of the forward kinematic mapping and the frame-invariance of the presented equations.

8.3.1.2 Coriolis Matrix

Taking advantage of the procedure presented for the derivation of the Generalized Inertia Matrix and given Eqs. (8.2.54) and (8.2.55) the Coriolis matrix may be easily determined, as proposed in [29].

$$C_{ln}(\Theta, \Theta_p, s) = \sum_{w=1}^{n_a} \left(\frac{\partial M_{ln}}{\partial \Theta_w} + \frac{\partial M_{lw}}{\partial \Theta_n} - \frac{\partial M_{wn}}{\partial \Theta_l} \right) \cdot \Theta_w \quad (8.2.57)$$

where

$$\frac{\partial M_{ln}}{\partial \Theta_w} = \sum_{x=\max(l,n)}^{n_a} \left([A_{wl}\xi_l, \xi_w]^T A_{xw}^T M_x A_{xn} \xi_n + \xi_l^T A_{xl}^T M_x A_{xw} [A_{wn}\xi_n, \xi_w] \right) \quad (8.2.58)$$

8.4 Design of a Metamorphic Structure

8.4.1 General Design Conditions for Simple Dynamics of Fixed Structure Robots

The simplification of a robotic manipulator system in order to enhance analysis and control has been on the forefront of research for the past decades. Robot structure design plays a key role on the dynamic behaviour of the manipulator. Studies presented in [33–37] specified some general design conditions for designing fixed structure manipulators. Robotic structure modification through *mass-inertia distribution* is the most common approach utilized. The discussed guidelines for eliminating the coefficients of non-linear terms in robot's energy equation, simplifying the energy equation from terms generated by relative motion of articulated bodies, and eliminating the configuration dependent terms in the elements of the GIM, lead to the redesign of the manipulator links and the alteration of the robot assembly. Although the physical interpretation is enhanced using these techniques, modifying the robot links for each desired task cannot be regarded as the optimal solution.

Serial Metamorphic Manipulators can overtake this obstacle through anatomy metamorphosis. Link mass can be redistributed through the change of the metamorphic parameters. Since links consist of several pseudo joints, altering the metamorphic parameters can lead to a new manipulator with different dynamic characteristics.

Utilizing the analytic computation of the dynamic model for each structure of a serial metamorphic manipulator, the dynamic performance of each structure can be evaluated. Given the desired performance characteristics an optimal structure can then be determined.

8.4.2 Dynamic Isotropy Investigation

Optimizing the dynamic characteristics of a Serial Metamorphic Manipulator is a complicated design problem. One of the key aspects is the determination of the effect of a metamorphic structure in the optimization of the dynamic characteristics of the manipulator. Here, the key attribute of interest is *dynamic isotropy*, as defined as a physical concept in [23, 39]. Dynamic isotropy is investigated, by examining global attributes of the metamorphic structure in the manipulator's configuration space. It is strongly dependent on manipulator's inertia characteristics and greatly varies within the manipulator's workspace. A physical interpretation of this characteristic can be given from different viewpoints. From the joints point of view, the moment of inertia of an isotropic manipulator remains constant, while from the end-effector point of view, uniform acceleration characteristics of the end-effector are achieved.

The *Dynamic Conditioning Index* (DCI) was proposed as a measure of the degree of isotropy of the Generalized Inertia Matrix in [39]. It is a configuration-dependant measure of the “distance” between the current manipulator configuration and a dynamically isotropic posture. Minimum DCI values correspond to configurations close to isotropy. Since DCI relates only to the Generalized Inertia Matrix, it is independent with respect to the motion of the first active joint of the manipulator. As such, DCI is calculated at each point of the configuration space as the sum of the weighted errors between the Generalized Inertia Matrix and a diagonal matrix and when appropriately expanded, exceeds the dimension variant limitation, and becomes suitable for comparing manipulator structures of different architectures. The DCI is determined using Eqs. (8.2.59)–(8.2.61) bellow.

$$E(\Theta, \Theta_p, s) = \frac{1}{\sigma} \cdot (M(\Theta, \Theta_p, s) - \sigma \cdot I) \quad (8.2.59)$$

$$\sigma = \frac{\text{tr}(M^2)}{\text{tr}(M)} \quad (8.2.60)$$

$$DCI = \frac{1}{2} e^T W e \quad (8.2.61)$$

where, W a $n \times n$ diagonal weighting matrix and e is an $n(n + 1)/2$ -dimensional vector composed of the upper triangular components of the matrix defined in Eq. (8.2.59) and I denote the identity matrix. Positive scalar σ defined in Eq. (8.2.60) is used as a strict value for the lower bound of the Generalized Inertia Matrix and for the

deletion of the dimensions in the index calculations. Although such a new definition renders the index dimensionless, its computation, however, is more complex when implemented for higher DoF.

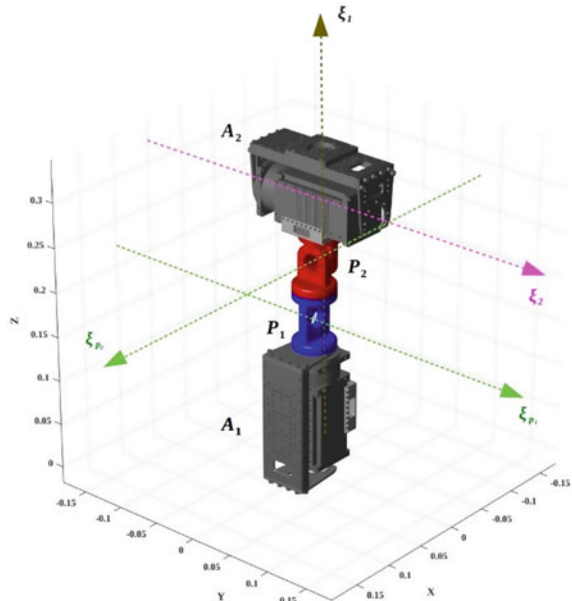
8.4.3 Evaluation and Synthesis of a Serial Metamorphic Structure

8.4.3.1 Evaluation of a 2 DoF Serial Metamorphic Structure

In this example, a simple investigation of the Generalized Inertia Matrix elements, for a simple Serial Metamorphic Manipulator structure, will be presented. The goal is to illustrate the benefits of anatomy metamorphosis considering inertia optimization. The 2 DoF Metamorphic Manipulator considered, presents the modular structure assembly sequence 0-1-1-0 and is illustrated in Fig. 8.8, at the reference anatomy, where the active joints axes are orthogonal. The first link of the manipulator consists of two pseudo joints in orthogonal configuration. Abstract pseudo joints are modelled in Fig. 8.8 in order to help visualize the metamorphic link.

For this structure the expressions to determine the optimal metamorphic parameters values for Generalized Inertia Matrix optimization can be analytically extracted as shown in [40]. The Generalized Inertia Matrix $M \in R^{2x2}$ elements are extracted from Eq. (8.2.56). \mathbf{M}_{11} is always positive and therefore only anatomies that achieve

Fig. 8.8 2 DoF
metamorphic manipulator at
reference anatomy



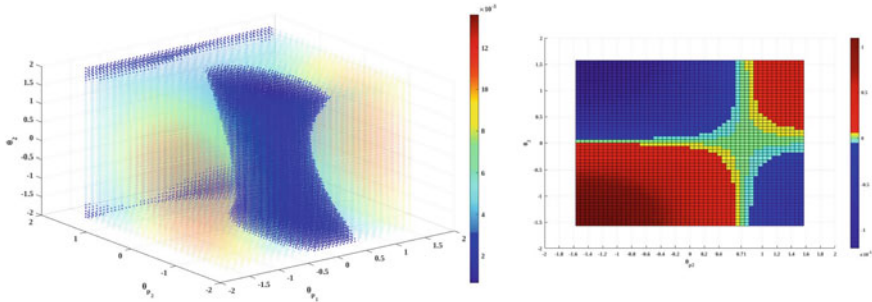


Fig. 8.9 Optimal metamorphic parameter values: (left) illustration of M_{11} , (right) illustration of the optimal value of θ_{p2} for decoupled inertia at $\theta_{p1} = 1.5708$ radians

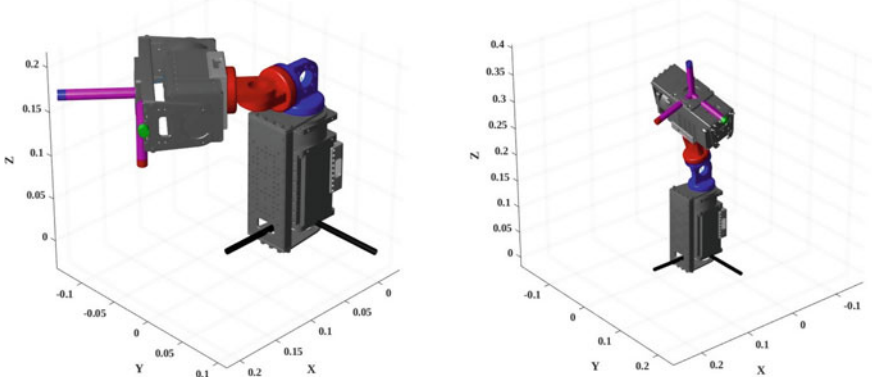


Fig. 8.10 Derived optimal anatomies: (left) dynamic decoupled anatomy, (right) anatomy with configuration invariant diagonal elements

minimal values are searched while for isotropy the off-diagonal element M_{12} is targeted to be equal to zero. In Fig. 8.9 the optimization results are presented graphically and two of the extracted anatomies are presented in Fig. 8.10.

Inertia redistribution leading to a decoupled and configuration invariant inertia matrix can be achieved through anatomy metamorphosis, without the need of disassembling the robot structure or adding new parts. Relative to fixed structure robots, orthogonality of the active joints axes is also preserved for dynamic decoupling.

8.4.3.2 3 DoF SMM Structure Synthesis

In this example, the synthesis of a metamorphic chain considering dynamic isotropy is presented. The modelling principles described in the previous sections and the methodology proposed in [41] are utilized to this effect. In order to simplify this

example two limitations are regarded. First, different connectivity surfaces are not considered, and a synthetic assembly is only introduced between the first pseudo joint of each link and the preceding active module.

For a metamorphic manipulator with n_s synthetic assemblies and n_p pseudo joints, dynamic isotropy is investigated by expanding the DCI local performance index presented previously to form a global \widehat{DCI} index of the manipulator's configuration space, as:

$$\widehat{DCI} = \underbrace{\text{minimize}}_{(\underline{R}_i, \underline{P}_i, \underline{w}, \Theta_p)} (\max(f_1)) \quad (8.2.62)$$

subject to $\underline{w} \in [0.1, 1]^3$, $\underline{R}_i \in [R_{\min}, R_{\max}]^3$, $\underline{P}_i \in [P_{\min}, P_{\max}]^3$, $i = 1 \dots n_s$, $\Theta_p \in [-\frac{\pi}{2}, \frac{\pi}{2}]^{n_p}$

$$\begin{aligned} f_1 &= \{DCI_{off}(\underline{R}_i, \underline{P}_i, \underline{w}_{off}, \underline{\Theta}_p, \Theta), \underline{w}_{off} \\ &= [0, w]DCI_{diag}(\underline{R}_i, \underline{P}_i, \underline{w}_{diag}, \underline{\Theta}_p, \Theta), \underline{w}_{diag} = [w, 0]\} \end{aligned} \quad (8.2.63)$$

Vector \underline{w} is constructed from the diagonal elements of weighting matrix W shown in Eq. (8.2.61). The assembly parameters R_i, P_i parameterize the local transformation induced by the synthetic assembly and Θ_p is the vector of the metamorphic variables of each structure. The double objective function given in Eq. (8.2.63) is selected since a separate DCI value is extracted for the diagonal and the off-diagonal Generalized Inertia Matrix elements, by setting the corresponding weighting factors of matrix W to zero. Due to the boundedness property of the Generalized Inertia Matrix, off-diagonal elements achieve zero values (dynamic decoupling) while diagonal elements lean towards a minimum value $\mu_i > 0$ (dynamic isotropy).

Structure synthesis is generated utilizing a genetic algorithm. The chromosome \underline{x} is formed using a floating-point number to randomly determine the configuration space points, the assembly parameters for each synthetic assembly of the structure and the DCI weighting factors. The DCI based objective functions are calculated for a set of points in the configuration space of the reference anatomy of each structure. The population size selected for each generation is 1000. The maximum number of generations produced is 2000. For each gene of the population two fitness values are extracted from Eq. (8.2.63) and the average Pareto distance is calculated. Tournament selection procedure is then implemented. The next generation is formed using 10% elite children from the previous one, 70% from the crossover operations and 20% from the mutation operations. Intermediate crossover and adaptive feasible mutation methods are implemented.

For the best structures extracted for each assembly sequence from genetic algorithm optimization, anatomy metamorphosis is exhaustively performed in order to examine the variation of the inertial properties for the set of structure's emerging anatomies. The score function, to determine the best structure considering anatomy

richness is:

$$f_2 = p_a^{f_{eas.}} f_{best}^{-1} \quad (8.2.65)$$

The ratio of optimal feasible anatomies to structure's total anatomies ($p_a^{f_{eas.}}$) is used as a factor that enhances the best (minimum) global DCI value (f_{best}) among all feasible anatomies. The overall results are presented in Table 8.1. The extracted optimal structures and the highest scoring anatomy of each structure are illustrated in Figs. 8.11, 8.12 and 8.13.

Table 8.1 Optimization procedure results

(a) Optimized parameters

i	MSR	Assembly parameters		f_{ref}	f_1	
1	0&10&10#	[0, -1.57, 1.26] [0.14, 0.14, 0.14]	[-1.22, -1.57, 1.08] [0.11, 0.11, 0.15]	0.0585	0	0.0550
2	0&10&110#	[0.03, -1.35, 0.81] [0.10, 0.09, 0.11]	[1.09, -1.46, - 1.08] [0.04, 0.03, 0.05]	0.0507	0	0.0585
3	0&110&10#	[0.15, 0.25, - 0.96] [0.03, 0.07, 0.13]	[-0.98, -1.41, 1.01] [0.05, 0.01, 0.05]	0.0653	0	0.0692
4	0&10&110#	[-1.03, -1.57, -1.27] [0.02, 0.06, 0.10]	[-0.13, -0.18, -0.52] [0.08, 0.02, 0.01]	0.1156	0	0.1295
5	0&110&110#	[0.01, -0.74, 1.01] [0.14, 0.10, 0.11]	[1.35, 1.06, - 1.33] [0.03, 0.09, 0.10]	0.0600	0.0001	0.0581
6	0&110&110#	[0.02, 0.51, - 1.32] [0.03, 0.12, 0.10]	[1.04, -1.36, 0.060] [0.06, 0, 0.04]	0.0540	0.0003	0.0647
7	0&110&10#	[0.15, 0.24, - 0.96] [0.03, 0.07, 0.13]	[-0.97, -1.41, 1.01] [0.05, 0, 0.05]	0.0607	0.0084	0.0758

(b) Exhaustive anatomy evaluation of optimization structures

i	N_p^{used}	N_a^{best}	$N_a^{f_{eas}}$	N_a^{tot}	f_{best}	$P_a^{f_{eas}}(\%)$	f_2
1	2	11	9	49	0.0517	18.37	3.5527
2	3	7	4	343	0.0507	1.17	0.2301
3	3	15	8	343	0.0611	2.33	0.3817
4	3	287	231	343	0.0959	67.35	7.0226
5	4	22	12	2401	0.0590	0.50	0.0847
6	4	20	12	2401	0.0531	0.50	0.0941
7	3	1	1	343	0.0607	0.29	0.0480

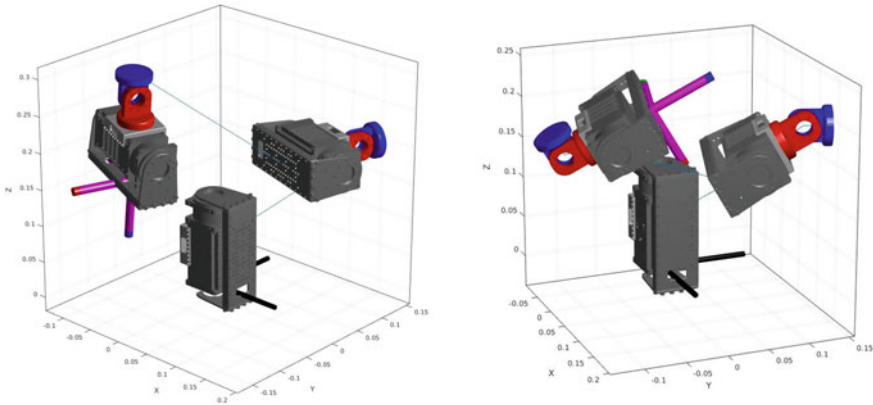


Fig. 8.11 Optimized structure ($i = 1$): (left) reference anatomy, (right) best anatomy $\theta_p = (-0.5236, -1.5708)$

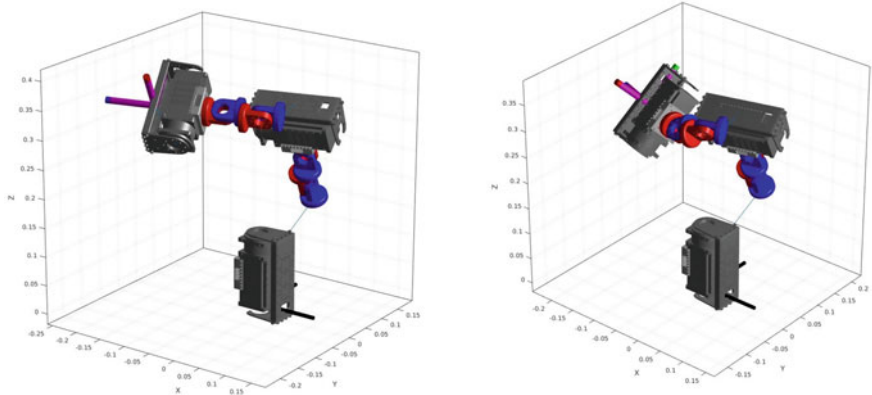


Fig. 8.12 Optimized structure ($i = 6$): (left) reference anatomy, (right) best anatomy $\theta_p = (0, 0, -0.5236, -0.5236)$

8.5 Conclusions

The implementation of robotic manipulators and systems in general to increasing aspects of human life and work presents a clear challenge to the research community and robot manufacturing organizations: “*How to best progress robot design in order to allow for a seamless and viable incorporation of robots everywhere and for every task?*” Since the beginning of their utilization as tools (mostly industrial and in lab applications) robots were adapted to different tasks requirements utilizing

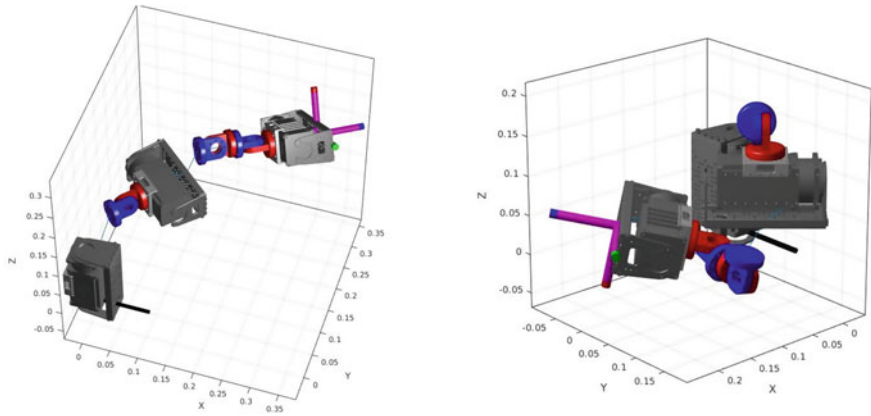


Fig. 8.13 Optimized structure ($i = 4$): (left) reference anatomy, (right) best anatomy $\theta_p = (-1.5708, -1.5708, -1.0472)$

indirect means, such as advanced control, censoring etc. As the field of their applications widened and subsequently the task requirements and performance requirements became more demanding and complex, different design paradigms were implemented, the most prominent one being that of modularity and reconfigurability. New systems designed under this paradigm were more complex and cost demanding as opposed to the widely used fixed anatomy systems, albeit being far more flexible with respect to the range of tasks to be performed. Up until now, such systems are shyly making their entrance to some robotic applications outside those of laboratory applications and demonstrators, as the requirements for higher task flexibility are becoming ever more increasing. The notion of investing to such a system lies in the balance of meeting the necessary requirements of the end user (higher task flexibility and increased performance in different applications by optimally matching the robots anatomy to each task) and the increased cost and time requirements of the system along with technical issues stemming from its complexity (such as control restructuring for each new anatomy, kinematic and dynamic problems solution for each new anatomy, fault tolerance, synchronization etc.). These issues aside however, reconfigurability has been identified formally as the main requirement of future robotic systems [1].

Metamorphic manipulators, as presented in the literature and the present chapter, present a solution to the aforementioned drawbacks of reconfigurable systems, and metamorphosis (and self-metamorphosis) has indeed also been identified as a future key aspect for robot implementation in the future [1]. Their main advantage stems from the segregation of the notions of *structure* and *anatomy* which is essentially the same for both fixed anatomy and reconfigurable robots. A single metamorphic structure may provide the possibility of being altered to a variation of different anatomies, without the requirement for physical changes in the structure and therefore requiring limited time and reducing the complexity of the process. Furthermore, the utilization of modular kinematics and dynamics (as presented in this chapter) allows

for the effortless and rapid control scheme adaptation, reducing the required effort, downtime, and man-hours for the process with respect to reconfigurable robots.

Research in the field of metamorphic manipulators is increasing and new designs and applications are already making their entrance in the relevant literature. Up to this point however, most, if not all, are mostly laboratory experimental systems and demonstrators, however efforts are coordinating to develop full scale systems in the near future. Due to their novelty, there are several research gaps or areas that require further research for this to take place. First and foremost, the design of hardware for these systems is still under consideration in the literature, with different approaches provided. Moreover, tools and methods for the optimal structuring, matching of anatomies to tasks, optimal control, optimal task planning etc. are still under heavy research, although several approaches are quite promising. Nevertheless, efforts should be steered in the direction of the design of an integrated metamorphic and self-metamorphic robotic system to allow its utilization in real applications.

Acknowledgements This research has been financially supported by General Secretariat for Research and Technology (GSRT) and the Hellenic Foundation for Research and Innovation (HFRRI) (Code: 1184)

References

1. Multi-Annual Roadmap (MAR) For Robotics in Europe (2022). <https://ec.europa.eu/digital-single-market/en/news/multi-annual-roadmap-call-ict-24-robotics-now-available>
2. Chirikjian, G.S.: Kinematics of a metamorphic robotic system. In: Proceedings of the 1994 IEEE International Conference on Robotics and Automation, pp. 449–455. IEEE (1994)
3. Koren, Y., Heisel, U., Jovane, F., Moriwaki, T., Pritschow, G., Ulsoy, G., Van Brussel, H.: Reconfigurable manufacturing systems. CIRP Ann. **48**(2), 527–540 (1999)
4. Mehrabi, M.G., Ulsoy, A.G., Koren, Y.: Reconfigurable manufacturing systems: key to future manufacturing. J. Intell. Manuf. **11**(4), 403–419 (2000)
5. Huang, C.C., Kusiak, A.: Modularity in design of products and systems. IEEE Trans. Syst. Man, Cybernet. Part A: Syst. Humans **28**(1), 66–77 (1998)
6. Schmitz, D., Khosla, P., Kanade, T.: The CMU reconfigurable modular manipulator system (1988)
7. Kereluk, J.A., Reza Emami, M.: A new modular, autonomously reconfigurable manipulator platform. Int. J. Adv. Robot. Syst. **12**.6, 71 (2015)
8. Matsumaru, T.: Design, and control of the modular robot system: TOMMS, robotics and automation. In: Proceedings of the International Conference on IEEE, vol. 2, pp. 2125–2131 (1995)
9. Tosi, D., et al.: Cheope: a new reconfigurable redundant manipulator. Mech. Mach. Theory **45**(4), 611–626 (2010)
10. Xu, W., et al.: A wireless reconfigurable modular manipulator and its control system. Mechatronics **73**, 102470 (2021)
11. Yun, A., et al. (2020). ModMan: an advanced reconfigurable manipulator system with genderless connector and automatic kinematic modeling algorithm. IEEE Robot. Autom. Lett. **5**(3), 4225–4232 (2020)

12. Carbonari, L., et al.: A new class of reconfigurable parallel kinematic machines. *Mech. Mach. Theory* **79**, 173–183 (2014)
13. Tang, X., Sun, D., Shao, Z.: The structure and dimensional design of a reconfigurable PKM. *Int. J. Adv. Rob. Syst.* **10**(6), 267 (2013)
14. Plitea, N., et al.: Structural design and kinematics of a new parallel reconfigurable robot. *Robot. Comp. Integrat. Manuf.* **29**(1), 219–235 (2013)
15. Hong, S., et al.: Design of manually reconfigurable modular manipulator with three revolute joints and links. In: 2016 IEEE International Conference on Robotics and Automation (ICRA). IEEE (2016)
16. Stravropodis, N.A., Valsamos, C., Moulianitis, V.C.: An integrated taxonomy and critical review of module designs for serial reconfigurable manipulators. In: International Conference on Robotics in Alpe-Adria Danube Region. Springer, Cham (2019)
17. Liu, G., Liu, Y., Goldenberg, A.A.: Design, analysis, and control of a spring-assisted modular and reconfigurable robot. *IEEE/ASME Trans. Mechatron.* **16**(4), 695–706 (2010)
18. Jia, G., et al.: Synthesis of a novel type of metamorphic mechanism module for large scale deployable grasping manipulators. *Mech. Machine Theory* **128**, 544–559 (2018)
19. Chen, I.-M.: Rapid response manufacturing through a rapidly reconfigurable robotic workcell. *Robot. Comp. Integrat. Manuf.* **17**, 199–213M (2001)
20. Stoy, K., et al.: Self-reconfigurable robots: an introduction. Cambridge: Mit Press (2010)
21. Bateau, J., et al.: Increasing the efficiency of distributed goal-filling algorithms for self-reconfigurable hexagonal metamorphic robots. In: Proceedings of the International Conference on Parallel and Distributed Processing Techniques and Applications (PDPTA). The Steering Committee of The World Congress in Computer Science, Computer Engineering and Applied Computing (WorldComp) (2012)
22. Salvi, A.Z., Simoni, R., Martins, D.: Enumeration problems: a bridge between planar metamorphic robots in engineering and polyforms in mathematics. In: Advances in Reconfigurable Mechanisms and Robots I. Springer, London, pp. 25–34 (2012)
23. Hogg, T.: Energy dissipation by metamorphic micro-robots in viscous fluids. *J. Micro-Bio Robot.* **11**(1), 85–95 (2016)
24. Ivanov, P., Walter, J.: Layering algorithm for collision-free traversal using hexagonal self-reconfigurable metamorphic robots. In: 2010 IEEE/RSJ International Conference on Intelligent Robots and Systems. IEEE (2010)
25. Craig, J.J.: Introduction to Robotics, Mechanics and Control. Addison – Wesley Publishing (1955)
26. Valsamos, C., Moulianitis, V., Aspragathos, N.: Index based optimal anatomy of a metamorphic manipulator for a given task. *Robot. Comp. Integrat. Manuf.* **28**(4), 517–529 (2012)
27. Valsamos, C., Moulianitis, V.C., Aspragathos, N.: Metamorphic structure representation: designing and evaluating anatomies of metamorphic manipulators. In: Advances in Reconfigurable Mechanisms and Robots I. Springer, pp. 3–11 (2012)
28. Moulianitis, V.C., et al.: Task-based optimal design of metamorphic service manipulators. *J. Mech. Robot.* **8**(6) (2016)
29. Murray, R.M., et al.: A mathematical introduction to robotic manipulation. CRC press (1994)
30. Selig, J.M.: Introductory Robotics. Prentice Hall Int, London (1992)
31. Stravropodis, N.A., et al.: Evaluation of serial metamorphic manipulator structures considering inertia characteristics. In: International Conference on Robotics in Alpe-Adria Danube Region. Springer, pp. 574–587 (2020)
32. Gao, Y.: Decomposable Closed-Form Inverse Kinematics for Reconfigurable Robots Using Product of Exponential Formula. Master Thesis, School of Mechanical and Production Engineering Nanyang Technological University (2000)
33. Yang, D.C.H., Tzeng, S.W.: Simplification and linearization of manipula-tor dynamics by the design of inertia distribution. *Int. J. Robot. Res.* **5**(3):120–128 (1986)
34. Youcef-Toumi, K., Asada, H.: The design of open-loop manipulator arms with decoupled and configuration-invariant inertia tensors (1987)

35. Chung, W.K., et al.: On the dynamic characteristics of balanced robotic manipulators. In: Japan-USA Symposium on Flexible Automation, Control and Design of Robotics. Japan-USA Symposium, pp. 119–126 (1986)
36. Park, H.S., Cho, H.S.: An approach to the design of ideal robotic manipulators having simple dynamic characteristics. In: Proceedings of the Institution of Mechanical Engineers, Part B: Management and Engineering Manufacture, vol. 201, no. 4, pp. 221–228 (1987)
37. Park, H.S., Cho, H.S.: General design conditions for an ideal robotic manipulator having simple dynamics. *Int. J. Robot. Res.* **10**(1), 21–29 (1991)
38. Matone, R., Roth, B.: Designing manipulators for both kinematic and dynamic isotropic properties. In: ROMANSY 11. Springer, pp. 99–106 (1997)
39. Ma, O., Angeles, J.: Optimum design of manipulators under dynamic isotropy conditions. In: Proceedings IEEE International Conference on Robotics and Automation, pp. 470–475. IEEE (1993)
40. Stravopodis, N.A., Moulianitis, V.C., Valsamos, C.: Investigation of dynamically decoupled anatomies for a serialmetamorphic manipulator. In: The International Conference of IFToMM ITALY, pp. 295–309. Springer (2020)
41. Stravopodis, N.A., Katrantzis, L., Moulianitis, V.C., Valsamos, C., Aspragathos, N.A.: Evaluation of serial metamorphic manipulator structures considering inertia characteristics. In: International Conference on Robotics in Alpe-Adria Danube Region, pp. 574–587. Springer, Cham (2000)

Chapter 9

Analysis of Redundancy and Elasticity of Actuators in Hopping Control of Bipedal Robot CARL Based on SLIP Model



Atabak Nejadfar, Nicolas Franz Schmitt, Steffen Schütz,
Krzysztof Mianowski, Patrick Vonwirth, and Karsten Berns

9.1 Introduction

Bipedal robotics strives to replicate human motion and locomotive skills. In [38], the authors elegantly emphasize the notion of embodiment in shaping biological intelligence. The embodiment essentially means that the design of control and body are intertwined. Bipedal control can be enhanced by an intelligent mechanical design that merges the technical characteristics of the robotic system with the insight provided by biomechanical studies.

It is widely established that human locomotion can be described by a simple mass and spring model [3, 4, 12]. This model is known as a spring-loaded inverted pendulum (SLIP) in which the whole leg acts like a virtual spring that is located between a lumped body mass and ground. However, the biological leg consists of a network of muscles that are coordinated so that the whole limb can act as a virtual spring.

Anatomical characteristics like muscle redundancy and elastic tendons in human musculature are equally important as the SLIP control policy itself. The stiffness of the Achilles tendon (AT) determines the frequency of human gait. The leg virtual spring stiffness during human hopping is modulated by the stiffness of the AT. The influence of the ankle complex on the spring-like action of the human leg is well documented.

Muscle redundancy in the form of biarticular muscles is another important feature that enables efficient locomotion. Biarticular muscles span more than two joints and

A. Nejadfar · N. F. Schmitt · S. Schütz · P. Vonwirth · K. Berns (✉)
Arbeitsgruppe Robotersysteme, Universitaät Kaiserslautern, Fachbereich Informatik, Postfach
3049, D-67653 Kaiserslautern, Germany
e-mail: berns@informatik.uni-kl.de

K. Mianowski
The Institute of Aeronautics and Applied Mechanics, Faculty of Power and Aeronautical
Engineering, Warsaw University of Technology, 00-665 Warsaw, Poland
e-mail: kmianowski@meil.pw.edu.pl

transfer power from proximal powerful muscles toward distal joints. This allows a better distribution of mass around the leg with heavy and power-producing muscles located close to the hip. The action of biarticular muscles in reducing the negative energy in movements is also elaborated in literature.

In this study, we focus on two mechanical features of the human limbs (a) muscle or motor redundancy and (b) spring-like tendons. Both of these attributes can be technically reproduced in robotic systems to understand their influence on locomotion control. Our objective is to analyze the intelligent design of the muscle-tendon system in a robotic platform in generating the desired virtual spring. Both of these characteristics of the human limb is widely ignored in SLIP analysis and control design.

We have implemented hopping control based on the SLIP model for musculoskeletal robotic leg CARL, shown in Fig 9.2a. This robot consists of elastic actuators with relatively soft springs that are associated with the action of the tendons in the human leg. The stiffness of the series elastic elements and their respective moment arms are similar as in human leg. CARL also features two biarticular actuators that demonstrate similar functionality as of biarticular muscles.

By comparing the robotic and human movements during hopping, we can experimentally analyze the influence of structural elements like elasticity and biarticularity on the efficiency of the locomotion. We report the biomechanical findings and provide experimental results that confirm our hypothesis that the bio-inspired mechanical design can indeed improve the performance of the SLIP control.

9.2 Literature Review

9.2.1 Virtual Spring in Robotics

As mentioned before, the major concept behind SLIP is the idea that the whole limb is acting as a virtual linear spring. This simple model provides a reduced-order dynamic representation of a legged system. Numerous studies have demonstrated its efficacy in stable locomotion [3, 12, 50, 58]. The control architecture of bipedal robots are implemented to deploy the virtual spring in robotic movements [49, 62]. New variations of control are recently released where the controller is either incorporating an extra swing leg or stability features [36, 64]. Several controllers are adapted to use the SLIP model in conjunction with classic optimal control or trajectory planning control of bipedal robots. For instance, the SLIP model is used to provide an open-loop stable trajectory where the classic controller is mapping the open-loop commands to the dynamics of the robot itself [11]. Such integration of upper-level SLIP control and lower level full dynamic control is also employed for control of robots *Cassie*, *ATRIAS* and *Biobiped* [13, 18, 46, 47, 59].

Apart from control implementation as a virtual spring, it is also possible to construct a robotic leg by directly deploying a physical spring. Pogo stick-like design

was introduced for hopping legs by Raibert in 80s [43, 44]. In this design, the leg is essentially one linear spring connected by a hip joint to the body of the robot. Afterward, more robots that have the capability to hop are designed that incorporate physical passive springs in their leg [51].

Recently the parallel mechanisms are introduced in leg structure to improve the maneuverability and increase ground reaction force (GRF) [60]. The parallel mechanisms are also used in the leg architecture of *Cassie* and *ATRIAS* robots [18, 47]. These mechanisms deviate from the series articulated structure of the biological limb to achieve a better actuator mass distribution and high force-to-mass density in the overall leg. The leg with parallel mechanisms often does not have an ankle joint to simplify the design and reduce the weight.

As we will discuss later on, the majority of the biomechanical studies of spring-like behavior are focused on the function of the ankle complex. The calf muscles and AT are the dominant contributors to efficient power production of virtual leg spring action. Unfortunately, the ankle joint is widely ignored in SLIP analyses. In fact, it is a common practice, to model a segmented leg only with hip and knee joint [32, 63]. Due to the simplicity of the mechanical design, the leg spring is rendered using only one knee joint. in this study, we will focus on influence of the active and passive elements of the ankle complex on leg spring control.

The SLIP model is intended to mirror the behavior of human locomotion without considering the underlying musculature architecture. The muscle activation and utilization of the passive elements in the body are critical to the efficiency of movements. Hopping movements are widely used in biomechanical studies to investigate the spring-like action of the leg. Especially that the recent advancement in measurement of the AT and its stiffness have shed light on how the central nervous system (CNS) can utilize the passivity in the joints to reach higher performance.

9.2.2 Biomechanics of Human Leg

Hopping Locomotion

During hopping, the human leg acts as a linear mass-spring system [5]. The human motion follows the same linear dynamics even when the stiffness and damping of the hopping surface are modified. When the hopping surface is less stiff, CNS responds by increasing the stiffness of the leg spring [10]. If the damping of the surface is increased, the leg would produce extra energy to compensate for the loss in the environmental damping [25]. The CNS adjusts the leg action during the stance phase of hopping so that the center of mass (COM) would act as a linear mass-spring system with respect to global ground.

When hopping on surfaces with different stiffnesses, the leg stiffness is mainly modulated with ankle stiffness. A 1.75-fold increase in ankle stiffness would result in a 1.7-fold gain in leg stiffness. To a lesser extent, the leg stiffness is sensitive to knee angle where the stiffness increases 1.3-fold by the change in the knee angle [10].

In the case of hopping over damped surfaces, most of the compensating mechanical energy is produced by ankle [25]. In a specific experiment, it is reported 52% of the positive energy is produced by the ankle and the rest of the energy is generated evenly by the hip and knee. In muscle level, the ankle and knee muscles have boosted their activity while the increase is much higher in the activity of ankle plantar flexor muscles. The stiffness of the leg is modulated by ankle stiffness and knee angle whereas the ankle joint is the dominant contributor.

Achilles Tendon

Achilles tendon is another influential element in modulating leg stiffness. Biological muscles consist of two major elements: fiber and tendon. The muscle fiber is the active unit producing the force and energy with an inherent damping characteristic. Tendons are passive elements that act as the series elastic element which can be deployed to store and recoil energy. Tendons belonging to proximal muscles in the thigh and pelvis are very stiff and therefore the recuperation of energy is minimal in these muscles. The structure of proximal muscles relies on producing work by changing

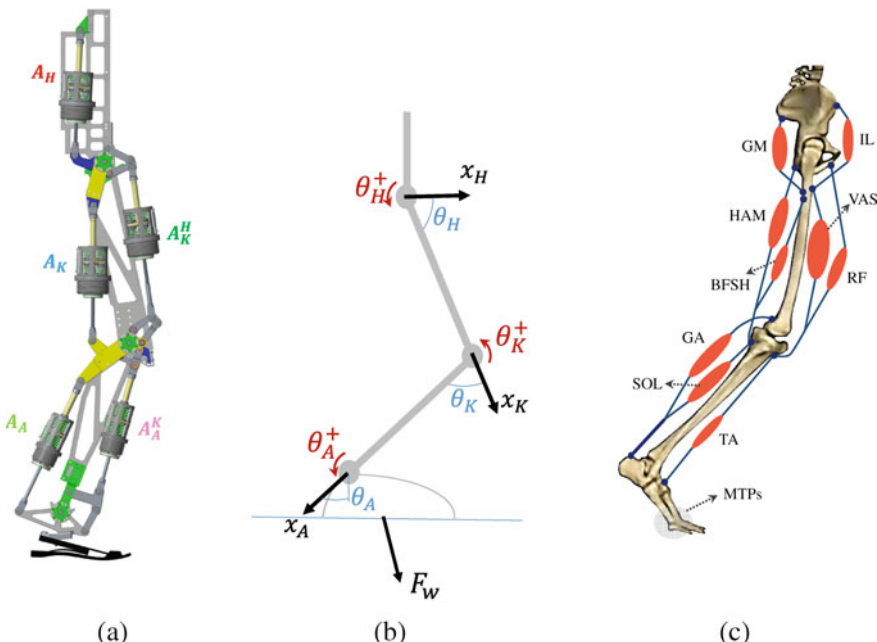


Fig. 9.1 **a** The CAD model of the planar robot CARL. CARL has 5 linear series elastic actuators. Three actuators in the backside of the leg are mono-articular. The two frontal actuators are the biarticular actuators. It is also equipped with a prosthetic foot. **b** The definition of the joint angles is illustrated which is used for calculating the moment arm values. **c** The abstraction of the major muscles, generating movements along the sagittal plane. The illustrated size of each muscle is associated with its physiological cross-sectional area. The insertion/origin sites of the muscles are inaccurately depicted for purpose of better visualization.

the fiber length. On the other hand, the distal muscles spanning the ankle joint are structured so that the muscle relies heavily on the tendon stretch and recoil [2, 65].

The ankle plantarflexors are Soleus (SOL) and Gastrocnemius (GA) muscles, see Fig 9.1c. They dominantly produce the force and work at the ankle joint. In order to increase their force and work yield, they have to store and release energy via AT. The stiffness of AT is relatively low in the range of 145–231 N mm⁻¹ which is suitable to recuperate energy during a variety of locomotive gaits [23]. It is reported that 35–40% of the work at the ankle is delivered by AT during vertical jump [1, 20]. In human walking gait, the energy is stored in the AT at the early stance phase and later on released during the push-off phase—known as catapult action [19].

The performance of the muscle fiber is restricted by the force-velocity and force-length characteristics so that muscle fiber's ability to generate contraction force depreciate significantly in higher velocities. By storing energy in the tendon, and releasing when high-velocity contraction occurs, e.g., during push-off, the muscle complex is able to generate required high forces in high velocities. This reduces the activity of the muscle fiber and hence its force output. It is shown during hopping, the natural frequency of movement is modulated based on the stiffness of AT. The optimal utilization of AT reduces the cost of producing force in the muscle over the range of the surface stiffnesses [9, 24].

Muscle Redundancy

CNS controls the movement of the limb in a way that its emergent behavior can be abstracted as a virtual spring. Legged locomotion is a consequence of the coordination of numerous muscles in the human body. Human leg has 11 kinematic degrees of freedom (DOFs) actuated by 57 muscles [37]. In addition to the complex dynamics of the human limb, each muscle has its own internal fiber and tendon dynamics.

Muscle redundancy contributes substantially to the efficiency of locomotion. One peculiar source of muscle redundancy is biarticular muscles (BiMs). They span two joints and when activated drive simultaneously either joints in contrast to the standard mono-articular muscles (MoMs) which span only one joint. These muscles are highly utilized in the locomotive limbs of humans and animals [52]. BiMs create a parallel structure in which this redundant muscle couples two neighboring joints to each other. The action of this linkage system is far more complex to interpret than MoMs. It is observed in biomechanics that the behavior of BiMs depends on overall leg movement rather than the local reflexes [41].

The major BiMs in the lower extremity are Hamstrings (HAM), Rectus femoris (RF), and Gastrocnemius (GA). RF is one of the upper-limb BiMs which acts as a hip flexor and knee extensor. This muscle mainly contributes to the torque demand in the knee. HAM is another upper limb biarticular that serves as a hip extensor and knee flexor. HAM is a much stronger muscle, unlike its pseudo-antagonist RF, which mainly acts on the hip joint since the moment arm of this muscle around the hip is almost double the one at knee joint [7, 15, 21, 61]. The main function of HAM is to stabilize trunk [37] and therefore it is highly active in all types of bipedal locomotion.

Lower leg biarticular GA is studied intensively in human locomotion. GA acts as knee flexor and ankle plantar flexor (extensor). It has a greater moment arm around

the ankle related to the knee joint [7, 15, 21, 61]. Its activation also is highly linked to the performance of movements due to its capability to modulate the passive energy flow in and out of the Achilles tendon.

Having motor redundancy in the form of BiMs would certainly result in better performance than a leg structure with only MoMs. However, adding more actuator/muscle units would burden the leg with extra heavy elements and complicates the control. The fact that the motor redundancy is naturally selected in the locomotive limbs implies the plausible improvement in the overall performance of the leg by utilizing BiMs. Synonymously, BiMs upgrade the energy efficiency and agility of the locomotive limbs. In literature, these advantages are attributed to the power transfer capability of BiMs. Cleland (1866) described this function of BiMs as *ligamentous action* [8]. It is also similarly termed as *tendon action* in [42].

BiMs experience much lower contraction velocity, near-isometric contraction, relative to MoMs which rationalize their tendon or ligament-like behavior. This allows the muscle to operate in a favorable zone of its force-velocity characteristic. In other words, the lower the muscle velocity, the higher the force it can generate with a greater thermal efficiency [45]. For instance, it is reported that during vertical jump biarticular HAM experiences contraction velocity which is one-quarter of the value compared to the hypothetical scenario in which they were mono-articular [7]. This suggests that HAM can generate three times more force relative to the hypothetical case.

However, due to the low contraction velocity, BiMs contribute a relatively small amount to the positive work required to perform the task. Instead, they transfer power between joints. For example, when GA is activated it generates the force that acts on ankle and knee joints simultaneously. In a favorable scenario, GA can generate negative power in the knee joint, act as knee break, and positive power in the ankle. GA itself generates a small amount of power but takes energy from the proximal knee joint and delivers it to the distal ankle joint. Proximal-to-distal power transfer capability of GA is well established in human vertical jump [6]. During the vertical jump, GA transfers 25 J from knee to ankle, in comparison, it produces 19 J additional positive energy.

The power transfer capability is more prominent in the case of RF. It is reported that during jumping, RF performs negative work on hip approximately 15 J and transfers all this energy to the knee joint. Comparatively, RF generates negligible positive power in its fibers only 2 J, clearly acting like a typical ligament. Contrary to RF, the pseudo-antagonist HAM transfer power in the opposite direction from knee to hip. During the vertical jump, HAM transfer power from knee to hip approximately 3 J and produce positive power in its fibers about 7 J [20]. Due to the high amount of muscle tissue with a big cross-section, HAM, unlike RF, acts commonly as active muscle contributing to the positive power needed for the overall movement. As mentioned earlier HAM is surprisingly a large muscle in mammals which accounts for 30% of the leg mass in some species.

In conclusion, RF and GA synergistically transfer power from the proximal hip joint to the ankle joint. This synergistic activation pattern is proven to increase the efficiency of movement in professional runners [14]. On the other hand, HAM act

less as a passive ligament but rather actively contributing to power production like other large muscles.

9.3 Compliant Robotic Leg CARL

The planar robotic leg CARL, shown in Fig. 9.2, is designed based on the human leg architecture [55, 56]. The actuation system consists of five linear SEAs that can replicate the action of the skeletal muscle fibers and tendons [53, 54]. Unlike muscles, the actuators generate contraction and extension forces and therefore each one replaces the antagonistic pair of muscles. CARL has three DOFs and five custom made series elastic actuators RRLAB SEA. In which Two extra redundant actuators are connected as biarticulars.

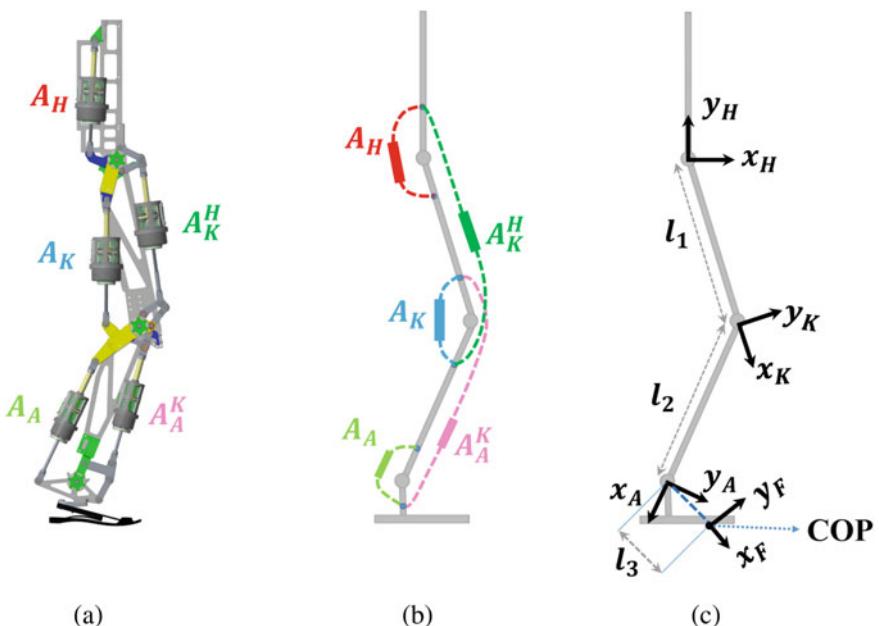


Fig. 9.2 **a** The CAD model of the planar CARL and **b** the abstract connection scheme of the actuator network. CARL has 5 linear series elastic actuators. Three actuators at the backside of the leg are mono-articular actuators generating positive torque on the joints during extension. The two frontal actuators are the biarticular actuators. They generate negative torque at the joints during extension. CARL is also equipped with a prosthetic foot. The characteristics of the actuators are given in Table 9.1. **c** The fD-H coordinates of the leg are defined. Notice that COP on the foot defines the location of the end-effector and also defines the length of the third link l_3 . The ankle angle θ_A in this figure is different from the definition in Fig. 9.1b since the ankle is dependent on the location of the CoP. The fD-H angles are used in the calculation of the Jacobian matrix of the leg

Table 9.1 Actuator properties in CARL

Actuator deployment	Hip	Knee	Ankle	Hip-knee	Knee-ankle
Notation	A_H	A_K	A_A	A_K^H	A_A^K
Associated muscles	GM/IL	VAS	SOL/TA	HAM/RF	GA
Max force (N)	1400	1400	600	1400	600
Max speed (mm s^{-1})	583.3	583.3	972.2	583.3	972.2
Nominal power (W)	816	816	576	816	576
Weight (g)	1558	1558	962	1558	962
Spring stiffness (N mm^{-1})	847	568	200	588	191
Used stroke ΔL (mm)	72.85	54.13	60	108.2	107.6
Reflected rotor inertial (kg)	32.7	32.7	10.5	32.7	10.5
Reflected rotor damping (kg/s)	618	618	352	618	352

CARL consists of three mono-articular actuators (MOAs), denoted as A_H , A_K and A_A , acting on the hip, knee and ankle joints, respectively, see Fig. 9.2b. The characteristics of the actuators and associated muscles are provided in Table 9.1. Large RRLAB SEAs are deployed as three upper limb actuators. The lower limb actuators A_A and A_A^K are small RRLAB SEAs with lower mass, power, and force ratings.

Moreover, there are two biarticular actuators, A_K^H , and A_A^K . The A_K^H is spanning the hip and the knee joint, reproducing the action of HAM and RF muscles. The biarticular A_A^K is spanning the knee and the ankle joints similar to GA muscle.

The thigh and shank links, l_1 , l_2 in Fig. 9.2c, have equal length of 42 cm where their masses are respectively 7.5 kg and 3.5 kg, comparable to the human leg morphology. The detailed characteristics of CARL are available in [56].

CARL like other sophisticated musculoskeletal robots utilizes BIAs; meanwhile, the actuation system in CARL is capable of precise force control. Actuators generate both push and pull forces which can replace the two antagonist natural muscles. Indeed, CARL is a combination of a high precision manipulation system and musculoskeletal robot. One drawback of having precise SEAs is that the leg structure is much heavier in CARL compared to other musculoskeletal systems, due to the heavy springs and high back-drivability requirement.

The (Denavit-Hartenberg) fD-H coordinates are depicted in Fig. 9.2c. These coordinates define the angles and moments in the joints. The angle of the ankle joint in this convention is defined as an angle between x_F and x_A . This angle is changing depending on the location of the center of pressure (COP) at the foot. This angle is only used in the calculation of the Jacobian matrix and is not used in the calculation of the moment arms. The ankle angle used for moment arm calculations is independent of the position of COP and is defined as in Fig. 9.1b.

CARL is equipped with a commercial prosthetic foot, shown in Fig. 9.3, that is delicately constructed from three carbon-fiber springs [57]. The elastic behavior of the foot provides a shock-absorbing functionality during ground contact, desirable for robotic systems. Additionally, strain gauges are glued to each of the three elastic

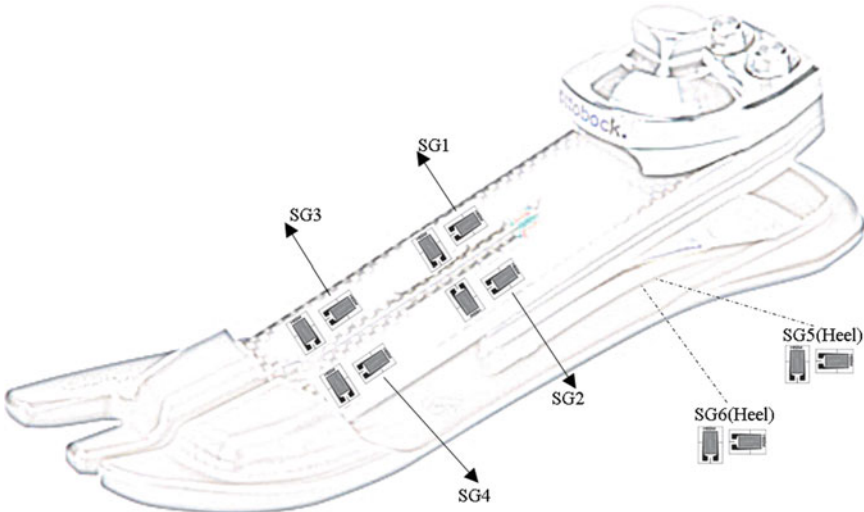


Fig. 9.3 Commercial prosthetic foot deployed in CARL. The foot is equipped with 6 strain gauges to measure the deflection of the carbon-fiber springs. The location of the strain gauges is illustrated in this figure

components of the foot. The measured strains are mapped via the neural network, as a function approximator, to estimate the vertical GRF and COP.

9.3.1 Series Elastic Actuators in CARL

The actuators of CARL are manufactured in-house and are named as RRLAB SEA whose schematics is given in Fig. 9.4a. Due to the high efficiency of 96%, the ball-screw transmission is used to convert the rotational motion to linear. Steel linear springs are positioned in series with a ball-screw axis to (a) measure the force, (b) absorb impacts and (c) ideally recuperate energy. Nevertheless, springs account for half of the mass of the actuator unit. The springs are located on the proximal side of the actuator, unlike leg muscles where the elastic tendons are placed on the distal side. The proximal side of the muscle/actuator is defined as a connection side to the leg segment with less movement.

Internal inertia and damping parameters of the small and large RRLAB SEAs are inserted in Table 9.1. SEAs have similar architecture as biological muscles. The electric motor is comparable to the muscle fiber, where both elements contribute to energy production, and both exhibit internal damping. The series elastic elements also exist both in SEAs and muscle-tendon complex where tendon sufficiently acts as a linear spring. However, SEAs have different dynamics than their biological counterparts. In general skeletal muscles do not have internal inertia, according to the

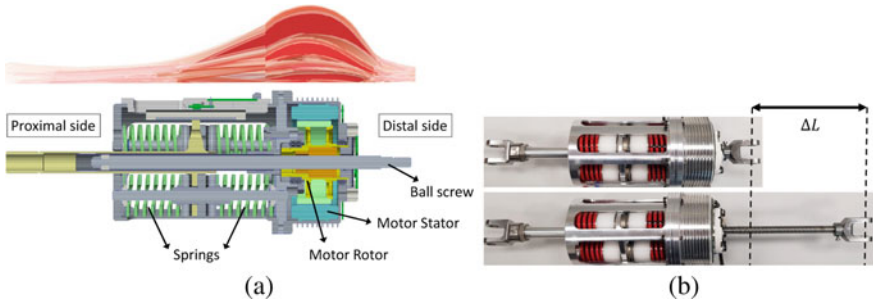


Fig. 9.4 **a** The CAD model of RRLAB SEA. The actuator consists of the electrical motor on its distal side acting as the contractile element. Steel springs on the proximal side would act as muscle tendons. ball-screw transmission is used to convert rotational motion to linear. There are two sizes of RRLAB SEA is used. There larger size actuator is located on the thigh and two small actuators are positioned on the shank. **b** Definition of the actuator stroke length ΔL

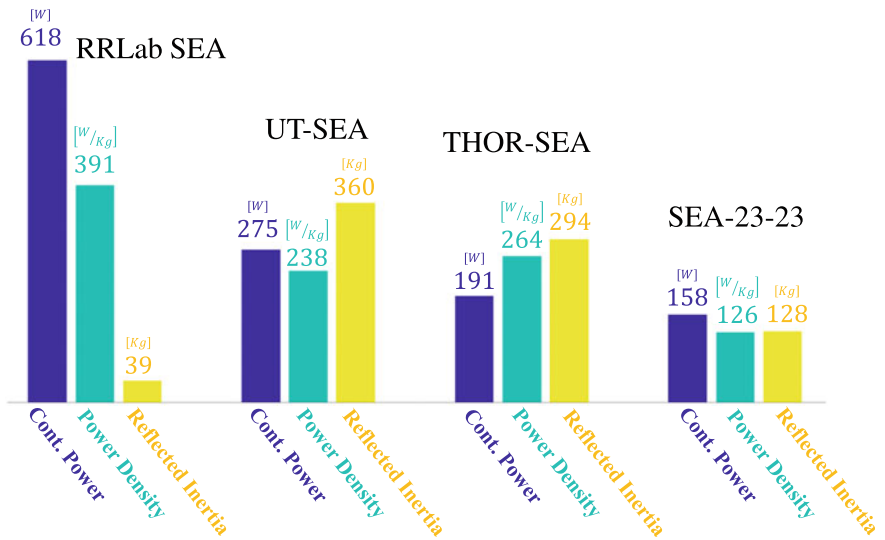


Fig. 9.5 The comparison between RRLAB SEA and other prominent actuators. The RRLAB SEA have considerably lower reflected inertia than others; therefore it features low gear ratio, back-drivability, high transparency. Due to the higher power of RRLAB SEA, it is much heavier than its peers. The compact design of RRLAB SEA and the proper integration of electric motor units have resulted in desirable power-to-mass density [53]. The characteristics of the actuators are adopted as follows: *UT-SEA* from [34], *THOR-SEA* from [22, 33] and original *SEA-23-23* from [39, 40, 48]

hill muscle model [66]. On the other hand, SEAs feature large rotor inertia which gets magnified by the high gear ratio. The internal inertia in the SEAs result in undesirable mass-spring oscillations that can adversely affect the force control performance of the actuators.

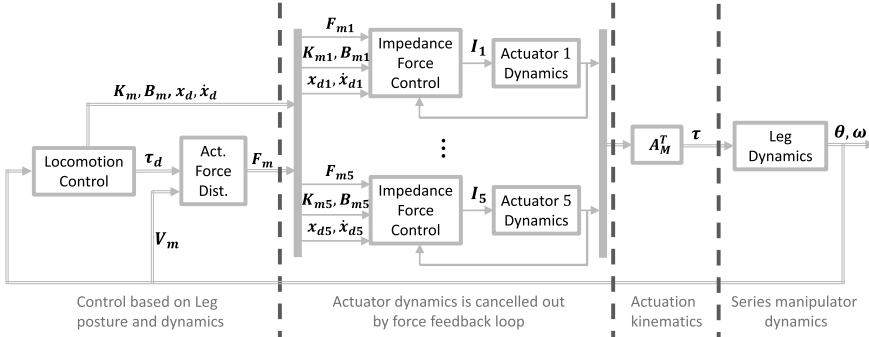


Fig. 9.6 The block diagram of the control hierarchy in CARL. The actuator and leg dynamics are separated. The force feedback loop cancels out the spring-mass-damping dynamics of the actuator due to the implementation of a high-bandwidth PID controller. Actuator forces are transmitted to the joints via moment arm matrix A_m . The controller can precisely track the desired joint torque $\tau \approx \tau_d$ regardless of the actuator dynamics and kinematics

RRLAB SEAs are designed to be highly back-derivable. This means that they have relatively much lower internal inertia and lower gear ratio in comparison to other state-of-the-art SEAs, see Fig. 9.5. Nevertheless, still, their dynamics greatly influence the leg dynamics which is one of the sources of inefficiency in CARL. By increasing the moment arm of the actuators, inefficiency due to the internal inertia would be magnified since the larger moment arm is equivalent to a higher gear ratio.

One of the drawbacks of the ball-screw transmission is that it results in the limited stroke of actuator ΔL , see Fig. 9.4b. This means that the actuator can extend and contract in a limited range similar to any linear actuation system.

9.3.2 Actuation Control

We have meticulously designed and constructed the mechatronics of RRLAB SEAs to achieve the highest performance in tracking the desired force. As a result, the control system of actuators can realize impedance and force precisely in actuator and joint domains.

The block diagram of the control feedback loop of CARL is depicted in Fig. 9.6. The *Locomotion Control* block is responsible for generating movements by producing desired joint torques τ_d based on the feedback from leg posture and kinematics. Additionally, the locomotion control can calculate the desired stiffness K_m and damping B_m for each actuator. The desired impedance is sent to the local actuator controller with position and velocity equilibrium of x_d and \dot{x}_d . The local actuator controller is running on an embedded PC with a very high sampling frequency. As a result, the local controller can emulate much higher stiffness and damping in the actuators.

The AFD block calculates the desired force of individual actuators. The force feedback loop of each actuator tracks the corresponding desired force F_{mi} . Actuator kinematics maps the actuator forces into joint torques τ , which are applied on the joints of the leg. τ acts as an input to the segmented leg dynamics. Our AFD strategy is discussed in detail in [28, 31].

Each actuator is comprised of a series spring which can be used to measure the force with high precision. The local force feedback controller fully eliminates the mass-spring internal dynamics of the actuator. This feedback loop is implemented with time cycle of 100 μ s and average control bandwidth more 30 Hz 20 Hz, respectively for large and small RRLAB SEAs. The control bandwidth is dependent on the stiffness of the series spring and the inverse of the reflected inertia. Force feedback loop decouples the dynamics of the actuator from the dynamics of the segmented leg. As a result, the actuation system acts as an almost perfect force source.

Actuator kinematics is represented by moment arm matrix A_m in Fig. 9.6, which defines the load sharing contribution of an individual muscle to each joint. A_m directly affects the action of the muscle and has to be carefully selected.

9.4 Hopping Control

To create the hopping motion, the controller is built to realize a virtual spring. We first select an equilibrium posture for the robot leg. This equilibrium posture is defined by desired joint angles θ_d . The equilibrium posture also clarifies the rest length of the virtual leg spring L_d . The stiffness of the virtual leg spring k_r is also predefined. The choice of this stiffness value depends highly on the capability and strength of the actuators in generating hopping motion. We were able to achieve a satisfactory hopping movements in stiffness value range of [4, 8] kN m⁻¹.

The leg spring can be created by controlling the impedance ellipse at the end effector or COP, see Fig. 9.8c. The stiffness requirements are quite high and the robot is equipped with relatively soft springs in the actuation system, which results in internal oscillations between actuators that can make the whole system unstable. To stabilize the system, we also render a damping ellipse in workspace similar to the stiffness ellipse, shown in Fig. 9.8c. We use two complementary kinematic methods for impedance control: (a) controlling joint impedance and (b) using the ground force feedback control. In the SLIP model, we assume that COM of the robot is positioned at the hip. The origin of the impedance ellipse is located in COP and the major axis of the ellipse is directed toward the hip.

The block diagram of the controller is depicted in Fig. 9.7. The amplitude of the desired force in workspace F_{w_r} is calculated as

$$F_{w_r} = k_r(L_d - L) \quad (9.1)$$

where k_r is the selected leg spring stiffness and the L_d and L are the desired and actual values of the leg spring length. PD controller is used to generate a feedback

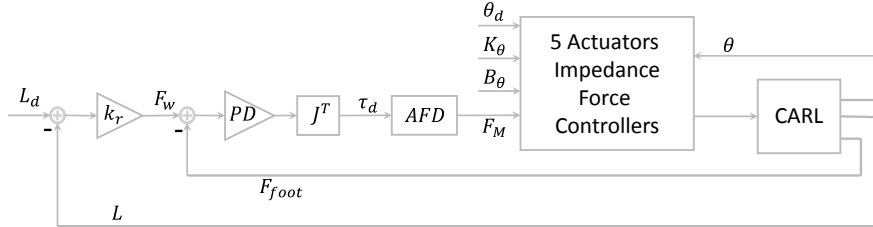


Fig. 9.7 This block diagram describes the various components of the hopping control

loop to track the desired leg force F_{w_r} . The feedback signal of ground reaction force F_{foot} is obtained by the strain gauges located on the foot. The corresponding joint torque vector τ_d is calculated by using the kinematic Jacobian matrix of the robotic leg. The desired three joint torques are distributed over 5 actuators using the actuator force distribution method.

Additionally, joint stiffness K_θ and damping B_θ are also calculated for joints based on the equilibrium joint angles θ_d . The calculation method will be discussed in detail later on. The joint stiffness and damping keep the posture of the leg fixed during the flight phase and landing phase. The desired joint impedance is realized in the local embedded PC with a very fast sampling frequency and therefore enables high stiffness and damping output.

The hip joint stiffness does not influence the hopping performance since the leg spring force exerts zero torque around the hip axis. We select an appropriate stiffness and damping for the hip joint to minimize the disturbance causing undesirable deviations from the hip joint equilibrium angle. The joint stiffness and damping are generated only by mono-articular actuators.

9.4.1 Joint Stiffness Calculations

One of the simple ways to control workspace stiffness in a robotic arm is to map the stiffness from the workspace into joint space. The objective is to control the stiffness of the leg spring k_r , illustrated in Fig. 9.8c. Since the ellipse is directed toward the hip, the amount of torque generated in the hip joint is negligible, assuming that the tangential stiffness k_t remains small. Therefore, only knee and ankle joint stiffness has to be calculated to render the desired stiffness ellipse.

According to [16], the mapping between workspace stiffness and joint stiffness is as follows:

$$\mathbf{K}_\theta = \mathbf{J}^T \mathbf{K}_w \mathbf{J}, \quad (9.2)$$

$$\Rightarrow \mathbf{K}_w = \mathbf{J}^{-T} \mathbf{K}_\theta \mathbf{J}^{-1}. \quad (9.3)$$

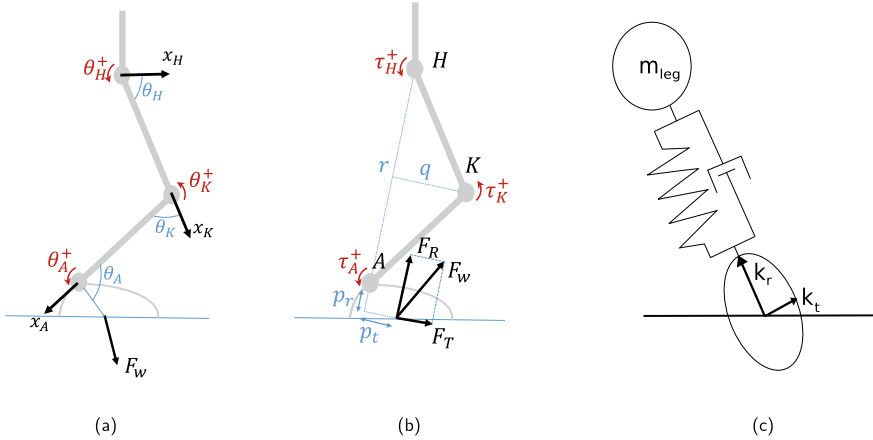


Fig. 9.8 **a** The definition of joint angles and their positive direction. This angle definition is used to calculate the kinematics of the leg. **b** The geometric illustration for linear Jacobian matrix calculation, adopted from [15]. **c** The impedance ellipse at the center of pressure and the illustration of the virtual leg spring between the hip and ankle

By removing the hip joint from the kinematic calculations, the reduced Jacobian becomes square invertible matrix $J_r 2 \times 2$. Here we use a geometrical approach to calculate the Jacobian matrix based on the coordinate system introduced in [15]. The definition of the so-called Hof-coordinate is illustrated in Fig. 9.8b. F_w is decomposed into radial F_R and tangential F_T components. The radial direction F_R is aligned with the hip-ankle line \overrightarrow{HA} and is dependent on the relative location of the hip and the ankle joints. The coordinate system rotates around the hip joint based and is aligned with the orientation of \overrightarrow{HA} .

By assuming the equal length of thigh and shank, the joint moments can be derived as

$$\tau_H = F_R p_t + F_T (p_r + r), \quad (9.4)$$

$$\tau_K = F_R (p_t - q) + F_T \left(p_r + \frac{r}{2} \right), \quad (9.5)$$

$$\tau_A = F_R p_t + F_T p_r. \quad (9.6)$$

The geometrical parameters are defined in Fig. 9.8b. By using the following relationship between force and torque, the reduced Jacobian J_r can be calculated as

$$\begin{bmatrix} \tau_K \\ \tau_A \end{bmatrix} = J_r^T \begin{bmatrix} F_T \\ F_R \end{bmatrix}, \quad (9.7)$$

$$J_r = \begin{bmatrix} p_r + r/2 & p_r \\ p_t - q & p_t \end{bmatrix}. \quad (9.8)$$

After calculating the Jacobian, we have to calculate the stiffness matrix in workspace. The stiffness matrix is commonly defined as:

$$\mathbf{K}_w = \mathbf{R} \begin{bmatrix} k_t & 0 \\ 0 & k_r \end{bmatrix} \mathbf{R}^T. \quad (9.9)$$

As mentioned before, k_r is the stiffness in the major axis direction of the stiffness ellipse and therefore is the stiffness of the leg spring. The matrix \mathbf{R} is a rotation matrix that rotates the stiffness matrix so that its major axis is aligned toward hip joint. This rotation matrix can be calculated as:

$$\mathbf{R} = \frac{1}{L} \begin{bmatrix} p_r + r & -p_t \\ p_t & r + p_r \end{bmatrix}. \quad (9.10)$$

Columns of rotation matrix are the direction of the axes of stiffness ellipse when aligned toward the hip joint. L is the length of the virtual spring. The joint stiffness matrix is defined as:

$$\mathbf{K}_\theta = \begin{bmatrix} k_k & 0 \\ 0 & k_a \end{bmatrix}. \quad (9.11)$$

where k_k and k_a are the joint stiffnesses at knee and ankle joints. Replacing the stiffness matrices in Eq. 9.3 yields

$$\mathbf{J}_r^{-T} \begin{bmatrix} k_k & 0 \\ 0 & k_a \end{bmatrix} \mathbf{J}_r^{-1} = \mathbf{R} \begin{bmatrix} k_t & 0 \\ 0 & k_r \end{bmatrix} \mathbf{R}^T. \quad (9.12)$$

By reformatting the above equations, we reach

$$k_r \mathbf{I}_r = k_k \mathbf{I}_k + k_a \mathbf{I}_a + k_t \mathbf{I}_t. \quad (9.13)$$

where I_* matrices are 2×2 symmetric matrices. To solve the above equations, we can decompose the matrix equality into four linear equations of its elements. However, since the I_* matrices are symmetric, only three independent equations can be achieved.

The resulting system of linear equations can be written as:

$$\mathbf{A}_{3 \times 3} \begin{bmatrix} k_a \\ k_k \\ k_t \end{bmatrix} = \mathbf{C}_{3 \times 1} k_r, \quad (9.14)$$

$$\mathbf{A} = \begin{bmatrix} M(p_t - q)^2 & Mp_t^2 & (p_r + r)^2 \\ -M(p_t - q)(p_r + \frac{r}{2}) & Mp_r p_t & p_t(p_r + r) \\ M(p_r - \frac{r}{2})^2 & Mp_r^2 & p_t^2 \end{bmatrix}, \quad (9.15)$$

$$\mathbf{M} = \frac{L^2}{\det(\mathbf{J}_r)^2}, \quad (9.16)$$

$$\mathbf{C} = [p_t^2 - p_t(p_r + r) (p_r + r)^2]^T. \quad (9.17)$$

The desired joint stiffness can be calculated directly by solving the above equations:

$$\begin{bmatrix} k_a \\ k_k \\ k_t \end{bmatrix} = \mathbf{A}^{-1} \mathbf{C} k_r. \quad (9.18)$$

The above formulations are advantageous since it provides a direct linear relationship between leg spring stiffness k_r and the joint stiffnesses. It is important to notice that the cross-stiffness between the knee and ankle joint is selected to be zero. The cross-stiffness values are the off-diagonal elements of the stiffness matrix \mathbf{K}_θ in Eq. 9.11. The cross-stiffness establishes a coupling between two joints and can have even negative stiffness value as long as \mathbf{K}_θ remains positive definite.

For any arbitrary stiffness ellipse in workspace \mathbf{K}_w , the joint stiffness matrix \mathbf{K}_θ is calculated by Eq. 9.2. By adding a constraint of zero cross-stiffness in the joint domain, we are restricting the stiffness in the workspace. This workspace restriction can be seen in Eq. 9.18, where the tangential stiffness k_t is linearly dependent on k_r . One of the advantages of the biological segmented Z-shaped leg as in human is that it produces stiffness ellipse in which $k_r >> k_t$. Therefore the stiffness ellipse will always be formed in the direction of the leg spring axis. We also use the above calculations to map the damping in workspace b_r into the knee and ankle damping matrix B_θ in the joint domain. The damping b_r is selected to be the minimum possible value that keeps the robotic leg stable.

In conclusion, to produce a hopping movement, first, we select a neutral or equilibrium posture for the robot that defines the equilibrium length of the virtual leg spring. By knowing the equilibrium joint angles θ_d , we can calculate the reduced Jacobian matrix \mathbf{J}_r and also the matrices \mathbf{A} and \mathbf{C} . The joint stiffness parameters k_k and k_a can be easily calculated by Eq. 9.18 for any desired leg spring stiffness k_r . By having k_k and k_a and equilibrium joint angles, the local actuator impedance control will be used to render the desired joint stiffnesses with the sampling frequency of 3 kHz. A similar approach will be used to calculate the joint dampings of the knee and ankle based on the desired damping ellipse in the workspace.

9.5 Hopping Experiment

The hopping experiment of CARL is performed on the test-rig platform. The platform and its schematics is shown in Fig. 9.9. The hip joint is located on the frame that moves up and down over the four vertical rails. The moving frame has the weight of approximately 15 kg where the leg itself also weight approximately 13 kg. The four vertical rails introduce a high amount of damping which adversely affects the hopping movement of the robotic leg. The movement of the hip frame in the vertical direction is controlled by a pulley and string system.

The trunk of the robot is restricted to vertical movements and can not rotate around the hip joint. The string is driven by a motor that controls the tension of the string.

The robotic leg is initially positioned at the equilibrium posture. The virtual leg spring control is fully active and the leg compensates its weight of 28kg. By a manual push, the leg starts to generate the hopping movements. There are several sources of damping in the system. One major source is the vertical rail in the test-rig that generates a considerable amount of damping. Additionally, the mono-articular actuators are also programmed to generate damping behavior that is essential to keep the stability of the robotic leg when producing the virtual leg spring. As a result, during the hopping experiment, a significant amount of energy is lost due to the damping.

Energetics of the hopping system can be investigated in two domains. One is the input domain where the actuators deliver/extract energy to/from the leg-testrig dynamics. The positive work/energy of the actuation system is assumed to describe the situation where actuators deliver energy to the system and inversely negative work/energy corresponds to the extraction of energy from the system.

The second domain indicates the output mechanical energy which consists of kinetic, potential, and friction loss of the mechanical elements. Our analysis is per-

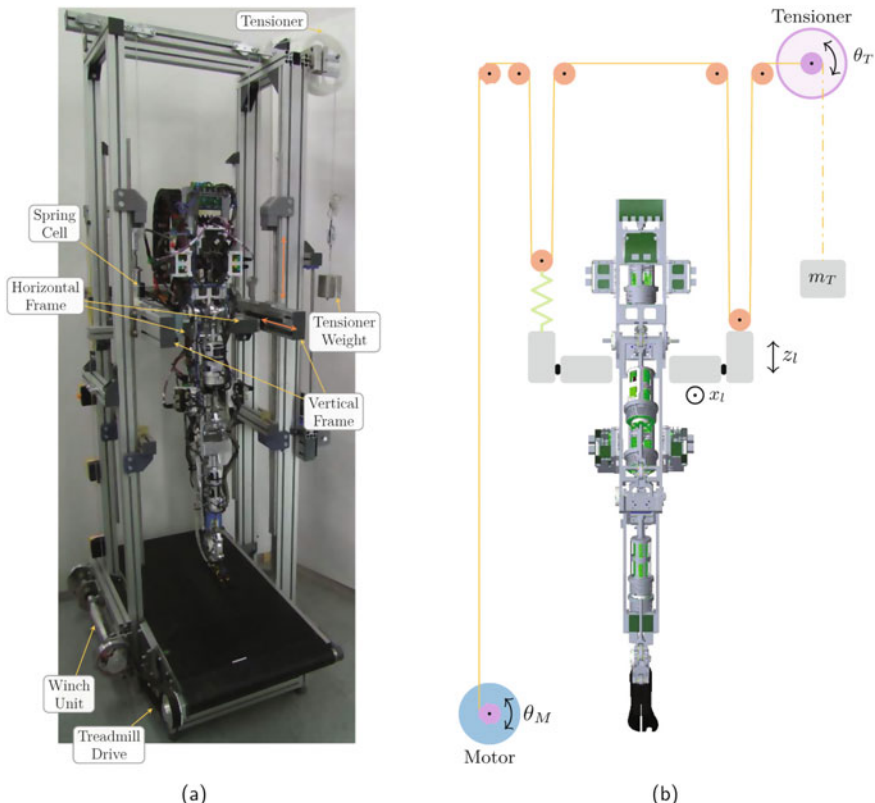


Fig. 9.9 Test-rig platform in which the hopping movement of CARL is performed

formed in the input(actuation) domain since we are interested in observing the behavior of the actuators and their internal elasticity. The amount of energy input exerted by actuators equals the total of kinetic, potential, and friction loss energy in leg-testrig platform.

To have a continuous hopping motion the energy loss due to friction is compensated in each cycle during the take-off phase. To reach a smooth movement we increase the stiffness of the leg during the take-off phase. The movement in this method was more stable and smooth than adding a constant force upward during the take-off phase, since the abrupt change in the ground reaction force would result in internal oscillations between compliant actuators. Consequently, we define two stiffness values for the hopping experiment, one is the landing stiffness which the leg experiences during the landing phase and second, the take-off stiffness is utilized to inject energy into the system.

Two experiments are performed on CARL, one with high and the other with low flexion in the knee joint. The experiment with low knee flexion results in a hard virtual spring stiffness and is denoted as hard stiffness posture (Hard-SP). The high flexion knee joint results in a lower leg stiffness and hence the name soft stiffness posture (Soft-SP). The parameters of the control are provided in Table 9.2. The data for each experiment is collected and is averaged over all the cycles.

Hopping cycle is divided into four phases: Mid-Stance (MS), Take-off (TF), Flight (FL) and Landing (LA). MS is assumed to be the starting phase of the cycle. It is a short phase immediately before take-off. At the start of TF, the controller detects the upward acceleration of the center of mass. It immediately increases the stiffness of the leg to propel the COM upward and exert energy into the leg dynamics. The brief moment between the full contraction of the leg and detection of the upward propulsion is defined as MS phase. After the robot loses the ground contact, FL starts until the touch-down happens. The landing phase takes place between touch down and full contraction of the leg spring. During LA, the robot acts as a damper and decelerate the COM. Afterward, in MS, the leg starts to extend reflectively until the take-off phase kicks in. Duration of each phase is provided in Table 9.3.

The work loop for the robot hopping is illustrated in Fig. 9.10. The area inside the curve equals the energy delivered by the actuation system. The work produced in each cycle compensates for the energy loss due to the damping and friction in the actuation system and test-rig [30]. The amount of total mechanical energy delivered during Soft-SP is 11.86 W compared to 6.66 W in Hard-SP. High energy loss in Soft-SP is due to the fact that the COM travels higher distances, 44 versus 30 mm spring deflection, and hence more friction loss.

During LA, the leg act as a linear virtual spring and the controller can successfully render the desired stiffness during landing. As shown in Fig. 9.10b, the $F_w - L$ characteristic is almost linear during Landing in Hard-SP. However, the linear leg stiffness is not desirably rendered in Soft-SP, see Fig. 9.10a. Such a poor control response could be caused by the saturation in actuator force due to high load and energy demand and dominance of damping forces during landing.

Work loop analysis is presented for each joint to understand the significance of each joint in the hopping action. As it can be seen in Fig. 9.11, the major joint

Table 9.2 The parameters of the controller and collected data during two experiments: soft stiffness posture (Soft-SP) and hard stiffness posture (Hard-SP)

Description	Notation	Soft-SP	Hard-SP	Unit
Leg rest length	L	977.6	962.6	mm
Take-off leg stiffness	k_{rT}	25	30	kN m^{-1}
Landing leg stiffness	k_{rL}	4	8	kN m^{-1}
Take-off tangential leg stiffness	k_{tT}	1.68	0.987	kN m^{-1}
Landing tangential leg stiffness	k_{tL}	0.269	0.263	kN m^{-1}
Take-off leg damping	b_{rT}	595	987	kg s^{-1}
Landing leg damping	b_{rL}	270	263	kg s^{-1}
Equilibrium hip angle	θ_H	-88	-82	Degree
Equilibrium knee angle	θ_K	-30	-26	Degree
Equilibrium ankle angle	θ_A	55.7	55.5	Degree
Landing hip stiffness	k_h	500	500	N m rad^{-1}
Landing knee stiffness	k_k	93	88.8	N m rad^{-1}
Landing ankle stiffness	k_a	50	85.6	N m rad^{-1}
Take-off hip stiffness	k_h	500	500	N m rad^{-1}
Take-off knee stiffness	k_k	580	333	N m rad^{-1}
Take-off ankle stiffness	k_a	311	332	N m rad^{-1}
Takeoff hip damping	b_h	15	15	N m rad^{-1}
Takeoff knee damping	b_k	1.85	0.44	N m rad^{-1}
Takeoff ankle damping	b_a	1	0.44	N m rad^{-1}
Number of cycles	N	19	72	cycle
Cycle duration mean	T_{av}	0.4243	0.3293	s
Cycle duration std	T_{std}	0.0074	0.0034	s
Maximum leg contraction	ΔL	44.3	30	mm
Actuator control frequency	f_{act}	3	3	kHz
Leg control frequency	f_{leg}	0.5	0.5	kHz

Table 9.3 Description of the hopping phases

Phase	Annotation	Start-end (%)	Description
Mid-stance	MS	0–7	After full leg contraction, until takeoff propulsion
Takeoff	TF	7–38	After take-off propulsion, until being airborne
Flight	FL	38–57	After being airborne, until touch down
Landing	LA	57–100	After touch down, until full leg contraction

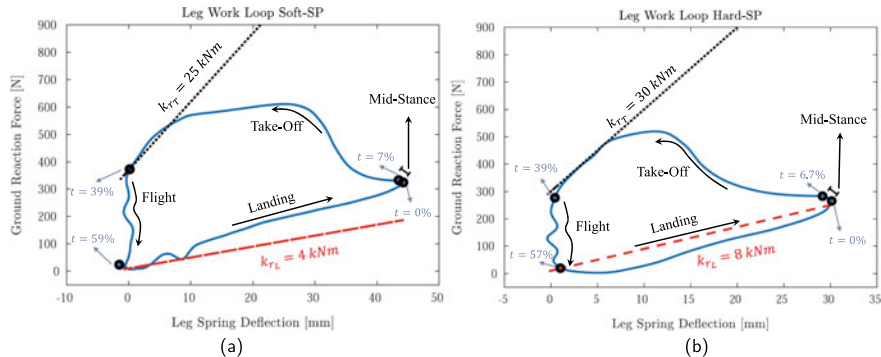


Fig. 9.10 Work loop of leg spring which shows the $F_w - L$ characteristics during hopping **a** Soft-SP and **b** Hard-SP. The amount of mechanical work produced in each cycle is equal to the area inside the curved loop. The work produced amounts to energy loss due to damping and friction in the test-rig and actuation system. The energy loss is higher in Soft-SP compared to Hard-SP

contributing to the hopping motion is the ankle joint. In fact, the area inside the work loop curve of the ankle is much higher compared to other joints. The energy produced in ankle is 9.22 W in Soft-SP which is considerably higher than 6.64 W in Hard-SP. Hip joint acts as a linear rotational spring with constant stiffness and very small energy production. The knee joint however is active in Soft-SP and generates 3.04 W mechanical work compared to negligible 0.1756 W produced by knee in Hard-SP.

Actuator activity is presented in Fig. 9.12. As expected, the actuators connected to the ankle, A_A and A_A^K , are the major contributors of either positive (during TF) and negative (during LA) power. As mentioned earlier, in the Soft-SP experiment, the knee joint and its actuators become relatively active. This can be seen by the high activity of A_K and A_K^H actuators during TF. Interestingly, knee actuators only contribute to positive power and do not absorb power (negative power) during landing. Needless to say, actuators during MS and FL are fairly inactive.

The activity of mono-articular and biarticular actuators spanning ankle joints is highly correlated; however, this correlation is lower in Soft-SP experiment during TF, in which the high activity of knee actuators drive the A_A^K to partially generate negative power ($t \approx 15\text{--}20\%$) contrary to the movement of the leg.

9.6 Experimental Results

The simple mass-spring model successfully describes the function of the human leg during locomotion. As discussed before, it is a common practice to control the robotic leg to demonstrate such a virtual spring behavior. However, in order to generate such a simple dynamics, CNS not only has to move all the 11 DOFs but also activate all the muscle-tendon units in the leg. In contrast, bipedal robots imitating SLIP control,

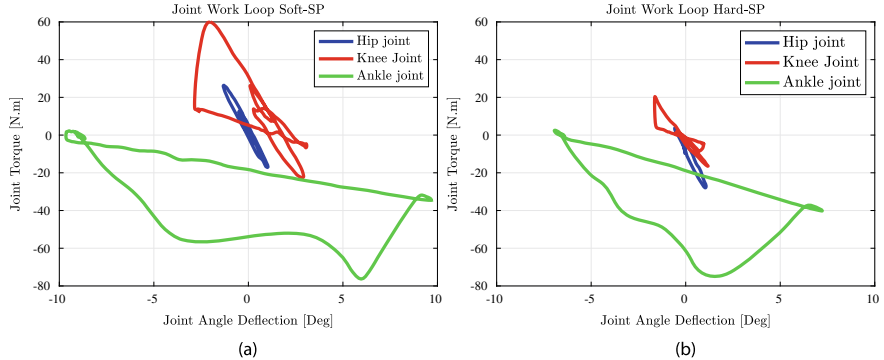


Fig. 9.11 Work loop for each joint which shows the $\tau - \theta$ characteristics during hopping **a** Soft-SP and **b** Hard-SP. The joint angle deflections are centered around zero for better visualization. The area inside the loop indicate the amount of produced energy by the corresponding joint. The energy produced in the ankle joint is dominant. Knee joint partially contributes to the energy production in Soft-SP

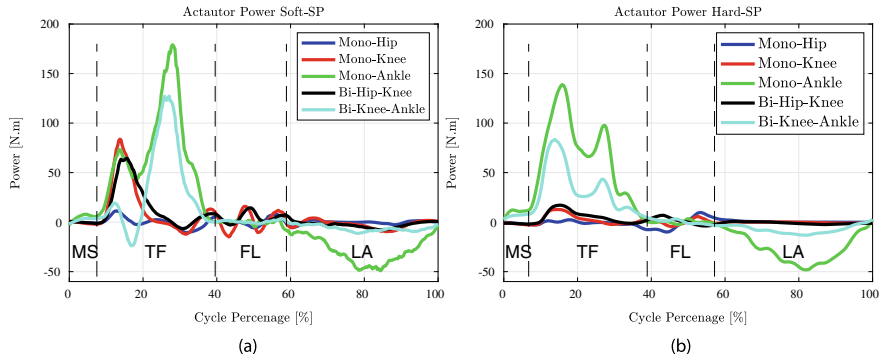


Fig. 9.12 Actuator power during hopping

either are relatively complex or very primitive. Complex robots are commonly stiff robots that emulate the SLIP control as a desirable control policy like *Cassie* and *ATRIAS* which have extra specialized internal dynamic controllers. The primitive robots commonly have one active knee joint to generate leg spring and perform hopping locomotions [32, 63].

CNS utilizes ankle joint and its plantarflexor muscle-tendon units excessively to generate leg spring function. The energy recuperation of Achilles tendon (AT) is used to realize virtual leg spring more efficiently. During hopping, leg spring stiffness is directly modulated based on the stiffness of the AT. Despite the fact that the SLIP model is inspired by human locomotion, unfortunately, few attempts are made in robotics to realize leg spring efficiently. To achieve such efficiency we report the influence of AT in an experimental hopping experiment. We also investigate

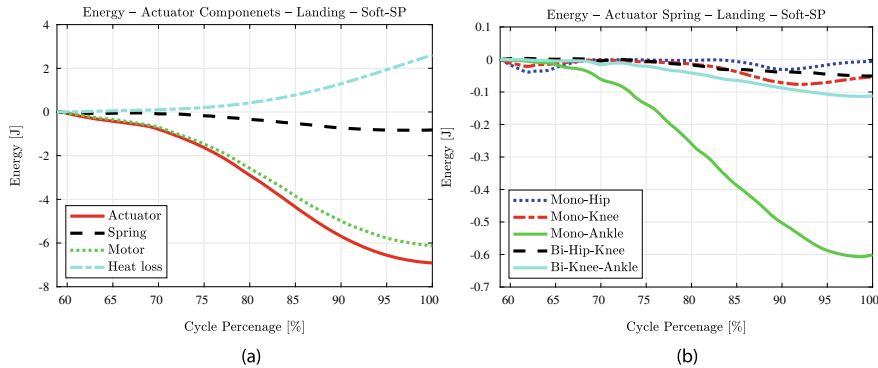


Fig. 9.13 **a** The amount of energy during landing in each component of the actuation system. Positive energy implies production of energy and negative energy means the absorption of energy. **b** Absorbed energy by series elastic elements of each actuator during landing. Both figures belong to the Soft-SP experiment

the influence of the actuator redundancy in improving the efficiency of leg spring function.

We examine two phases of hopping: (a) deceleration of COM during landing phase (LA) and (b) acceleration of COM during the take-off phase (TF). The actuators perform negative work during LA and it is interesting to investigate how much of this negative work is absorbed in the series spring of the actuators. During TF, the explosive leg extension can be studied and investigate the contribution of each actuator in creating positive work. Only Soft-SP experiment is investigated in this section since both knee and ankle joints are contributing to the movement unlike Hard-SP with a highly dominant ankle joint activity.

9.6.1 Investigation of Landing Phase

The landing phase starts from touch down and ends when the leg is fully compressed and ready to bounce back up. LA takes 0.175 s in average over 19 cycles. The controller maintains a constant leg spring stiffness during landing, see Fig. 9.11a. As mentioned in Table 9.2, the local controllers of mono-articular actuators adjust the knee stiffness at 93 N m rad^{-1} and ankle stiffness at 50 N m rad^{-1} .

In this phase, all the actuators perform negative work by acting as a brake. Part of this negative energy is stored in the series elastic elements of actuators. However, the bulk of negative work is done by an electric motor by acting as a generator and returning energy back to batteries. In Fig. 9.13a, the work performed by each component is reported. In total leg performs -6.91 J where 11.91% of this energy is absorbed in series elastic elements of actuators.

Role of Series Elastic Elements During Landing

As illustrated in Fig. 9.13b, the majority of elastic energy is saved in actuators A_A and A_A^K which span ankle joints. The series elastic elements of these actuators are associated with AT, the strongest tendon in the body. Stiffness of series elements in each of the ankle actuators is approximately 190–200 kN m⁻¹ which is in the similar range of the stiffness for AT at 145–231 kN m⁻¹ [23]. The moment arm of the mono-articular actuator around equilibrium angle is approximately 5.1 cm comparable to the moment arm of the AT 5.8 cm [17, 29]. Therefore the stiffness that AT induces on the joint is comparable to the series spring of A_A . However, there is a small difference between the muscular structure of the ankle complex between CARLand the human. In the biological leg, AT acts as an elastic element for both mono-articular muscle SOL and biarticular GA. However, in CARL, the mono-articular A_A and biarticular A_A^K are separate actuators with different elastic elements and moment arm values. Since the majority of energy absorption occurs in the elastic element of A_A actuator, we can assume that this particular series spring biologically corresponds to AT.

It is reported that during human hopping the percentage of energy saved in AT is about 16% of the total mechanical energy [23]. It is noteworthy to mention that AT is only capable to return 74% of this energy, which accounts for 11.8% of the total energy. Coincidentally, this value is similar to what we have reported in our hopping experiment. Despite the fact that we can not compare directly the energy values in robot and human due to differences in dynamics and control of human and robot, our experiment clarifies that the series of elastic springs in the ankle joint is an indispensable feature that improves the performance of robotic locomotion as in human. It also demonstrates the ineffectiveness of the elastic elements of proximal muscles in the knee and hip actuators. Unfortunately, a high quantity of research in bipedal robotics, particularly SLIP studies, focus on the knee joint as a dominant stiffness modulator of the leg spring; whereas both biomechanics and our experiment clearly point to only one dominant spring in the ankle joint. In fact, in our experiment, only 14% of the mechanically absorbed energy is in non-ankle actuators.

CNS modulates the stiffness of the leg spring by two important parameters: (a) the ankle stiffness and (b) the knee extension angle [10]. We incorporated these findings in designing the impedance control for hopping. The knee DOF is important in rendering appropriate leg spring by adjusting leg length and Jacobian. However, knee stiffness plays a negligible role in improving the efficiency of hopping locomotion.

Proximal-Distal Transfer of Energy During Landing

Due to the actuator redundancy, each joint is powered by two or three actuators. Biarticular actuators improve the efficiency of movement by transferring power from the hip down to the ankle. Such a synergy between actuators is illustrated in Fig. 9.14. The landing phase starts with the ground impact which generates a negative impulse response in hip and knee joints, which attenuates by $t \approx 70\%$. In the ankle joint, the negative power is gradually accumulated and peaks at half of the landing phase. The transfer of energy occurs in both biarticular actuators, though it is more tangible in A_A^K .

During LA, the knee joint is performing negative work as do the A_K and A_K^H actuators with the exception of A_A^K . As seen in the middle plot in Fig. 9.14, A_A^K , dashed line, generates significant positive power in the knee joint. By doing so, A_A^K increases, even more, the negative load of other knee actuators. In fact, A_K and A_K^H actuators, not only have to break the movement of the whole leg but also locally act against A_A^K . The resulting extra negative energy produced in the knee joint is directly transferred to the demanding ankle joint.

The peak power at the ankle is -65 W which is substantially higher than -11.6 W in the knee joint. By overloading big stronger knee actuators, A_A^K transfers the power to the ankle joint where the power is most needed. As reported in Fig. 9.15a, A_A^K generates -1.5 J in the ankle joint where 26% of this negative work is transferred from knee. A similar transfer of energy is reported for GA during locomotion [20]. The moment arm of the GA acting on the ankle is double its moment arm at the knee. Therefore, when it is activated it generates greater torque at the ankle than the knee. Mechanical placement of GA significantly enhances its action to transfer power from knee to ankle [27].

9.6.2 Investigation of Take-Off Phase

During the take-off phase, the positive energy is inserted into the system by the actuators to provide an explosive leg extension. TF starts when the COM starts its upward movement and ends when the foot loses the ground contact. This phase takes 0.105 s in average over 19 cycles. The controller abruptly increases the stiffness of the leg spring to 25 kN m $^{-1}$ to provide additional positive energy. Consequently, mono-articular actuators adjust the knee stiffness at 580 N m rad $^{-1}$ and ankle stiffness at 311 N m rad $^{-1}$, see Table 9.2.

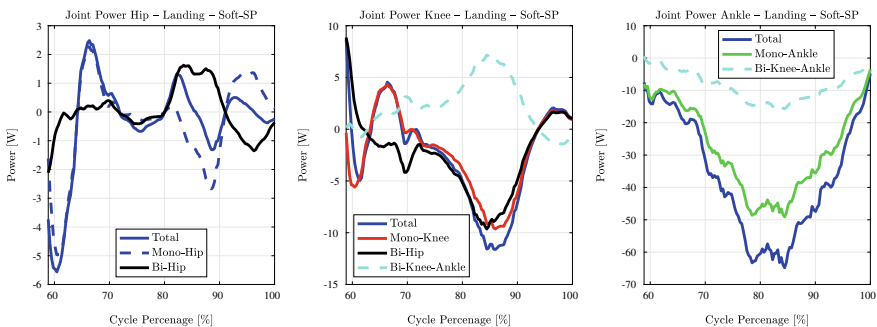


Fig. 9.14 Distribution of actuator power in each joint during landing in Soft-SP experiment

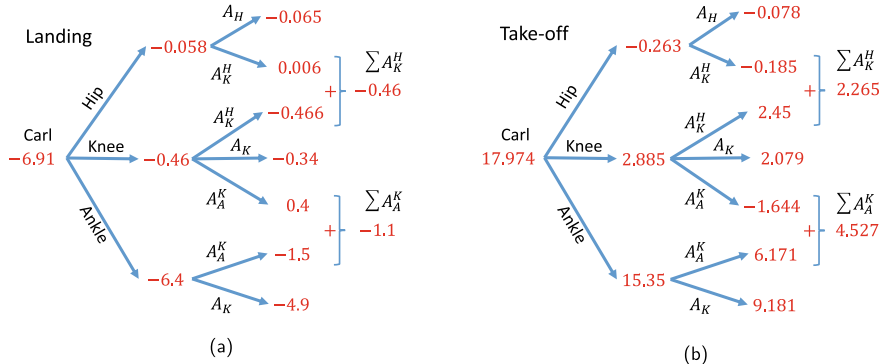


Fig. 9.15 Distribution of work performed by leg over joints and actuators in **a** landing and **b** take-off. The physical unit of reported work data is in Joules. Data belongs to the Soft-SP experiment

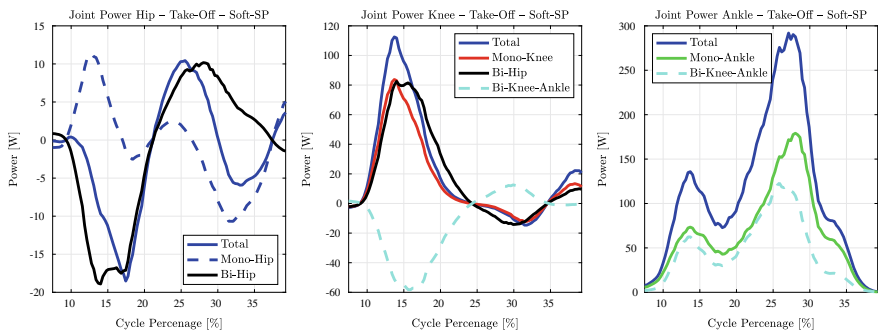


Fig. 9.16 Distribution of actuator power in each joint during take-off in Soft-SP

Proximal-Distal Transfer of Energy During Take-Off

Unlike LA, during take-off leg performs positive energy of 18J, see Fig. 9.15b. Almost 85% of total energy is performed by the ankle joint. The transfer of energy by biarticular actuators is prominent. Upper limb biarticular A_K^H transfers 0.185 J from hip toward knee joint. Therefore 6% of the energy required in the knee is transferred from the hip joint. Lower limb biarticular A_A^K transfers 1.644 J from the knee toward ankle joint which is 10% of the energy requirement at the ankle. Both biarticular actuators are highly activated and contribute to the produced positive power.

The power transfer of biarticulars during human hopping locomotion is not well-documented in biomechanics. However, vertical jump movement is extensively studied in the literature which is similar to the take-off movement of CARL. It is reported that during vertical jump 25% of the energy needed in the ankle is transferred by GA [6]. To the authors' knowledge, this study is reporting for the first time the power transfer capability of the biarticular actuators during the hopping movement.

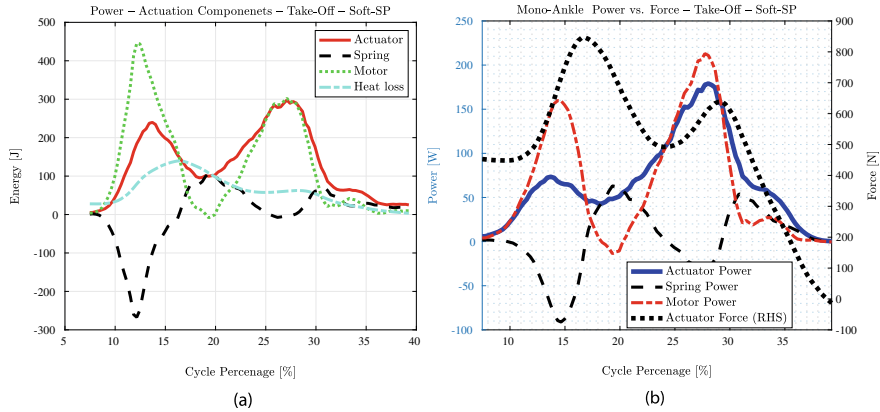


Fig. 9.17 **a** The power of each component of the actuators during take-off. **b** The power and force analysis for mono-articular at the ankle joint. Data belongs to the Soft-SP experiment

It is important to notice that the energy distribution between joints is highly unbalanced. As we discussed, the ankle joint is the main energy contributor during hopping both in humans and CARL. In our experiments, the actuators working at the ankle were highly overloaded and after 19 cycles we have to stop the experiment since they were overheated. This power imbalance can be seen in Fig. 9.16. The peak power in the ankle joint is about 300 W which is almost triple the peak power in the knee joint. The action of biarticular actuator A_A^K stands out between knee and ankle joints, see the middle figure. A_A^K power at the knee is totally against the action of other knee actuators. During the peak power at $t \approx 14\%$, A_K and A_K^H produce 160 W, however only 112 W is needed in the knee joint. The additional power is directly transferred to the distal ankle joint.

In the hip joint, the action of mono-articular actuator A_H is interesting, see leftmost plot in Fig. 9.16. The power profile of A_H is completely opposite to the joint power, especially during peak power. At peak power, negative work is required by the hip joint, where A_H produces positive power. This positive power is transferred to the knee joint by upper limb biarticular A_K^H . The proper design of biarticular actuation can alleviate the issue of energy imbalance and peak power conditions in the robotic leg [26].

Spring-Motor Interaction During Take-Off

Take-off is a high power and a peak torque movement where the actuators are overloaded to provide positive power. The power output for all the active and passive elements of the actuation system is provided in Fig. 9.17a. There are two peak power events at $t \approx 14\%$ and $t \approx 27\%$. The first peak defines the moment when the springs are overloaded and stored energy produced by the motors. Later this energy in the

spring is returned to the system which has two effects on the movement (a) Oscillation between motor and spring power, and (b) amplification of the actuator force.

We analyze the motor-spring interaction of the A_A to provide a better understanding of such internal interplay in the actuator. The power produced by motor, spring, and actuator in A_H is provided in Fig. 9.17b. The actuator consists of an electric motor and spring. Both components experience equal force which is also depicted in Fig. 9.17b.

At the first power peak $t \approx 14\%$, the spring gets fully loaded and therefore it reaches its peak negative energy. At this point, the electric motor produces extra power to not only move the joint but also compress the spring. The softer the spring, the higher the temporary motor power load. This also results in peak current and high thermal loss. It also adds to the response time of the actuator to the load disturbances and adversely affects the force control bandwidth of the actuator. Indeed, the existence of a soft spring system reduces the efficiency of the actuator during high power movements. This is one of the main reasons that the high-power generator muscles in the human leg are positioned near the hip joint with very stiff tendons.

The negative energy saved in the spring is fully recovered at $t \approx 17\%$, which pushes the actuator force to its maximum. The nominal peak force of the actuator A_A is 600 N. The recovery of the energy absorbed in the spring pushes the actuator force to 850 N or 40% higher, without an increase in actuator current. To electrically generate such a high force, motor current has to be increased by approximately 60%, since the motor current-torque curve get saturated in an overload condition.

CARL is a heavy robotic leg with 28 kg weight. Without force amplification of the spring system in the ankle joint, it would be almost impossible to perform the hopping experiment. We have to emphasize that hopping robots are usually built lightweight with passive elements, unlike bipedal robots that include heavy and stiff actuation systems for high power/torque movements. Power and force amplification in the ankle joint is one of the major advantages of the spring in the actuation system, which is also studied before-hand in the design of the ankle prosthesis devices in [35]. It was shown that by choosing the appropriate spring constant, it is possible to amplify the output power by 40%. During the vertical human jump, the amount of power needed in the ankle joint is far higher than the capability of the shank muscles. It is reported that 25% of power is delivered by the AT during the jump.

9.7 Discussion and Conclusion

In this study, we reported a hopping experiment with robotic leg CARL. Our objective was to report the influence of actuation redundancy and elasticity in the performance of the leg spring system. CARL as a musculoskeletal robot is constructed to contain the biological characteristics like elasticity and redundancy in the actuation system. Unlike, other hopping robots, CARL is developed as a bipedal robot which means that it is comprised of heavy actuators with precise force and position control.

The heavy mass of CARL makes the hopping experiment unique since not only do we have to push the robot to its hardware limits but also we can observe the joint stiffness and torques at the same level as a human. For instance, hopping experiment is performed with leg stiffness of $142 \text{ N m}^{-1} \text{ kg}^{-1}$ and 285 kN m^{-1} during landing. These stiffness values are in the same range for human hopping at the preferred frequency at $265 \text{ N m}^{-1} \text{ kg}^{-1}$. Similarly, the joint stiffness values are also in the same range for both robots and humans.

Our comparison of robotic and human hopping is very instructive, and essentially demonstrates the significance of the ankle complex in generating the virtual leg spring. Both active and passive elements of the actuators connecting to the ankle are the main contributors to the efficiency of leg spring action. We already mentioned numerous biomechanical studies that point to the same fact that the Achilles tendon and triceps surae muscles (SOL, GA) are influential in all types of human locomotion. The preferred frequency of locomotion is dependent on the stiffness of the AT. Without power amplification of AT, the human can not jump. Interestingly, we demonstrated these advantageous actions in robotic hopping which confirms the importance of bio-inspired robotic construction.

It is common practice in robotics to render leg springs using knee joint stiffness and completely avoid complex ankle mechanics. This approach is in contrast to the notion of being inspired by biology. Our investigation implies that the SLIP strategy has to be embodied in the mechanical structure of the leg, otherwise it may not be an efficient approach. Indeed, it is claimed that the mass-spring control policy in human hopping may not be energetically efficient and there is a possibility that CNS minimizes different objectives such as movement jerk [5]. If the robotic leg has different actuation and mechanical characteristics, it may not be feasible to imitate spring-like behavior in bipedal control. The control and construction of the robotic system are intertwined and should not be separated.

This study successfully establishes the feasibility of human-like robotic construction and shows how a robotic system can exhibit similar actuation functionality as a human. None of the biological similarities discussed in this research is encoded in the robotic control. We used a purely kinematic controller with no dynamic calculation that controls the workspace impedance. The recuperation of energy using series springs or transfer of power between joints is the emergent behavior of the actuation architecture and was not the intended objective of the control.

We observed a crucial difference in the control of the actuation system and biological muscles. In CARL, every actuator has a local controller that adjusts the output force, impedance, and position of the actuator. This controller does not consider the action of each component of the actuator like spring and motor. The priority of the controller to remove the undesirable internal mass-spring oscillations of the actuator. However, CNS only controls the muscle fiber which associates with the control of the only motor in the actuator. Leg muscles have different fiber structures based on their force and power demand. The dominant mono-articular ankle muscle, SOL, is composed highly of slow-twitch fibers. Therefore, SOL favors long-term contractions which generates force for a long period with relatively low fatigue. This muscle is also slow to increase its force and therefore is not capable of high power output.

The muscle action of SOL more resembles a very good damper or in its extreme like a clutch which generates high force with limited displacement. This type of muscle fiber is desirable to latch energy inside the AT. A similar policy is also possible to be included in the control of the motor component of the actuator. Electric motors can generate very high and efficient damping in which the energy is recuperated into the battery. However, this requires a different control architecture for series elastic actuators. Since there will be competing control objectives for high precision force control of the whole actuator or only motor control with probable oscillations in the system.

Our research demonstrated that there are numerous details in the control and structure of the human leg that contributes to the efficiency and grace of human locomotion. We draw a comparison between actuator redundancy and tendon spring influence in human and robotic locomotion. Consequently, SLIP control is only feasible if it is deployed in the bipedal robot with bio-inspired mechanical architecture.

References

1. Anderson, F.C., Pandy, M.G.: Storage and utilization of elastic strain energy during jumping. *J. Biomech.* **26**(12), 1413–1427 (1993)
2. Biewener, A.A.: Locomotion as an emergent property of muscle contractile dynamics. *J. Exp. Biol.* **219**(2), 285–294 (2016)
3. Blickhan, R.: The spring-mass model for running and hopping. *J. Biomech.* **22**, 1217–1227 (1989)
4. Blickhan, R., Seyfarth, A., Geyer, H., Grimmer, S., Wagner, H., Günther, M.: Intelligence by mechanics. *Philos. Trans. R. Soc. London Ser. A* **365**, 199–220 (2007)
5. Bobbert, M.F., Casius, L.R.: Spring-like leg behaviour, musculoskeletal mechanics and control in maximum and submaximum height human hopping. *Philos. Trans. R. Soc. B Biol. Sci.* **366**(1570), 1516–1529 (2011)
6. Bobbert, M.F., Huijing, P.A., van Ingen Schenau, G.J.: An estimation of power output and work done by the human triceps surae muscle-tendon complex in jumping. *J. Biomech.* **19**(11), 899–906 (1986)
7. Cleather, D.J., Southgate, D.F., Bull, A.M.: The role of the biarticular hamstrings and gastrocnemius muscles in closed chain lower limb extension. *J. Theoret. Biol.* **365**, 217–225 (2015)
8. Cleland, J.: On the actions of muscles passing over more than one joint. *J. Anatomy Physiol.* **1**(1), 85 (1867)
9. Farley, C.T., Blickhan, R., Saito, J., Taylor, C.R.: Hopping frequency in humans: a test of how springs set stride frequency in bouncing gaits. *J. Appl. Physiol.* **71**(6), 2127–2132 (1991)
10. Farley, C.T., Houdijk, H.H., Strien, C.V., Louie, M.: Mechanism of leg stiffness adjustment for hopping on surfaces of different stiffnesses. *J. Appl. Physiol.* **85**(3), 1044–1055 (1998)
11. Garofalo, G., Ott, C., Albu-Schäffer, A.: Walking control of fully actuated robots based on the bipedal slip model. In: 2012 IEEE International Conference on Robotics and Automation, pp. 1456–1463. IEEE (2012)
12. Geyer, H., Seyfarth, A., Blickhan, R.: Compliant leg behaviour explains basic dynamics of walking and running. *Proc. R. Soc. B Biol. Sci.* **273**(1603), 2861–2867 (2006)
13. Gong, Y., Hartley, R., Da, X., Hereid, A., Harib, O., Huang, J.-K., Grizzle, J.: Feedback control of a cassie bipedal robot: walking, standing, and riding a segway. In: 2019 American Control Conference (ACC), pp. 4559–4566. IEEE (2019)
14. Heise, G., Shinohara, M., Binks, L.: Biarticular leg muscles and links to running economy. *Int. J. Sports Med.* **29**(08), 688–691 (2008)

15. Hof, A.: The force resulting from the action of mono-and biarticular muscles in a limb. *J. Biomech.* **34**(8), 1085–1089 (2001)
16. Hogan, N.: Impedance control: an approach to manipulation. *J. Dyn. Syst. Meas. Control* **107**, 1–24 (1985)
17. Horsman, M.K.: The Twente lower extremity model. Consistent dynamic simulation of the human locomotor apparatus. Ph.D. thesis, University of Twente (2007)
18. Hubicki, C., Grimes, J., Jones, M., Renjewski, D., Spröwitz, A., Abate, A., Hurst, J.: ATRIAS: design and validation of a tether-free 3d-capable spring-mass bipedal robot. *Int. J. Robot. Res.* **35**(12), 1497–1521 (2016)
19. Ishikawa, M., Komi, P.V., Grey, M.J., Lepola, V., Bruggemann, G.-P.: Muscle-tendon interaction and elastic energy usage in human walking. *J. Appl. Physiol.* **99**(2), 603–608 (2005)
20. Jacobs, R., Bobbert, M.F., van Ingen Schenau, G.J.: Mechanical output from individual muscles during explosive leg extensions: the role of biarticular muscles. *J. Biomech.* **29**(4), 513–523 (1996)
21. Jacobs, R., Bobbert, M.F., et al.: Function of mono-and biarticular muscles in running. *Med. Sci. Sports Exer.* **25**(10), 1163–1173 (1993)
22. Knabe, C., Lee, B., Orekhov, V., Hong, D.: Design of a compact, lightweight, electromechanical linear series elastic actuator. In: Proceedings of the ASME International Design Engineering Technical Conferences & Computers and Information Engineering Conference (IDETC/CIE), pp. 1–8 (2014)
23. Lichtwark, G., Wilson, A.: In vivo mechanical properties of the human achilles tendon during one-legged hopping. *J. Exp. Biol.* **208**(24), 4715–4725 (2005)
24. Lichtwark, G., Wilson, A.: Is achilles tendon compliance optimised for maximum muscle efficiency during locomotion? *J. Biomech.* **40**(8), 1768–1775 (2007)
25. Moritz, C.T., Greene, S.M., Farley, C.T.: Neuromuscular changes for hopping on a range of damped surfaces. *J. Appl. Physiol.* **96**(5), 1996–2004 (2004)
26. Nejadfar, A., Berns, K., Vonwirth, P.: Technical advantages and disadvantages of biarticular actuators in bipedal robots. *Robots Human Life* **166** (2020)
27. Nejadfar, A., Schütz, S., Mianowski, K., Vonwirth, P., Berns, K.: Design of the musculoskeletal leg based on the physiology of mono-articular and biarticular muscles in the human leg. *Bioinspiration Biomimetics* **14**(6), 066002 (2019)
28. Nejadfar, A., Schütz, S., Vonwirth, P., Mianowski, K., Berns, K.: Coordination of the biarticular actuators based on instant power in an explosive jump experiment. In: IEEE International Conference on Advanced Intelligent Mechatronics (AIM) (2018)
29. Nejadfar, A., Schütz, S., Vonwirth, P., Mianowski, K., Karsten, B.: Moment arm analysis of the biarticular actuators in compliant robotic leg carl. In: Conference on Biomimetic and Biohybrid Systems, pp. 348–360. Springer, Springer International Publishing (2018)
30. Nejadfar, A., Yazdanpanah, M.J., Hassanzadeh, I.: Friction compensation of double inverted pendulum on a cart using locally linear neuro-fuzzy model. *Neural Comput. Appl.* **22**(2), 337–347 (2013)
31. Nezhadfar, A.: Integration and design of actuation redundancy in robotic leg CARL based on the physiology of biarticular muscles. Dissertation—Technical University of Kaiserslautern. Verlag Dr. Hut. (2020).<https://www.dr.hut-verlag.de/9783843945981.html>
32. Oehlke, J., Beckerle, P., Seyfarth, A., Sharbafi, M.A.: Human-like hopping in machines. *Biol. Cybern.* **113**(3), 227–238 (2019)
33. Orekhov, V.L., Knabe, C.S., Hopkins, M.A., Hong, D.W.: An unlumped model for linear series elastic actuators with ball screw drives. In: IEEE/RSJ International Conference on Intelligent Robots and Systems (IROS), pp. 2224–2230. IEEE (2015)
34. Paine, N.A.: High-performance series elastic actuation. Ph.D. thesis, The University of Texas, Austin (2014). <https://repositories.lib.utexas.edu/handle/2152/26938>
35. Paluska, D., Herr, H.: The effect of series elasticity on actuator power and work output: implications for robotic and prosthetic joint design. *Robot. Auton. Syst.* **54**(8), 667–673 (2006)
36. Pelit, M.M., Chang, J., Takano, R., Yamakita, M.: Bipedal walking based on improved spring loaded inverted pendulum model with swing leg (slip-sl). In: 2020 IEEE/ASME International Conference on Advanced Intelligent Mechatronics (AIM), pp. 72–77. IEEE (2020)

37. Perry, J.: Gait Analysis: Normal and Pathological Function. Thorofare, NJ: SLACK. OCLC: ocm27816876 (1992)
38. Pfeifer, R., Bongard, J.: How the body shapes the way we think: a new view of intelligence. MIT press (2006)
39. Pratt, J., Krupp, B.: Design of a bipedal walking robot. In: Unmanned Systems Technology X, vol. 6962, p. 69621F. International Society for Optics and Photonics
40. Pratt, J., Krupp, B., Morse, C.: Series elastic actuators for high fidelity force control. *Ind. Robot J.* **29**(3), 234–241 (2002)
41. Prilutsky, B.I., Gregor, R.J.: Strategy of coordination of two-and one-joint leg muscles in controlling an external force. *Motor Control* **1**(1), 92–116 (1997)
42. Prilutsky, B.I., Zatsiorsky, V.M.: Tendon action of two-joint muscles: transfer of mechanical energy between joints during jumping, landing, and running. *J. Biomech.* **27**(1), 25–34 (1994)
43. Raibert, M.H.: Legged robots. *CACM* **29**(6) (1986)
44. Raibert, M.H.: Legged Robots That Balance. MIT Press, Cambridge, MA (1986)
45. Rall, J.A.: Energetic aspects of skeletal muscle contraction: implications of fiber types. *Exer. Sport Sci. Rev.* **13**, 33–74 (1985)
46. Ramezani, A., Hurst, J.W., Hamed, K.A., Grizzle, J.W.: Performance analysis and feedback control of atrias, a three-dimensional bipedal robot. *J. Dyn. Syst. Meas. Control* **136**(2) (2014)
47. Reher, J., Ma, W.-L., Ames, A.D.: Dynamic walking with compliance on a cassie bipedal robot. In: 2019 18th European Control Conference (ECC), pp. 2589–2595. IEEE (2019)
48. Robinson, D.W.: Design and analysis of series elasticity in closed-loop actuator force control. Ph.D. thesis, Massachusetts Institute of Technology (2000)
49. Rummel, J., Blum, Y., Maus, H.M., Rode, C., Seyfarth, A.: Stable and robust walking with compliant legs. In: 2010 IEEE International Conference on Robotics and Automation, pp. 5250–5255. IEEE (2010)
50. Rummel, J., Seyfarth, A.: Stable running with segmented legs. *Int. J. Robot. Res.* **27**(8), 919–934 (2008)
51. Sayyad, A., Seth, B., Seshu, P.: Single-legged hopping robotics research-a review. *Robotica* **25**(5), 587 (2007)
52. Schenau, G.J.V.I., Pratt, C.A., Macpherson, J.M.: Differential use and control of mono-and biarticular muscles. *Human Movement Sci.* **13**(3–4), 495–517 (1994)
53. Schütz, S., Mianowski, K., Köttig, C., Nejadfar, A., Reichardt, M., Berns, K.: RRLAB SEA—a highly integrated compliant actuator with minimised reflected inertia. In: IEEE International Conference on Advanced Intelligent Mechatronics (AIM) (2016)
54. Schütz, S., Nejadfar, A., Berns, K.: Influence of loads and design parameters on the closed-loop performance of series elastic actuators. In: IEEE International Conference on Robotics and Biomimetics (ROBIO) (2016)
55. Schütz, S., Nejadfar, A., Köttig, C., Berns, K.: An intuitive and comprehensive two-load model for series elastic actuators. In: IEEE 14th International Workshop on Advanced Motion Control (AMC) (2016)
56. Schütz, S., Nejadfar, A., Mianowski, K., Vonwirth, P., Berns, K.: CARL—a compliant robotic leg featuring mono- and biarticular actuation. In: IEEE-RAS International Conference on Humanoid Robots, pp. 289–296 (2017)
57. Schütz, S., Nezhadfar, A., Dorost, N., Berns, K.: Exploiting the intrinsic deformation of a prosthetic foot to estimate the center of pressure and ground reaction force. Bioinspiration Biomimetics (2020)
58. Shahbazi, M., Babuška, R., Lopes, G.A.: Unified modeling and control of walking and running on the spring-loaded inverted pendulum. *IEEE Trans. Robot.* **32**(5), 1178–1195 (2016)
59. Sharbafi, M.A., Radkhah, K., von Stryk, O., Seyfarth, A.: bHopping control for the musculoskeletal bipedal robot: Biobiped. In: 2014 IEEE/RSJ International conference on Intelligent Robots and Systems, pp. 4868–4875. IEEE (2014)
60. Shin, H., Ishikawa, T., Kamioka, T., Hosoda, K., Yoshiike, T.: Mechanistic properties of five-bar parallel mechanism for leg structure based on spring loaded inverted pendulum. In: 2019 IEEE-RAS 19th International Conference on Humanoid Robots (Humanoids), pp. 320–327. IEEE (2019)

61. Soest, A.J.V., Schwab, A.L., Bobbert, M.F., van Ingen Schenau, G.J.: The influence of the biarticularity of the gastrocnemius muscle on vertical-jumping achievement. *J. Biomech.* **26**(1), 1–8 (1993)
62. Tamaddoni, S.H., Jafari, F., Meghdari, A., Sohrabpour, S.: Biped hopping control based on spring loaded inverted pendulum model. *Int. J. Humanoid Robot.* **7**(02), 263–280 (2010)
63. Verstraten, T., Furnémont, R., Beckerle, P., Vanderborght, B., Lefeber, D.: A hopping robot driven by a series elastic dual-motor actuator. *IEEE Robot. Autom. Lett.* **4**(3), 2310–2316 (2019)
64. Vonwirth, P., Nejadfar, A., Mianowski, K., Berns, K.: Slip-based concept of combined limb and body control of force-driven robots. In: Zeghloul ,S. Laribi, M.A., Sandoval Arevalo, J.S. (eds.) *Advances in Service and Industrial Robotics*, vol. 84, pp. 547–556. Springer International Publishing, Cham (2020)
65. Ward, S.R., Eng, C.M., Smallwood, L.H., Lieber, R.L.: Are current measurements of lower extremity muscle architecture accurate? *Clin. Orthopaed. Rel. Res.* **467**(4), 1074–1082 (2009)
66. Winter, D.A.: *Biomechanics and Motor Control of Human Movement*, 4th ed. Wiley (2009)

Chapter 10

Dynamic Modeling of an Asbestos Removal Mobile Manipulator for Stability Evaluation



Siddharth Maraje, Chedli-Belhassen Bouzgarrou, Jean-Christophe Fauroux, and Lounis Adouane

The H2020 project **Robots to Reconstruction** [3] was started with an aim to bring automation into the construction industry. A general concept of the robotized asbestos removal process is illustrated in Fig. 10.1. Multiple semi-autonomous robotic units equipped with the grinding tool are deployed in the cleaning environment. They also possess asbestos detectors which provide input to the mobile base localization. The local process monitoring then controls the grinding process through tool path planning. The two prototypes developed during the project are shown in Fig. 10.2. The version-1 prototype has 6 caster wheels in total. The two central wheels are the drive wheels while the four corner wheels stay non actuated. The version-2 prototype however has four Swedish wheels. The two versions also differ in terms of the arm architecture integrated into them. Version-1 is added with the P-6R arm while version-2 has 7R architecture.

This chapter presents an extract of the work done by authors during the course of the project. Initially, the state of the art consisting of a variety of stability indices (margins) relevant to mobile manipulators is presented. Thereafter, dynamic modeling of the asbestos removal environment and the use-case in different cleaning scenarios is shown. Two methods of stability evaluation are then demonstrated in detail and an example of zig-zag tool trajectory.

S. Maraje · C.-B. Bouzgarrou (✉) · J.-C. Fauroux · L. Adouane
Universität Clermont Auvergne, CNRS, Clermont Auvergne INP, Institut Pascal,
Clermont-Ferrand 63000, France
e-mail: belhassen-chedli.bouzgarrou@sigma-clermont.fr

L. Adouane
Université de technologie de Compiègne (UTC), CNRS, Heudiasyc, Compiègne 60200, France

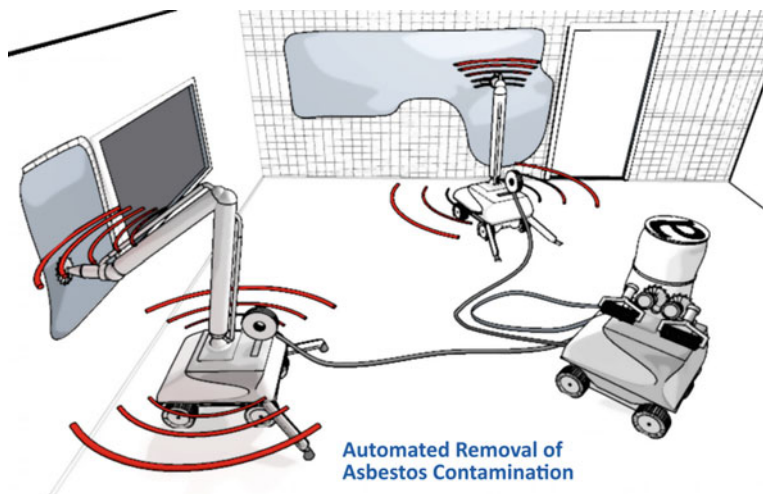


Fig. 10.1 The concept of robotized asbestos removal process [3]



(a) Prototype version-1

(b) Prototype version-2

Fig. 10.2 Two prototypes developed by the consortium of Bots2ReC

10.1 Stability Indices for Mobile Manipulators

For mobile manipulators and robots in general, including wheeled and legged ones, numerous attempts to accurately evaluate stability can be seen through the literature. A condition to determine the state of stability or instability is called a *criterion*, while a quantitative measure of stability is termed as *margin*. A review of static and dynamic margins was presented in [2]. In [12], based on stability metric, criteria were further classified into five types namely: distance, angle, force, moment and energy. This classification is adapted for presenting the state of the art through the following sections.

10.1.1 Distance Based Indices

Distance-based criteria use the minimum distance between the projection of the centre of gravity on the support polygon C.G and an edge of the support polygon to define instantaneous stability. In [13] and [14], a static stability criterion based on the C.G was proposed. The claim was, a vehicle (wheeled or legged) is statically stable if '*the projection of its centre of mass lies within the supporting polygon*'. Support polygon of the footprint of the robot was defined as a convex polygon formed by connecting ground-wheel contact points.

Figures 10.3 and 10.4 respectively show statically stable and unstable poses of the mobile manipulator. Rectangular support polygon of the mobile manipulator defined by points $S_{11}S_{12}S_{21}S_{22}$.

Sreenivasan [21] proposed a distance-based dynamic stability margin (Fig. 10.5). It projected the dynamic force F_g applied on the C.G of the robot to the ground and measured the distance d between the line of action of the force and a parallel line

Fig. 10.3 Statically stable pose

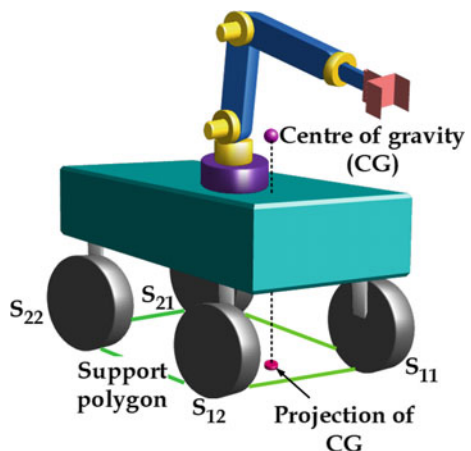


Fig. 10.4 Statically unstable pose

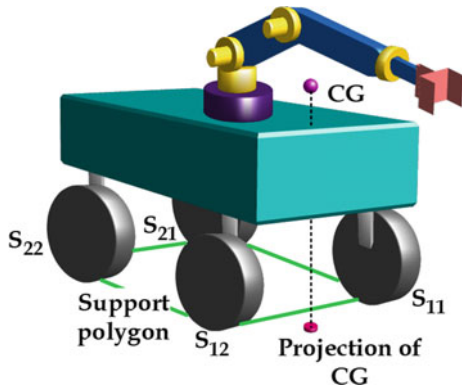
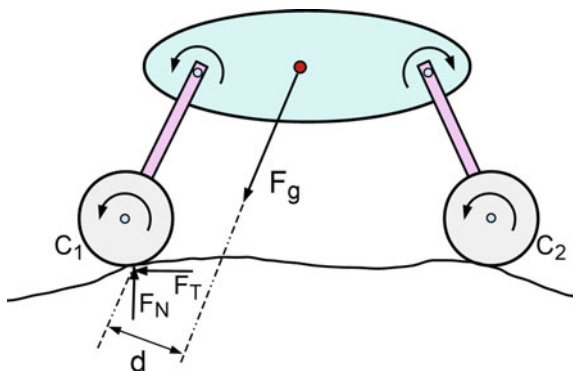


Fig. 10.5 Distance based dynamic stability margin [21]



passing through ground contact point. But this margin had a limitation of not being able to handle dynamic torques applied on the mobile platform.

Davidson and Schweitzer [4] proposed a static stability margin for four-legged robots. In their method, external forces, the force from a tethering cable-winch and inertial force were included in a quasi-static manner as a wrench. Possible rotation of the vehicle around the axis defined by each edge of the support polygon is defined as a twist of zero pitch. Virtual power generated by a resultant wrench and zero-pitch virtual twist was determined for all edges of the support polygon. A negative value of virtual power was identified as a condition of instability. The minimum magnitude of this power was used as a value for stability margin.

10.1.2 Angle Based Indices

In [5], subtended angle (θ) between normal of the i th tip-over axis and i th resultant force is considered as a measure of stability about i th tip-over axis. The minimum of all such angles calculated for respective axes is the stability margin of the entire system.

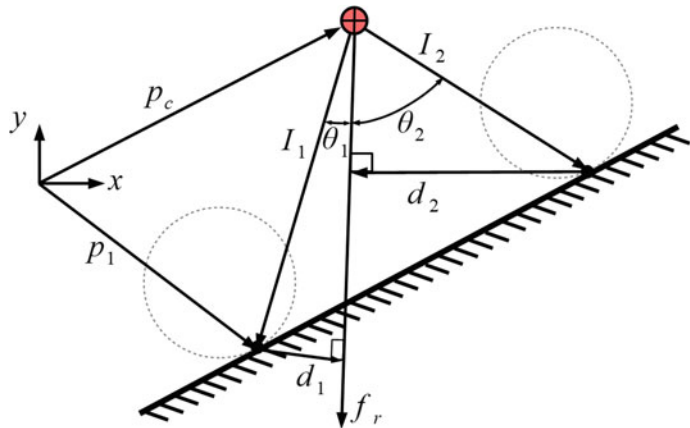


Fig. 10.6 Concept of force angle stability margin [19]

$$\theta = \min(\theta_i) \quad (10.1a)$$

$$\theta > 0 \rightarrow \text{stable}; \quad \theta = 0 \rightarrow \text{marginally stable}; \quad \theta < 0 \rightarrow \text{unstable} \quad (10.1b)$$

Another tip-over stability margin called force-angle stability measure (FASM) was proposed in [19]. The claim was an easy calculation and sensitivity to top-heaviness. According to the author—‘force-angle stability measure is based on the computation of *minimum of the angle between the net force vector and a normal to each of the tip-over axis* (Fig. 10.6)’.

$$\beta = \theta_i \cdot \|d_i\| \cdot \|f_r\| \quad (10.2)$$

Critical tipover instability occurs when β goes to zero, i.e., any θ_i becomes zero, or either of $\|d_i\|$ or the force f_r become zero.

10.1.3 Energy Based Indices

Messuri and Klein [15] proposed **energy stability margin** (ESM) as an improvement to the static stability margin. Energy stability level associated with a particular edge of a support polygon is equal to the mechanical work required to rotate the body centre of gravity about an edge to a position where the vertical projection of CG lies along that edge of the support polygon (to the verge of instability). The energy stability margin is equal to the minimum of the energy stability levels associated with all the edges of the support polygon.

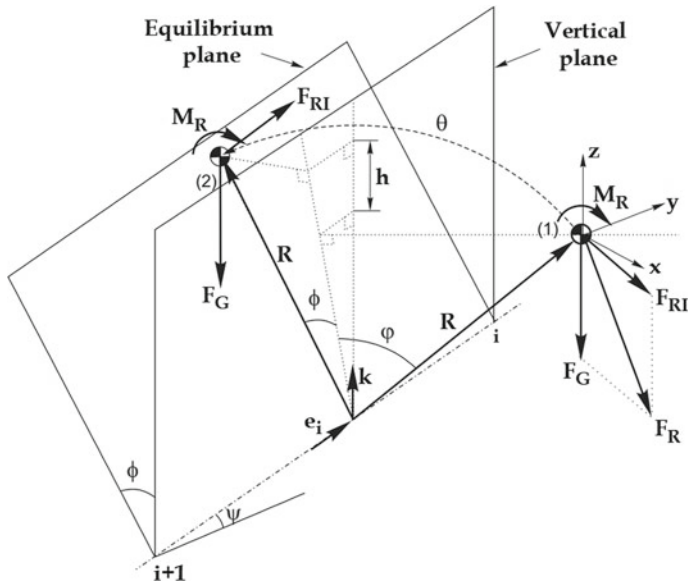


Fig. 10.7 Equilibrium plane corresponding to the tip-over edge, [8, 9]

$$S_{ESM} = \min_{i=1}^{n_s} (mgh_i) \quad (10.3)$$

'i' is a vertex of the support polygon which form a rotational axis with $i + 1$, n_s is the number of supporting legs and h_i is the elevation of C.G during the tip-over process (Fig. 10.7).

Ghasempoor and Sepehri [8] extended ESM for mobile manipulators by including other factors affecting stability—vehicle top-heaviness, uneven terrain conditions, external forces arising from the manipulation of payload and inertial forces due to vehicle motions. ESM is intended to monitor the tip-over potential of mobile manipulators. An *equilibrium plane* (π_s) associated with each edge of the support polygon was defined such that, the plane contains the centre of gravity at the hypothetical tilted position of the mobile manipulator system for which projection of the centre of gravity on p_s is on the respective edge. Figure 10.8 shows the hypothetical tip-over of the mobile robotic system. For this state of tilt, the projection of the centre of gravity lies on the edge $S_{11}-S_{22}$. The equilibrium plane denoted by π_s is thus defined to pass through edge $S_{11}-S_{22}$ and centre of gravity.

The energy stability level associated with each edge was defined as the mechanical work required to rotate the system about the respective edge till the centre of gravity lies in the equilibrium plane. The minimum of all the energy levels was regarded as a dynamic energy stability margin (DESM). Energy associated with the supporting edge defined by points $(i)-(i+1)$ was calculated as,

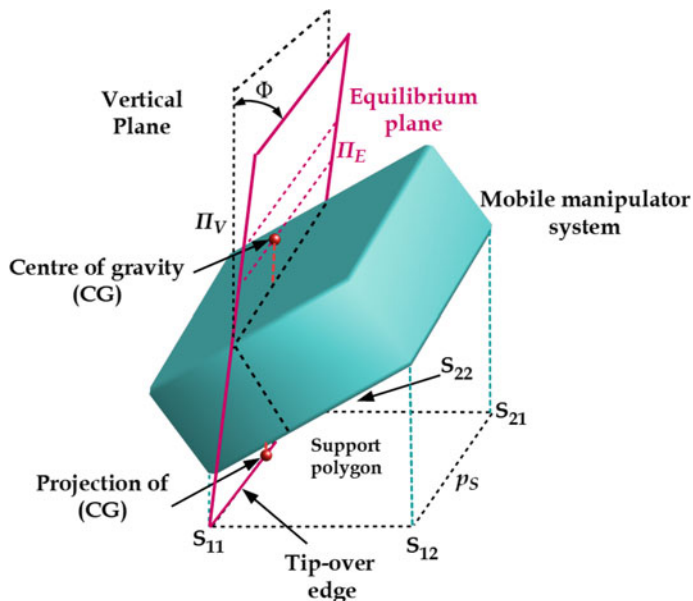


Fig. 10.8 Hypothetical tipover of the robotic system

$$\text{Energy Stability Level}_{(i,i+1)} = [W_1 - W_2]_{(i,i+1)}; \quad (10.4)$$

Here, W_1 is work done by stabilizing weight force and W_2 is work done by destabilizing forces and moments.

In [9] normalized energy stability margin was proposed as the difference between the initial position of the center of gravity and its highest position in the process of tumbling.

$$S_{NESM} = \frac{S_{ESM}}{mg} = \min_{i=1}^{n_s} (h_i) \quad (10.5)$$

Here, the n_s is the number of edges of the support polygon, and h_i is the elevation of the height of the C.G during tip-over. In [7] this concept was extended to walking machines considering leg dynamic effect a disturbance. It was stated that a walking machine is dynamically stable if every moment M_i around the edge i of the support polygon due to robot/ground forces moments is positive. The positive direction was the clockwise direction of the force around the support polygon. Energy stability level for all the edges was calculated as a *difference of potential and kinetic energy*. Thus, the **normalised energy stability margin** (S_{NEDSM}) was defined as:

$$S_{NEDSM} = \frac{\min(E_i)}{mg} \quad (10.6)$$

10.1.4 Moment Based Indices

Dynamic stability margin was proposed in [11] as the smallest of all moments M_i around the edges of the support polygon. This margin considered robot/ground interaction forces and was normalized by the weight of the system.

$$S_{DSM} = \min_{i=1}^n \frac{e_i \cdot (F_R \times P_i + M_R)}{mg} \quad (10.7)$$

Yoneda and Hirose [24] presented tumble stability criterion and introduced a counter-force limit as an index to indicate manipulation capabilities. The concept of stability is based on the ability of virtually lost wheel-ground contact points to generate support force required to suppress tumbling. Mathematical expression to calculate this margin is:

$$\text{Tumble stability margin} = \frac{\min \left| \bar{M} \cdot \frac{(p_a - p_b)}{|p_a - p_b|} + \bar{F} \cdot \frac{(p_b \times p_a)}{|p_a - p_b|} \right|}{mg} \quad (10.8)$$

Here, \bar{M} and \bar{F} are net moment and force acting at CG, p_a and p_b are the coordinate vectors of the adjacent ground contact points that define axis of rotation.

Sugano et al. [22] was one of the initial works to introduce zero moment point (ZMP) as a stability criteria for mobile manipulators. It was identified that the stability of a mobile manipulator is closely related to the motion of the mobile base, posture and motion of the onboard manipulator and external forces on the end-effector. Based on ZMP, two concepts named *stability degree* and *valid stable region* are proposed. The former defined the stable limit while the later was used to discuss the influence of disturbances in the task environment.

In this chapter, the support polygon of the mobile manipulator system was called *stable region*. A maximal stability curve (which is a straight line) was identified inside the stable region such that, stability is highest when ZMP lies on this curve. To ensure the safety of the mobile manipulator under the influence of external forces or environmental disturbances, a valid stable region was defined such that, if ZMP lies within this region, stability is ensured. i.e. ZMP lies within the stable region (support polygon) after being displaced (Fig. 10.9).

In [16, 17] Moment Height Tip-over Measure (MHS) was proposed. This index was proved to be computationally less expensive than energy and force-based margins. The resultant of force and moments exerted by the manipulator on the mobile base was calculated. Then the moment of this resultant about corner points of the support polygon was found. These moments were then projected on the respective edges of the support polygon. To make the criterion sensitive to the height of the CG, a multiplicative term h_{cm} was added to the MHS. In order to calculate the MHS, requirements are: all joint angles, velocities and accelerations of onboard manipulator, linear and angular accelerations of a mobile base, knowledge of external forces and torques exerted on the system.

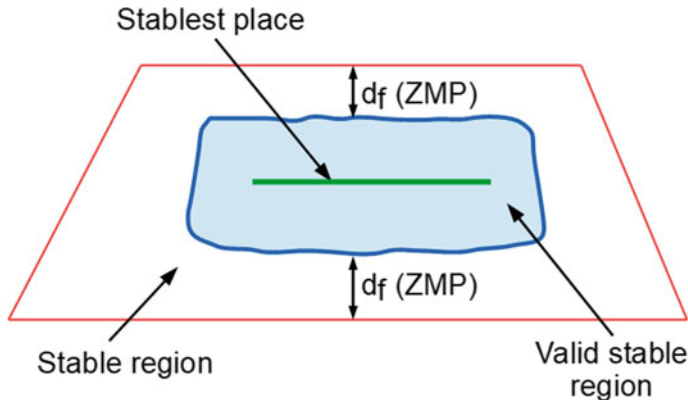


Fig. 10.9 Concept of stable and valid stable region [22]

MHS measure α is computed in (10.9),

$$\alpha = \min_i(\alpha_i) \quad i = \{1, 2, 3, 4, \dots\} \quad (10.9)$$

Here, α_i denotes dynamic MHS measure about i th edge which is given as,

$$\alpha_i = (I_i)^\sigma M_i \quad (10.10)$$

Here, I_i is the moment of inertia of mobile base about i th axis, M_i is moment about i th axis and $\sigma = 1$ if $M_i > 0$ else -1 .

Roan et al. [20] presented a real-world validation of three tip-over algorithms: Zero-Moment point (ZMP), Force-Angle stability measure (FA) and Moment-Height Stability (MHS). A scoring scheme was implemented to record values of criteria at the actual time of tip-over, to record lag/lead of criteria and to count false positives. FA and MHS are found to be quite identical except for negative values.

Lee et al. [10] proposed the concept of a modified zero moment point for evaluating tip-over of mobile robots over uneven terrain. The turnover stability index for linear acceleration and rotational velocity are defined with the modified ZMP. The turnover stability space (TSS) with turnover stability indices is presented to control the mobile robot in order to avoid turnover effectively.

10.1.5 Force Based Indices

Mahdi and Nestinger [12] proposed a foot force criterion as an attempt to provide a quantitative measure to determine how far away the robot is from either instability or from the maximum stable pose. Mathematically foot force stability criterion is expressed as

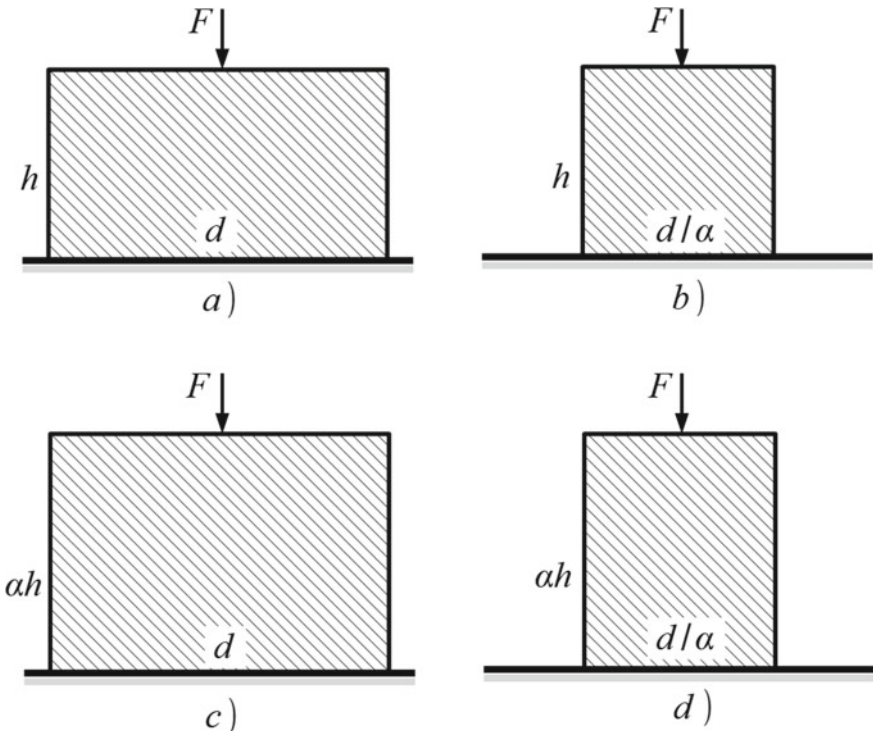


Fig. 10.10 Effect of top-heaviness on stability [12]

$$FFSM = \frac{f_1 f_2 \dots f_n}{\bar{f}^n} \quad 0 \leq FFSM \leq 1 \quad (10.11)$$

Here, n is the number of supporting legs with strictly positive foot force, f_i is the magnitude of i^{th} normal foot force and $\bar{f} = \frac{1}{n} \sum_{i=1}^n f_i$. An important feature of the stability margins that are based on foot forces that all the effects of gravity, external forces, inertial forces and disturbances are reflected in foot forces [18].

Figure 10.10 presents cross-sections of four different mobile bases with different aspect ratios. Considering lateral disturbances, these systems differ in terms of tip-over potential: Fig. 10.10a has the highest while Fig. 10.10d has the lowest geometric tip-over potential. Depending on the magnitude of the force F , the potential changes for all cases. This is defined as a sensitivity to top-heaviness.

Modified foot force stability margin is given by following equation:

$$MFFSM = FFSM \cdot \frac{(P_i)^j}{h_i} \cdot f \quad (10.12)$$

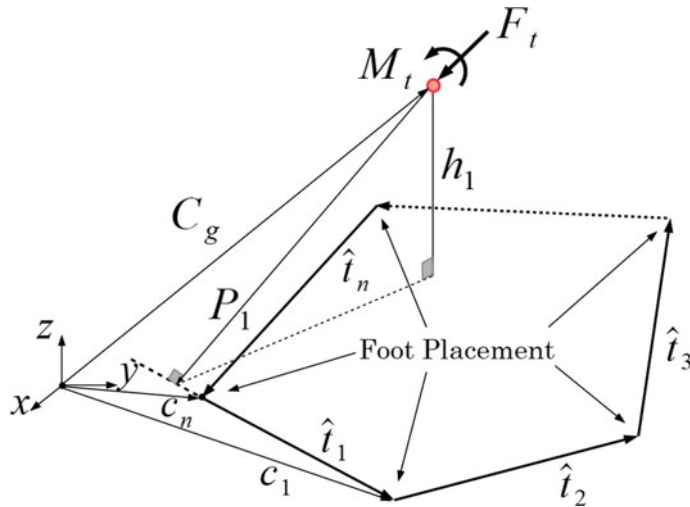


Fig. 10.11 Schematic of general n -legged robot [12]

Here, $j = 1$ if the projection of CG is inside support polygon else, 0. h_i is the height of the CG with respect to tip-over the axis and P_i is tip-over axis normal as shown in Fig. 10.11.

Ding et al. [6] presented an improved tip-over moment stability criterion taking into account wheel-ground and vehicle-manipulator interaction. Based on this criterion a real-time tip-over avoidance algorithm was proposed to minimize the tip-over moment transfer. It used two sets of corrective actions: adjusting the posture of the onboard manipulator or changing the running velocity of the vehicle.

10.2 Dynamic Modeling of the Asbestos Removal Environment

The dynamic nature of the asbestos removal process generates the need for setting up a simulation model for assessing the behaviour of the robotic unit while performing removal operation. The primary objective of this assessment is stability evaluation of the robotic unit to ensure safe and stable operation. In this context, the chapter presents a methodology adapted to study the dynamic behaviour of the robotic unit. Initially, the environment to be cleaned and its key components are presented. Thereafter, cleaning scenarios arising due to the presence of different entities like wall, ceiling and ground are analysed to identify the reaction wrench and its effect on the stability of the robotic unit. Finally, two methods of stability evaluation, MATLAB-numerical and ADAMS-MATLAB co-simulation are explained in detail.

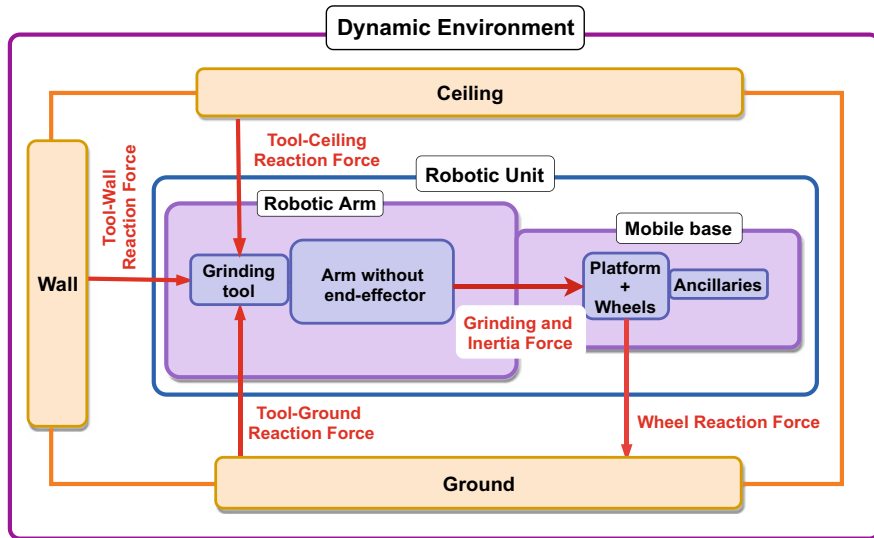


Fig. 10.12 Interaction model of asbestos removal use case

10.2.1 Need of Dynamic Modeling

The process of asbestos removal involves dynamic interaction between the cleaning environment and the robotic unit. This interaction occurs at two levels. Firstly, a grinding tool mounted on the robotic arm interacts with the cleaning surface and generate reaction forces. Secondly, wheels of the mobile base are subjected to ground reaction forces due to:

- weight of the robotic unit
- grinding forces (normal and tangential reaction forces, three reaction wrenches)
- inertia forces generated due to the motion of robotic arm and tool rotation.

In Fig. 10.12 a typical interaction model existing within the process of asbestos removal is detailed. Reaction forces generated by tool-surface interaction (ground, wall and ceiling) are transmitted to the arm through tool-arm connection. Since, arm performs accelerated motions, varying inertial forces are generated in addition to the grinding reaction forces. The connection of the arm to the mobile base transmits these forces to the mobile base which are further passed on to the ground surface through wheels. Due to these transmissions, stability of the robotic unit is significantly affected. Therefore, in order to study the effects of arm motion and grinding reaction forces on the stability of robotic unit, a dynamic simulation model capable of simulating a realistic asbestos removal scenario must be constructed.

For realistic simulation of the process, intended dynamic model should incorporate following components:

- Cleaning environment consisting of elements like wall, ground and ceiling.
- Multi-body dynamic model of the robotic unit localized inside cleaning environment (with inertial parameters: mass, centre of mass, inertia).
- Geometric and kinematic models (direct and inverse) of the robotic arm for motion generation.
- Tool-wall and wheel-ground contacts to simulate robot-environment dynamic interaction.
- Control scheme to govern the motion of the robotic arm.
- Formulation for dynamic stability of the robotic unit.

In the following sections, components of dynamic model are explained in detail.

10.2.2 Cleaning Environment

A cleaning environment is typically a rehabilitation site located in a residency building. The site consists of rooms like a bedroom, office/study room, living room, kitchen, dining room, front entrance, garden, laundry room, etc. They vary in terms of dimensions (ceiling height, room width and length) as well as materials used for construction (resurfacing concrete, plaster, bricks, tiles etc.). However, one obvious commonality for all the rooms is that the surfaces to clean can be on the ground, the walls or the ceiling.

10.2.3 Description of Representative Frames

To represent the environment as well as the robotic unit, coordinate frames are defined for individual entities (Fig. 10.13). Here, we consider the surfaces of the room are perfectly planar and perpendicular to each other. Also, an important assumption for the placement of the robotic unit throughout the cleaning operation is to have a longitudinal axis of the robotic unit perpendicular to the frontal wall. Let, \mathbf{w} and \mathbf{h} be the width and the height vectors of the frontal wall. The frames consist of three mutually perpendicular unit vectors. A detailed description of these frames goes below:

Environment frame (\mathcal{F}_E) Environment mainly consists of three surfaces i.e. wall, ceiling and ground. In most of the cases where walls are planar (i.e. without curvatures), these three surfaces can help to define the global environment frame of reference. The origin of the frame is named as O_E . Position of O_E can be assumed at a convenient location e.g. centre of the room, corner of the room etc. Axis \mathbf{x}_E is defined as normal to plane P_W point inside the room. Then, axes \mathbf{x}_E and \mathbf{y}_E can be

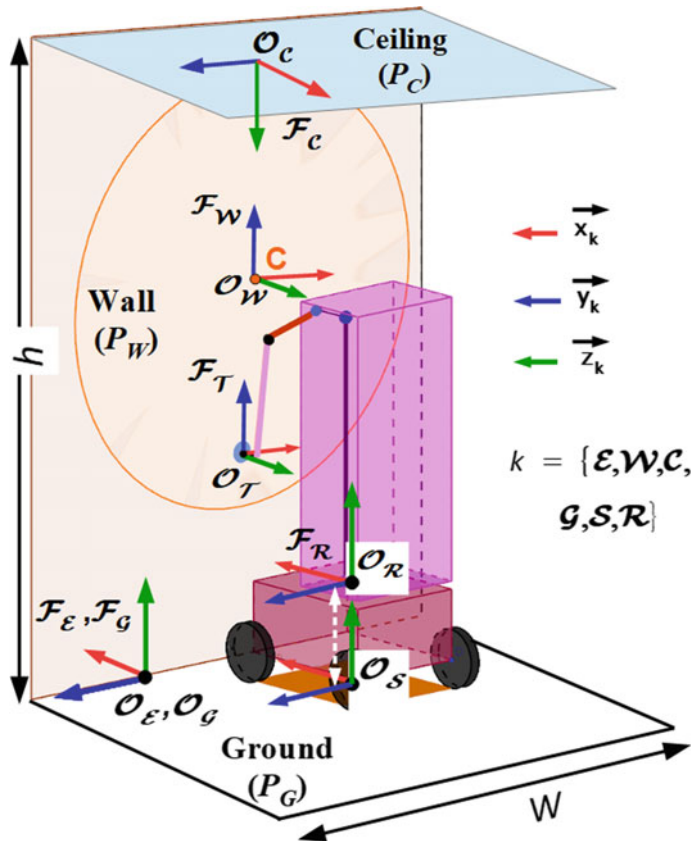


Fig. 10.13 Description of cleaning environment and frames

defined as mutually perpendicular axes that lie in the ground plane P_G . Axis y_E is selected along the line of intersection of planes P_W and P_G and its direction is shown in Fig. 10.13. According to general conventions, $\mathbf{x}_E = \mathbf{y}_E \times \mathbf{z}_E$.

Ground frame (\mathcal{F}_G) Ground frame \mathcal{F}_G is assumed to be oriented parallel to the frame \mathcal{F}_E . So the axis \mathbf{z}_E is normal to the plane P_G . Position of the origin O_G can be assumed at any convenient on the plane P_W . Here, the assumption is that the room is parallelepipedic in shape.

Ceiling frame (\mathcal{F}_C) The ceiling plane P_C is parallel to the ground plane P_G and is separated by height \mathbf{h} and located on the ceiling. Thus, the orientation of the ceiling frame (\mathcal{F}_C) is parallel to that of the ground frame (\mathcal{F}_G).

Wall frame (\mathcal{F}_W) Origin of the front wall frame O_W is fixed on the wall surface. Z -axis \mathbf{z}_W is normal to the wall plane P_W . Axes \mathbf{x}_W and \mathbf{y}_W are mutually perpendicular and lie in plane P_W . Also, $\mathbf{z}_W = \mathbf{x}_W \times \mathbf{y}_W$. Thus, with respect to the frame \mathcal{F}_E , \mathbf{z}_W is parallel to \mathbf{x}_E , \mathbf{x}_W is parallel to \mathbf{y}_E and \mathbf{y}_W is parallel to \mathbf{x}_E (Table 10.1).

Table 10.1 Description of frames

Frame (\mathcal{F})	Position (\mathcal{P})	Orientation (\mathcal{O})
Environment (\mathcal{F}_E)	At a convenient position on P_G	$\mathbf{z}_E \perp P_G$
		$\mathbf{y}_E = \text{any of the two directions along } P_G \cap P_W$
		$\mathbf{x}_E = \mathbf{y}_E \times \mathbf{z}_E$
Ground (\mathcal{F}_G)	At a convenient position on P_G	$\mathbf{z}_G \perp P_G$
		$\mathbf{y}_G = \mathbf{y}_E$
		$\mathbf{x}_G = \mathbf{x}_E$
Wall (\mathcal{F}_W)	At a convenient position on P_W	$\mathbf{z}_W \perp P_W$
		$\mathbf{y}_W = \mathbf{h}, \mathbf{y}_W \in P_W$
		$\mathbf{x}_W = \mathbf{w}, \mathbf{x}_W \in P_W$
Ceiling (\mathcal{F}_C)	At a convenient position on P_C	$\mathbf{z}_C \perp P_C$
		$\mathbf{y}_C = \mathbf{y}_E$
		$\mathbf{x}_C = \mathbf{x}_E, \mathbf{x}_W \in P_W$
Robotic unit (\mathcal{F}_R)	Center of the top face of the mobile base	$\mathbf{z}_R \perp P_G$
		$\mathbf{y}_R = \mathbf{y}_G$
		$\mathbf{x}_R = \mathbf{x}_G$
Support polygon (\mathcal{F}_S)	Geometric centre of the support polygon	$\mathbf{z}_S \perp P_G$
		$\mathbf{y}_S = \mathbf{y}_G$
		$\mathbf{x}_S = \mathbf{x}_G$

Frame of the Robotic Unit (\mathcal{F}_R) The frame of the robotic unit with origin O_R is attached to the centre of the top face of the mobile base. Axes \mathbf{x}_R and \mathbf{y}_R are directed along the length and the width of the mobile base and are parallel to plane P_G . Thus on a flat standard ground, orientation of axis \mathbf{z}_R is parallel to axis \mathbf{z}_E .

Frame of the support polygon (\mathcal{F}_S) The frame of the support polygon with origin O_S is attached to the centre of the support polygon of the mobile base. Axes \mathbf{x}_R and \mathbf{y}_R are directed along the length and the width of the mobile base and are parallel to axes \mathbf{x}_R and \mathbf{y}_R respectively. Naturally, orientation of axis \mathbf{z}_R is parallel to axis \mathbf{z}_E .

Transformation between frames There exists a fixed transformation between environment frame (\mathcal{F}_E) and frames representing components of the environment. i.e. wall frame (\mathcal{F}_W), ground frame (\mathcal{F}_G) and ceiling frame (\mathcal{F}_C). These transformations are summarized in the Table 4.2. $\mathbf{R}_k E$ denotes a rotation matrix around axis \mathbf{k}_E where, $k = x, y, z$ (Table 10.2).

Table 10.2 Transformation of frames w.r.t environment frame

Frame	Position w.r.t $\mathcal{F}_{\mathcal{E}}$	Orientation w.r.t $\mathcal{F}_{\mathcal{E}}$
Wall frame (\mathcal{F}_w)	$^E [o_{w_x} \ o_{w_y} \ o_{w_z}]$	$[\mathbf{R}_{z_E} (-\frac{\pi}{2}), \mathbf{R}_{x_E} (-\frac{\pi}{2})]$
Ground frame (\mathcal{F}_G)	$^E [o_{g_x} \ o_{g_y} \ 0]$	
Ceiling frame (\mathcal{F}_C)	$^E [o_{c_x} \ o_{c_y} \ o_{c_z}]$	$[\mathbf{R}_{y_E} (-\pi)]$
Support polygon (\mathcal{F}_S)	$^E [o_{s_x} \ o_{s_y} \ 0]$	$[\mathbf{R}_{z_E}]$
Robotic unit (\mathcal{F}_R)	$^E [o_{r_x} \ o_{r_y} \ H_b \hat{k}]$	$[\mathbf{R}_{x_E}]$

10.3 Modeling of Asbestos Removal Use Case

The process of asbestos removal involves positioning the mobile platform base in the cleaning environment at a suitable distance so as to access the maximum possible area at a given base position and be able to grind the surfaces with optimal grinding posture while maintaining the stability of the overall robotic unit.

Figure 10.14 shows robotic unit placed at a distance b from wall surface P_w . At this distance, the 3D workspace (W_A) of the robotic arm intersects with surface P_w for giving circle (C). The area of (C) is the area available for cleaning at a given base placement such that collision-free (arm-cleaning environment) continuous trajectories are feasible. However, since the robotic arm is mounted on a vertical slider Fig. 10.15, circle (C) can move along a vertical axis to sweep a surface with a geometric shape called ‘stadium’ (rectangle with semicircles on either of two opposite sides). Thus, even at a fixed base position, the workspace of the robotic arm is extended due to the presence of functional redundancy (P-joint).

10.3.1 Evaluation of Reaction Wrench

While realizing robotized grinding operation, it is inevitable to consider the difference in the geometry of the cleaning environment for precise modeling and simulation of the process. Moreover, the grinding operation generates a reaction wrench being applied to the end-effector. Since, the end-effector while cleaning different surfaces, takes different orientations, it is quite intuitive to conclude that the reaction wrenches acting on the robotic unit while cleaning these surfaces have different positions and orientations. Thus, the stability of the robotic unit is affected differently while performing the grinding operation of these surfaces.

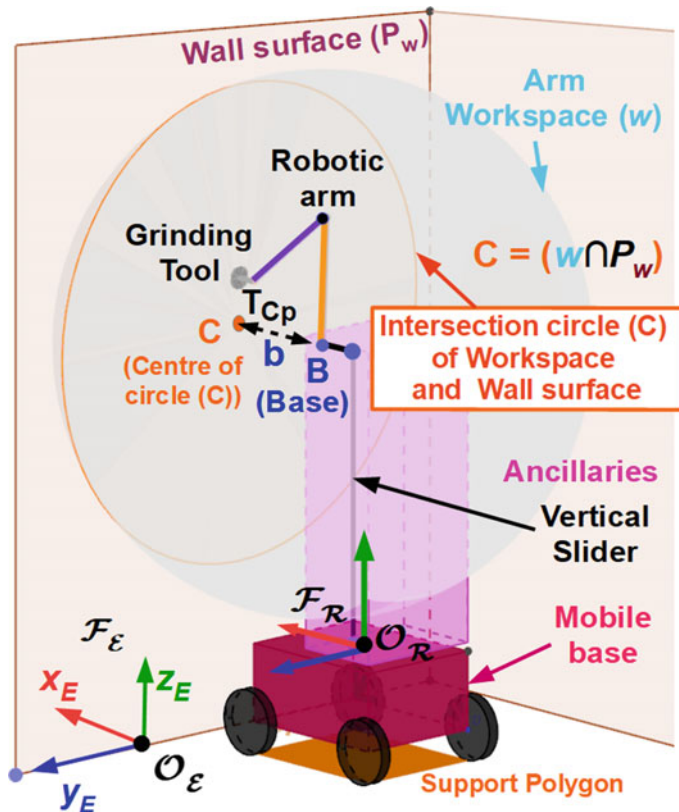


Fig. 10.14 Representation of workspace

10.3.2 Cleaning of Frontal Wall

Figure 10.16a shows reaction wrench being applied to the end-effector (tool) during the grinding operation while $\mathcal{F}_w : \{x_w, y_w, z_w\}$ indicates wall frame. Reaction wrench consists of normal reaction forces $[(F_{NZ})_w]$, tangential reaction forces $[(F_{TY})_w], [(F_{TX})_w]$ and reaction torque $[(T_Z)_w]$. Here, subscript ‘ w ’ indicates that components of the reaction wrench are expressed in wall frame (\mathcal{F}_w). Normal and tangential reaction forces are responsible for producing moments that act on the robotic unit through the end-effector. These moments and the distances responsible for creating them are summarized in Table 10.3. Also, the effect of these forces on stability are identified.

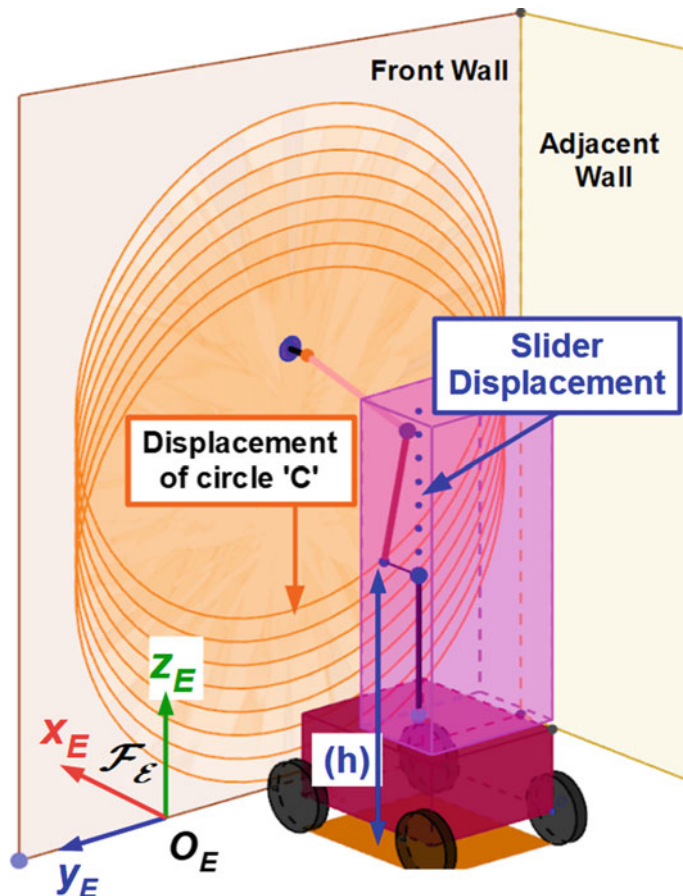


Fig. 10.15 Extension of workspace

Table 10.3 Generation of moments in wall scenario

Reaction force	Normal distance	Resulting moment	Probable effect on the robotic unit
$(F_{NZ})_w$	y_d	M_{z_S} (Moment around z_S)	Yaw motion of the robotic unit
	z_d	M_{y_S} (Moment around y_S)	Pitch motion affecting longitudinal stability
$(F_{TY})_w$	x_d	M_{z_S} (Moment around z_S)	Yaw motion causing rotation of the platform
	z_d	M_{x_S} (Moment around x_S)	Roll motion affecting lateral stability
$(F_{TX})_w$	x_d	M_{y_S} (Moment around y_S)	Pitch motion affecting longitudinal stability
	y_d	M_{x_S} (Moments around x_S)	Roll motion affecting lateral stability
		$(R)_w \cdot x_S$ (Reaction moment around x_S)	Roll motion affecting lateral stability

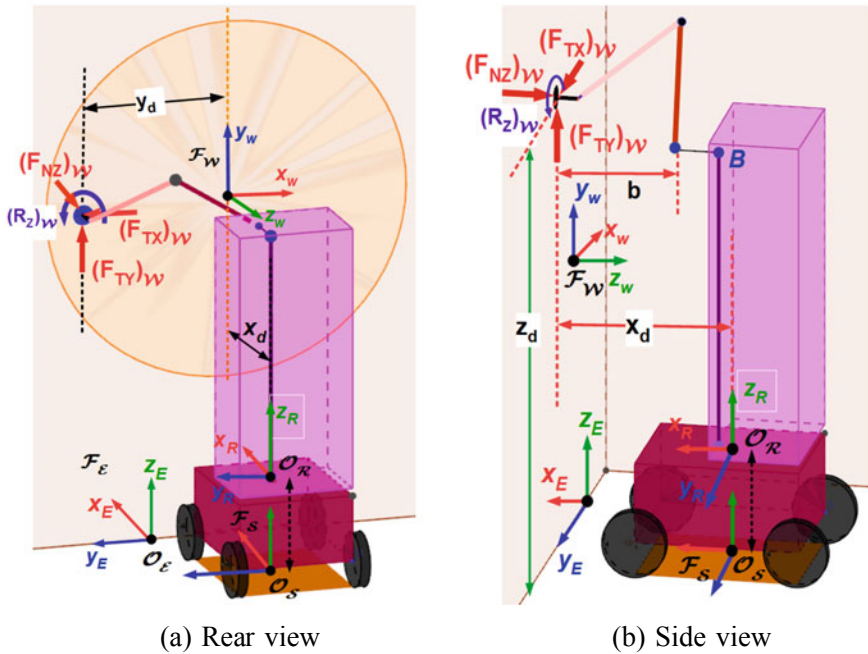


Fig. 10.16 Forces and moments acting during wall cleaning scenario

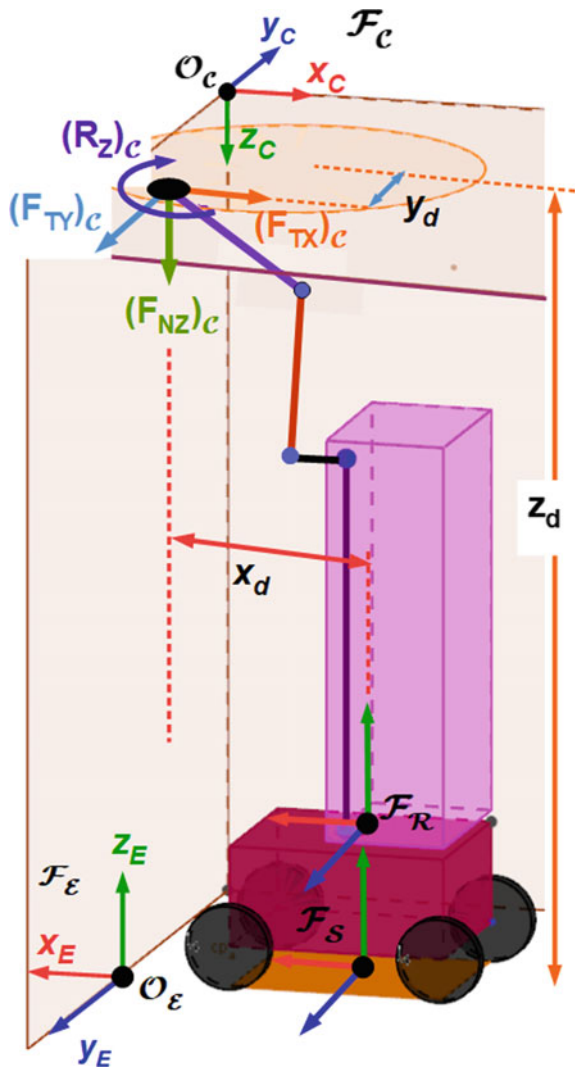
Table 10.4 Generation of moments in ceiling cleaning scenario

Reaction component	Normal distance	Resulting moment	Probable effect on the robotic unit
$(\mathbf{F}_{\mathbf{N}Z})_C$	x_d	\mathbf{M}_{yS} (Motion around y_S)	Pitch motion affecting longitudinal stability
	y_d	\mathbf{M}_{xS} (Moment around x_S)	Roll motion affecting lateral stability
$(\mathbf{F}_{\mathbf{T}Y})_C$	y_d	\mathbf{M}_{zS} (Moment around z_S)	Yaw motion of the robotic unit
	z_d	\mathbf{M}_{yS} (Moment around y_S)	Pitch motion affecting longitudinal stability
$(\mathbf{F}_{\mathbf{T}X})_C$	z_d	\mathbf{M}_{xS} (Moment around x_S)	Roll moment affecting lateral stability
	x_d	\mathbf{M}_{zS} (Moment around z_S)	Yaw motion of the robotic unit
		$(R_Z)_C \cdot z_S$ (Reaction moment around z_S)	Yaw motion of the robotic unit

10.3.3 Cleaning of ceiling

For cleaning the ceiling portion of the environment, the directions of reaction forces differ from those during cleaning frontal walls. Reaction wrench consists of normal reaction force $[(\mathbf{F}_{\mathbf{N}Z})_c]$, tangential reaction forces $[(\mathbf{F}_{\mathbf{N}Y})_c], [(\mathbf{F}_{\mathbf{N}T})_c]$ (Fig. 10.17 and Table 10.4).

Fig. 10.17 Tool forces while cleaning ceiling



10.3.4 Cleaning of Ground

Ground cleaning is a scenario, as shown in Fig. 10.18, where the cleaning surface plane P_G and the plane defined by axes x_E - y_E of the environment frame are same. Reaction wrench consists of normal reaction force $[(F_{NZ})_G]$, tangential reaction forces $[(F_{TX})_G]$, $[(F_{TY})_G]$ and reaction torque $[(R_z)_G]$. Since, tangential reaction forces lie in the plane of the support polygon, moments produced by these forces are zero in the ground plane. Thus, normal reaction force and reaction torque are the two entities that affect the stability of the robotic unit (Table 10.5).

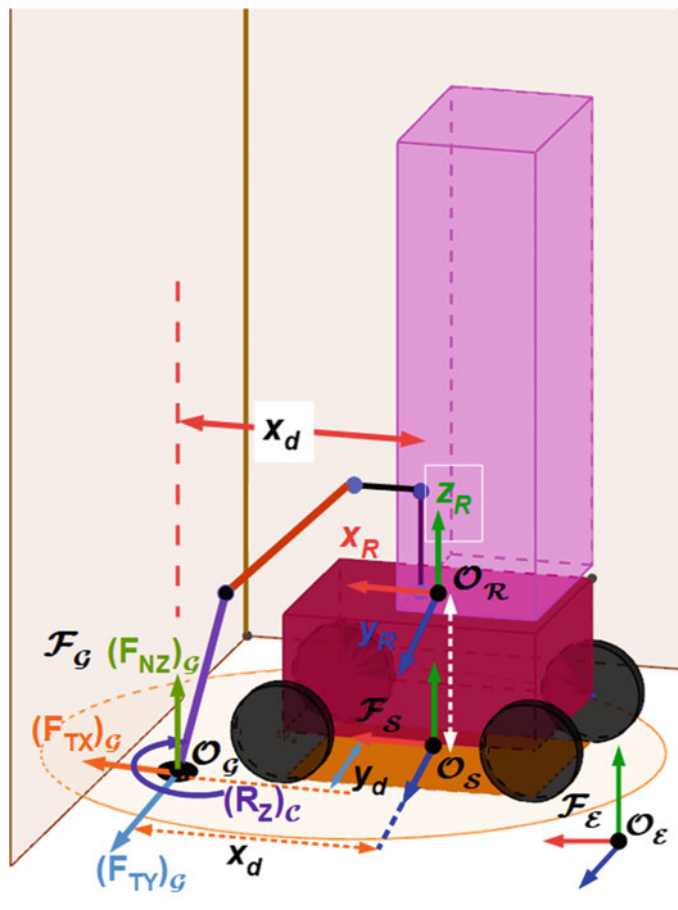


Fig. 10.18 Tool forces while cleaning ground

Table 10.5 Generation of moments in ground cleaning scenario

Reaction force	Normal distance	Resulting moment	Effect on the robotic unit
$(\mathbf{F}_{\text{NZ}})_G \cdot (\mathbf{z}_S)$	z_d	\mathbf{M}_{y_S} (Moment around \mathbf{y}_S)	Pitch moment affecting longitudinal stability
	y_d	\mathbf{M}_{x_S} (Moment around \mathbf{x}_S)	Roll motion affecting lateral stability
		$(\mathbf{R}_z)_G \cdot \mathbf{z}_S$ (Reaction moment around \mathbf{z}_S)	Yaw motion of the platform

10.3.5 Stability Criteria Based on Zero Moment Point

Issues regarding the stability of the robotic unit during grinding operation are already discussed in previous sections. In order to ensure safe and stable operation, a suitable stability margin must be defined. For a dynamically operating system, ZMP is widely used in the field of biped locomotion. ZMP is defined as a point on the ground at which the net moment of the inertial forces and the gravity forces has no component along the horizontal axes [23]. The two components of ZMP are determined by:

$$x_{zmp} = \frac{\sum_{i=1}^n m_i(\ddot{z}_i + g)x_i - \sum_{i=1}^n (m_i\ddot{x}_i)z_i - \sum_{i=1}^n (\mathcal{L}_y)_i}{\sum_{i=1}^n m_i(\ddot{z}_i + g)} \quad (10.13a)$$

$$y_{zmp} = \frac{\sum_{i=1}^n m_i(\ddot{z}_i + g)y_i - \sum_{i=1}^n (m_i\ddot{y}_i)z_i - \sum_{i=1}^n (\mathcal{L}_x)_i}{\sum_{i=1}^n m_i(\ddot{z}_i + g)} \quad (10.13b)$$

where, i indicates number of rigid bodies, (x_i, y_i, z_i) indicate coordinates of the CoM of the i th body and $(\mathcal{L}_x, \mathcal{L}_y)$ indicate the components of angular momentum derivatives, where, $\mathcal{L}_i = I_i\dot{\omega} + \omega_i \times I_i\omega_i$; ω_i is the angular velocity of link i and I_i is its inertia matrix.

From the definition of ZMP, we see that each term in the numerator represents a moment acting on the system. Thus, to integrate grinding reaction forces in ZMP, moments produced by normal and tangential reaction forces must be taken into account. These moments are already identified in the Sect. 10.3.1.

$$x_{zmp} = \frac{\sum_{i=1}^n m_i(\ddot{z}_i + g)x_i - \sum_{i=1}^n (m_i\ddot{x}_i)z_i - \sum_{i=1}^n (\mathcal{L}_y)_i - \mathbf{M}_{ys}}{\sum_{i=1}^n m_i(\ddot{z}_i + g)} \quad (10.14a)$$

$$y_{zmp} = \frac{\sum_{i=1}^n m_i(\ddot{z}_i + g)y_i - \sum_{i=1}^n (m_i\ddot{y}_i)z_i - \sum_{i=1}^n (\mathcal{L}_x)_i - \mathbf{M}_{xs}}{\sum_{i=1}^n m_i(\ddot{z}_i + g)} \quad (10.14b)$$

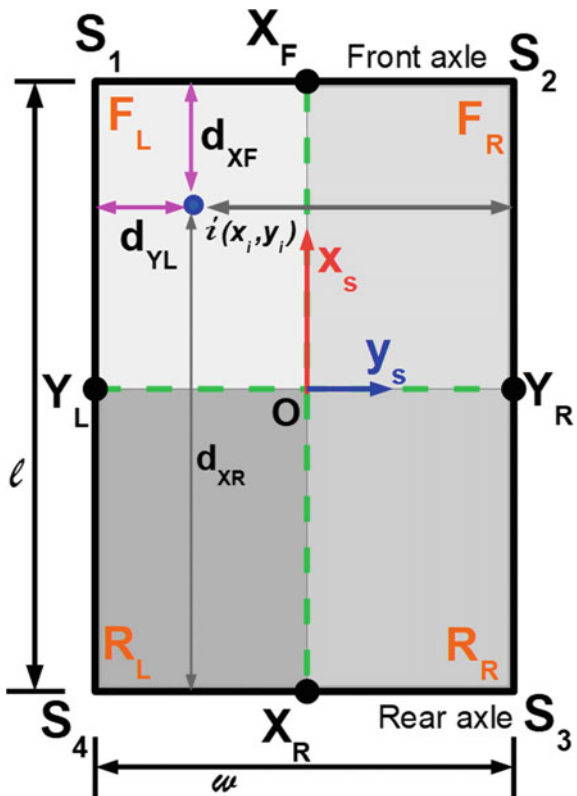
Stability Index

In our case, the mobile base has rectangular support polygon $S_1S_2S_3S_4$ of dimensions $(l \times w)$ mm with lateral and longitudinal axes $Y_L Y_R$ and $X_F X_R$ respectively (see Fig. 10.19). The polygon is divided in four quadrants namely, front-left (F_L), front-right (F_R), rear-left (R_L) and rear-right (R_R). Longitudinal (S_{long}) and lateral (S_{lat}) percentage stability of point ' i ' having ZMP coordinates (x_i, y_i) is calculated as,

$$S_{long} = \left(\frac{\min(d_{XF}, d_{XR})}{0.5 \times l} \right) \times 100, \quad S_{lat} = \left(\frac{\min(d_{YL}, d_{YR})}{0.5 \times w} \right) \times 100 \quad (10.15)$$

where, $d_{XF} = |\frac{l}{2} - x_{zmp}|$, $d_{XR} = |\frac{l}{2} + x_{zmp}|$, $d_{YL} = |\frac{w}{2} - y_{zmp}|$, $d_{YR} = |\frac{w}{2} + y_{zmp}|$.

Fig. 10.19 Notations for stability in the support polygon



10.4 Numerical Evaluation of Stability

An algorithm to carry out a numerical evaluation of stability is implemented using MATLAB computing software (Fig. 10.20). The main objective of developing numerical method is to exploit the computational efficiency of MATLAB script execution, which is much higher than that of the co-simulation with a black-box dynamic model in ADAMS. Numerical simulation is a fast way to simulate the simplified dynamics of the robot as it simplifies the process of simulation by avoiding repetitive steps like modifying the initial posture of the arm for different trajectories.

A general approach adapted in defining the algorithm is explained below:

- *Cartesian trajectory input:* Targeted operational surfaces in construction applications can be 3-dimensional in nature (curved walls, ceiling or ground). However, in the chapter, the focus is limited to non-curved surfaces. Thus, 2-D Cartesian trajectories are defined while performing simulations. Cartesian poses of the end-effector frame corresponding to trajectory coordinates serves as an input to the algorithm.

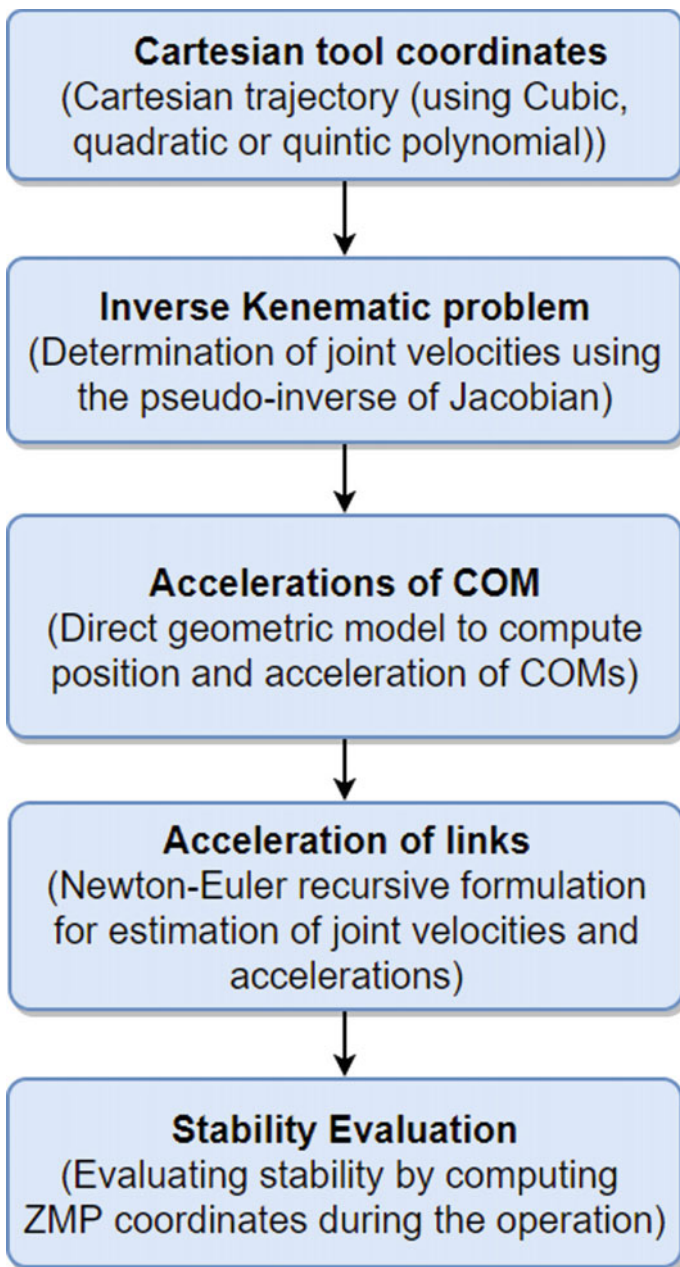


Fig. 10.20 Workflow of numerical evaluation of stability based on ZMP

Table 10.6 Features of ADAMS and MATLAB

ADAMS	MATLAB/Simulink
-Modeling of Mechanical system	
-Importing CAD parts (e.g. CATIA)	-Designing control architecture using block diagrams
-Parameterization of design	Predefined blocks
-Modeling contacts (with friction)	-Defining MATLAB function blocks within control model
-Applying external force	
-Defining input-output variables	-Data logging and processing
control variables	
-Robust dynamic solver	
-Measuring output variables	

- *IKS*: Inverse kinematics solution is needed to generate arm motion. Since, arm is kinematically redundant, IKS is determined using the redundancy resolution method that uses pseudo-inverse of the kinematic Jacobian matrix.
- *Recursive computation of link accelerations*: Angular velocities and accelerations of moving links contribute to generating dynamic effects on the robotic unit. Newton-Euler recursive algorithm is used to compute these entities.
- *Stability Evaluation*: Zero moment point for the instantaneous dynamic state of the robotic unit is computed using Eqs. 10.14a and 10.14b. Stability is then evaluated as per Eq. 10.15.

For evaluating stability during a continuous trajectory, the algorithm runs in loops defined by end positions of the trajectory.

10.5 Stability Evaluation Using Co-Simulation

Cooperation of dynamic modeling and simulation tool—ADAMS with the computing software MATLAB is a known methodology in the robotics research community. In [1], the importance of co-simulation is highlighted for the robotics domain by simulating a 2-link planar robot. Several other notable works are also mentioned. Co-simulation combines features of both software and provides a robust and efficient tool for dynamic system analysis (Fig. 10.21 and Table 10.6).

10.5.1 Development of Cosimulation Model

It is a multi-body dynamic model positioned inside cleaning environment consisting of ground, ceiling and frontal wall (Fig. 10.22). Peculiarities of the model are enlisted below:

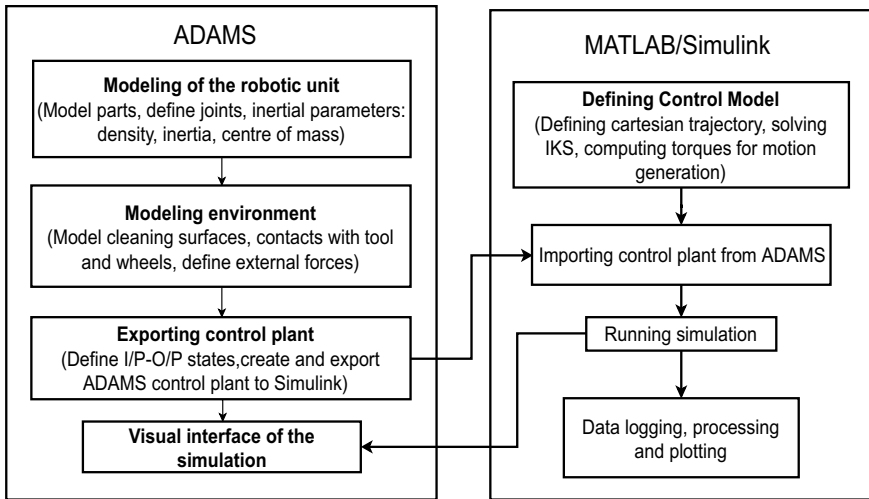


Fig. 10.21 Flow-chart of ADAMS-Matlab co-simulation

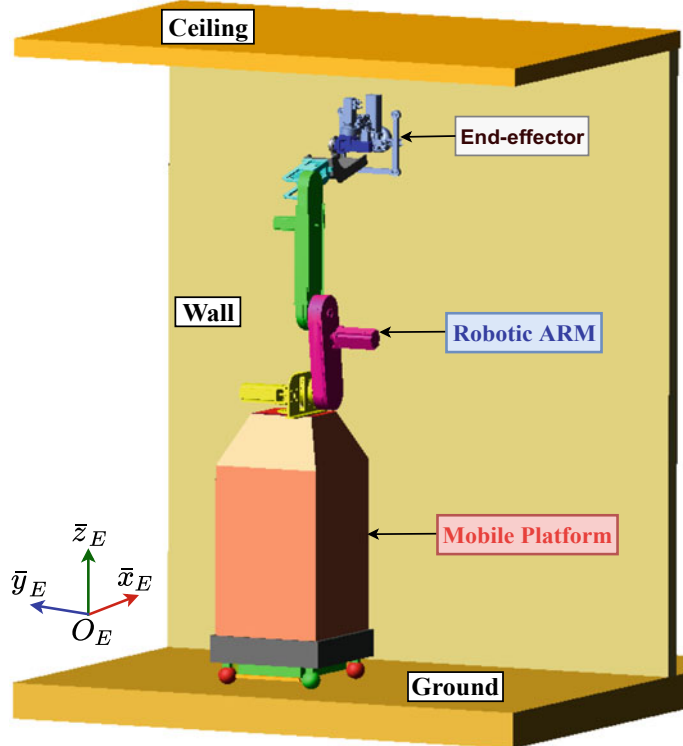


Fig. 10.22 Multibody dynamic model of the robotic unit version-2 in ADAMS

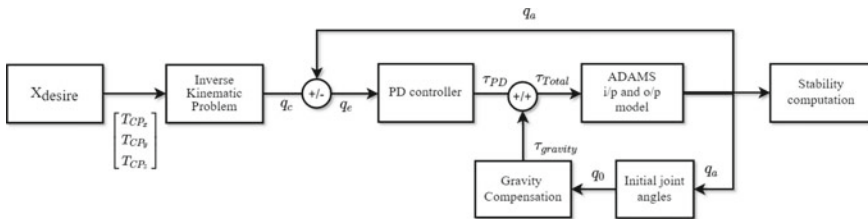


Fig. 10.23 ADAMS-simulink control model for stability evaluation

- **Part modeling:** Simple geometric shapes like sphere, cylinder, cuboid etc. are used to create a multi-body model of the robotic unit. These are solid rigid bodies that can mutually interact to generate displacement, reaction forces etc. Construction of robotic arm is performed by importing parts from CATIA as .stl files.
- **Parameterization:** It can be achieved through design variables (DV). They are used as an input (length, width etc.) to the geometric shapes. By changing the value assigned to the DVs, geometries can be quickly modified or re-positioned in the environment.
- **Joints/motion constraints:** Prismatic and revolute joints are added to create suitable joint angles between bodies. Static components are connected using fixed joints. Joints can also be parameterized to change the posture of the arm (or individual link). This is helpful in achieving suitable initial posture during co-simulation.
- **Contact modeling:** Contacts between the grinding tool and cleaning surface is created to generate reaction forces. Similarly, contacts between wheels of the mobile manipulator and ground surface are created to restrict the motion of the robotic unit in the plane and record ground reaction forces. Contact feature in ADAMS allows selecting coefficients of static and dynamic friction.
- **Inertia parameters:** Values of mass, inertia matrices and positions of CoM are determined through CAD models and are added to the components (Fig. 10.23).

q_c : command joint position.

q_a : actual joint position.

q_e : $(q_c - q_a)$ i.e. error in the joint position.

τ_{PD} : torque generated by PD-controller.

$\tau_{Gravity}$: torque input for gravity compensation.

τ_{Total} : total torque input for joint.

T_{CP_x} : x -coordinate of the tool.

T_{CP_y} : y -coordinate of the tool.

T_{CP_z} : z -coordinate of the tool.

X_{desire} : desired Cartesian coordinates of tool centre point.

For the sake of simplification, the following assumptions are made while developing the model:

1. the ground surface is even.
2. the center of mass (CoM) of the platform coincides with its center of geometry.

Table 10.7 MDH parameters

(i)	σ	θ	d	α	r
1	1	0	0	0	r_1^*
2	0	q_2	0	0	0.1
3	0	q_3	0.1	$\frac{pi}{2}$	0.9
4	0	q_4	0.6	0	0
5	0	q_5	0.6	$-\frac{pi}{2}$	0
6	0	q_6	0.13	$-\frac{pi}{2}$	0.13
7	0	q_7	0	0	0

* $r_1 = h = (0.5, 1.8) m$

3. all wheels are always in contact with the ground. i.e., no slippage of the wheels occurs.
4. the onboard manipulator is rigidly connected with the platform, and the links of the onboard manipulator are rigid.

10.5.2 Validation of Stability Evaluation Approaches

In this section, the stability of the version-1 prototype is demonstrated while performing a vertical zig-zag trajectory. MDH model of the P-6R arm architecture mounted on the robotic unit is presented in Table 10.7 and Fig. 10.24.

Figure 10.25 represents the path traversed by the tool. It traverses two trajectories—SE₁ and SE₂. Figure 10.26 shows front half of the support polygon. Axis AB defines the front axle. The black dotted lines are 25% stability lines. The figure shows variation of ZMP obtained for the cleaning trajectory.

The black line shows ZMP trace calculated using numerical approach while the pink line traces ZMP from co-simulation. The approximate overlapping of the two traces validates the numerical approach.

10.6 Conclusion

This chapter detailed the dynamic modeling of the robotic unit for stability evaluation. Initially, the robot-environment interaction model was presented to highlight the need for developing the dynamic model. Thereafter, the cleaning environment and the robotic unit were described through representative frames. This representation provided a base for developing the numerical model. Using Geogebra illustrations, the process of asbestos removal was analyzed to identify reaction wrench acting on the robotic unit during different cleaning scenarios namely wall, ceiling and ground.

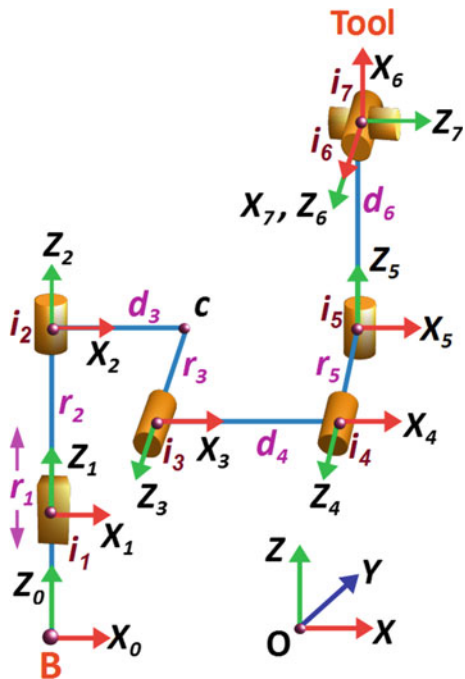


Fig. 10.24 Visualization of the P-6R architecture

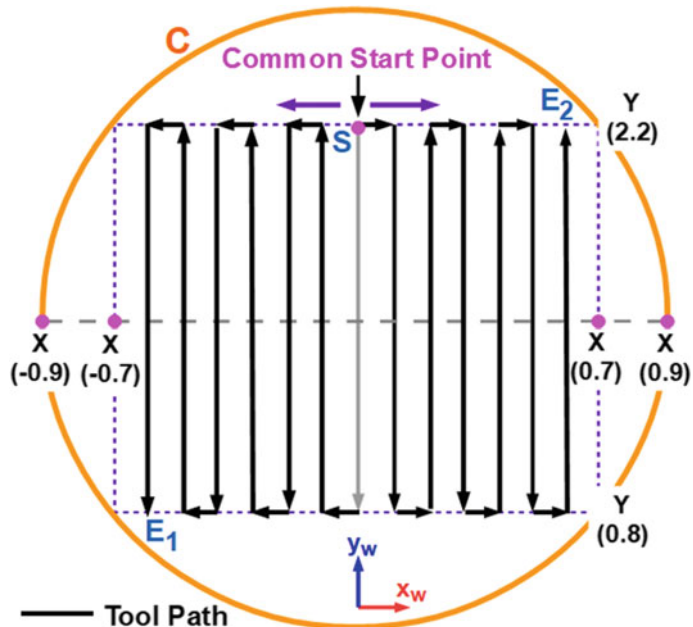
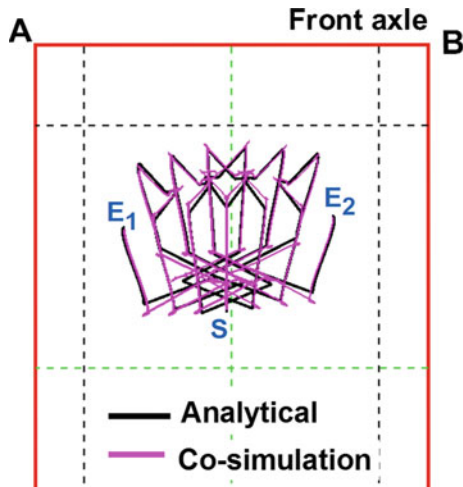


Fig. 10.25 Path traced by tool on the wall

Fig. 10.26 ZMP estimation through analytical and co-simulation



Further, the approach for the numerical evaluation of dynamic stability based on the zero moment point (ZMP) was elaborated. The steps of this approach are, kinematic modeling of the robotic unit, trajectory generation and solving the inverse kinematic problem have been explained in detail. The method of co-simulation for evaluating stability was developed so as to validate the results to be obtained by the numerical approach. A multi-body dynamic model of the robotic unit was developed in MSC ADAMS software which provides information on the behavior of the system (joint velocities, accelerations, etc.). Control commands of this model were fed in the Simulink environment.

References

1. Angel, L., Pèrez, M.P., Diaz-Quintero, C., Mendoza, C.: ADAMS/MATLAB co-simulation: dynamic systems analysis and control tool. *Appl. Mech. Mat.* **232**, 527–531 (2012)
2. Armada, E.G., Estremera, J., Santos, P.G.D.: A classification of stability margins for walking robots. In: Proceedings of International Symposium on Climbing Walking Robots, pp. 799–808 (2002). <http://digital.csic.es/handle/10261/8031>
3. Bots2ReC: HomeBots2ReC (2016). <https://www.bots2rec.eu>. Accessed on 25 Oct 2018
4. Davidson, J.K., Schweitzer, G.: A mechanics-based computer algorithm for displaying the margin of static stability in four-legged vehicles. *J. Mech. Des. Trans. ASME* **112**(4), 480–487 (1990)
5. Diaz-Calderon, A., Kelly, A.: On-line stability margin and attitude estimation for dynamic articulating mobile robots. *Int. J. Robot. Res.* **24**, 1–41 (2005)
6. Ding, X., Liu, Y., Hou, J., Ma, Q.: Online dynamic tip-over avoidance for a wheeled mobile manipulator with an improved tip-over moment stability criterion. *IEEE Access* **7**, 67632–67645 (2019)
7. Garcia, E., De Santos, P.G.: An improved energy stability margin for walking machines subject to dynamic effects, vol. 23 (2005)

8. Ghasempoor, A., Sepehri, N.: Measure of machine stability for moving base manipulators. In: Proceedings—IEEE International Conference on Robotics and Automation, vol. 3, pp. 2249–2254 (1995)
9. Hirose, S., Tsukagoshi, H., Yoneda, K.: Normalized energy stability margin and its contour of walking vehicles on rough terrain. In: Proceedings 2001 ICRA. IEEE International Conference on Robotics and Automation (Cat. No.01CH37164), vol. 1, pp. 181–186 (2001)
10. Lee, J.H., Park, J.B., Lee, B.H.: Turnover prevention of a mobile robot on uneven terrain using the concept of stability space. *Robotica* **27**(5), 641–652 (2009)
11. Lin, B.-S., Song, S.-M.: Dynamic modeling, stability and energy efficiency of a quadruped walking machine. In: IEEE International Conference on Robotics and Automation, vol. 18(11), pp. 367–373 (1993)
12. Mahdi, A., Nestinger, S.S.: Foot force criterion for robot stability, pp. 23–26 (2012)
13. McGhee, R., Frank, A.: On the stability properties of quadruped creeping gaits. *Math. Biosci.* **3**, 331–351 (1968)
14. Mcghee, R.B., Iswandhi, G.I.: Adaptive locomotion of a multilegged robot over rough terrain. *IEEE Trans. Syst. Man Cybern.* **9**(4), 176–182 (1979)
15. Messuri, D.A., Klein, C.A.: Automatic body regulation for maintaining stability of a legged vehicle during rough-terrain locomotion. *IEEE J. Robot. Autom.* **1**(3), 132–141 (1985)
16. Moosavian, S., Alipour, K.: Moment-height tip-over measure for stability analysis of mobile robotic systems. In: 2006 IEEE/RSJ International Conference on Intelligent Robots and Systems, pp. 5546–5551 (2006)
17. Moosavian, S.A.A., Alipour, K.: On the dynamic tip—over stability of wheeled mobile manipulators. *Int. J. Robot. Autom.* **22**(4) (2007)
18. Papadopoulos, E., Poulakakis, J.: Planning and model-based control for mobile manipulators. In: 2000 IEEE/RSJ International Conference on Intelligent Robots and Systems, 2000. (IROS 2000). Proceedings, vol. 3, pp. 1810–1815. IEEE (2000)
19. Papadopoulos, E., Rey, D.: A new measure of tipover stability margin for mobile manipulators. In: Proceedings of the IEEE International Conference on Robotics and Automation, Minneapolis, MN, pp. 3111–3116 (1996)
20. Roan, P.R., Burmeister, A., Rahimi, A., Holz, K., Hooper, D.: Real-world validation of three tipover algorithms for mobile robots. In: Proceedings—IEEE International Conference on Robotics and Automation, pp. 4431–4436 (2010)
21. Sreenivasan, W.B.H.: Stability and tractson control of an actively actuated micro-rover. *J. Robot. Syst.* **11**(6), 487–507 (1994)
22. Sugano, S., Huang, Q., Kato, I.: Stability criteria in controlling mobile robotic systems. In: Proceedings of 1993 IEEE/RSJ International Conference on Intelligent Robots and Systems (IROS '93), (C), pp. 832–838 (1993)
23. Vukobratovic, M., Juricic, D.: Contribution to the synthesis of biped gait. In: Proceedings of IFAC Symposium on Technical and Biological Problems on Control, Erevan, USSR (1971)
24. Yoneda, K., Hirose, S.: Stability criterion of integrated locomotion an manipulation. In: Proceedings IROS 96, pp. 870–876 (1996)